Development of a universal alignment medium for the extraction of RDCs and structure elucidation with tensorial constraints

Zur Erlangung des akademischen Grades eines
Doktors der Naturwissenschaften
(Dr. rer. nat.)

von der KIT-Fakultät für Chemie und Biowissenschaften des
Karlsruher Instituts für Technologie (KIT)
genehmigte

Dissertation

von

Dipl.-Chem. Thomas Gloge
aus Herbolzheim

Dekan: Prof. Dr. Manfred Wilhelm
Referent: Prof. Dr. Burkhard Luy
Korreferent: Prof. Dr. Michael Meier
Tag der mündlichen Prüfung: 23.04.2020

Publications

P. Tzvetkova, U. Sternberg, T. Gloge, A. Navarro-Vázquez, B. Luy, *Configuration determination by residual dipolar couplings: Accessing the full conformational space by molecular dynamics with tensorial constraints*, *Chem. Sci.*, 10(38):8774–8791, 2019.

M. E. Di Pietro, P. Tzvetkova, T. Gloge, U. Sternberg, B. Luy, *Fundamental and practical aspects of molecular dynamics using tensorial orientational constraints*, *Liq. Cryst.*, accepted manuscript, 2020.

Contents

List of Abbreviations

AIBN	2,2′-azobisisobutyronitrile
AMPS	2-(acrylamido)-2-methylpropanesulfonic acid
APP	amyloid precursor protein
APS	ammonium peroxydisulfate
BIS	N,N′-methylenebisacrylamide
BPP	Bloembergen-Purcell-Pound
BTA	benzo-1,3,5-tricarboxamides
CHAPSO	3-[(3-cholamidopropyl)dimethylammonio]-2-hydroxy-1-propane-sulfonate
CLIP-HSQC	clean in-phase HSQC
COSMOS	computer simulation of molecular structures
CSA	chemical shift anisotropy
DCM	dichloromethane
DHPC	dimyristoylphospatidylcholine
DI	de-ionized
DIODPC	1,2-di-O-dodecyl-sn-glycero-3-phosphocholine
DMAA	N,N-dimethylacrylamide
DMPC	dihexanoylphosphatidylcholine
DMSO	dimethylsulfoxide

DTT	dithiothreitol
EFG	electric field gradient
FID	free induction decay
FWHM	full width at half maximum
GO	graphene oxide
HSQC	heteronuclear single-quantum correlation
INEPT	insensitive nuclei enhanced by polarization transfer
MAS	magic angle spinning
MD	molecular dynamics
MDOC	molecular dynamics with orientational constraints
ME	maximum entropy
MS	mass spectrometry
NMR	nuclear magnetic resonance
NOE	nuclear Overhauser enhancement
NQR	nuclear quadrupole resonance
PAA	poly(acrylamide)
PAN	poly(acrylonitrile)
PAS	principal axis system
PAGE	poly(acrylamide gel electrophoresis)
PBLG	poly-γ-benzyl-L-glutamate
PCBLL	poly-ϵ-carbobenzyloxy-L-Lysine
PDMS	poly(dimethylsiloxane)
P.E. COSY	primitive exclusive COSY
P.E. HSQC	primitive exclusive HSQC

PELG	poly-γ-ethyl-L-glutamate
PEO	poly(ethylene oxide)
PEO-DA	poly(ethylene oxide)-diacrylate
PMMA	poly(methyl methacrylate)
ppm	parts per million
PRE	paramagnetic relaxation enhancement
PS	poly(styrene)
PVAC	poly(vinylacetate)
RCSA	residual chemical shift anisotropy
RDC	residual dipolar coupling
rf	radio-frequency
RQC	residual quadrupolar coupling
SAG	strain-induced alignment in a gel
SEC	size exclusion chromatography
S/N	signal-to-noise-ratio
SVD	singular value decomposition
TEA	triethylamine
TEMED	tetramethylethylenediamine
TFE	trifluoroethanol
TFEMA	trifluoroethyl methacrylate
UV	ultraviolet
VAS	variable angle spinning
XRD	X-ray diffraction

1 | Abstract

In high resolution nuclear magnetic resonance (NMR) spectroscopy, residual anisotropic parameters like residual dipolar couplings (RDCs), residual chemical shift anisotropies (RCSAs), and residual quadrupolar couplings (RQCs) provide valuable information complementary to parameters derived in isotropic (standard) conditions for the structure elucidation and refinement. For their measurement, homogeneous and appropriate weak partial alignment in so-called alignment media are needed to induce the suitable anisotropy. Although a multitude of different alignment media does exist, they are applied rather seldom, because common alignment media presently available are either specifically developed for application with small organic molecules or for big macromolecules and their use is restricted to a narrow range of certain solvents.

Besides liquid crystalline phases, mechanically strained polymer gels are used for the adequate alignment of solutes. The preparation of samples can take up to weeks and even months, which renders these methods rather unfavorable for commercial use. Earlier investigations with poly(ethylene oxide) (PEO) hydrogels showed considerable swelling in a wide variety of solvents. Unfortunately, cross-linking procedures required the use of β- or γ-radiation, or radiation with ultraviolet (UV) light for weeks. This work presents a quick, optimized synthesis route to yield homogeneous alignment media sticks based on PEO that can be followed using standard equipment available in every modern laboratory. The swelling compatibility in a large variety of pure solvents and mixtures is compared and evaluated and the influence of the mass content during the cross-linking is demonstrated.

By using a starting material with small dispersity, control over the distribution of inter cross-link chain lengths is introduced, yielding quite homogeneous gels with narrow line-widths. Different mass containing swollen PEO-DA gels are therefore investigated with double quantum NMR (DQ-NMR) to reveal the amount of cross-linked network fractions and the sol fraction. PEO-DA allows inducing scalable anisotropy both in compressing as well as in stretching devices and is successfully applied with pure solvents and mixtures in this work. Here, a method is introduced, allowing fast equilibration and transfer into the sample

tubes. In accordance with parameter fine-tuning, cross-linked PEO-DA is shown to be suitable for the alignment of solutes reaching from small natural products up to proteins, making it a universal alignment medium.

The existing manual method for extraction of couplings is time-consuming and subjective. A method for the semi-automated extraction of couplings is introduced, utilizing a procedure based on autocorrelation. For the data evaluation of RDCs on small organic molecules, molecular dynamics with orientational constraints (MDOC), is applied. It enables the elucidation of the conformational space based on experimentally derived anisotropic data that is incorporated as tensorial orienting constraints into the force field. When solute molecules show flexibility and occur in different conformations, data interpretation with so far existing approaches can be difficult because of the averaged nature of extracted data. In these cases the MDOC approach is preferred as the RDC evaluation is not hampered based on the modeling of choice.

2 | Zusammenfassung

In der hochauflösenden Kernresonanzspektroskopie (*engl.*: nuclear magnetic resonance (NMR) spektroscopy) liefern rest-anisotrope Parameter wie dipolare Restkopplungen (*engl.*: residual dipolar couplings (RDCs)), restliche chemische Verschiebungsanisotropien (*engl.*: residual chemical shift anisotropies (RCSAs)) und quadrupolare Restkopplungen (*engl.*: residual quadrupolar couplings (RQCs)) wertvolle Informationen, die zu den unter isotropen (standard-) Bedingungen gemessenen NMR Parametern für die Strukturverfeinerung und -aufklärung komplementär sind. Daher ist ein homogenes und ausreichend schwaches sogenanntes *Alignment* in sogenannten Alignmentmedien erforderlich, um eine geringe Anisotropie in der Probe zu induzieren. Obwohl eine Vielzahl unterschiedlicher Alignmentmedien und -methoden existiert, werden sie recht selten genutzt, da die derzeit verfügbaren üblichen Alignmentmedien entweder speziell für die Anwendung mit kleinen organischen Molekülen oder für große (Bio-) Makromoleküle entwickelt wurden und ihre Verwendung auf bestimmte Lösungsmittel beschränkt ist.

Neben flüssigkristallinen Phasen werden mechanisch gestreckte oder gestauchte Polymergele zur adäquaten Ausrichtung von gelösten Stoffen eingesetzt. Oft kann die Präparation von Proben bis zum Äquilibrieren bis zu Wochen und Monaten dauern, was die Nutzung dieser Methoden im kommerziellen Bereich eher erschwert. Frühere Untersuchungen mit vernetzten Polyethylenoxid-Hydrogelen (PEO) zeigten eine erhebliche Quellung in einer Vielzahl von Lösungsmitteln. Leider erforderte die Vernetzung die Verwendung von β- oder γ-Strahlung oder wochenlange Bestrahlung mit ultraviolettem Licht. In dieser Arbeit wird ein schneller Syntheseweg optimiert und vorgestellt, um homogene Gelstäbchen auf Basis von PEO als Alignmentmedien herzustellen, der mit den in jedem modernen Labor verfügbaren Mitteln nachvollzogen werden kann. Darüberhinaus wird das Quellverhalten in einer Vielzahl von reinen Lösungsmitteln und Gemischen aufgezeigt und der Einfluss des Massengehalts während der Vernetzung untersucht.

Durch Verwendung eines Ausgangsmaterials mit geringer Dispersität wird Kontrolle über die Verteilung der Kettenlängen zwischen den Vernetzungspunkten ermöglicht, wodurch homogene Gele mit schmalen Linienbreiten erhalten werden. Gequollene PEO-DA-Gele, die mit unterschiedlichem Massenanteil vernetzt wur-

den, werden zusätzlich mit Doppelquanten NMR (DQ-NMR) untersucht, um das Verhältnis von vernetztem Anteil und der Solfraktion inklusive der Defekte im Netzwerk zu ermitteln. Die Anwendbarkeit von PEO-DA in skalierbaren Streck- und Kompressionsapparaturen wird präsentiert und erfolgreich mit reinen Lösungsmitteln und Gemischen demonstriert. Hierbei wird eine Methode eingeführt, die ein schnelles externes Äquilibrieren und Übertragen in die Probenröhrchen ermöglicht. Es wird gezeigt, dass durch Feinabstimmung verschiedener Parameter, vernetztes PEO-DA als universelles Alignmentmedium für gelöste Substanzen, die von kleinen Naturstoffen bis zu Proteinen reichen, geeignet ist.

Die bisher angewandte Methode der manuellen Extraktion von Kopplungen ist zeitaufwändig und subjektiv. Es wird ein Verfahren zur halbautomatischen Extraktion von Kopplungen vorgestellt, welches mathematisch auf der Anwendung von Kreuz- bzw. Autokorrelationen beruht. Für die Auswertung von RDCs an kleinen organischen Molekülen, wurden Moleküldynamiksimulationen mit orientierenden Randbedingungen evaluiert und angewandt (*engl.*: molecular dynamics with orientational constraints, MDOC), einer Molekülmechanik-Methode, die ohne Annahmen über die Ausgangskonformation auskommt. Die Methode ermöglicht die Bestimmung des Konformationsraums anhand experimenteller anisotroper Daten, die als tensoriell orientierende Bedingungen in das Kraftfeld einfließen. Wenn gelöste Moleküle flexibel sind und in unterschiedlichen Konformationen auftreten, ist die Interpretation der Daten mit bisherigen Methoden aufgrund der gemittelten Natur der extrahierten Daten schwierig und Annahmen über auftretende Konformere müssen getroffen werden, die unter Umständen nicht gerechtfertigt sind. In diesen Fällen ist der MDOC Ansatz vorzuziehen, da die Interpretation der RDCs nicht durch die Wahl der Modellierung beeinflusst wird.

3 | Introduction

One of the most important tasks in analytical science is the structural elucidation of matter. This is the precondition for any progress whether to identify or recognize new interesting substances, to control the outcome of syntheses or to improve the properties of materials. Until the beginning of the 20th century methods of thermodynamics and kinetics provided insights only in the bulk behavior of matter. Then, within the last century spectroscopic methods have been invented to unclose an atomistic view regarding the characteristics of individual molecules.[1] Furthermore, the progressing computer technology accelerated the way, extracted data can be processed and allows *in silico* simulations to deliver not only structural but also dynamical information. The most prominent methods for structural elucidation are mass spectrometry (MS), X-ray diffraction (XRD) and NMR spectroscopy. In contrast to MS, with the last two methods direct information about spatial distribution and chemical bonds between atoms can be obtained. XRD determines the electron density and by this allows drawing conclusions about the atomic structure, whereas NMR gives insights into arrangements and connectivities of atoms with nuclear spins. For X-ray diffractometric investigations, the substance to be examined must be present either as a single crystal or powder, yet materials often do not crystallize. The actual disadvantage of the XRD structure analysis, however, is the requirement for a single crystal. Since most of the times one is interested in the structural features in dilute solutions, potentially large structural deviations may arise, when the structure in solid crystalline state is explored. Indeed, most natural substances are highly diluted in solution and cannot be crystallized or prepared as a solid.

X-ray structure analysis, in contrast to NMR spectroscopy, is therefore generally unsuitable to analyze the occurrence of different conformations in solution. Hence, with NMR spectroscopy, it is possible to study substances in different condensed phases (liquids, solids, liquid crystals, solid-liquid phases and even gases) and temperatures. In this way, one does not only gain information about the static arrangement of the atoms in the molecule, but also about their dynamics, leading to a deeper understanding of molecular functionality.

Already in the early 1980s, conformation and configuration were determined

simultaneously: oligonucleotide[2] and biopolymer[3,4] structures were determined exploiting distances from nuclear Overhauser enhancement (NOE) measurements and dihedral angles derived from extracted ^3J couplings. In the field of low molecular weight compounds (with molecular weights below $800\,{}^{\mathrm{g}}/_{\mathrm{mol}}$), the spectroscopic parameters that are measured by liquid state NMR spectroscopy are usually chemical shifts (δ), scalar couplings (J) and NOE distances. However, various conformations present within the NMR timescale render precise structural elucidation difficult or even impossible, because only an average of these parameters is obtained. Furthermore, in experiments to determine the constitution, configuration and conformation with NMR spectroscopy, highly mobile molecules encounter difficulties in assigning, for example, diastereotopic protons.

Additionally, these *classical* NMR parameters (δ, J, and NOE) in liquid state NMR spectroscopy generate information only within a short range. The reason behind this is that chemical shifts are affected mostly by nuclei only within the first and second order sphere of surrounding atoms around the nucleus. Exploiting ^3J couplings to gain dihedral relations via the Karplus equation requires NMR active spins covalently connected to each other via three bonds. The NOE distances are commonly found only up to a distance of 5 Å to each other.

The correlation of distant parts within molecules that may belong to different spin systems is amenable by so-called *anisotropic* parameters, which depend not only on the distance but also the orientation of the interacting spins relative to the external magnetic field $\vec{B}_0$. In solids, molecules possess a high degree of order and are strongly aligned with each other. In solid state NMR, hence far-ranging interactions between the spins via dipolar (DC) and quadrupolar (QC) couplings lead to complex spectra and increased line-broadening due to chemical shift anisotropy (CSA).

To gain the orientation-dependent structural information while maintaining the simplicity of liquid state NMR spectra, the degree of order needs to be downscaled to establish a so-called *weak* or *partial alignment* of the solutes. For this reason, homogeneous and appropriate so-called *alignment media* are needed to induce the suitable anisotropy avoiding extensive line-broadening. This way, *residual* anisotropic parameters like RDCs, RQCs and RCSAs are accessible with adequate accuracy and have provided valuable information for the structure refinement of biomacromolecules[5,6] as well as for small organic molecules[7–13] and are still subject of ongoing research.[14]

When partially aligned, with regard to rigid molecules, a single so-called *global molecular order* ($\mathbf{S}$) or *alignment tensor* ($\mathbf{A}$) is defined by the molecular topology. The most straightforward to measure residual anisotropic parameters that correspond to this alignment tensor are RDCs. The evaluation of RDCs is achieved by fitting the experimental data to the alignment tensors of a set of putative struc-

tures. The most plausible proposal is then represented by the best correlation between experimental and back-calculated data. The fitting is commonly carried out by a least square fit singular value decomposition (SVD)[15] but also other methods do exist.[16–22]

Since the turn of the millennium,[23] anisotropic NMR parameters have solved stereochemical issues within numerous cases concerning prochiral assignment, conformation, relative and even absolute configuration. Nevertheless, the methodology is far from being used routinely, *e.g.* in industry, and has remained an academic problem. There are two main reasons hampering the general applicability. First, the alignment media presently available are either specifically developed for application with small organic molecules or for big macromolecules. Furthermore, their use is restricted to certain solvents.[23] When working with various types of compounds, the arising questions, concerning solubility, availability and applicability hinder effective workflows for a broad commercial use. A second reason is the evaluation of the gained data. As stated above, the *single tensor* approach depends on a proposed model that is fitted to the experimental data, which means that the outcome correlates with the reliability of the model. Since molecules often show conformational flexibility, even so-called *multi tensor* approaches, where a small set of (weighted) lowest energy structures is assumed to reflect the observed measurements, may be ill-defined.[24]

3.1 Outline

The scope of this thesis is to provide a general protocol for both a universally applicable alignment medium and a new type of molecular dynamics with orientational constraints (MDOC) as key elements for the alignment, measurement, extraction and data interpretation to open a way for a broader use of residual anisotropic NMR parameters. Therefore in the introduction of chapter 4 a brief outline on basic NMR theory and anisotropic parameters is given. Furthermore, a set of experiments is explained that allow the extraction of RDCs of solute and alignment medium and the monitoring of alignment strength throughout the sample via residual quadrupolar couplings (RQCs).

After a brief overview on existing alignment methods and media in chapter 5, chapter 6 is dedicated to the invention of covalently cross-linked poly(ethylene oxide) (PEO) as a new versatile alignment medium. Earlier investigations with PEO hydrogels[a] that were covalently cross-linked by irradiation with β- or γ-rays have shown considerable swelling in a wide variety of solvents[25] ranging from po-

[a] In this work the term *hydrogel* is used even when the swollen material may not contain any water, since the correct term amphigel describing the amphiphilic properties of cross-linked PEO networks is used rather seldom.

lar, like water, to apolar solvents, like toluene. Via a free radical polymerization route, based on an α,β-bisacrylated PEO derivative, an alternative reaction protocol has been developed to avoid the use of radiation sources. In this chapter, it is described, how homogeneous cross-linked PEO-DA sticks of different cross-link density for structure elucidation are derived avoiding significant amounts of residual radical species in the polymer matrix. The suitability of PEO-DA as an alignment medium for the use in a variety of solvents and mixtures is demonstrated with six different molecules ranging from small organic molecules (sucrose, borneol, ethinylestradiol) over a peptide derivative (Gramicidin $S^{D\text{-}Pro\text{-}SW}$) to proteins (amyloid precursor protein and malectin) in chapter 7. Here, also a new method for the semi-automatic extraction of couplings is introduced and compared with the existing manual method.

In chapter 8, the received RDCs are used to gain information about both structure and dynamics. This is achieved with a new type of molecular dynamics (MD) calculations that is implemented in the COSMOS software (MDOC). In order to evaluate the new method and to check its reliability, calculations with one bond RDCs are demonstrated with selected examples (borneol, spiroindene, staurosporine, ethinylestradiol).

In chapter 9 the properties of the PEO-DA are evaluated by means of physical properties and the swelling behavior in different solvents and mixtures is discussed. Since the initial starting material used was PEO with a low dispersity Đ and the cross-linking of the α,β-bisacrylated PEO was carried out without additional cross-linking agents, the distribution of inter-chain links is assumed to be less stochastic. To investigate the ratio of the different network fractions represented by cross-linked chains, dangling ends and highly mobile components, double quantum relaxometric measurements were carried out. In the last chapter, the outcome of the study is summarized and the results are discussed.

4 | NMR Theory

NMR spectroscopy is, as described in the introduction, the method of choice, when the investigation of relative configuration and conformation of organic molecules is desired. This chapter aims to introduce the basic principles and theoretical background of NMR spectroscopy. Therefore, the measurable parameters like chemical shift, scalar, dipolar and quadrupolar couplings are described. For a better understanding of alignment media in chapter 5 and the description of MDOC in chapter 8, the phenomena isotropy, anisotropy, and residual anisotropy are introduced and the influence on the above parameters is explained. Furthermore NMR experiments for the extraction of couplings and the monitoring of the alignment state are presented.

4.1 Nuclear spin and the resonance condition

4.1.1 Quantum mechanical description

Spin is a form of angular momentum, but generated without apparent rotation and a quantum mechanical intrinsic property. Nuclei with a non-zero nuclear spin quantum number $I \neq 0$ possess an intrinsic or nuclear angular momentum $\vec{I}$ (the *spin*), which is quantized[26]

$$|\vec{I}| = \hbar\sqrt{I(I+1)} \tag{4.1}$$

with Planck's constant h divided by 2π (the so-called reduced Planck constant $\hbar$). The nuclear spin quantum number I of known NMR active nuclides takes up half-integer ($^1/_2$, $^3/_2$, $^5/_2$, $^7/_2$, ...) or – more seldom – integer values (1, 3, 4, ..., 7) [a]. The angular momentum $\vec{I}$ leads to a magnetic moment $\vec{\mu}$, which is related by the expression:

$$\vec{\mu} \;=\; \gamma \cdot \vec{I} \tag{4.2}$$

[a] So far, no stable nuclide is known with a nuclear spin quantum number $I = 2$ in its nuclear ground state.

with the magnetogyric ratio γ (also called the gyromagnetic ratio, in $^{rad}/_{T\,s}$) of the particular nucleus. The quantization allows the z-component of the nuclear angular momentum $\vec{I}_z$ to take up only quantum mechanically allowed eigenvalues

$$I_z \;=\; \hbar \cdot m_l \tag{4.3}$$

m_l is the magnetic quantum number and characterizes the corresponding eigenstates of the nucleus. The magnetic quantum number m_l is related to the spin quantum number I according to the condition

$$m_l \;=\; I, I-1, I-2, \ldots, -I \tag{4.4}$$

The spin quantum number I sets the number of possible eigenstates or energy levels $(2I+1)$ whereas the strength of the magnetic moment and therefore the distance between these levels (Equation 4.7) is determined by the magnetogyric ratio γ. According to Equation 4.2, the z-component of the nuclear magnetic moment μ_z is expressed by

$$\mu_z \;=\; m_l \cdot \gamma \cdot \hbar \tag{4.5}$$

Nuclei with the spin quantum number $I = {}^1/_2$ (*e.g.* ^{1}H, ^{13}C, ^{15}N) exist only in one of two eigen- or spin states that are degenerate in the absence of magnetic fields. In a static magnetic field $\vec{B}_0$ the potential energy of a nucleus possessing a magnetic moment μ is:

$$E \;=\; -\mu \cdot \vec{B}_0 \;=\; -m_l \cdot \gamma \cdot \hbar \cdot \vec{B}_0 \tag{4.6}$$

For nuclei with a positive magnetogyric ratio γ, the energy difference between the upper (excited) state, denoted with β ($m_l = -{}^1/_2$) and the lower (ground) state, denoted with α ($m_l = +{}^1/_2$) is evaluated with Equation 4.6:

$$\Delta E \;=\; \gamma \cdot \hbar \cdot \vec{B}_0 \tag{4.7}$$

The energy gap between the nuclear spin states is proportional to the strength of the static magnetic field $\vec{B}_0$ and to the so-called *nuclear Zeeman splitting* in analogy to the Zeeman effect, which describes the splitting of electronic levels in magnetic fields. The energy needed to stimulate a transition between the states is calculated with the Bohr frequency condition ($\Delta E = h \cdot \nu$) leading to the *resonance condition*[27]

$$\nu_0 \;=\; \frac{\gamma \cdot \vec{B}_0}{2\pi} \quad \text{or} \quad \omega_0 \;=\; \gamma \cdot \vec{B}_0 \tag{4.8}$$

For protons with $\gamma_{\mathrm{H}} = 2.675 \times 10^8\ \mathrm{T^{-1}s^{-1}}$ the so-called *Larmor* frequency ν_0 is 500 MHz at a field strength $\vec{B}_0$ of 11.7 T. The energy needed for a transition is so

low that at room temperature according to the Boltzmann equation (Equation 9.2) the occupation difference is only about few parts per million (see also section 9.1).

4.1.2 Measurement principle

To meet the resonance condition, one can basically vary the magnetic flux density $\vec{B_0}$ at a constant transmission frequency (*field sweep method*) or the transmission frequency ν_1 at a constant magnetic field (*frequency sweep method*), while continuously recording a spectrum. These so-called continuous wave (CW) methods were mainly used until the end of the sixties. For practical reasons they were replaced by the pulse Fourier transform method developed by Ernst, Anderson, *et al.*[28,29] Here, NMR active nuclei with the same Larmor frequency are simultaneously excited in the sample by a radio-frequency (rf) pulse. One takes advantage of the fact that a short time-switched rf pulse contains a continuous frequency band centered around its transmission frequency ν_1. The width of the frequency band required for excitation is inversely proportional to the duty cycle length τ_p, which in practice is on the order of a few microseconds (µs). Furthermore, the shape and duration of pulses can be chosen to increase the mentioned bandwidths (broadband excitation) or to selectively excite, suppress or decouple areas of interest. Therefore, the possibility to apply sequences of pulses gave rise to elaborate one-dimensional experiments and enabled the acquisition of two- and higher dimensional NMR spectra (see section 4.5).

The radio-frequency pulses induce oscillating magnetic fields, which interact with the precessing nuclei (see section 9.1 and section 9.2), leading to a very complex movement of the magnetization. Their description by the Bloch equations can be greatly simplified by using a rotating coordinate system whose transversal components x and y inversely rotate around z with the Larmor frequency. In this so-called rotating frame, the rf pulses are characterized not by their field strength and duration but by the axis of rotation and the flipping angle exerted on the net magnetization of the spins (see Figure 9.3).

When recording so-called one-dimensional (1D) spectra with the pulse Fourier transform method, directly after the rf pulse, a so-called free induction decay (FID) is recorded that contains all resonance frequencies of the sample. A scheme of the pulse sequence for the most simple version of a one-dimensional NMR experiment to acquire an FID is shown in Figure 4.1.

As the FID represents the decay in intensity with time, it is Fourier transformed to obtain the spectral information in the frequency domain.

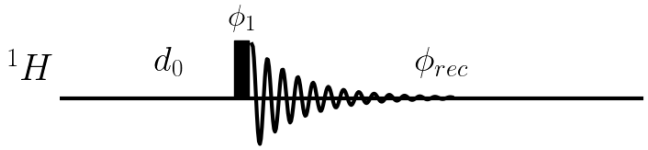

Figure 4.1: Sequence of a 1D-^{1}H NMR experiment: d_0 is a delay, chosen such that the equilibrium magnetization is restored. The pulse is illustrated as a vertical rectangle, its phase ϕ_1 describes the effective flip angle and rotation axis (*e.g.* 90°_x), directly afterwards the FID is recorded. The receiver phase is denoted by ϕ_{rec}. The Larmor frequency of the operating channel is indicated by the nucleus on the left (^{1}H).

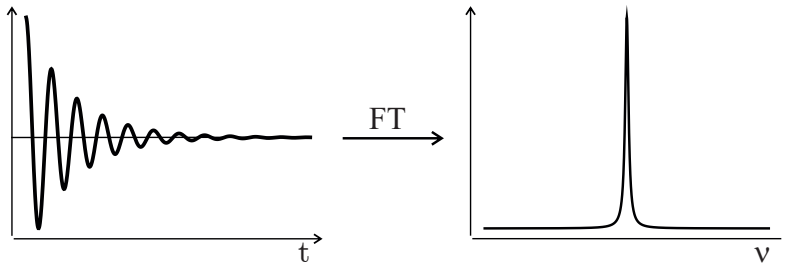

Figure 4.2: Time domain data contained in the FID is Fourier transformed to the frequency domain resulting in a (nuclear magnetic resonance) frequency spectrum, where chemical shifts are represented by peaks at the corresponding frequency.

4.2 NMR parameters

The most common parameters gained by NMR spectroscopy are the chemical shifts (δ), scalar (J) couplings and inter-spin distances determined with the NOE.

4.2.1 Chemical shift

As stated above, nuclei with a magnetic moment μ have characteristic Larmor frequencies, where transitions are induced when the resonance condition is obeyed, that is, matching the energy difference between the occurring spin states. The interesting feature of NMR spectroscopy for chemists surely is not the distinction of miscellaneous nuclides on the basis of their different magnetogyric ratios but the possibility to differentiate nuclei according to their electronic environment. Under the influence of the outer magnetic field $\vec{B_0}$, the electrons create a counteracting magnetic field $\vec{B_{e^-}}$. The nuclei experience a local magnetic field $\vec{B_{loc}}$ that deviates from $\vec{B_0}$ by the amount of $\vec{B_{e^-}}$.

$$\vec{B_{loc}} = \vec{B_0} - \vec{B_{e^-}} \tag{4.9}$$

The outer static magnetic field $\vec{B_0}$ is shielded at the location of the nucleus depending on the electron density.

$$\vec{B_{\text{loc}}} = \vec{B_0} - \boldsymbol{\sigma}\vec{B_0} = \vec{B_0}(1 - \boldsymbol{\sigma}) \tag{4.10}$$

The term $\boldsymbol{\sigma}$ is called *shielding* or *screening* constant, a non-dimensional anisotropic tensorial quantity that has a directional dependence with respect to $\vec{B_0}$. Its diagonal form is

$$\boldsymbol{\sigma} = \begin{pmatrix} \sigma_{11} & 0 & 0 \\ 0 & \sigma_{22} & 0 \\ 0 & 0 & \sigma_{33} \end{pmatrix} \tag{4.11}$$

In solids, generally $\sigma_{11} \neq \sigma_{22} \neq \sigma_{33}$, but in liquids, fast molecular tumbling within the time-scale of the NMR experiment leads to an averaged isotropic shielding value that is represented by the average of the trace of the symmetric matrix:

$$\sigma_{iso} = \frac{Tr(\boldsymbol{\sigma})}{3} = \frac{\sigma_{11} + \sigma_{22} + \sigma_{33}}{3} \tag{4.12}$$

Unperturbed electrons from spherical s-orbitals lead to a diamagnetic (attenuating) contribution σ_{dia} that can be calculated by the Lamb formula from the electron density ρ(r) around the nucleus.

$$\boldsymbol{\sigma} = \frac{\mu_0 e^2}{3m_e} \int_0^\infty r\rho(r)dr \tag{4.13}$$

When the spherical symmetry of the electron distribution in molecules is perturbed, the diamagnetic effect is reduced. This diminution corresponds to a paramagnetic contribution, which amplifies the effect of the static outer magnetic field $\vec{B_0}$. The shielding $\boldsymbol{\sigma}$ in molecules then coincides with the sum of diamagnetic and paramagnetic components.

$$\boldsymbol{\sigma} = \boldsymbol{\sigma}_{dia} + \boldsymbol{\sigma}_{para} \tag{4.14}$$

Since it is not possible to evaluate absolute values for the shielding experimentally, it is convenient to determine the resonance frequencies *relative* to a reference. These so-called *offset* frequencies still depend on the field strength of the spectrometer. To be able to compare NMR spectra, the so-called *chemical shift* δ in parts per million (ppm) is introduced by determining the deviation of observed signals (ν_{sample}) relative to the position of a reference compound (ν_{ref}) and then dividing this difference by the resonance frequency of the reference ν_{ref},

$$\delta = \frac{\nu_{sample} - \nu_{ref}}{\nu_{ref}} \times 10^6 \tag{4.15}$$

The resulting quantity reflects the influence of the chemical environment on the static magnetic field, which is *shifted* on the order of ppm.

4.2.2 Anisotropy of the chemical shift

Only scarce molecules are symmetric and therefore in general the distribution of electrons is not symmetric in chemical compounds. For this reason the shielding $\boldsymbol{\sigma}$ introduced by the electrons is directionally dependent and accordingly the chemical shift $\boldsymbol{\delta}$ is an anisotropic quantity. The mathematical description of the *anisotropy* of the chemical shift (or the nuclear shielding) requires a tensor of second rank, $\boldsymbol{\delta}$ (a 3×3 matrix).

$$\boldsymbol{\delta} = \begin{pmatrix} \delta_{11} & \delta_{12} & \delta_{13} \\ \delta_{12} & \delta_{22} & \delta_{23} \\ \delta_{13} & \delta_{23} & \delta_{33} \end{pmatrix} \tag{4.16}$$

In low viscous liquids molecules adopt all possible orientations during the measurement because the Brownian motion causes molecules to tumble very fast (*isotropic averaging*) and the chemical shift δ appears to be a scalar quantity, even though relaxation effects reveal the anisotropic nature of chemical shifts (see also section 9.3). The resulting isotropic chemical shift δ_{iso} is represented by the average of the trace of the diagonal form of $\boldsymbol{\delta}$

$$\delta_{iso} = Tr(\boldsymbol{\delta})/3 = \frac{\delta_{11} + \delta_{22} + \delta_{33}}{3} \tag{4.17}$$

Low viscous liquids therefore allow observing highly resolved signals with isotropic chemical shifts giving full width at half maximum (FWHM) below 1 Hz where all orientational information is lost.

Depending on the direction with respect to the outer magnetic field, the chemical shift spans about several ppm for protons in powders, resulting in the so-called powder patterns in solid state NMR. In the solid state, this orientation dependent information is present, but the overlapping of broad signals complicates their assignment. Figure 4.3 gives a schematic comparison of isotropic and anisotropic signals.

There are different conventions, describing the chemical shift tensor. In the following, the Herzfeld-Berger and the Haeberlen-Mehring convention are explained.

Herzfeld-Berger convention

In the Herzfeld-Berger convention the tensor of the chemical shift is described by three parameters, the isotropic value, the skew κ and the span Ω. The principal components are ordered according to their size (Figure 4.3).

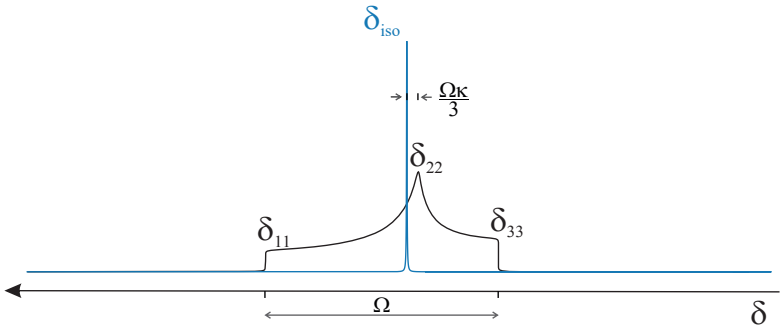

Figure 4.3: Anisotropic chemical shift resulting in a spread powder pattern for solids (black line) and isotropic chemical shift δ_{iso} in liquids (blue line). Numbering of components according to the Herzfeld-Berger convention.[30]

$$\delta_{11} \geq \delta_{22} \geq \delta_{33} \tag{4.18}$$

The span Ω describes the maximum width of the powder pattern and is approximated by the difference between the components δ_{11} and δ_{33}.

$$\Omega = \frac{\delta_{11} - \delta_{33}}{1 - \sigma_{ref}} \approx \delta_{11} - \delta_{33} \tag{4.19}$$

The skew κ characterizes the amount of asymmetry and the orientation of the tensor. It is given by 3 times the displacement of δ_{22} to the isotropic value δ_{iso} divided by the span Ω.

$$\kappa = 3\frac{\delta_{22} - \delta_{iso}}{\Omega} \qquad -1 \leq \kappa \leq 1 \tag{4.20}$$

Haeberlen-Mehring convention

Following the Haeberlen-Mehring convention, the principal components are ordered according to their separation from the isotropic value in the traceless representation.[30]

$$|\delta_{zz} - \delta_{iso}| \geqslant |\delta_{xx} - \delta_{iso}| \geqslant |\delta_{yy} - \delta_{iso}| \tag{4.21}$$

The isotropic chemical shift is the average over the components:

$$\delta_{iso} = (\delta_{11} + \delta_{22} + \delta_{33})/3 \tag{4.22}$$

and the so-called *reduced* anisotropy δ_{red}

$$\delta_{red} = \delta_{zz} - \delta_{iso} \tag{4.23}$$

A characteristic measure for the chemical shift anisotropy $\Delta\delta$ is then defined by:

$$\Delta\delta = \delta_{zz} - \frac{\delta_{xx} + \delta_{yy}}{2} = \frac{3}{2}\delta_{red} \tag{4.24}$$

In the Haeberlen-Mehring convention the *asymmetry* parameter η indicates how much the line shape deviates from that of an axially symmetric tensor.

$$\eta = \frac{\delta_{yy} - \delta_{xx}}{\delta_{red}} \qquad 0 \leq \eta \leq 1 \tag{4.25}$$

4.2.3 Scalar couplings

The magnetic moments of the nuclear spins can interact with each other, whereby the measured signals show a fine structure – they are split into multiplets. This so-called *coupling* is mediated by different mechanisms: via covalent bonds (indirect-, spin-spin-, scalar or J coupling), or through space (direct-, dipole-dipole-, or D coupling). J couplings are mediated (indirectly) through chemical bonds between spins. The reason is the hyperfine interaction between the nuclei and the local electron shell. It then is mediated via a nuclear-electron interaction between the nuclear spin and a non-spherical electron orbital or by Fermi contact interaction due to a non-vanishing electron charge at the nucleus in s-orbitals. As a result, the dependence of J couplings on the molecular orientation and the strength of the external magnetic field $\vec{B_0}$ can be neglected. Therefore, J couplings are considered as scalar constants. Scalar couplings operate commonly intramolecularly. The occurring couplings are field independent and allow conclusions to be drawn about the contribution of the s-orbital or the hybridization and give information about bond angles, distances and on the basis of the coupling patterns (multiplets) information about the connectivities in molecules.

For the quantum mechanical description of J couplings it is useful, to introduce the nuclear spin Hamilton operator $\hat{H}$. It allows to calculate the evolution of nuclear spin states with the *time-dependent Schrödinger equation*. The basis is the simplifying assumption that the electromagnetic fields of the relatively fast moving electrons are averaged within the duration of the acquisition and bears on the separation of time-scales between electronic and nuclear motion (spin Hamiltonian hypothesis).[31]

$$\hat{H}_{ij}^{J} = 2\pi J_{ij}(\hat{I}_{ix}\hat{I}_{jx} + \hat{I}_{iy}\hat{I}_{jy} + \hat{I}_{iz}\hat{I}_{jz}) \tag{4.26}$$

In case that the coupling constant is at least ten times smaller than the difference of the Larmor frequencies between the coupled spins, the secular approximation can be applied (weak coupling approximation). It states that only the

energy, but not the wave function, is altered by a secular perturbation. Here, as a consequence, the terms $\hat{I}_{ix}\hat{I}_{jx}$ and $\hat{I}_{iy}\hat{I}_{jy}$ can be neglected, leading to

$$\hat{H}_{ij}^{J} = 2\pi \hat{I}_{iz}\hat{I}_{jz} \tag{4.27}$$

Heteronuclear J couplings for example between a carbon (^{13}C) and a hydrogen (^{1}H), therefore can always be considered weakly coupled because their magnetogyric ratios separate their Larmor frequencies by several 100 MHz when operating at high magnetic field strength. In the case of homonuclear J couplings, the difference in the chemical shift might be small enough that the transversal components also contribute to the coupling and second order effects hinder the extraction of the coupling constant as the secular approximation does not hold anymore.

The magnitude of the J coupling interaction depends crucially on the number n and types of bonds between the spins denoted by a leading superscript and the type of involved nuclei. The J couplings that were measured in this work are heteronuclear $^{1}J_{\mathrm{CH}}$ coupling constants that take up values between 120 and 250 Hz, the homonuclear vicinal $^{2}J_{\mathrm{HH}}$ couplings that are almost always negative between -20 Hz and -10 Hz and furthermore, $^{3}J_{\mathrm{HH}}$ couplings that take up values between 0 and 20 Hz. The size of $^{3}J_{\mathrm{HH}}$ and $^{3}J_{\mathrm{CH}}$ couplings allow estimation of the dihedral angles between the coupling nuclei with the semi-empirical Karplus relation[32] or more recent approaches.[33–35]

4.2.4 Dipolar couplings

The dipolar coupling of spins corresponds to the through-space interaction between two macroscopic magnets. This interaction can be attractive or repulsive, depending on the orientation of the respective orientation of the north and south poles against each other and disappears at certain internuclear angles with respect to the outer magnetic field. The magnetic field induced by a spin I_i contributes to the external static field $\vec{B}_0$ and alters the field experienced by a adjacent spin I_j. The approximate equal occupation of parallel and anti-parallel spins with respect to $\vec{B}_0$ leads to a split signal (see also Figure 4.4) – a dipolar coupling D_{ij} is observed.

The full Hamiltonian for the dipolar coupling is

$$\hat{H}_{ij}^{D,tot} = -\frac{\mu_0}{4\pi}\frac{\gamma_i\gamma_j}{r_{ij}^3}\left(3(\hat{I}_i\vec{e}_{ij})(\hat{I}_j\vec{e}_{ij}) - \hat{I}_i\hat{I}_j\right) , \tag{4.28}$$

where μ_0 is the permeability of the vacuum, the magnetogyric ratios of the coupling nuclei are γ_i and γ_j with the distance r_{ij}. $\vec{e}_{ij}$ is a unit vector aligned parallel to the internuclear vector. $\hat{I}_i$ and $\hat{I}_j$ are the angular momentum operators of the spins with the dot product

$$\hat{I}_i \cdot \hat{I}_j = \hat{I}_{ix}\hat{I}_{jx} + \hat{I}_{iy}\hat{I}_{jy} + \hat{I}_{iz}\hat{I}_{jz} \tag{4.29}$$

The fraction before the operator term represents the magnitude of the dipolar coupling. It depends only on the inverse cube of the internuclear distance and the magnetogyric ratios of the coupling nuclei.

$$b_{ij} = \frac{\mu_0}{4\pi}\frac{\gamma_i\gamma_j\hbar}{r_{ij}^3} \tag{4.30}$$

If the vector operators in Equation 4.29 are multiplied, Equation 4.28 can be represented in the form

$$\hat{H}_{ij}^{D,tot} = b_{ij}\ \hat{I}_i \boldsymbol{D} \hat{I}_j \quad . \tag{4.31}$$

The tensor of the dipolar coupling $\boldsymbol{D}$ reflects the directional dependence of this interaction. In the principal axis system (PAS) of the dipolar interaction tensor, it is traceless in its diagonalized form and therefore its isotropic mean value is zero. Neglecting the non-secular parts of the dipolar coupling (*high field approximation*), the shape of the obtained secular Hamilton operator $\hat{H}_{ij}^{D,sec}$ depends on whether the spin system is homo- or heteronuclear. The reason for this is that the secular approximation neglects the differences of near-related energy levels. However, their location is crucially influenced by the type of the nucleus. In the homonuclear case, the secular Hamiltonian is given by

$$\hat{H}_{ij}^{D,hom} = b_{ij}\ \frac{1}{2}(3\cos^2\theta_{ij} - 1)\ (3\hat{I}_{iz}\hat{I}_{jz} - \hat{I}_i\hat{I}_j)\ , \tag{4.32}$$

where the term $(3\cos^2\theta_{ij} - 1)$ reflects the angular dependence between the internuclear vector $\vec{r}_{ij}$ and the direction of the static magnetic field $\vec{B}_0$ (see also Figure 4.4).

In the heteronuclear case, for different nuclei, the secular Hamiltonian for the dipolar coupling is given by

$$\hat{H}_{ij}^{D,het} = b_{ij}\ \frac{1}{2}(3\cos^2\theta_{ij} - 1)\ 2\hat{I}_{iz}\hat{I}_{jz} \tag{4.33}$$

The dipolar coupling D depends therefore on the internuclear distance r_{ij}, the angle θ_{ij} between the internuclear vector and the static magnetic field $\vec{B}_0$, and the magnetogyric ratios γ_i and γ_j.

$$D = -\frac{\mu_0}{8\pi}\frac{\gamma_i\gamma_j\hbar}{r_{ij}^3}\ (3\cos^2\theta_{ij} - 1) \tag{4.34}$$

If the internuclear distance r_{ij} and the angle θ_{ij} vary within the NMR timescale, an average dipolar coupling is obtained. The source for a varying internuclear

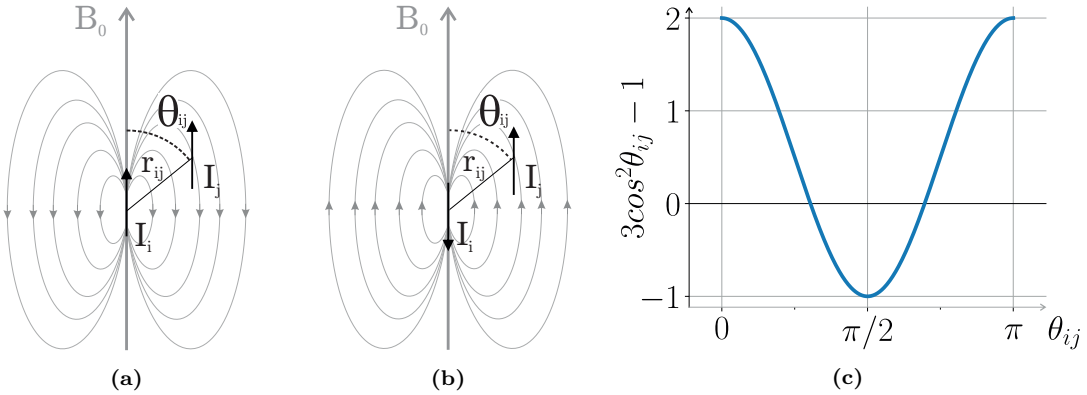

(a) **(b)** **(c)**

Figure 4.4: Illustration on the dependency of the internuclear angle θ_{ij} with respect to the outer static magnetic field $\vec{B_0}$ and the dipolar coupling D_{ij} for two spins I_i and I_j with positive magnetogyric ratios. The coupling arises from the fact that the spins can be oriented towards each other either parallel (a) or anti-parallel (b). The (average) angle between the outer static magnetic field $\vec{B_0}$ and the internuclear vector $\vec{r_{ij}}$ scales the size of the interaction. Note that the graph (c) intercepts the zero line and changes the sign at about 54.7° and 125.3° that both represent the magic angle. In powder spectra the dipolar coupling leads to a characteristically split signal, the *Pake pattern* (Figure 4.5). Adapted from reference[8]

.

distance r_{ij} may arise from vibrational or conformational changes depending on the separation of interacting atoms. For example the distance between a hydrogen directly bound to a carbon may vary within 10 to 100 fs[36] with a fundamental wavenumber $\tilde{\nu}$ near 3000 cm^{-1}, such as an acetylenic CH stretch, or for a low frequency molecular mode respectively. Therefore the average distance $\langle r_{ij} \rangle_t$ scales the dipolar coupling. The analysis of more distant parts is hampered through the inverse dependency on the third power of r_{ij} and conformational averaging for flexible molecular entities. If two or more molecular conformations are present in the sample, the dipolar couplings represent an ambiguous average over the entire conformational ensemble.

$$D(\theta_{ij}, r_{ij}) = -\frac{\mu_0 \gamma_i \gamma_j \hbar}{8\pi} \left\langle \frac{3\cos^2\theta_{ij} - 1}{r_{ij}^3} \right\rangle_t \tag{4.35}$$

The indexed bracket in Equation 4.35 expresses the averaging of the angle θ_{ij} and distance r_{ij} over time. Hence in powder spectra the rotational averaging is hindered and the orientation of r_{ij} is preserved within the NMR time-scale. Powder spectra therefore show characteristic *Pake patterns*,[37] representing the uniform distribution of (fixed) orientations in the sample (Figure 4.5). In solid state the dipolar coupling D results in splittings on the order of kilohertz and takes up negative and positive values depending on the angle θ_{ij} and the magnetogyric ratios. The one-bond dipolar coupling of a sp^3-hybridized ^{13}C-^{1}H pair aligned

with the field with an internuclear distance of 109.3 pm is 23.15 kHz,[38] the same orientation of a sp^2-hybridized ^{15}N-^{1}H pair of a peptide (100.9 pm) gives rise to a dipolar coupling of -11.85 kHz.

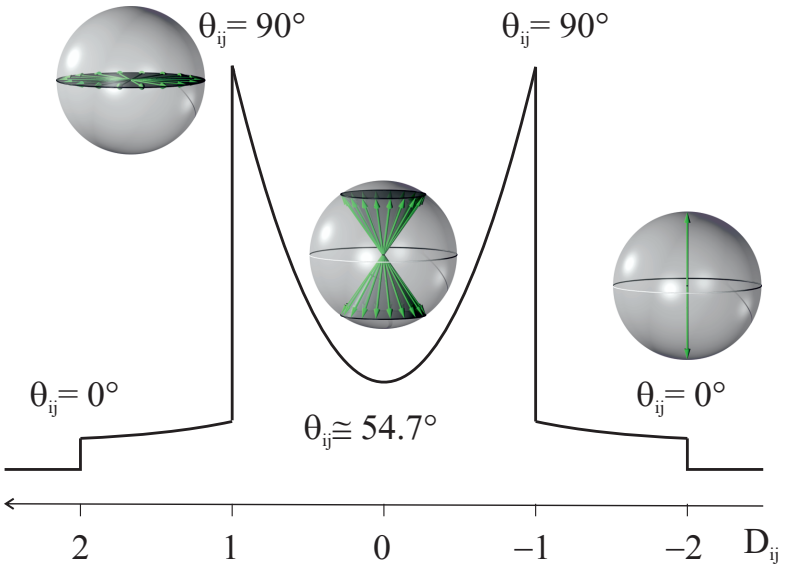

Figure 4.5: The *Pake pattern* arises from the fact that the internuclear alignment of the two spins can take up only two possible orientations (parallel or anti-parallel) along the field $\vec{B}_0$ (0°), but an arbitrary amount perpendicular to it (90°). At the magic angle (54.7°) the dipolar coupling interaction vanishes.

In practice, all NMR active nuclei in solid state spectra couple within a radius of 800 pm which means that signals chemically shifted by several parts per million with couplings of few Hz can no longer be resolved due to several tens of kHz wide dipolar splittings and consequently, bands are acquired. In isotropic liquids, no dipolar coupling is observed, as during the measurement time the nuclear spins are rapidly reoriented by Brownian motion, allowing the internuclear vector between the coupled spins to take up all possible orientations θ_{ij} towards the static magnetic field $\vec{B}_0$, and $\langle \cos^2 \theta \rangle_t = 1/3$. In liquids, still the non-secular contributions of the dipolar coupling become observable through the cross-relaxation phenomenon of NOE.

In solids, dipolar couplings contain valuable orientational information resulting in broadened spectra that lack of resolution of chemical shifts and J couplings, while in liquids high resolution of chemical shifts and J couplings are obtained at the expense of orientational information. By applying partially orienting conditions, the advantages of solid and liquid state NMR can be combined while compensating the disadvantages.

4.2.5 Quadrupolar couplings

More than two-thirds of the NMR active nuclei have a nuclear spin $I > 1/2$ and thus have quadrupole electric moments in addition to the magnetic dipole moment. This quadrupole moment results from the charge distribution of the nucleus. Instead of a spherical charge distribution, as found in nuclei with $I = 0$ or $I = 1/2$, they show a prolate ($eQ > 0$) or oblate ($eQ < 0$) charge distribution around the nuclear angular momentum axis. Analogous to the electric dipole moment (the product of charge and distance), the quadrupole moment results as a product of charge and area. Electric quadrupoles can interact with the electric field gradient (EFG). The strength of this quadrupole interaction depends on both the magnitude of the quadrupole moment and the size of the present EFG. While the size of the quadrupole moment eQ is a scalar constant characteristic of each nuclide, the size of the EFG acting on the nucleus is essentially determined by the chemical environment of the nucleus, determined by existing coordination and bonding conditions. In the simplest case (first order quadrupolar interaction, axially symmetric EFG), the following Hamiltonian is obtained, describing the position of their energy levels

$$\hat{H}_Q^1 = \omega_Q^1 \frac{1}{6}(3\hat{I}_z^2 - I(I+1)\hat{1}) \quad . \tag{4.36}$$

With the *quadrupole coupling constant* $\mathcal{X}_q$

$$\mathcal{X}_q = \frac{e^2 qQ}{h} \tag{4.37}$$

consisting of the electric field intensity e, the electric charge q and the nuclear quadrupolar moment Q, the first-order quadrupolar coupling ω_Q^1 then is given in terms of $\mathcal{X}_q$ by the following expression

$$\omega_Q^1(\theta) = \frac{3\pi\mathcal{X}_q}{I(2I-1)}\frac{1}{2}(3\cos^2\theta - 1) \quad \text{for } \eta = 0 \tag{4.38}$$

with the angle θ between the principal z-axis of the electric field gradient tensor and the static magnetic field $\vec{B}_0$. This directional dependency leads to quadrupolar split signals ($\Delta\nu_Q$) in the range of kHz to MHz. In liquids, the quadrupolar coupling is not observable for the same reasons as for dipolar couplings, since all possible orientations are taken up by the spins throughout the acquisition time.

4.2.6 Residual anisotropic NMR parameters

In order to obtain valuable structural information from anisotropic interactions without sacrificing the high chemical shift resolution present in liquids, low residual orientation of mobile molecules must be maintained to scale down (*full*) anisotropic

parameters to *residual* anisotropic parameters (close to zero, but not zero). The ^{13}C-^{1}H dipolar coupling of 23.15 kHz, for example, leads to a splitting of 46.3 Hz if 0.1 % of the orientation is not canceled during the measurement time. This is achieved with the help of so-called *aligning* conditions. Here, to reveal the anisotropic parameters while maintaining the chemical shift resolution, a so-called *partial alignment* of solutes is established. Then a small fraction of anisotropic interactions between spins remains, as the molecular tumbling fails to average out all anisotropic interactions. In this work RDCs and RQCs were measured and evaluated. Therefore, an introduction on the considerations and concepts for the description of the partial alignment and measurement of residual anisotropic parameters is given.

4.3 Description of partial alignment

Theoretically, Equation 4.34 could be used to calculate the desired distance and angle information using RDCs. Unfortunately the remaining average orientation is not known *a priori*. Moreover, one cannot readily separate the fractions of θ_{ij} and r_{ij}. To solve this problem, Saupe *et al.* proposed an approximation,[39] with which it is possible to describe the partial alignment.

4.3.1 The alignment tensor

When neglecting internal vibration and rotation, and assuming the distances between coupled nuclei to be constant (rigid molecule, one- or two-bond interactions), the averaging of the dipolar coupling in Equation 4.35 only depends on global molecular rotations and therefore on the angles θ_{ij} between the internuclear vectors $\vec{r}_{ij}$ and $\vec{B}_0$. However, for the description of the orientation-dependent averaging by the molecular motion, it is helpful to choose a freely selectable reference coordinate system that is anchored to the molecule.

The principal axes system

This molecule-fixed coordinate system is called principal axis system (PAS), in which the position and orientation of the magnetic field vector $\vec{B}_0$ changes depending on the tumbling motion of the molecule.

The PAS can be chosen such that the diagonal representation of the tensor of the dipolar coupling is derived.

$$\boldsymbol{D}_{\boldsymbol{ij}}^{\boldsymbol{PAS}} = \begin{pmatrix} -b_{ij}/2 & 0 & 0 \\ 0 & -b_{ij}/2 & 0 \\ 0 & 0 & b_{ij} \end{pmatrix} \tag{4.39}$$

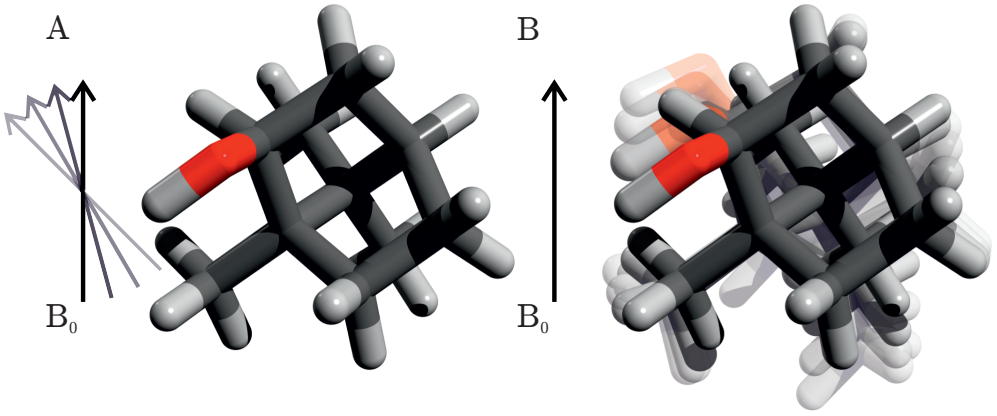

Figure 4.6: The reference frame of the principal axis system (PAS) in borneol, a rigid molecule, follows the molecular motion and leads to an effective variation of the magnetic field orientation. In the laboratory frame (LAB), the molecule is tumbling with the field $\vec{B_0}$ defining the z-direction.

The probability tensor

Due to the axial symmetry of the magnetic field $\vec{B_0}$ and by assuming an axial-symmetric alignment environment pointing in the same direction as the magnetic field $\vec{B_0}$, one can now describe the possible arrangements of the magnetic field with the probability tensor $\boldsymbol{P}$.

$$P_{\alpha\beta} = \langle \cos\vartheta_\alpha \sin\vartheta_\beta \rangle \qquad \alpha, \beta \in x, y, z \tag{4.40}$$

This tensor is a second-order approximation of the orientation-dependent probability distribution of the magnetic field vector with respect to the molecule-fixed coordinate system. It is represented by a 3×3 matrix with the matrix elements of $P_{\alpha\beta}$. These describe the average probability of finding the magnetic field at an angle ϑ_x, ϑ_y or ϑ_z with respect to the molecule-fixed coordinate system (see also Figure 4.7). The residual dipolar coupling of a coupled heteronuclear spin pair I_i and I_j (Equation 4.33) along the unit vector of constant distance $\vec{r_{ij}}$ for a known probability matrix $\boldsymbol{P}$ is given by:

$$D_{ij} = -\frac{\hbar\gamma_i\gamma_j\mu_0}{16\pi^2}\left(\frac{1}{r_{ij}^3}\left(3\vec{r_{ij}}^{\,T}\boldsymbol{P}\vec{r_{ij}} - 1\right)\right) \tag{4.41}$$

For the probability distribution, the condition applies,

$$P_{xx} + P_{yy} + P_{zz} = 1 \tag{4.42}$$

Thus, the symmetric probability tensor can be determined with five independent parameters. The graphical representation of this tensor is an ellipsoid linked

to the molecule. The three main axes x, y and z of this ellipsoid correspond to the eigenvectors of $\boldsymbol{P}$, and the length of its three semi-axes is defined by their eigenvalues P_x, P_y and P_z. Usually they are arranged so that $P_x \leq P_y \leq P_z$.

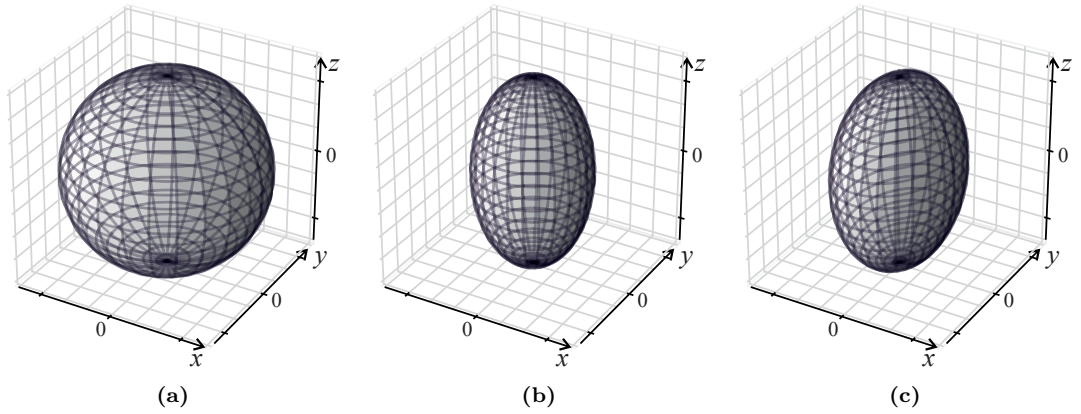

Figure 4.7: Probability tensors $\boldsymbol{P}$, (a) spherical or isotropic, (b) axially symmetric and (c) with three different components $P_x \leq P_y \leq P_z$.

The alignment tensor

Although the probability tensor P adequately describes the behavior of static molecular structures in an anisotropic environment and appears to be easy to understand, another description has been established using the alignment tensor $\boldsymbol{A}$. It is proportional to the probability tensor $\boldsymbol{P}$ and linked to it via

$$\boldsymbol{A} = \boldsymbol{P} - \frac{1}{3}\mathbb{1} \tag{4.43}$$

Here, $\mathbb{1}$ is the unity matrix. The PASof the alignment tensor corresponds with that of the probability tensor. The alignment tensor describes how much the behavior of a molecule deviates from the isotropic mobility and hence directly the magnitude of the alignment. It is a real, traceless, symmetric matrix and like the probability tensor $\boldsymbol{P}$, it is defined by five independent elements. Thus, for its evaluation at least five independent RDCs need to be known. The relation of the alignment tensor $\boldsymbol{A}$ to the dipolar coupling D_{ij} can be deduced from Equation 4.43 giving

$$D_{ij} = -\frac{\hbar\gamma_i\gamma_j\mu_0}{16\pi^2}\left(\frac{3}{r_{ij}^3}\left(3\vec{r_{ij}}^{\,T}\boldsymbol{A}\vec{r_{ij}} - 1\right)\right) \tag{4.44}$$

It is custom to arrange the main values of the alignment tensor $\boldsymbol{A}$ according to the absolute values $|P_x| \leq |P_y| \leq |P_z|$, whereby the respective axis assignment can change in comparison to the probability tensor $\mathbf{P}$.

The Saupe matrix

Originally, Alfred Saupe was involved in the research and interpretation of partial alignment in nematic liquids.[39,40] He proposed the so-called Saupe or order matrix $\boldsymbol{S}$, which is also used in place of the alignment tensor $\boldsymbol{A}$. It differs only by a factor $^2/_3$ of the alignment tensor $\boldsymbol{A}$.

$$\boldsymbol{S} = \frac{2}{3}\boldsymbol{A} \tag{4.45}$$

The alignment can also be characterized by axial (D_a) and rhombic (D_r) components of the alignment tensor $\boldsymbol{A}$

$$D_a = \frac{3}{2}A_z \qquad D_r = A_x - A_y \tag{4.46}$$

With the determination of RDCs, it is thus possible to determine the alignment tensor, which allows statements about the mean time alignment of a molecule in the magnetic field. Conversely, with a known alignment tensor for arbitrary spin pairs I_i and I_j of a known structure, one can predict RDCs. In this context, it is important that these statements apply only to rigid molecules in which the coordinates of atoms within the PAS can be assumed as fixed. With the help of a singular value decomposition (SVD) (*vide infra*) a structure proposal can then be evaluated by the correlation between the experimental to the calculated parameters based on the alignment tensor.[41–44] It is therefore not surprising that many RDC-based applications for structure elucidation are carried out with molecules having an assumed rigid structure.

However, most organic molecules tend to be more flexible, so methods have been developed to make this type of molecules available for structure elucidation using anisotropic NMR parameters. Using the alignment tensor, it was possible to obtain information on molecules that are present in different conformations.

Flexible molecules

In flexible molecules, the assumption of a constant internuclear distance r_{ij} is no longer permissible. The internuclear distance r_{ij} and the angle θ_{ij} now depend on the conformation. In addition, the global rotation and translation of molecules is superimposed by conformational transformations. If these two effects differ in their duration, they can be separated. For example, for two conformers, which are slowly interconverted in comparison to the reorientation in the medium, two separate alignment tensors are obtained. Molecular vibrations interact with external mobility, resulting in a measured RDC error typically less than 5%.[45] If the measured RDCs have a larger error, the error from molecular vibrations can usually be neglected. A prerequisite for this, however, is a certain minimum molecule

size, since otherwise the error may play a role, which could be demonstrated by means of molecules with tetrahedral symmetry such as methane or tetramethylsilane. According to the static approximation, such molecules should actually show no anisotropic behavior and demonstrate limitations of this simplification.[46]

4.3.2 Mean field theory

A different approach than calculating the alignment tensor of a discrete structure is provided by the mean field theory.[47] Instead of the alignment tensor, which effects the averaging over all orientations of a rigid molecule, one can reconstruct the averaging of the measured RDCs with a diversely weighted ensemble populating the conformational space. This way flexible systems have been described via the rotational isomeric state model (RIS),[48] where molecules are treated as if they only occupy a set of discrete dihedrals corresponding to their potential minima. Sampling a conformational space that resembles the averaged parameters obtained by the experiment can be achieved when describing the conformationally dependent probabilities of finding a molecule in a certain orientation as a sum of anisotropic and isotropic potentials (Additive potential theory, AP).[49] The method requires the definition of a functional form for the isotropic limit conformational distribution and allows the separate treatment of molecular fragments. Another method involves thermodynamical considerations of the entropy for determining conformational diversity (maximum entropy (ME)). Furthermore, combinations of AP and ME have been reported (APME[50]).

4.3.3 Single and multi tensor approaches

With the knowledge of contributing conformers, for example, from measured ^3J couplings and NOE distances or from quantum mechanical calculations, the alignment tensor can be deduced from an averaged conformer based on the structural ensemble (single tensor fit). The same applies to a variant, in which RDCs are calculated from several alignment tensors from the entire ensemble, weighted according to their respective population (multi tensor fit) and verified with measured experimental RDC for structure elucidation. The combination into a theoretical conformation (single tensor fit) is suitable rather roughly, as the multi tensor fit is more physically sound, but a large number of RDCs needs to be acquired that may not be approachable.

If the interconversion of conformers is fast, only an averaged alignment tensor is observed. To gather a minimum set of relevant (weighted) conformations resembling the experimental data, a method has been reported recently, (computer assisted 3D structure elucidation, CASE-3D) where the simplest data explaining conformational model is selected to represent the conformational flexibility.[22,51]

4.3.4 Separate treatment of molecular subunits

Another possibility is to determine the individual alignment tensors for molecular subunits and to correlate these local alignment tensors[52,53] with each other. The one structural proposal is considered most realistic, whose eigenvectors of the respective alignment tensors are co-linear with one another. Since flexibility increases the number of discrete subunits, highly flexible molecules, as well as in the multi tensor approach, require many RDC values (*i.e.*, at least five per local alignment tensor) for this method.

4.3.5 Molecular dynamics simulations

Molecular dynamics (MD) simulations provide the sampling of huge conformational ensembles at a relative low computational effort compared to *ab initio* methods. Here, a parametric classical force field simplifies the calculation of occurring conformations and their energies. It is also possible to incorporate NMR parameters into the force field that act as restraints or constraints respectively. In restrained MD (r-MD) runs, the force field potential functions are extended with energetic penalty terms.[54] Via a simple alignment model, RDCs are predicted and the conformations are elucidated by a structure determination approach based on anisotropic parameters. Both angular as well as combined angular and distance restraints have been utilized.[55–59] The direct combination with other NMR observables such as scalar couplings or NOE-derived distances as constraints has proven to be an effective tool for structure verification and refinement.[44,60,61] Unfortunately, the single alignment tensor approximation to a molecular frame of reference represents a fundamental problem in such so-called scalar methods. The resulting ensembles can fulfill experimental conditions, but do not necessarily reflect the actual structural ensembles.

Sternberg *et al.* have proposed the analysis of anisotropic NMR properties,[62–66] such as quadrupolar couplings (QC), chemical shifts anisotropies (CSA) or dipolar couplings, by performing molecular dynamics which make use of the full tensorial properties as constraints (molecular dynamics with orientational constraints (MDOC)). In chapter 8 this fundamentally different approach is applied with one-bond carbon-proton RDCs that does not make any assumptions on the molecular shape or the corresponding overall alignment (*tensor-free* approach).[24]

4.4 Extraction of residual dipolar couplings

To measure RDCs, the molecules need to be partially aligned, as stated in subsection 4.2.6. The RDCs then manifest themselves as difference departing the so-called *total* couplings T from the scalar J couplings measured as reference in isotropic conditions. The line splittings of these total coupling constants correspond to the sum of the scalar J coupling and induced residual dipolar coupling $\Delta\nu_{ij}^{D}$.

$$T_{ij} = J_{ij} + \Delta\nu_{Dij} \tag{4.47}$$

If the sign of the magnitude $\Delta\nu_{Dij}$ is known, the (residual) dipolar coupling in this work is denoted by the symbol D_{ij}. In order to differentiate splittings (a frequency distance $\Delta\nu$) from couplings (corresponding rise or fall of energy according to the dipolar coupling Hamiltonian) the following definition is applied

$$|D_{ij}| \equiv \Delta\nu_{Dij} \tag{4.48}$$

Based on the nomenclature of the scalar J couplings, indexing such as ${}^{n}D_{ij}$ or ${}^{n}T_{ij}$ couplings are adapted in this work. Here, n denotes the number of bonds connecting the spin pair I_iI_j, but it is important to remember that this is done only formally and for easier comparability and assignment of corresponding T, J and D couplings. However, for $n>1$, the dipolar coupling is mediated along the connecting line between the spins (*beeline*, across the space) rather than along the chemical bonds, and at $n=1$ the bonding and internuclear vectors are identical. One should therefore not rely on the fact that with increasing number of bonds between coupled spins, the spatial distance automatically increases.

4.4.1 Choice of NMR experiments

In principle all experiments can be used for the extraction, where scalar J and total T couplings emanate as detectable splittings. In one-dimensional ^{1}H experiments, homonuclear proton-proton couplings ${}^{n}J_{\mathrm{HH}}$ are routinely used for the assignment of signals. At high resolution, the coupling between carbon and hydrogen becomes visible as split satellite signals. The coupling ${}^{1}J_{\mathrm{CH}}$ of these satellite signals is also present in non-decoupled one-dimensional ^{13}C spectra. Unfortunately, due to overlapping signals and poor signal-to-noise-ratio (S/N), only a low accuracy of the couplings is commonly achieved. In the following, general considerations and experiments are presented that allow accurate and unambiguous data acquisition.

General considerations

As previously described, dipolar couplings have a positive or negative sign depending on the alignment of the coupled spins. Scalar ^1J couplings are positive for nuclei with a positive magnetogyric ratio γ, whereas geminal $^2J_{\mathrm{HH}}$ couplings can be both positive or negative. For the exact determination of RDCs with sign two consequences result from Equation 4.47.

First, it is crucial that the order of magnitude of the alignment must be such that the scalar J coupling is about an order of magnitude greater than the respective RDC to clearly determine the effect of the RDC on the total coupling.

This is related to the fact that couplings are measured as a frequency distance $\Delta\nu_{Dij}$ between two peaks which only reveal the magnitude but not the sign. If the alignment is too strong, (among other problems like broadening of lines and fast relaxation) the above equation (Equation 4.47) provides ambiguous values for $\Delta\nu_{Dij}$. For example in the case of a proton bound directly to a carbon, their scalar coupling $^1J_{\mathrm{CH}}$ can take up a typical value of 130 Hz. If the total coupling is determined with 500 Hz the dipolar splitting $\Delta\nu_{Dij}$ could be either positive 370 Hz or, as the coupling peaks might have exchanged their order, a negative value of -630 Hz. When operating at lower alignment, *e.g.* $\Delta\nu_{Dij}$ values within $\pm$50 Hz are observed, the $^1J_{\mathrm{CH}}$ coupling is increased or decreased such that the order of all peaks is preserved and the residual dipolar coupling D_{ij} can be extracted with the sign. To meet these requirements, in this work an alignment medium was designed, offering the necessary weak and scalable aligning conditions.

The second consequence results from the necessity to measure geminal $^2J_{\mathrm{HH}}$ couplings sign-sensitive, therefore an experiment was applied that reveals the sign of the geminal homonuclear scalar couplings $^2J_{\mathrm{HH}}$ (see also Figure 4.14). For the extraction of $^1D_{\mathrm{CH}}$ couplings, an altered two-dimensional heteronuclear single-quantum correlation (HSQC) experiment for the necessary accuracy was carried out which will be presented below. For the extraction of $^1D_{\mathrm{NH}}$ couplings in malectin and APP, complementary J-coupled IPAP-HSQCs were acquired.[67]

Not only the alignment strength but also its homogeneity essentially influence quality and reliability of acquired RDCs. The homogeneity of the alignment correlates strongly with the homogeneity of the medium of the sample. Deviations in the magnetic susceptibility of the sample cause an inhomogeneous magnetic field distribution that lead to experimental errors. In general, any high resolution NMR experiment requires an initial homogenization of the $\vec{B}_0$ conditions, which are perturbed by the sample itself, fluctuations in the superconducting magnet and changes in the environment. This is performed by *shimming* that is inducing additional magnetic fields with the help of so-called *shim coils*. To differentiate between sample and field induced inhomogeneities a spatial chemical shift profiling experiment is applied to monitor strength and homogeneity of the alignment as

well as the field homogeneity.

Monitoring the alignment

When analyte molecules are subjected to partial orientation by one of the methods described in the following chapter 5, it is of interest to examine the condition and quality of the alignment state.

Deuterium NMR

A very simple method to check if a partial alignment has been established is, to record a one-dimensional deuterium (1D ^{2}H) spectrum, when working in deuterated solvents (see Figure 4.8). The quadrupole moment of the deuterium spin-1 nucleus leads to the occurrence of so-called residual quadrupolar splittings $\Delta\nu_Q$ (see also subsection 4.2.5) that are a sensitive indicator for partial orienting conditions in the sample.[68] Throughout this work, quadrupolar splittings $\Delta\nu_Q$ have been used exclusively, to monitor and evaluate the quality and strength of aligned samples. However, structural analysis approaches using residual quadrupolar couplings (RQCs) with respective methods presented in section 4.3 were omitted since the low natural abundance of ^{2}H of 0.0115% demands either isotope substitution protocols, NMR spectrometers equipped with specifically developed probeheads[69] or tremendous experimental times.[70]

4.5 2D NMR based coupling determination

The invention of the Fourier transform method enabled the practical application of two- and higher dimensional NMR methods. The basic concept is the implementation of elements that can be incremented into the pulse sequence that are transformed to gain further dimensions. This can be carried out only on a single channel (homonuclear) or extended by further channels for other nuclei (heteronuclear) and/or additional experimental techniques that alter the magnetic field profile (gradients) or trigger other stimuli (*e.g.* light, orientation). Unlike multi-dimensional spectra, where all axes represent frequencies or chemical shifts, respectively, in so-called array NMR spectra a set of individual spectra is acquired sequentially and at least one dimension represents an observable other than a resonance frequency. In the following, a short introduction on the experiments for evaluation of the alignment and the extraction of RDCs that were utilized in this work is given.

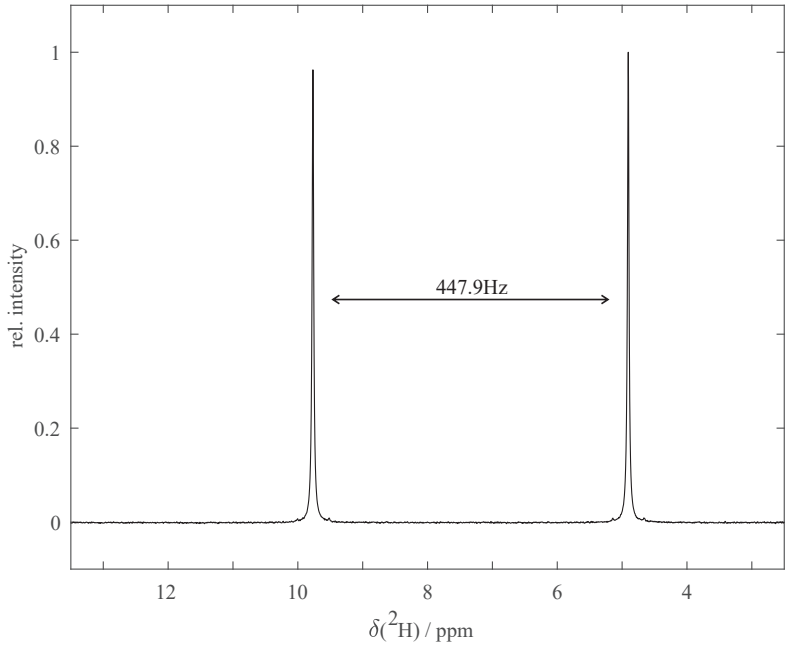

Figure 4.8: 1D ^{2}H spectrum: the residual quadrupolar coupling $\Delta\nu_Q$ splits the observed peak of the deuterium resonance of partially aligned cloroform-d ($CDCl_3$) in poly-γ-benzyl-L-glutamate (PBLG).

Deuterium NMR chemical shift profile

As mentioned above, one-dimensional deuterium NMR spectra reveal the occurrence of anisotropy. As all deuterium spins in the whole active volume give rise to the spectrum, it is not possible to distinct if broadened lines result from inhomogeneities of the field or from the sample. To overcome this problem a so-called deuterium NMR imaging experiment has been developed[71] to probe the spatial distribution of alignment in a two-dimensional fashion.

In Figure 4.9 pulsed field gradients of constant duration with incremented gradient strength lead to a deviating phase of the chemical shift depending on the position along the z-direction within the sample (see also Figure 4.10). The indirect dimension is then acquired by sequential mapping of the Fourier transformed FIDs (second dimension) according to the respective gradient strength (first dimension).

One-bond heteronuclear RDCs

The most accessible RDCs are one-bond heteronuclear couplings. In organic chemistry, CH- and NH-groups form the most common directly bound heteronuclear spin pairs and for the evaluation of their coupling constants, HSQC experiments

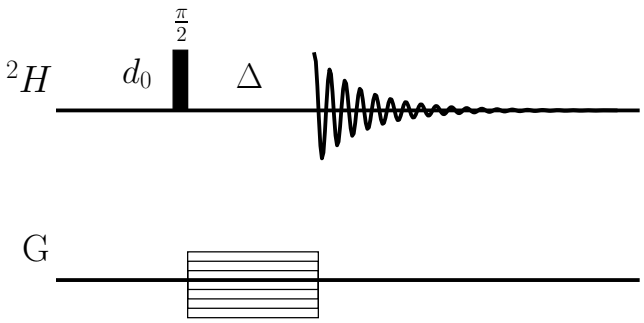

Figure 4.9: NMR imaging pulse sequence: after an excitation pulse a z-gradient is incremented in a series of acquired FIDs.

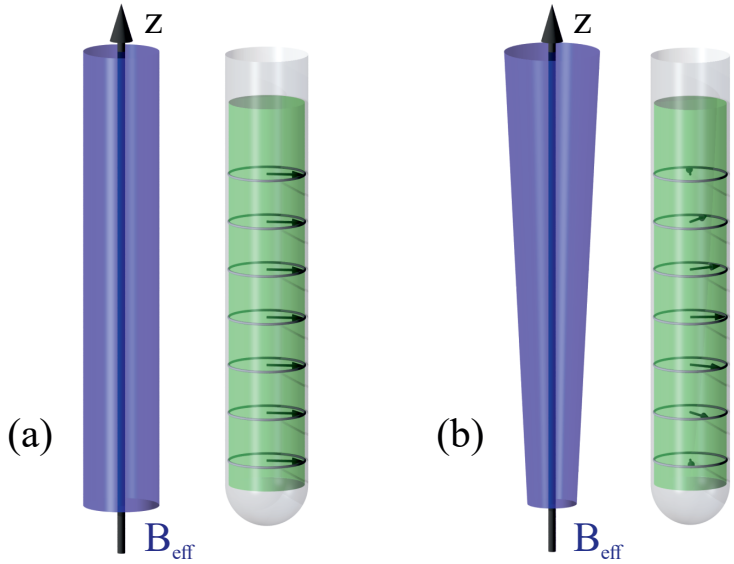

Figure 4.10: After the excitation pulse, the spins throughout the sample (green) rotate along the z-axis with the same Larmor frequency ω_0 (a). The blue cylinder represents the transversal distribution of the field strength of $\vec{B_0}$ along the z-direction and the arrows coherent spins in the x/y plane after the $\pi/2$ excitation pulse. When the gradient is switched on (b), the effective field $\vec{B_{\text{eff}}}$ becomes a function of z as it is now the sum of $\vec{B_0}$ and the field gradient $\vec{B}_{\text{grad}}(z)$. The gradually shifted field experienced by the spins alters the Larmor frequencies leading to shifted phases according to their position along the z-direction (*phase encoding*). The amount of the relative phase shift depends on the strength and duration of this pulsed field gradient. When the gradient is switched off, the phase shift remains and only the spins within a slice of the sample (with the same phase) contribute to the recorded FID.

are in principle suitable when heteronuclear decoupling is omitted (see also Figure 4.11, the gray decoupling element during acquisition).[72] The splittings can then be extracted from the coupled dimension. There exist various types where fast and accurate measurement in the indirectly acquired dimension is feasible without loss of information and the smaller line-widths of the heteronuclei give the advantage of defined splittings.[73] However, when taking heteronuclear spin multiplicity of methylene (I_2S) and methyl groups (I_3S) into account, it is convenient to apply an HSQC experiment, which is coupled only in the direct dimension (t_2-coupled HSQC, see Figure 4.11). This way RDCs of prochiral methylene protons can be assigned individually.

Commonly, the HSQC sequence consists of an initial so-called insensitive nuclei enhanced by polarization transfer (INEPT) from proton (^{1}H, for historical reasons often denoted by "I") to an insensitive nucleus, for example carbon (^{13}C, denoted by "S"). In the following, during an incremented period t_1 with a centered π pulse on the protons, carbon-proton single quantum coherence evolves. The π pulse refocuses the coupling evolution in the first (indirect) dimension. Finally, in a reverse INEPT step, spin magnetization is transferred from carbons back to protons, where the recorded FIDs are Fourier transformed twice, first with respect to t_2 for the direct dimension, then to t_1 for the indirect carbon dimension.

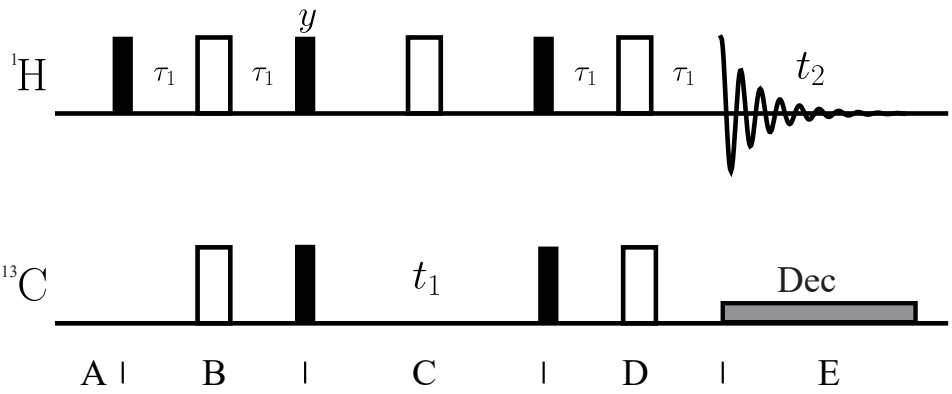

Figure 4.11: Schematic of a conventional HSQC experiment. Equilibrium magnetization of protons turned into the transversal plane by a $\pi/2$ excitation pulse on protons (A). The proton transversal magnetization is transferred on carbon using an INEPT step (B). During the following period t_1 carbon-proton couplings and chemical shifts evolve while proton chemical shifts and (heteronuclear) couplings are refocused by a π pulse on protons (C). In the following reverse-INEPT step, magnetization is transferred back to protons (D), where it is observed. In conventional HSQC, where heteronuclear couplings are not desired, additional broadband decoupling is applied on carbon during the acquisition (gray box, E). Without broadband decoupling in the direct dimension, t_2-coupled spectra are derived. Adapted from Reference.[74]

In conventional t_2-coupled HSQC experiments in isotropic media, the narrow range of ^1J couplings (in aliphatics $^1J_{\mathrm{CH}}$: 135±15 Hz, in peptides $^1J_{\mathrm{NH}}$: 92±6 Hz) allows a nearly optimal setting of the transfer time τ_1. With

$$\tau_1 = \frac{1}{4J} \tag{4.49}$$

for a typical value for a $^1J_{\mathrm{CH}}$ of 135 Hz the optimal value for τ_1 is about 1.9 ms. With the rise of additional residual dipolar couplings (^1D), occurring total couplings (^1T) depart within a larger range, so that the INEPT no longer contains transfer times appropriate for all spin pairs. Residual *anti-phase* (AP) magnetization causes artefacts and perturbed signal forms that hamper reliable coupling extraction. Another usually unwanted effect in the coupled HSQC experiment is the appearance of primarily dispersive anti-phase cross-correlations of more distant protons. The reason for this are present ^nJ couplings ($n > 1$) that neither match the transfer times of the INEPT step. A strategy to circumvent this problem is to utilize the so-called clean in-phase HSQC (CLIP-HSQC), which provides excellent quality spectra, by removing heteronuclear anti-phase magnetization.[75] This is achieved by a $\pi/2$ pulse in the ^{13}C channel just before the data acquisition, which converts any existing anti-phase coherence into undetectable multi-quantum coherences.

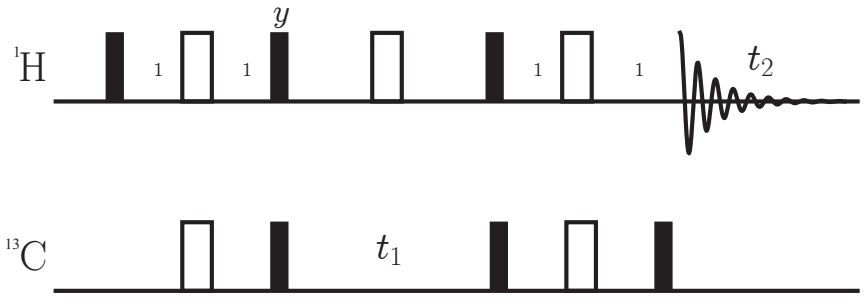

Figure 4.12: Schematic of a t_2-coupled CLIP-HSQC experiment. The last $\pi/2$ pulse converts anti-phase coherence into undetectable multi-quantum coherence. Broadband decoupling is omitted to derive the couplings in the direct dimension. For a more detailed description with phase cycling and gradients see Reference.[75]

Geminal homonuclear residual dipolar couplings

The geminal couplings acting in methylene groups represent another easily measurable quantity. Therefore the two-dimensional so-called primitive exclusive HSQC

(P.E. HSQC) experiment[76] has proven to provide the simultaneous and sign-sensitive measurement of heteronuclear one bond ${}^1J_{\mathrm{CH}}+{}^1D_{\mathrm{CH}}$ couplings and geminal homonuclear ${}^2J_{\mathrm{HH}}+{}^2D_{\mathrm{HH}}$ couplings and has therefore been utilized in this work. As with the CLIP-HSQC both homo- and heteronuclear couplings are extracted in the direct dimension and are therefore easily comparable. In contrast to previous experiments for extraction of homonuclear couplings, only one spectrum has to be captured, without the need to consider multiplicities of methinyl (CH), methylene (CH_2) and methyl groups (CH_3).

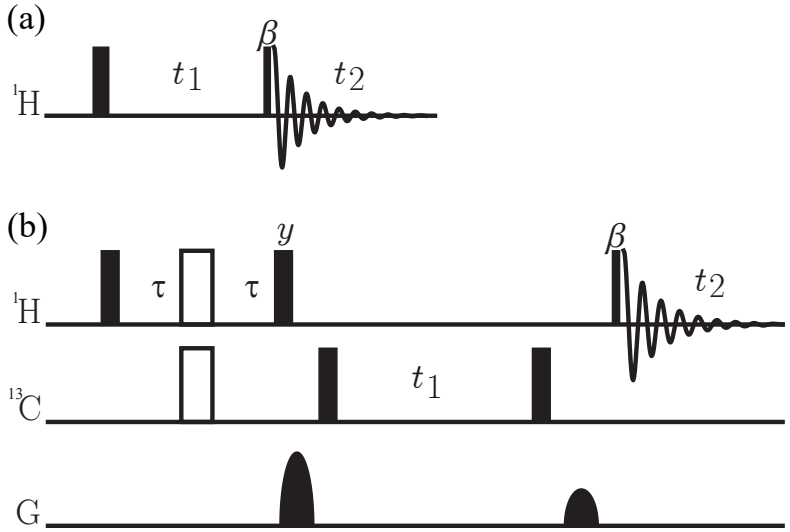

Figure 4.13: Schematic of the homonuclear P.E.COSY experiment (a)[77] and a simple version of its heteronuclear version, the P.E.HSQC (b).[76]

The P.E. HSQC is the heteronuclear version of the exclusive correlation spectroscopy (E. COSY)[78,79] and the primitive exclusive correlation spectroscopy (P.E. COSY)[77] experiment, which allow the sign-sensitive coupling measurement between three coupled spins. With the E.COSY principle, simplified cross-peak multiplets are obtained by exclusive excitation of so-called *connected transitions*. The cross-peaks of a spin pair I_iI_j in a three-spin system $I_iI_jI_k$ then appear only in those parts of the multiplet pattern in which the spin states of the third nucleus I_k remains conserved. A prerequisite for obtaining such an E.COSY pattern is that the mixing of spin states with the *passive* spin I_k is prevented. The coupling between I_i and I_j then becomes visible from the passive coupling of the I_iI_j cross peak as a displacement of two in-phase multiplets, which are separated in the indirect dimension. For this, the coupling between I_iI_j must be weak and greater than the line width. The highest sensitivity E.COSY technique is primitive exclusive COSY (P.E. COSY), in which retention of spin states is achieved by a small flip angle β of the mixing pulse and subtraction of the dispersive diagonal over a ref-

erence spectrum in a phase cycle. The resulting cross peaks contain strong signal intensities for connected transitions, but disappear on unconnected transitions.[80]

The P.E. COSY is easily transferred to the heteronuclear P.E.HSQC[76] by simply introducing an INEPT step, to transfer and convert the evolving magnetization to gain cosine modulated in-phase signals in the indirect dimension. In Figure 4.13b the most simple version with purge gradients is shown.

The homonuclear geminal couplings can be extracted with sign according to the tilt of the multiplets in a similar fashion as in the homonuclear P.E.COSY experiment.

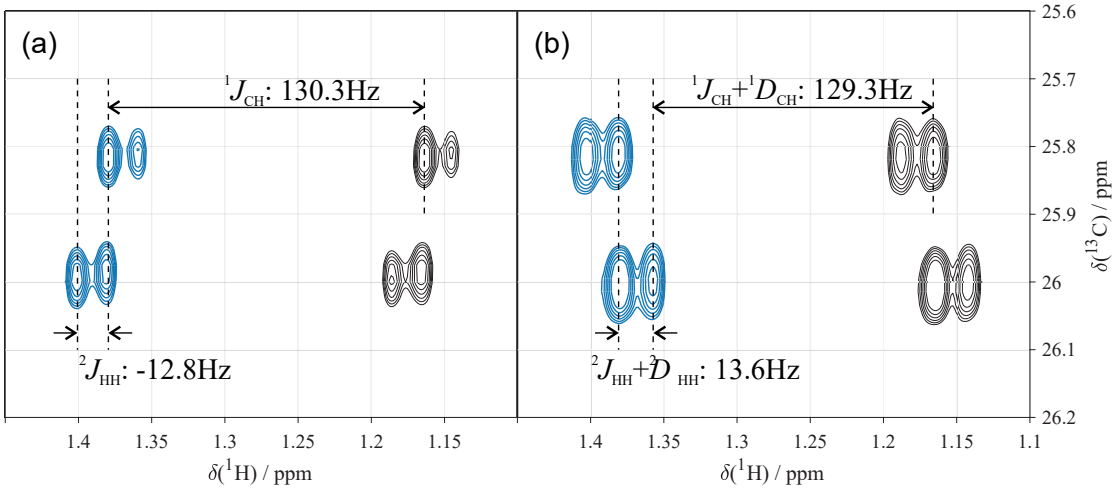

Figure 4.14: Sign-sensitive extraction of couplings using a P.E.HSQC spectrum with positive (black) and negative (blue) peaks: shown is the region of the methylene proton H6$_{exo}$ multiplet of borneol in P.E.HSQC experiments recorded in isotropic conditions (dissolved in chloroform-d) (a) and anisotropic conditions (in cross-linked poly(ethylene glycol)-diacrylate (PEG-DA) swollen and uniaxially stretched in chloroform-d)(b). Both heteronuclear one bond $^1J_{CH}+^1D_{CH}$ couplings and geminal homonuclear two-bond $^2J_{HH}+^2D_{HH}$ couplings can be extracted with sign according to the tilt of the signals. In this example the $^1D_{CH}$ is only -1.0 Hz, the homonuclear geminal residual dipolar coupling $^2D_{HH}$ is +26.4Hz.

Note that the value of the homonuclear geminal residual dipolar coupling $^2D_{HH}$ in Figure 4.14 would be estimated as -0.8Hz, when no sign sensitive experiment was used neglecting the change of the sign in the geminal homonuclear two-bond total coupling $^2J_{HH}+^2D_{HH}$ while the correct value is +26.4 Hz! The P.E. HSQC clearly reveals this sign inversion by the tilt of the E.COSY-type multiplets.

4.5.1 Extraction of couplings

To extract the couplings, the frequency difference of doublets is evaluated. When evaluating $^1J_{NH}$ couplings in proteins and peptides, it is straightforward to directly

subtract the resonance frequencies from the peaks, as they are quickly derived by so-called *peak picking*. Peak picking can be applied in this case because the resonance frequency of the amide protons is well-separated from other proton resonance frequencies and second order artefacts due to strong coupling can be neglected. This is especially convenient, when spectra contain numerous signals. As the signals of the amide protons are already broad due to exchanging protons, one can assume an error that corresponds to the line widths.

However, in the general case, second order artifacts arising from strong coupling need to be considered. Aside from that, in small organic molecules usually much sharper lines are obtained. Therefore, a method has been developed and demonstrated[81] that allows the evaluation of individual errors for each peak. The method consists of overlaying slices of doublets with themselves (heteronuclear couplings) or overlaying displaced rows (from P.E.HSQC) with each other (homonuclear couplings). One slice is then manually shifted along the frequency axis until a maximum overlap is reached. The obtained shift is identical with the coupling value. To evaluate left and right errors, the peaks are shifted towards the left and the right, to find the least overlapping borders of the peaks. This way, regarding the line shape, errors are received that represent about three times the standard deviation σ.

Even though this method has shown to be very valuable, the drawback is that every single coupling has to be extracted in a manual fashion, which consists at least of copying, overlaying and shifting three times to get main value, left and right error. There are cases, where this tedious procedure was not applied and errors were omitted or approximated to be related to the resolution of the acquisition. Unfortunately, any further use of this data fails to provide insights about the quality of applied fitting procedures, as reasonable quality criterions rely on physically sound error estimation. The same is valid for the molecular dynamics approach used in this work that is able to utilize the errors as boundary conditions, emphasizing the importance of realistic errors.

Another problem with the manual extraction is displayed by the subjective nature of the operator, whose experience and perception of what is defining the *border* of a spectral line, influences the outcome, the more, the lower the signal-to-noise ratios are. For this reason, an algorithm for the semi-automatic extraction of couplings with errors has been developed in this work (see section 7.2).

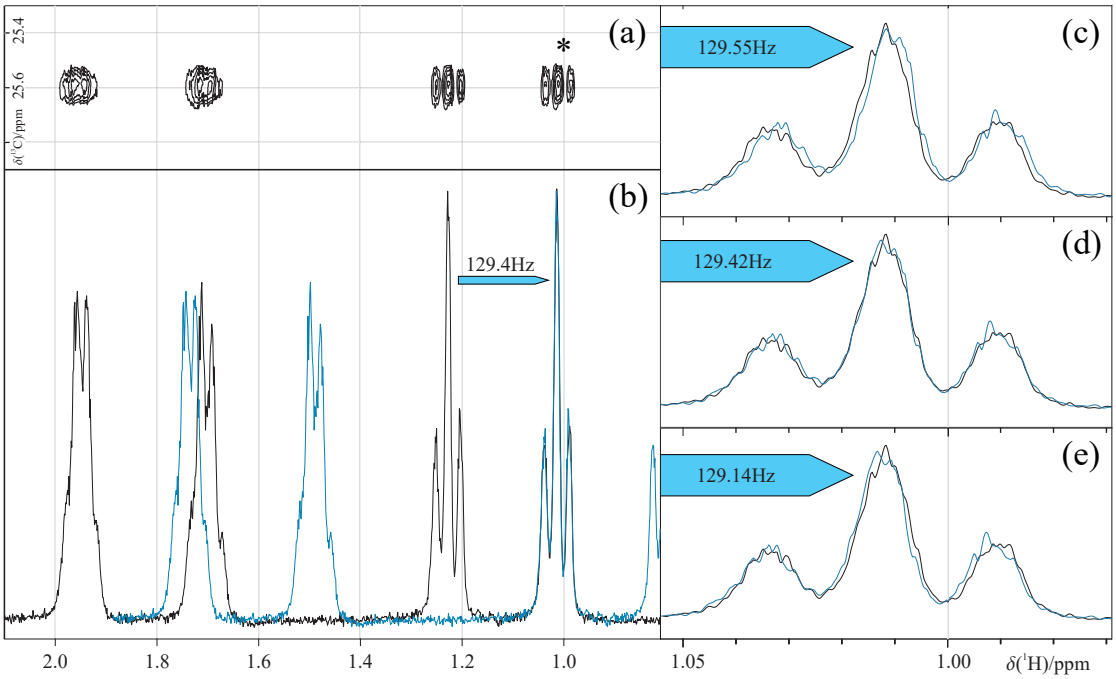

Figure 4.15: Extraction of total couplings ($^1T_{\mathrm{CH}}$) from a CLIP-HSQC with corresponding errors: shown is the region of the methylene group CH6 multiplet of borneol (a) recorded under anisotropic conditions (swollen and uniaxially stretched in chloroform-d). The projection along the carbon chemical shift $\delta(^{13}\mathrm{C})$ at 25.6 ppm (also called *row* or *slice*) is shown as the black spectral line with the two split signals of $\mathrm{CH6}_{exo}$ and $\mathrm{CH6}_{endo}$ in (b). When the slice is copied and superimposed, maximum overlap of the split peaks for the $\mathrm{CH6}_{exo}$ group is achieved by a shift about 129.4 Hz (blue line). An excerpt for the signals at $\delta(^1\mathrm{H}) = 1.01$ ppm (*) is shown in (d). For evaluating the error, the copied slice is shifted to the right (c) and the left (e) to find the borders of where the peaks just cease to overlay. The resulting shifts are denoted within the blue arrows, indicating a total heteronuclear one-bond coupling $^1T(\mathrm{CH6}_{exo})$ of $129.4^{+0.2}_{-0.3}$ Hz.

5 | Alignment media

5.1 Introduction - State of the art

As stated in subsection 4.2.6, for the extraction of directional-dependent residual anisotropic parameters for structural elucidation, it is necessary to partially align the molecules of interest. In the following an overview is given on the principle methods for establishing partial alignment and existing alignment media are reviewed. Furthermore, methods are described to adapt the alignment strength. These preliminary works found the base for the following chapter 6, where the synthesis and casting of PEO-DA sticks are described and its universal applicability is demonstrated and discussed with selected analyte molecules.

5.2 Methods for partial alignment in NMR

In principle, the measures to induce partial alignment in a sample can be differentiated into *internal* and *external* alignment methods. Internal alignment is a self-imposed phenomenon whereas external alignment requires an alignment medium.

5.3 Internal alignment and paramagnetic tags

Actually, most molecules take up a preferred orientation in the presence of a magnetic field, because the tensor of their magnetic susceptibility $\mathcal{X}_s$ is commonly anisotropic.[82] Therefore, depending on the orientation towards the field, different magnetic moments are induced, leading to a torque tending to turn the molecule into its minimum energy orientation. An expression for the distribution function that results from sampling with a Boltzmann distribution in a low-energy limit is given by

$$P(\theta,\phi) = \frac{1}{N}\left[1 + \frac{\vec{B_0}^2}{4kT}\left(\frac{2\Delta\mathcal{X}_s^a}{3}\left(3\cos^2\theta - 1\right) + \Delta\mathcal{X}_s^r\left(3\sin^2\theta\cos^2 2\phi\right)\right)\right] \quad (5.1)$$

with the static magnetic outer field $\vec{B_0}$, $\Delta\mathcal{X}_s^a$ and $\Delta\mathcal{X}_s^r$ are the axial and rhombic anisotropies of the susceptibility tensor respectively, θ and ϕ describe the orientation of the susceptibility tensor relative to the field. N is a normalization constant. In many circumstances, however, the deviation of $P(\theta,\phi)$ from $1/N$ is insignificant, rendering the observed phase to be apparently isotropic. The susceptibility induced perturbation thus can be neglected for small molecules as their molecular (anisotropic) susceptibilities are small, unless paramagnetic species are present. Conditions, where the partial orientation becomes significant, require strong molecular susceptibilities and fields.[83] This method of self-alignment is also known as *alignment induced by magnetic susceptibility anisotropy* (MSA) and has been exploited for example with cyanometmyoglobin, a 17.5 kDa protein, which has a highly anisotropic paramagnetic susceptibility. Kung *et al.* demonstrated the self-alignment of DNA duplexes and quadruplexes.[84] Furthermore, the molecular susceptibility is efficiently enhanced with so-called *paramagnetic tags*, species containing unpaired electrons that are bound or coordinated with the molecule of interest (*e.g.* cobalt in the yeast regulatory protein ADR1,[85] zinc finger tag in N- or C-terminus of barnase[86]). Since susceptibilities in paramagnetic molecules are usually much larger than in diamagnetic molecules, the degree of alignment is correspondingly greater. However, paramagnetic tagging for small molecules is not advisable as the molecular properties of the paramagnetic derivatives and hence the structural information will be tampered. Another reason is that due to paramagnetic relaxation enhancement (PRE) signals within up to 35 Å are eliminated, a radius that might affect the whole molecule or at least significant parts.

5.4 External alignment

For molecules that do not bear enough anisotropic magnetic susceptibility to self-align within the strong outer magnetic field against the thermal motion, alignment can be induced with the help of alignment media. Such media can be subdivided into two main classes, lyotropic liquid crystalline phases (LLC media) or uniaxially mechanically stressed (compressed or stretched) cross-linked polymer gels. In the following, a few examples and their properties for both types of alignment media are given.

5.4.1 Lyotropic liquid crystalline phases

The first partially aligned molecules were reported 1953 by Spence *et al.*,[87] who investigated the proton resonance of pure para-azoxyanisole at different temperatures. Para-azoxyanisole is a thermotropic mesogen that forms a nematic phase between 118 °C and 136 °C. Above the transition temperature, the benzene protons show a sharp line, which upon cooling below 136 °C reveal a broad triplet as they become magnetically nonequivalent due to the residual, non-vanishing dipolar interaction. The anisotropy is considered to be induced according to Saupe by the rod-shaped mesogens *getting aligned more or less ... parallel to the field*, hindering each other and guest molecules to take up all possible orientations. Saupe and Englert extended the properties of para-azoxyanisole and its derivatives (R-O-C_6H_4-N_2O-C_6H_4-O-R, where R=C_nH_{2n+1} with n = 1 to 7) by taking advantage of its lyotropic property to form concentration-dependent liquid-crystalline phases for example with benzene and other aromatics. In 1968, the different NMR spectra were observed for enantiomers within an optically active nematic crystalline liquid (a mixture of cholesteryl chloride and cholesteryl myristate[88]).

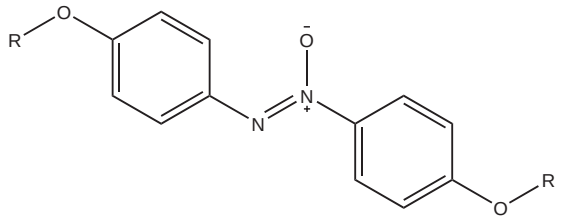

Figure 5.1: p-azoxyanisole.

Since then, many lyotropic liquid crystalline (LLC) phases have proven to provide aligning properties. Unfortunately, the dependence on the concentration defines the lower limit of the mesophase state. This is, because these mesophases lose their orienting properties below a limit concentration for the first order phase transition, rendering too strong lowest alignment conditions. In addition, the solubility and the type of solvent contribute decisively to whether the liquid crystalline state is formed. It has, therefore, been appropriate to classify the liquid crystalline phases according to their solubility in aqueous, apolar organic and polar organic solvents[7] (see also Table 5.1).

Many biomolecules like lipids, cellulose and DNA form LLC phases and have been used to align aqueous proteins. It is not surprising that a large variety of LLC phases of lipid bilayers, micelles and bicelles,[89–91] but also carbohydrate structures like cellulose crystallites[92] and even nucleic acids forming DNA tubes[93] or G-tetrad structures[94] have been utilized to induce anisotropic alignment, since they all represent molecular ordering building blocks that enable cells to be functional.

Fragments of cells (discotic purple membranes[95]) can be used for the alignment of proteins and yet negatively charged virus particles from the phage Pf1[96,97] were applied to align nucleic acids and proteins. Besides the biochemical compounds, also inorganic LLC systems, so-called mineral liquid crystals (MLC), magnetically oriented mesophases, for example, based on vanadium pentoxide (V_2O_5)[98] or phosphatoantimonates ($H_3Sb_3P_2O_{14}$)[99] were applied for the RDC extraction of pentacarbohydrates.

None of these systems provided a universal applicability in terms of pH-ranges, salt concentration, temperature or molecular sizes even within the range of aqueous buffered solvents. As the systems made of dihexanoylphosphatidylcholine (DMPC) and dimyristoylphospatidylcholine (DHPC) forming bicelles between 35°C and 45°C suffer from irreversible degradation at low pH due to hydrolysis, a complementary system consisting of 1,2-di-O-dodecyl-sn-glycero-3-phosphocholine (DIODPC) and 3-[(3-cholamidopropyl)dimethylammonio]-2-hydroxy-1-propanesulfonate (CHAPSO) was reported[100] to be stable at pH between 1 and 6.5, but not above. A second limitation of lipid type liquid crystals (bicelles, micelles, purple membranes, phage particles, cell fragments) is that certain proteins tend to bind to the mesogens, resulting in excessive dipolar couplings, which makes them impossible to be measured by high resolution NMR techniques. Finally, dilute bicelles are not stable and tend to precipitate with time.

No precipitation is shown by so-called Helfrich lamellar phases. They consist of cetylpyridinium chloride[101] or -bromide[102] in hexanol, require high to medium salt concentrations, respectively, and need to be set into a high magnetic field for several hours. Alignment of biological macromolecules in non-ionic liquid crystalline media composed of n-alkyl-poly(ethylene glycol)/n-alkyl alcohol mixtures (C12E5/n-hexanol/water, C8E5/n-octanol/water, C12E6/n-hexanol/water) were introduced by Rückert and Otting.[103] These *Otting* phases are uncharged and therefore insensitive to pH, little sensitive to salt concentration and tolerate high protein concentrations. The different alkyl-poly(ethylene glycol) molecules are denoted as C_mE_n, where m is the number of carbons in the n-alkyl group and n is the number of glycol units in the poly(ethylene glycol)-moiety.[104] A further example based on the poly(ethylene glycol)-alkyl ethers (C12E5) but also compatible with aqueous dimethylsulfoxide (DMSO) mixtures was reported by the group of Thiele *et al.* The thermotropic crystalline liquid 4-n-pentyl-4′-cyanobiphenyl-d_{19} (PCBP) above the liquid-crystalline transition temperature was shown in 2002 to act as an apolar aligning *solvent* with the aromatic condensed compound 2-acetylphenanthrene.[105]

Further measurements also with small organic molecules in apolar solvents were investigated with chiral polypeptide liquid crystalline phases in chloroform and allowed the relative enantiodiscrimination of (small organic) analyte molecules

with poly-γ-benzyl-L-glutamate (PBLG),[106–109] poly-γ-ethyl-L-glutamate (PELG), poly-ϵ-carbobenzyloxy-L-lysine (PCBLL)[110] and poly(n-methyl-n-(R-phenylethyl)-guanidin) (R-PPEMG).[111] In particular, the use of the homopolypeptides PBLG, poly-γ-ethyl-L-glutamate (PELG) and poly-ϵ-carbobenzyloxy-L-Lysine (PCBLL), impelled the development of polymer-based, liquid-crystalline alignment media and lead to an increasing range of compatible apolar organic liquids (methylenechloride-d_2, tetrahydrofuran-d_8, dimethylformamide-d_7, 1,4-dioxane-d_8). By increasing the size of the polymeric backbone to obtain high molecular weight (HMW) polypeptides, the required concentrations for the lyotropic first order phase transition could be decreased, resulting in feasible lower alignments.[112] Based on amino acids, a so-called trans-2-aminocyclohexanecarboxylic acid (ACHC) rich decamer β-peptide forming LC phase was synthesized for aligning aqueous solutes.[113] Recently the sequence AAKLVFF, derived from a fragment of the amyloid β-peptide Aβ-(16-20), KLVFF, was reported to allow the enantiodiscriminating measurement of anisotropic parameters at very low concentrations in more polar protic organic solvents and mixtures like methanol-d_4, methanol-d_4/acetone-d_6 and methanol-d_4/dimethylsulfoxide-d_6.

In 2014 graphene oxide (GO) was reported to induce sufficiently weak alignment very fast just by dispersing it in low concentrations.[114] It was derived including two oxidizing steps, utilizing sulfuric acid, potassium peroxydisulfate ($K_2S_2O_8$), and phosphorous pentoxide (P_2O_5) to obtain a so-called pre-oxidized graphite and further oxidation with concentrated sulfuric acid, potassium permanganate ($KMnO_4$) and concentrated hydrogen peroxide to yield a so-called GO. To enhance the usability for pure dimethylsulfoxide (DMSO), the initial material compatible only with water and mixtures of water with methanol, acetone and DMSO was grafted with trifluoroethyl methacrylate (TFEMA) via a free radical polymerization with 2,2′-azobisisobutyronitrile (AIBN). A selected overview on the multitude of LC alignment media is summarized in Table 5.1.

Recently a supramolecular type of alignment medium, so-called *sergeant-and-soldier* liotropic liquid crystals (SaS-LLCs) was reported.[115] They build up an ordered mesophase based on n-alkylated benzo-1,3,5-tricarboxamidess (BTAs). An interesting feature is that blending achiral with chiral substituted BTAs allows scalable enantiodifferentiating properties, by forming chiral helical mesophase aggregates, induced by hydrogen bonds and π-π-stacking effects. Unfortunately, SaS-LLCs so far do not tolerate functional groups, as they perturb the formation of aggregates big enough for the alignment of solutes. Therefore RDCs from SaS-LLCs have been measured only for alkanes in chloroform and tetrachlormethane by now. Upon derivatizing BTA with amino acid-alkyl groups, the formation of organogels (without aligning properties) is obtained.[116] Hence, this supramolecular BTA mesophases can be regarded as an intermediate state between LC and

swollen polymer gels, which are subject of the next section.

Table 5.1: Summary of LC based alignment media and compatible solvents.

Substance class	**Mesogen**	**Compatible solvents**[a]	**Remark Reference**
Virus particle	Pf1	D_2O	Charged[96,97,117]
	TMV	D_2O	[118]
Phospho-lipids	Bicelles /micelles	D_2O	[89–91,119,120]
Cell fragments	Purple membranes	D_2O	[95,121]
	Flagella	D_2O	[122]
Carbo-hydrates	Cellulose crystallites	D_2O	[92]
	Xanthane	D_2O	[123]
Inorganic	V_2O_5	D_2O	[98]
	$H_3Sb_3P_2O_{14}$	D_2O	[99]
Otting phases	CmEn/n-alkyl alcohol	D_2O	[103]
	C12E5	D_2O	[124]
Helfrich phases	CPCL halogenides /hexanol	D_2O	[101,102,125]
	C12MPB	D_2O	[126]
Immobilized media	LC in gel	D_2O	[127–129]
Nucleic acids	DNA nanotubes	D_2O	[93]
	G-tetrads	D_2O	[94]
Nucleo-tides	5'-GMP	D_2O	[130]

Table 5.1: Summary of LC based alignment media and compatible solvents.

Substance class	**Mesogen**	**Compatible solvents[a]**	**Remark Reference**
Other	Folic acid	D_2O	[131]
	Cromolyn	D_2O	[132]
Polypeptides	PBLG/PBDG	$CDCl_3$, CD_2Cl_2, THF, Dioxane DMF	Chiral[106–108,110] Chiral, HMW[112]
	PCBLL/PCBDL	$CDCl_3$	Chiral[110]
	PELG/PEDG	$CDCl_3$, CD_2Cl	Chiral[109]
	PSMBLG/PSMBDG	$CDCl_3$	Chiral[133]
	PPLA/PPDA	$CDCl_3$, $C_2D_2Cl_4$	Chiral[134]
	PBPMLG	$CDCl_3$, THF	Chiral[135]
	PBLA	$CDCl_3$, $C_2D_2Cl_4$	Chiral[136]
Polyguanidines	(R)-PPEMG	$CDCl_3$	Chiral[111]
Polyphenyl-acetylenes	L-Ala-based PPA	$CDCl_3$	Chiral[137]
	L-Phe-based PPA	$CDCl_3$	Chiral[137]
	L-Val-based PPA	$CDCl_3$	[138]
Polyphenyl-isocyanides	L-Ala-based PPI	$CDCl_3$, CD_2Cl_2, THF	Chiral[139]
Polyisocyano-peptides	L,L-PIAF-OBn	$CDCl_3$	[23]
Peptides	ACHC-rich-β-peptides	D_2O	Chiral[113]
	AAKLVFF	CD_3OD, CD_3OD/Acetone, CD_3OD/DMSO	Chiral[140]
Graphene oxides	GO	D_2O/DMSO, D_2O/Acetone, D_2O/CD_3CN	[114]
	GO-g-TFEMA	DMSO	[141]

Table 5.1: Summary of LC based alignment media and compatible solvents.

Substance class	**Mesogen**	**Compatible solvents[a]**	**Remark Reference**
Supra-molecules	SaS-LLCs	$CDCl_3$,CCl_4	Chiral[115]
Orienting solvent	PCBP		Thermotropic[105]

[a]Commonly, deuterated solvents are used.

5.4.2 Uniaxially strained polymer gels

In 1981, Deloche and Samulski introduced a conceptually different approach when they were investigating RQCs of deuterated organic solvents in swollen mechanically uniaxially stretched polymer gels.[142] Nevertheless, it took until 2000 that RDCs of solute proteins in stretched and compressed aqueous poly(acrylamide) (PAA) hydrogels[127,143] and immobilized media[127] were investigated. The latter represents an interesting hybrid method, where alignment of solutes is implemented by embedding magnetically preoriented mesogens into a polymer matrix, and does not necessarily require mechanic strain. Here, the pre-orientation is obtained from anisotropic magnetic susceptibility of a mesogen which is fixed by cross-linking additional monomers together with the solutes in a strong magnetic field. Consequently, mesogens and solutes must be sufficiently inert towards the selected polymerization protocol.

Without the use of magnetically aligned mesogens, anisotropy can be induced into swollen polymer gels with mechanical strain (strain-induced alignment in a gel (SAG)). The most simple way to establish a homogeneously uniaxially stretched polymer gel sample, is to allow a (dry/non-saturated) polymer stick to swell in an NMR tube with analyte dissolved in a suitable swelling solvent. Provided the glass wall is reached, absorbing more swelling solvent causes the polymer gel to expand exclusively along the longitudinal axis of the NMR tube (*self-stretching*). Such stretched cross-linked polymer gels force diffused solutes to align along the yet anisotropic gel matrix. Depending on the degree of cross-linking of the polymer gel and the deformation aspect ratio, a stronger or weaker alignment is obtained.

Complementary, compressing of swollen hydrogels was also applied already in initial works by the use of susceptibility matched plugs (Aurum spacers, Doty susceptibility plugs, Wilmad)[143] or Shigemi tubes.[127] When compressing swollen gels, best results were obtained when the swollen gels were cast at a diameter

which was only slightly smaller (0.5 mm) than the inner diameter of the NMR tube, preventing the gels to form coils.

With charged acrylamide co-polymers, pronounced electro-osmotic swelling was reported, altering the alignment of proteins[144] and membrane-bound peptides[145] in aqueous solution. To enhance the solvent compatibility, a co-polymerizate of 2-(acrylamido)-2-methylpropanesulfonic acid (AMPS) and N,N-dimethylacrylamide (DMAA) was developed, allowing the alignment in water, but also in the non-protic solvents DMSO and DMF.[146] When formally exchanging the two methyl groups in AMPS enantioselectively by one phenyl group, an enantiodiscriminating chiral co-polymerizate could be obtained, compatible with water, DMSO and methanol. Here a variant of the compression method, the so-called confinement method (see also Figure 5.2) was described[147] allowing to extract RDCs after 4 days of re-swelling. Instead of compressing a swollen gel stick, a dry polymer was allowed to swell radially while restricting its final length with a Shigemi plunger (self-compression).

Chiral natural products like gelatin[148] and collagen[149,150] as well could be utilized *e.g.* for the enantiodiscrimination of D- and L-amino acids. Further cross-linking of gelatin with β-rays resulted in a covalently cross-linked gelatin based chiral alignment medium compatible also with DMSO[151] that does not dissolve as conventional gelatin at elevated temperatures above 35°C. In the course of the search for further chiral alignment media, covalently cross-linked PBLG gels were developed,[152] utilizing the *per se* chiral helicity of the polymer similar to gelatin. Inducing chirality into polymer networks by functionalizing pro-chiral monomers like styrene with chiral elements like (+)- or (-)-menthol is subject of current research.[153]

To measure RDCs on small organic molecules in apolar organic solvents, swollen poly(vinylacetate) (PVAC),[154] poly(dimethylsiloxane) (PDMS),[155] poly(methylmethacrylate) (PMMA)[156] and poly(styrene) (PS)[157,158] gels were introduced. Another DMSO compatible polymer system was obtained by cross-linked poly(acrylonitrile) (PAN).[159] To remove the polymer backround signals present in HSQC spectra of aligned samples, perdeuterated PS[158] (dPS) and PAN[160] (dPAN) were introduced. Removing polymer backbone and partial suppression of side chain proton signals could also be achieved with the help of a z-filter element, exploiting a vanishing nuclear Overhauser enhancement for the polymer, based on the different magnitude of correlation times in comparison to the solute correlation times.[161]

Starting from linear PEO, which shows a large solubility range (it is soluble in water but also in non-polar organic solvents such as toluene), polymer gels could be prepared by application of various cross-linking protocols showing considerable swelling in an outstanding range of swelling agents.[25] Unfortunately, these

proposed methods require either three weeks of irradiation with UV light (poly-(ethylene oxide methyl methacrylate)), five days of irradiation with γ-rays from a ^{60}Co source and additional irradiation with β-rays (γ-poly(ethylene oxide)) or final β-irradiation of a step-growth polycondensate (poly(ethylene oxide)methylene diphenyl diisocyanate).

In this work, the idea of PEO as a precursor for versatile alignment media is taken up, and a bisacrylated derivative is presented that allows simple cross-linking methods without the need of β- or γ-irradiation sources. A selected overview on the multitude of polymer gel based alignment media is summarized in Table 5.2.

Table 5.2: Summary of polymer gel based alignment media and compatible solvents.

Polymer	**Compatible solvents**[a]	**Chirality**	**Reference**
Gelatin	D_2O	Chiral	[148,162]
e^-–Gelatin	D_2O, DMSO	Chiral	[151]
Collagen	D_2O	Chiral	[149,150]
PAA	D_2O	Achiral	[127,143,163]
Acrylamide copolymers	D_2O	Charged	[144,145]
Poly(AMPS/acrylamid)	D_2O, DMSO, DMF	Achiral	[146]
APhES-PH	D_2O, DMSO, CD_3OD	Chiral	[147]
PAN, dPAN	DMSO, DMF	Achiral	[159,160]
PEO	D_2O, DMSO, $CDCl_3$, CD_2Cl_2, CD_3OD, THF, CD_3CN, Dioxane, Acetone, Toluene	Achiral	[25]
PVAc	DMSO, $CDCl_3$, CD_2Cl_2, CD_3OD, CD_3CN, EtOAc, THF, Dioxane, C_6D_6, Acetone	Achiral	[154]
PMMA	$CDCl_3$, CD_2Cl_2, CD_3CN, EtOAc, THF,	Achiral	[156]

Table 5.2: Summary of polymer gel based alignment media and compatible solvents.

Polymer	**Compatible solvents**[b]	**Chirality**	**Reference**
	C_6D_6, Acetone,		
PS, dPS	$CDCl_3$, CD_2Cl_2, THF, Dioxane C_6D_6,	Achiral	[157,158,161]
PDMS	$CDCl_3$, CD_2Cl_2, THF, Dioxane, C_6D_6, n-Hexane	Achiral	[155]
PBLG gel	$CDCl_3$, CD_2Cl_2, THF, Dioxane, C_6D_6	Chiral	[152]
p-HEMA	DMSO	Achiral	[164]
p-DEGMEMA	CD_3OD	Achiral	[165]
Poly(urethan)	$CDCl_3$, CD_2Cl_2, TFE, DMF, n-Hexane		[166]

[a]Commonly, deuterated solvents are used.

5.5 Scaling the alignment

With the media described above, a variety of possibilities is available to realize partial orientation of guest molecules. A crucial parameter for choosing a suitable method is the sufficiently weak partial orientation of guest molecules, to prevent extensive line-broadening. In general, the alignment strength is given crucially by the amount of interactions, available for a given solute molecule. Hence, the orientation strength of lyotropic liquid crystalline alignment media depends on the concentration of the mesogens, as mentioned above. Lyotropic LC media require specific minimum concentrations for first order phase transitions to occur, which then prescribes the lowest limit of the alignment strength. In addition, LC phases orient more strongly or require lower concentrations for the same alignment, the higher the molecular weight of the mesogen-forming polymer chains is. Further-

more, the alignment properties of the mesogens can be triggered by number and type of substituents, capable of non-covalent interactions like hydrogen-bonds, stacking effects, and steric hindrance or the magnetic susceptibility anisotropy (see also section 5.3), and by choosing solvent properties, such as ionic strength or pH. Thermotropic liquid crystal media display the dependence of the strength of orientation and the possibility to invert the chirality by means of temperature.[135] Unfortunately, such systems require multi-hour equilibration in a strong magnetic field to build up a scaled homogeneous alignment. However, if the alignment strength of a chosen LC medium still is too large, a more sophisticated technique exists, called variable angle spinning (VAS).[167–169] It is adapted from magic angle spinning (MAS), usually applied in solid-state NMR to average out anisotropic interactions, by rotating the sample at high frequency along the so-called *magic angle* (see also subsection 9.4.2). In so-called VAS probe-heads this angle can be adjusted arbitrarily between 0° and 90°, so anisotropic interactions can be reintroduced.

In comparison to LC based alignment media, for cross-linked polymer gels the alignment strength can also be varied by the temperature and the amount of available interactions with respect to the polymer chains, but additionally on the solvent type and conditions that influence, whether significant swelling occurs and to which degree. The degree of swelling in non-covalently physically entangled polymer networks like gelatin can be varied by the concentration of the swelling agent. Within a temperature range limited by melting, evaporation, crystallization and gelling point, the alignment also changes, triggered by a varying degree of swelling.

In covalently cross-linked polymer gels the swelling can be varied by the saturation with the solvent, but also by controlling the amount of cross-linking of the polymer, for example by the amount of cross-linker or the radiation dose, and in consequence the magnitude of all residual anisotropic NMR interactions (RCSAs, RDCs, RQCs). The amount of a peroxide initiator has been reported to lower the intrinsic alignment strength of swollen PS gels[46,157] and it was concluded that hence shorter polymer chains were formed, inducing smaller alignments, as in the case of polymer based LC media. Nevertheless, in the studies carried out in this work, polymer chain formation and cross-linking were performed separately, and the use of longer chains as monomers led to weaker alignment.

In contrast to LC phases, cross-linked polymer gels have a defined shape and the type and degree of uni-axial mechanical deformation along the outer magnetic field governs the alignment strength. This deformation aspect ratio can be controlled by adapting the macroscopic dimensions that is by choosing the diameter of the polymerization mold and the length of the fabricated cylindrical polymer sticks. In conjunction with diameter and length confining the sticks when uni-axially

compressed or stretched, a specific alignment strength is obtained. If the polymer stick is swollen in an isotropic state, no alignment is present. This means that in contrast to LC media no lower limits for the alignment exists and isotropic data can be extracted in non-strained but chemically identical environment, which is an advantage for RCSA measurements, where the isotropic chemical shift is needed as a reference.

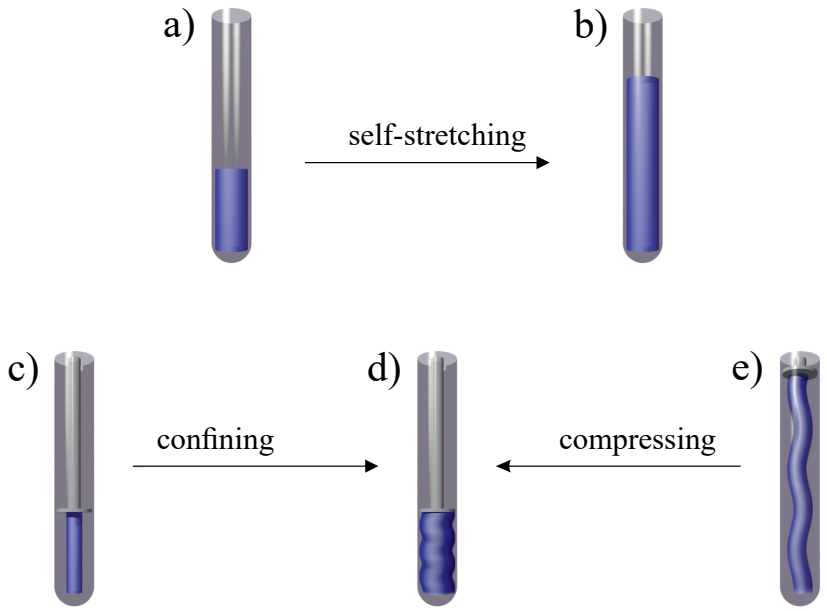

Figure 5.2: Strategies to induce alignment by mechanical strain. The most simple way to achieve an uni-axially stretched polymer gel is to swell it in a tube. As soon as the polymer reaches the tube walls (a), further swelling is only possible along the tube axis (b). A different possibility is, to similarly confine the length instead of the diameter (c), and to let a polymer gel stick swell radially (self-compression). Active compression of an equilibrated swollen polymer stick can be induced by Shigemi plungers or a specifically developed compressing apparatus (e). Here it is important to have a swollen radius that is only slightly smaller that the NMR tube, otherwise irregular curling renders exact measurement impossible as the perturbed medium fails to provide a homogeneous environment. The confining method allows to downscale the achieved alignment by releasing the plunger with excess swelling agent being present, but this process is irreversible, since this type of micro-porous gels is not compressible. The compressing method on the other hand allows reversible compressing and relaxing the gel, which can be utilized, to increase diffusion times of guest molecules or washing procedures respectively.

Stretching and compressing device

Since the intrinsic scaling methods prescribe the alignment, besides VAS, measures were taken to alter the alignment of partially oriented samples. A possibility to achieve two different alignment strengths with a single swollen polymer gel sample

can be realized within so-called two-stage NMR tube,[170] which possess two different inner diameters and have both ends open, to allow to shift the swollen polymer gel from one end to the other. The lower end then is sealed with a rubber plug and the two different stretching degrees cause different alignments.

The introduction of alignment media swollen within silicone elastomer tubes enhanced the self-stretching approach to a continuously tunable method, which was demonstrated first by measuring quadrupolar splittings ($\Delta\nu_Q$) of sodium and caesium dissolved in an aqueous gelatin matrix.[162] By pulling the elastomer tubing, the swollen gel is stretched and fixed in this elongated state at the outer glass NMR tube (Figure 5.3). One can additionally adjust the degree of orientation of the molecules effectively just by choosing the amount of elongation imposed to the gel. The method was improved further to be applicable with standard 5 mm NMR glass tubes by Kummerlöwe *et al.*, by introducing a set of clamps, screws and plugs, allowing the straightforward preparation of fixed, stretched gels to be measured with standard high resolution NMR probes.[171] Since silicone rubbers are not inert against more apolar organic solvents and are permeable for water, an inert perfluorinated, transparent elastomer without additives[c] was developed in cooperation with DuPont[172] (Kalrez® 8002UP), allowing the preparation of stretched gels in all gel/solvent combinations. The fixing of this perfluorinated transparent elastomer tubings required an improved teflon® sealing screw at the bottom, to prevail slipping of the stretched tube and ensure impermeable closed tubes. To be able to apply the tunable stretching method also for small quantities of analytes, the method was enhanced to be applicable for 3 mm tubes.[173]

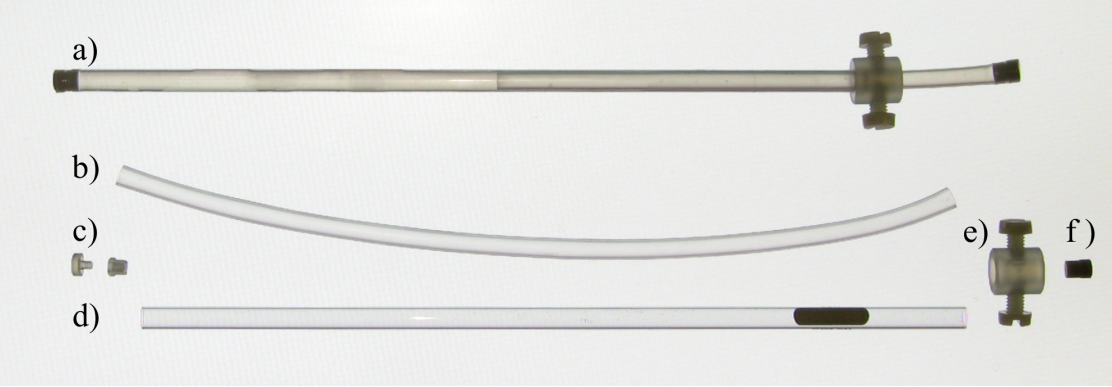

Figure 5.3: Composite stretching apparatus with swollen aqueous PEO-DA-polymer gel inside a silicone tubing (a) and parts: (Kalrez® 8002UP) elastomer tubing (b), bottom sealing screw and plug (c), cut standard 5 mm NMR tube (d), fixing clamp (e) and upper teflon® plug (f).

With PMMA, a slightly different strategy for compressed gels was reported,

[c]To prevent background signals in the spectra

offering reversible tunable alignment.[174] Here, a dry PMMA stick with a diameter of 2 mm and 10 mm length is allowed to swell radially in an organic deuterated solvent while restricting its length with a plunger. Such compressed equilibrated sticks display the strongest alignment in this initial state which can be decreased down irreversibly to zero upon releasing the plunger, provided no anisotropic strain is left or reintroduced (Figure 5.2, from d) to b).

Figure 5.4: Compressing apparatus, consisting from a special NMR tube with a burl on top and screw nuts to fix the teflon® plunger at a certain height.

When compressing the swollen gel cylinders, curling leads to a helical arrangement within the glass tube and pockets are leftover, filled with solvent and analyte. As in here no alignment is present, isotropic scalar J and anisotropic total T couplings can be extracted at once. In Figure 5.5 this is indicated by the appearance of two peaks for the undeuterated chloroform trace, representing the two fractions within and outside the gel.

Another advantage is that the introduction of solutes into the gel matrix can be accelerated, with pre-swollen gel sticks that have a sufficiently small diameter (Figure 5.2 e). This is achieved by repeated compression and release of the gel stick within the analyte solution. After the measurement, the analyte can be regained, when compressing and releasing the gel stick repeatedly while exchanging and collecting the washing solvent.

This approach also has helped to bypass the formation of cracks when applying strong swelling agents like chloroform on brittle polymer materials like PMMA or PS (Figure 5.6). In this case, the dry polymer stick is pre-swollen in an intermediate solvent that diffuses slower into the gel matrix, and is exchanged afterwards with the desired (stronger swelling) solvent with the protocols described above.

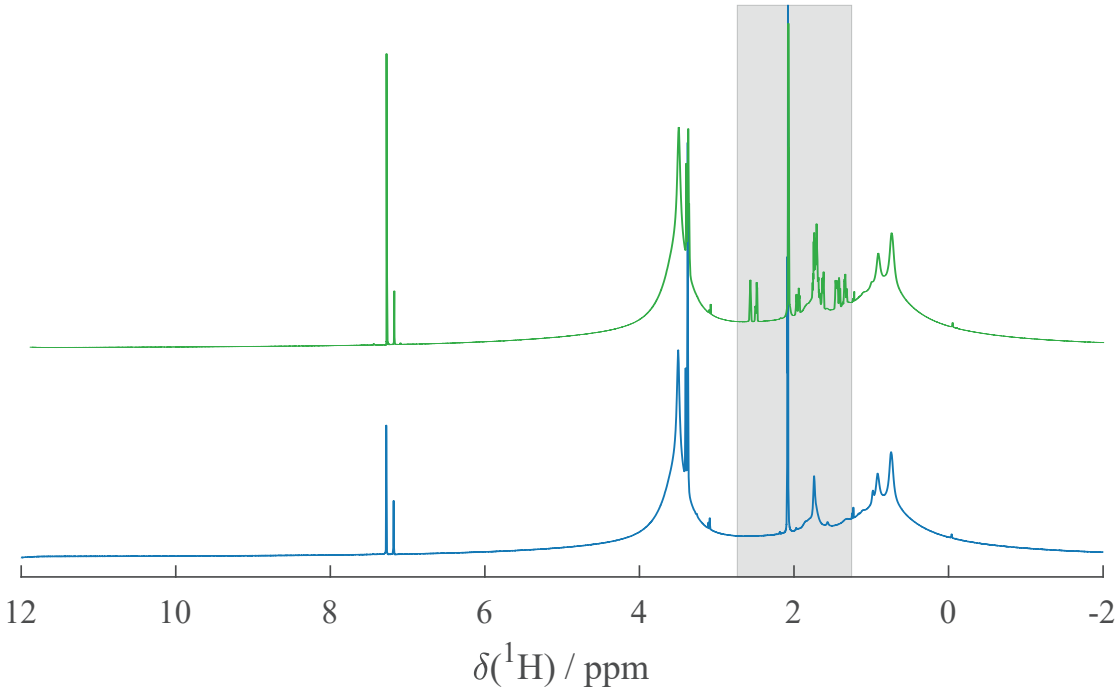

Figure 5.5: ^{1}H NMR spectrum of PMMA gel before (blue) and after (green) four series of 20 times compressing and releasing within a 100 mM solution of norcamphor in chloroform. The two peaks at 7.3 ppm indicate non-deuterated chloroform being present within and outside the gel.

Figure 5.6: PMMA gel stick in chloroform with inner cracks due to fast swelling.

6 | Development of PEO-DA as a versatile alignment medium

6.0.1 Introduction and motivation

As described above, there exists a multitude of techniques and media to align solutes for the extraction of residual anisotropic NMR parameters. Nevertheless, as stated in the introduction, in comparison to *classical* NMR parameters, they are used rarely. The most important reasons are restricted availability, poor compatibility towards a desired solvent or against the analyte, the price, or complicated synthesis routes. In the case of polymer gels, background signals overlapping with the analyte may render the accurate extraction of anisotropic parameters impossible. In this chapter, proceedings to provide a universally applicable alignment medium based on PEO are given. Former cross-linking methods on PEO to derive alignment media sticks were time consuming and required special radiation sources, but led to an alignment medium with excellent solvent compatibility and giving rise to only one background signal of the ethylene oxide units in the proton and carbon spectra. This chapter is dedicated to the invention of a protocol to derive covalently cross-linked PEO sticks. The main emphasis lies on a preferably simple synthesis route, applicable with easily accessible materials and methods. Inspired by the work of Raic in the group of Lee-Thedieck *et al*[175] and Hahn *et al*,[176] who used PEO-DA as polymeric substrates as scaffolds for stem cells, the α,ω-bisacrylated PEO derivative was synthesized and cross-linked via free radical polymerization.

Hence, in the following sections, after a brief outline on the choosen network formation strategy, the dispersity of commercially available PEOs as educts is evaluated, then the synthesis of PEO-DA is described and the yielded acrylation of the product is quantified with ^{1}H-1D NMR. In the next step the cross-linking of PEO-DA is optimized and practical considerations with respect to the concentration of the macromer and the initiator and the mold material to obtain homogeneous PEO-DA sticks are pointed out. Then the preparation and casting of PEO-DA35000 sticks is explained and to be able to achieve higher mass con-

centrations, an additional photo-chemical cross-linking protocol is developed. The next sections describe the work-up of the cast gel sticks. Then their compatibility with different solvents and mixtures and how they influence the swelling behavior are evaluated. Furthermore, the influence of the initial mass content of the polymer sticks on the swelling and hence, on the induced alignment strength is shown. Subsequently, the applicability in stretching and compressing devices to scale the alignment and the suitability of PEO-DA for the fast preparation protocol is demonstrated.

6.0.2 Network formation

In this work, the PEO network formation is carried out in a two-step manner. In gel syntheses, for example to produce media for poly(acrylamide gel electrophoresis) (PAGE), usually the small monomeric molecule acrylamide is mixed with the cross-linker N,N′-methylenebisacrylamide (BIS) and network *and* chain formation take place simultaneously, resulting in a stochastic distribution of inter-cross-link chain lengths. In this work, existing chains of a *macromer* with a small dispersity Đ are derivatized to bear acrylic terminal groups (Figure 6.1), which are separately connected covalently via free radical polymerization. In comparison to the simultaneous network and chain formation, a network is obtained, where the distribution of inter-cross-link distances is assumed to be more uniform and governed by the chosen chain length and the distribution thereof. Also the length distribution of dangling ends should correspond to the narrow length distribution of available macromers if side reactions like hydrolysis are prevented. The aim of this approach is to increase the homogeneity within cross-linked networks used as alignment media. The former strategies of controlling the cross-link density via radiation dose or amount of cross-linker will be compared with a synthesis route that separates chain and network formation and avoids the necessity of radiation sources and additional cross-linker. For the application as an alignment medium various advantages result: Radical species can be minimized and possible network defects induced by radiation can be avoided. Another consequence of waiving additional cross-linking agents is the reduced background, as the network will contain only the signals of the repeating monomeric unit and fewer parameters to optimize. To be able to create swelling polymer sticks made of PEO routinely as alignment media, the production process is optimized to be as simple as possible while maintaining high spectral qualities.

Dispersity of commercially available PEOs

PEO 35000 and PEO 6000 were purchased from Sigma Aldrich and their dispersities Đ were evaluated using size exclusion chromatography (SEC)(subsection 11.1.1).

For PEO 35000 the number average molar mass M_n was determined to be 35880 $\pm 810\,g/mol$ with a mass average molar mass M_w of $41300 \pm 413\,g/mol$ resulting in a dispersity Đ of 1.15 ± 0.03. For PEO 6000 the number average molar mass M_n was determined to be $6730 \pm 153\,g/mol$ and a mass average molar mass M_w of $7299 \pm 77\,g/mol$ resulting in a dispersity Đ of 1.08 ± 0.03.

6.0.3 Diacrylation of PEO

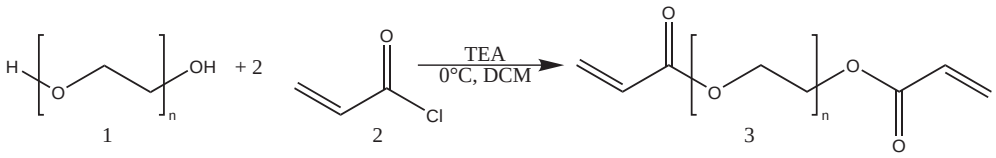

Figure 6.1: Reaction scheme of the esterification of the terminal hydroxy groups of PEO (1) with acryloyl chloride (2) in dichloromethane (DCM) with triethylamine (TEA) to form an α,ω-bisacrylated poly(ethylene oxide)(3).

Macromer synthesis of PEO-DA 35000

Diacrylation: PEO 35000 (21 g, 0.6 mmol, 1.00 equiv) was dried over night under vacuum at 60°C (250 ml two neck flask). It was dissolved in 100 mL dry dichloromethane. The reaction was conducted in dry glass ware under inert atmosphere (Argon). Then triethylamine (0.182 g, 0.525 ml, 1.8 mmol, 3.00 equiv) and afterwards acryloyl chloride (0.163 g, 0.150 ml, 1.8 mmol, 3.00 equiv) were added via Eppendorf pipettes. The reaction mixture was covered by aluminium foil and stirred over night at room temperature.

Work-up: The yellow, viscous reaction solution was poured over neutral Al_2O_3 (in a frit with filter pore 4 and filter paper on top, rinsing with DCM) directly into a 500 mL round bottom flask (by vacuum). Then 7 g of K_2CO_3 were added and stirred for 1.5 h. The product was separated from K_2CO_3 by filtrating over Celite/DCM directly into a 500 ml round bottom flask. Then it was reduced to about 50 mL in a rotary evaporator. Precipitation was carried out in a 500 ml cooled diethyl ether using a dropping funnel. The precipitate was filtrated on a 500 ml frit with filter pore 4 followed by drying in a vaccuum oven at 35°C over night yielding 18.2 g (86%) of a white powder. The dry powder was transferred into snap lid glass and stored in the freezer at -18°C. The degree of acrylation was determined by NMR. [a]

[a]The diacrylation and work up were carried out by Birgit Huber from the Soft Matter Lab IBG3 in cooperation within the SFB1176, project C3 (Dr. Leonie Barner)

Macromer synthesis of PEO-DA 6000

For PEO-DA 6000 same equivalents (1:3:3) were used in the same mass concentration (w/v) in dry dichloromethane. For the work up precipitation, 500 ml of a cooled mixture of 9:1 diethylether:cyclohexane were used. The degree of acrylation was determined by NMR.

Analysis and characterization of the product

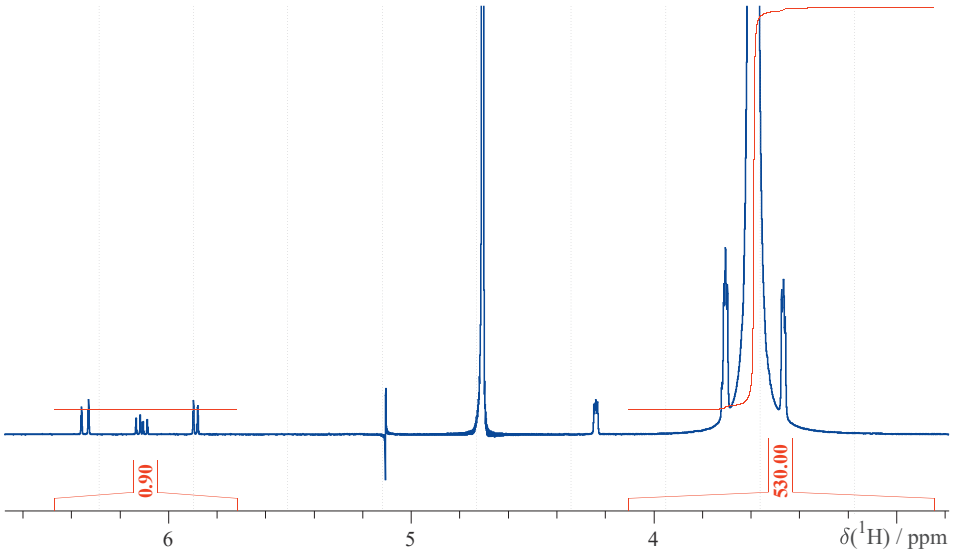

Figure 6.2: ^{1}H spectrum of PEO-DA35000 dissolved in D_2O (4.7 ppm) with the peaks and integrals for the terminal vinyl groups between 5.9 ppm and 6.4 ppm and the ethylene oxide protons at 3.6 ppm. The signal at 4.2 ppm stems from the methenyl groups next to the acrylic end groups.

When assuming an average molecular weight of 35000 $^{g}/_{mol}$, a PEO35000 chain contains 795 repeating ethylene oxide units. After the diacrylation, 6 vinyl protons are added. The *trans*-vinyl protons appear at 6.4 ppm, the *cis*-vinyl protons at 5.9 ppm and the single protons next to the carbonyl group at 6.1 ppm and are therefore easily distinguishable from the approximated 3180 ethylene oxide protons appearing at 3.4 ppm. For 100% bisacrylated chains, one would expect to obtain a ratio of vinyl to ethylene oxide protons of 1:530. Hence, the measurements carried out with product of the above described synthesis resulted in 90% acrylation (Figure 6.2). In D_2O the $^{1}J_{CH}$ couplings of the satellite signals of ^{13}C bound protons is 143.0±0.4 Hz, the main peak has a full width at half maximum (FWHM) of 3.48 Hz. The determined acrylation ratio for PEO-DA6000 reveals an almost

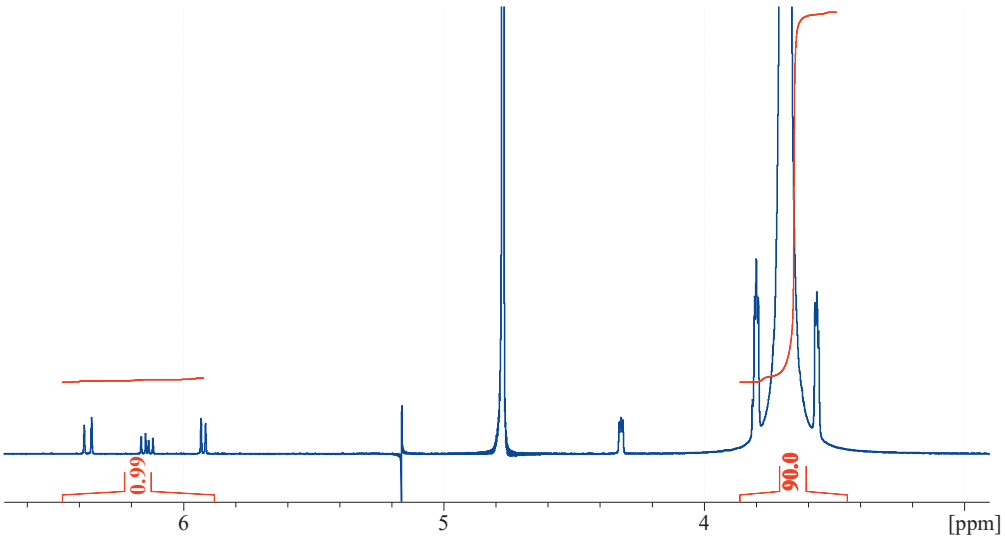

Figure 6.3: ^{1}H spectrum of PEO-DA35000 dissolved in D_2O (4.7 ppm) after two years storing protected from light below 8°C. The peaks and integrals remain a the same positions as for PEG35000. According to the determined integrals, the acrylation turnover was almost quantitative.

quantitave turnover of the terminal hydroxy groups: Assuming an average molecular weight of 6000 $^{g}/_{mol}$, a PEO6000 chain contains about 136 ethylene oxide units corresponding to 544 hydrogen atoms within the chain. 100% bisacrylated chains here therefore correspond to a ratio of one vinyl proton to 90 aliphatic protons in the aliphatic PEO chains.

6.0.4 Cross-linking PEO-DA

For the cross-linking of the bisacrylated macromers PEO-DA 6000 and PEO-DA 35000, free radical polymerization was adapted from PAGE, where acrylamide is cross-linked with ammonium peroxydisulfate (APS) and the aliphatic amine co-catalyst tetramethylethylenediamine (TEMED) in water. Since the macromers are bifunctional, no other bifunctional cross-linker is needed to build polymeric 3D networks. Both, the initator and the co-catalyst are introduced in very small amounts (solutions of 1wt% and 1vol% respectively) and decompose or are washed out after the first swelling and are not detected in the later spectra. Also no radical species or paramagnetic line-broadening was observed.

Reaction mechanism

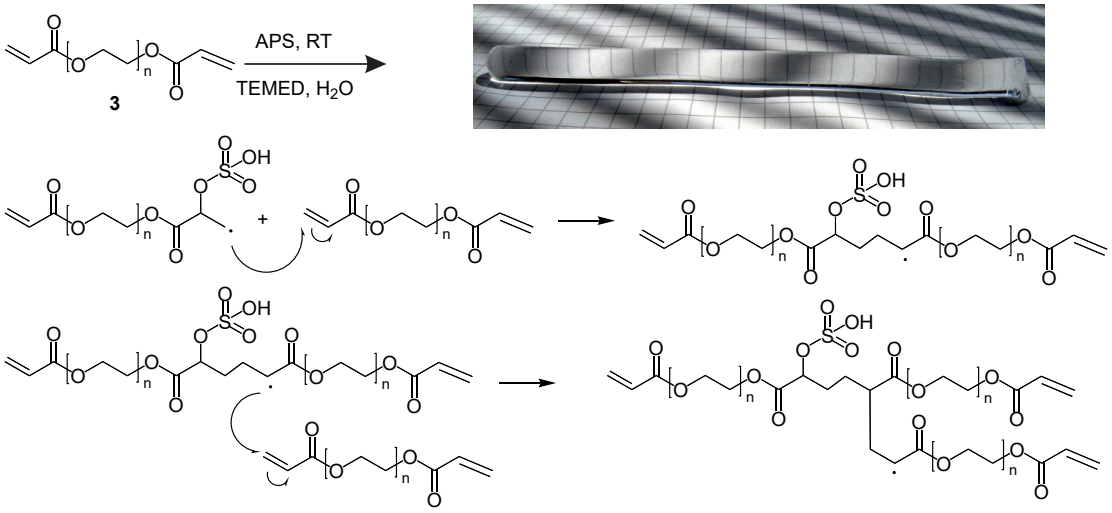

Figure 6.4: Initiation and propagation steps for the cross-linking of PEO-DA with ammonium peroxydisulfate (APS) and tetramethylethylenediamine (TEMED).

In the reaction scheme Figure 6.4 the picture of a polymer stick cast in an NMR tube indicates that very little is known about the topologies within the formed gel. It is for example not known, how many chains reach the radical center, which becomes more sterically hindered, the longer the growing *chain* is. Note that n is $\approx$ 136 for PEO-DA6000 and 795 for PEO-DA35000, and therefore, the distance between the cross-links and the length of so-called dangling end should therefore always correspond to a multiple of n. On one hand, this should allow a better control over distribution of chain lengths within the network compared to the conventional formation of covalently cross-linked small monomer units with a cross-linker. The sterical hindrance of the bisacrylated macromer chains on the other hand prevents high cross-link degrees and a complicated topology with loops, rings, entanglements, and chains that are not cross-linked at all might be formed. The evaluation of the cross-linking degree is part of section 9.5

Practical considerations

Optimization of the macromer concentration: To obtain homogeneous, cross-linked sticks for aligning solutes of different molecular weights, different concentrated PEO-DA 35000 solutions in water were tested to investigate the influence on the alignment strength. The initial idea to concentrate PEO-DA in water as high as possible to create strong alignments was discarded, as above 30%(w/w) containing solutions were highly viscous and the problem to mix and distribute a

thermal initiator and co-catalyst evenly in the solution within few minutes arose. A further disadvantage of this viscous high concentrated macromer solutions was the difficulty to transfer the reaction mixture into the tubings. Since the average test volumes were between 200 and 2000 µl, transferring the reaction mixture into glass or plastic tubes via capillaries or cannulas was also superseded by a method, where the reaction mixture is directly transferred into the mold teflon® tubes via vacuum by connecting one end with a syringe. Doing so, much less material was lost on the surface of syringes, capillaries and/or cannulas enabling cross-linking effectively on small scales while suppressing the formation of bubbles and foam.

Optimization of the initiator concentration: In comparison to PAGE, the concentration of vinyl groups is by far much smaller since the molecular weight of PEO-DA is about 500 times larger than the molecular weight of acrylamide. Therefore, an optimal concentration for the amount of APS and TEMED had to be evaluated to obtain a pot life time of about 15 minutes. This is important to transfer the reaction mixture into an appropriate mold. An initial approach to perform the cross-linking at ambient temperature failed, because the found initiator concentrations were too sensitive to be reproducible throughout the seasons, therefore an initiator system concentration for a reaction at 40°C was established. Also the idea to minimize the concentration of the initiator APS to derive *long* chains was discarded. The first reason is that low initiator concentrations showed poor reproducible cross-linking behavior. The second reason to work at an elevated initiator concentration is that in contrary to a conventional free radical polymerization reaction, the chains are already present and only need to be joined rather than being formed. With regard to the later use as an alignment medium, the formation of (aliphatic) chains consisting from units differing from ethylene oxide units, visible in hydrogen or carbon spectra, is not desired.

The *per se* low concentration of vinyl groups in the PEO-DA chain requires, furthermore, a higher concentration of radicals to effectively initiate the ligation of a few (but not too many) PEO-DA chains. To increase the effective concentration of radicals available for the initiation and propagation, the reaction mixture was degassed with vacuum. Applying a protocol to degass the de-ionized (DI) water by freezing and melting before the mixing was discarded, since the PEO-DA powder absorbs air. Therefore, PEO-DA, water and TEMED were mixed in eppendorf vessels or falcon tubes depending on the volume of the reaction mixture and then degassed with vacuum and flushed with argon or nitrogen several times to remove residual oxygen. After adding the initiator APS and transferring the reaction mixture, the mold was overlayed with argon. This was necessary to prevent the upper first centimeter in the tubes to remain liquid because of the inhibiting properties of oxygen. Oxygen in small amounts can initiate radical polymerizations, but also

inhibits the propagation, as it adds to the growing polymer chains with a rate constant about five orders higher than the propagation step and forms peroxides that are less reactive.[177] Consequently, the desired propagation reaction only takes place, when the residual oxygen is consumed. Since the above described degassing protocol only serves to minimize the amount of dissolved oxygen, residual traces were compensated by an increased amount of initiator.

Appropriate mold material: Since the diameter of the cross-linked polymer stick influences the swelling behavior itself but also the applicability within NMR tubes and the chosen alignment method (stretching, compressing), tubes with different diameters and materials (glass, teflon®) were investigated as molds. As a method to prevent the hardened gels sticking to the glass walls, silylation protocols have been described. Nevertheless, this approach was not successful for PEO-DA gels synthesized in this work, and to obtain the cross-linked sticks the glass tubes containing the product had to be broken. With teflon® tubes as molds, this problem could be solved, as teflon® is known for its non-sticking properties. For the compression device, PEO-DA gels with a stronger consistency had to be tested to prevent excessive curling. To also be able to cross-link 50% (w/w) concentrated PEO-DA solutions, a water-soluble photoinitiator was applied, allowing to start the polymerization with UV light. This method concedes enough time for homogeneous mixing of the educts. Also here, the use of teflon® tubes is beneficial, because of its high transmittance for UV light (in comparison to glass). Further advantages of teflon® tubes are their availability in different diameters and its chemical stability. A drawback was to adequately seal these tubes, as no general fitting plugs for all the diameters tested were available. To solve this problem, a method was invented that utilizes short (2 - 5 mm) cut elastomer silicone tubes closed with a glas bead that can be fixed on the ends of the teflon® tubes when having a smaller inner diameter than the outer diameter of the mold (Figure 6.5). Using elastomeric silicone parts as adapters between different diameters also allows to connect cut pipette tips to one end, allowing better control and yields, when transferring the reaction mixture into the mold, and prevents the formation of bubbles by unintended air suction.

6.1 Gel preparation

For the development of a reproducible protocol for the cross-linking of PEO-DA, about 30 different formulations were tested (see Table 11.1) concerning the above mentioned reaction conditions and mold materials. As a result, four formulations with 16, 20, 25 and 30%(w/w) were developed. To also cross-link highly concentrated, viscous PEO-DA, the photocatalyst Irgacure2959® (IR2959®, 1-[4--

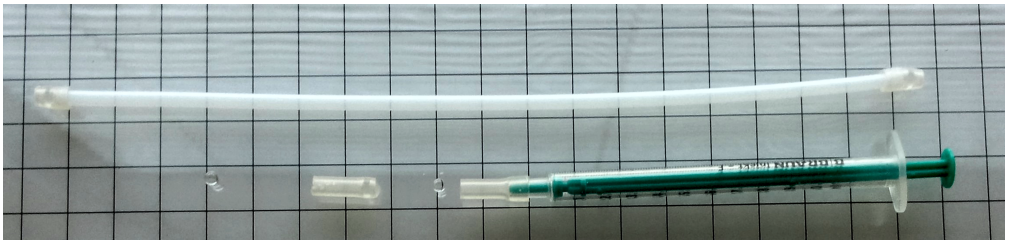

Figure 6.5: Equipment for the transfer and the mold: teflon® tube, silicone adapters and beads for the sealing, and syringe to transfer the reaction mixture with vacuum.

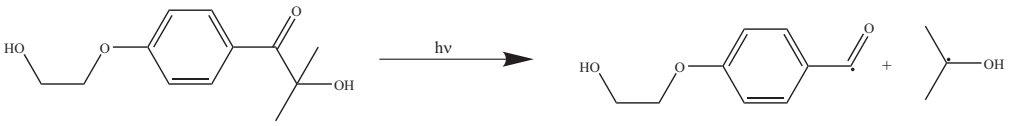

Figure 6.6: Photo-initiated radical formation of IR2959®.

(2-Hydroxyethoxy)-phenyl]-2-hydroxy-2-methyl-1-propane-1-one, Figure 6.6) was used to replace the thermal initiator APS.

6.1.1 Preparation of PEG-DA-35k sticks

Preparation of a casting mold: Depending on the amount needed and the desired diameter, a teflon® tube is selected and cut to the desired length. Silicone tube fragments serve as connectors to a syringe, pipette tips, and glass beads. The assembled mold is placed in a vacuum bearing glass vessel, *e.g.* a cooling trap and the air is exchanged with argon by multiple application of vacuum and flushing with argon.

Preparation #		45	46	47	48	UV
Mass content	% (w/w)	**16**	**20**	**25**	**30**	**50**
m (total)	g	1	1	1	1	1
V (H_2O)	ml	0.74	0.70	0.65	0.60	0.40
m (PEG-DA-35k)	g	0.16	0.20	0.25	0.30	0.50
V (TEMED, 1% (v/v)	ml	0.05	0.05	0.05	0.05	0.05
V (APS, 1% (w/w)	ml	0.05	0.05	0.05	0.05	-
V (IR2959, 1% (w/w)	ml	-	-	-	-	0.05

Table 6.1: Formulations for the cross-linking of PEO-DA35000 to cast polymer sticks as alignment media.

Figure 6.7: The assembled mold is placed in a cooling trap. The syringe will be filled with argon, which is later pushed into the vessel containing the cross-link reaction mixture. A micro pipette tip connected to the left end helps to transfer the liquid without bubbles.

Thermal initiation: PEO-DA35000 from the freezer is left to warm up to room temperature while protected from light to prevent condensation of humidity into the powder. Meanwhile, aqueous 1% solutions of APS (w/w) and TEMED (v/v) are dissolved and mixed thoroughly. Then, depending on the desired mass fraction and target volume, the respective amount (adapted according to Table 6.1) of the PEO-DA35000 is weighed into an eppendorf vessel (1 to 2 ml), falcon tube (15 or 50 ml) or other container that can be sealed, stirred with a vortex mixer, and centrifuged.

Then water and the 1% (v/v) solution of co-catalyst TEMED are added. The educts are vortexed and afterwards degassed applying vacuum and flushing with argon (so-called *sparging*). This can be achieved by stinging the plastic container lid with a cannula and placing it in a vacuum bearing glass flask. When lowering the pressure, not only dissolved gas is removed, but also water starts to boil. Therefore, it is recommended to monitor the volume to maintain the desired concentration.

Foam and bubbles are removed afterwards by centrifuging. In the next step, the initiator APS is injected into the middle of the solution with a micropipette. Then it is mixed thoroughly on the vortexer and centrifuged to remove residual bubbles and to collect potential insoluble remains originating from the synthesis (*e.g.* Celite®) at the bottom as a pellet.

Casting of the gel: The mold assembled with pipette tip and syringe, filled with argon, is removed from the cooling trap. The containing argon is pressed out of the syringe into the reaction vessel (eppendorf vessel, falcon tube), ensuring a significantly reduced amount of oxygen left in the mold. Then the initiated and de-foamed PEO-DA solution is taken up into the teflon® tube with the syringe. To prevent formation of bubbles in the mold and for better yields, the pipette tip should be placed and kept shortly below the meniscus when transferring the initiated macromer solution. The filled teflon® tubes are sealed with the silicone

(a) **(b)**

Figure 6.8: PEO-DA powder and degassing setup. (a) 50 ml Falcon tube filled with 1 g of PEO-DA35000. (b) Degassing of 2 ml PEO-DA35000 solution by sparging argon into a 15 ml Falcon tube with a cannula.

tube/glass beads and placed in a water bath at 40°C for 12 hours (Figure 6.9). Eventually formed bubbles may be removed with additional centrifuging of the mold. To ensure low oxygen content within left over volume above the liquid, it is advisable to add a layer of argon on top by flushing with argon.

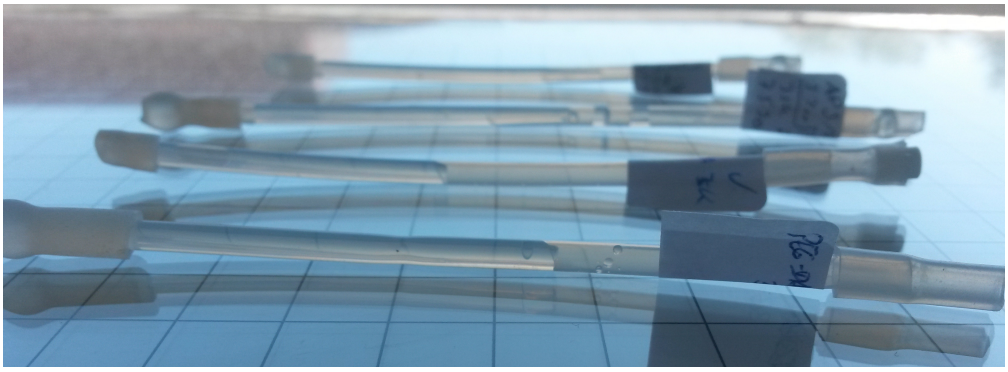

Figure 6.9: Cross-linked PEO-DA sticks after polymerization at 40°C for 12 hours within the sealed teflon® tubes.

Removing from the mold tube: The cross-linked PEO-DA gel can be pushed out of the teflon® tube with air or water, connecting one end to a syringe (filled with air or water). When cross-linking thermally with APS and TEMED, a small layer remains liquid at the outside of the gel, allowing the above described easy removal of gels.

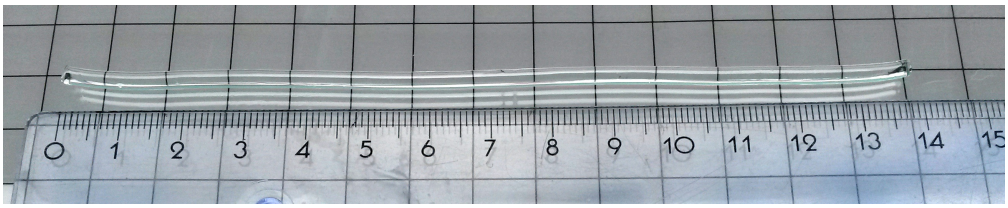

Figure 6.10: Cast gel after removal from the teflon® mold. PEO-DA with 16%(w/w) was cross-linked and cast in a teflon® tube with an inner diameter of 3 mm. After the polymerization, the length of the stick (l_{pol}) is about 13.8 cm and the diameter (d_{pol}) 3 mm.

Photochemical initiation: When initiating the radical polymerization thermally, for the above steps, the formulation scheme allows a pot time of about 10 to 15 minutes. The degassing, centrifuging and transfer can be managed for weight contents up to 30%(w/w) PEO-DA35000 solutions. Higher concentrations exhibit higher viscosities that complicate the above described procedures, because the slower diffusion increases the effort to stir the educts evenly in the reaction mixture, while the formation of foam and bubbles is amplified and their removal is

more difficult. Besides, a higher monomer concentration also accelerates the reaction time, further impeding the production of homogeneous gel sticks. Therefore, a formulation has been developed that can be initiated with UV light, enabling a steady casting protocol also for higher concentrated, viscous reaction mixtures. The technique exploits the low absorption of UV light at teflon® and ethylene glycol units.

500 mg of PEO-DA35000 are mixed in a falcon tube with 400µl of water. Then 50µl of TEMED are added. To obtain a homogeneous transparent viscous liquid, the mixture is centrifuged several times up and down and afterwards the mixture is degassed applying vacuum as described for the thermal initiation. Then 50µl of a saturated solution of IR2959® (with a solubility of about 1%(w/v) in water) are added to the honey like, viscous solution. Again the mixture is thoroughly mixed by the help of centrifuging, degassed and overlayed with argon. Bubbles and foam are removed by centrifugation. Then the mixture is transferred into a mold with the desired diameter and placed directly below a UV-lamp with a wavelength of 254 nm for 8 minutes. The tubing is turned around and irradiated again another 8 min placing the lamp again on top of it. The tube is left for 12 hours at room temperature for the cross-linking. In contrast to the thermally initiated sticks, the polymerized 50% gel adheres strongly to the tube walls and can not be pushed out by applying pressure. For this reason the stick is removed by cutting the teflon® tube lengthwise. The yielded polymer string is washed and dried as it is done for the thermally initiated sticks.

The cylindrical gel strings are weighed, diameter and length are measured. To remove residual components that are not cross-linked to the gel network, the gel strings are placed for 24 h in 500 ml water at 40°C.

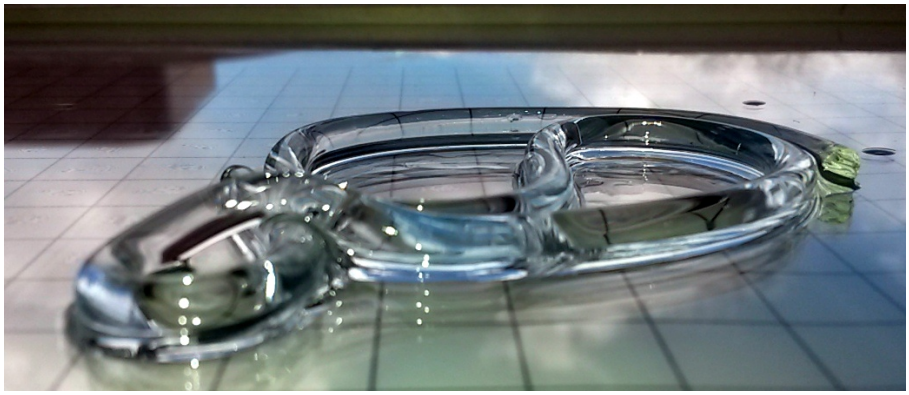

(a)

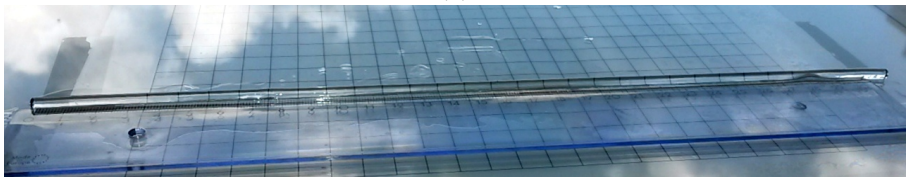

(b)

Figure 6.11: Cast PEO-DA gel after free swelling in water (a) and elongated (b).

Drying method: To prepare straight and homogeneous PEO-DA gel sticks applicable in NMR tubes, the gel strings are cut into pieces and dried. Choosing lengths depends on the desired method to induce uni-axial stress (stretching, self-stretching, compressing, or confining), the diameter, and the swelling behavior related to the swelling agent (see also subsection 5.4.2 and Figure 5.2 in section 5.5. Drying at room temperature can take up to several days and its duration can be shortened to one day at 40°C. Unfortunately, simple drying in a horizontal arrangement results in strongly bent sticks due to a mechanical response to an inhomogeneous distribution of still swollen (bottom) and more dry (top) zones. The radii of such bent dry sticks prevent them to be placed into NMR tubes. (seeFigure 6.12).

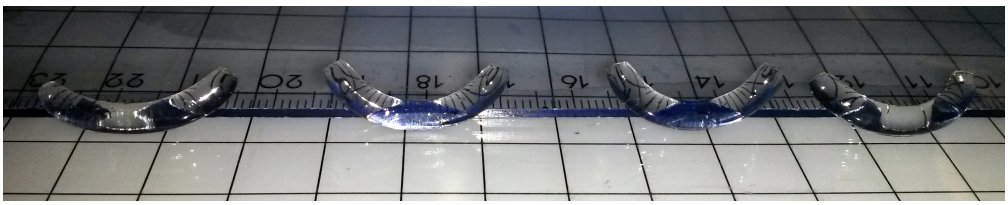

Figure 6.12: Occurrence of bent gels when drying horizontally.

To circumvent the occurrence of bending, the sticks are arranged vertically within cylindrical glass vials with a diameter of 1 cm. The effect of the higher

evaporation on top effects a longitudinal drying along the axis of the gels, yielding straight and homogeneous sticks (see Figure 6.13.

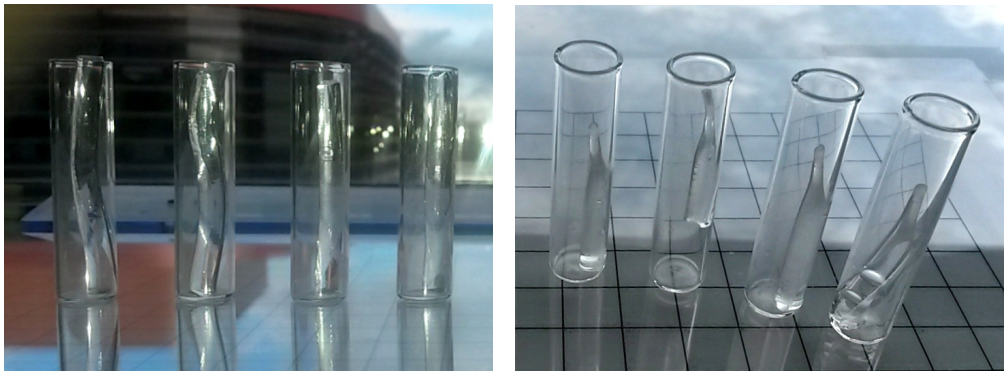

(a) **(b)**

Figure 6.13: Vertically placed gel sticks before (a) and during (b) drying.

Figure 6.14: Cross-linked PEO-DA sticks with different polymerization mass contents (%(w/w)) after vertical drying.

6.2 Swelling behavior

As the amounts of swelling and inducable deformation by mechanic stress play a crucial role for the suitability of cross-linked PEO-DA sticks as a versatile alignment medium, the influence solvent composition and mass content were investigated. Based on the results, cross-linked PEO-DA sticks could be adapted for scaling tests in stretching and compressing apparati.

6.2.1 Solvent compatibility

To test the assumed swelling capability in pure solvents with different polarities and mixtures, PEO-DA35000 was cross-linked with a mass content of 25% to be tested in pure solvents and with a mass content of 16% to be tested in selected mixtures (Figure 6.15). Both formulations were cast in an NMR glass tube with an inner diameter of approximately 3.9 mm. Deviating from the standard protocol described in section 6.1, the sticks were cut *after* the initial washing in water and drying. Therefore all the dry sticks had an initial length of 1 cm and and a diameter of 2.4 mm and were subsequently placed with excess of pure solvent or mixture for two days at room temperature in glass vessel of 10 ml volume and closed with screw caps. Then dimensions and weight of the swollen gels were determined and their volume was calculated geometrically based on diameter and length, assuming a cylindrical shape. Furthermore, the volume was calculated alternatively from the ratio of weight to density, neglecting possible (small) deviations due to the temperature and the fact that the densities of PEO-DA mixtures deviate from the pure solvent densities provided in the respective technical data sheets of the suppliers. The densities of the mixtures were evaluated by weighing 1 ml of each mixture. Both the resulting volume increase factors (related to $V(M) = \rho/m$ and $V(geom) = (\text{ø}/2)^2 \pi l$) relative to the dry state are recapped in Figure 6.15 and a more detailed listing is found in Table 11.2 in the appendix.

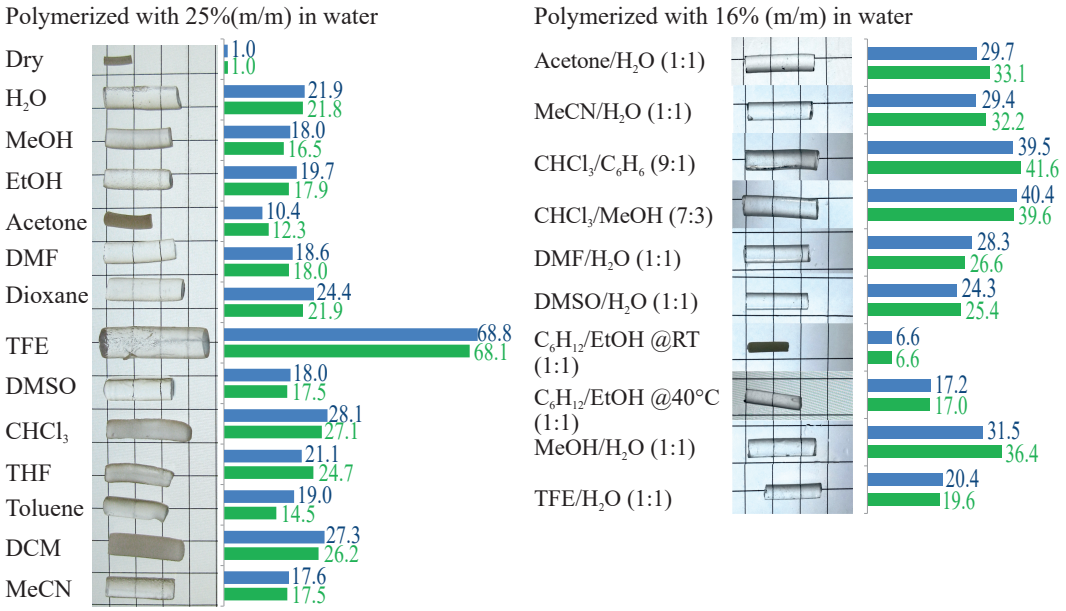

Figure 6.15: Dry PEO-DA stick and swollen sticks in different solvents and corresponding volume increase factors relative to the dry stick. The grid size is 1 cm. The opalescence occurs due to evaporation, therefore, the pictures of the sticks polymerized with 16%(w/w) were taken individually.

Acetone showed the smallest swelling between the selected pure solvents and the initial transparent stick turned opaque during exposition to air due to evaporation. The effect was reversible upon exposition to excess acetone. The mixture of cyclohexane and ethanol remained in a yet swollen but brittle state at room temperature that could be remarkably swollen when heated to 40°, showing the limits of the cross-linked PEO-DA.

The swelling behavior plotted against the second virial coefficients of the pure solvents is shown in Figure 6.16 and indicate a raw correspondence, nevertheless, the values of B are partially interpolated or measured values from different sources (see Table 11.3) and strongly depend on the temperature. Besides, the swell factor Q_m might deviate due to incomplete swelling and measurement errors, which in sum prevents a straightforward interpolation.

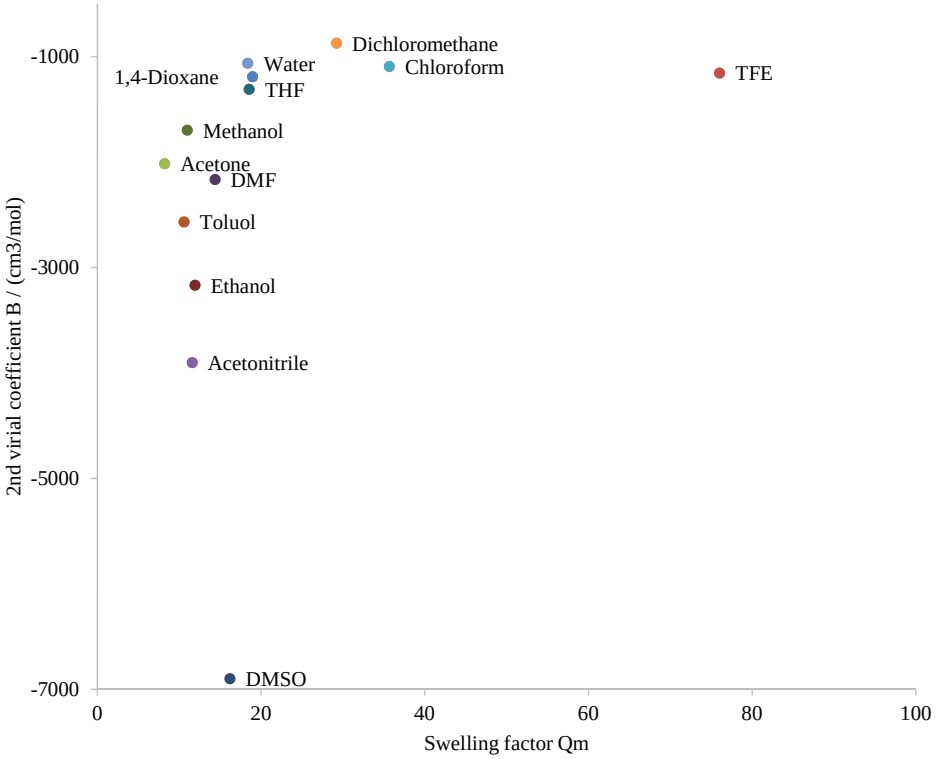

Figure 6.16: Second virial coefficient B and the relative degree of swelling with reference to the volume swelling factor Q_m. The respective values can be found in Table 11.3

6.2.2 Scalability with stretching apparatus

PEO-DA was cross-linked with a mass content of 20% (PEO-DA-35k-20%), in a teflon® tube with an inner diameter of 2.5 mm according to the above described protocol including washing and cutting the polymerized gels into pieces of 2 cm and dried. One dry stick with a diameter ($\varnothing_{dry}$) of approximately 0.9 mm was then inserted into a stretching device (see Figure 5.3) equipped with a silicone elastomer tubing. Then 300 µl D_2O were added while care was taken to prevent bubbles. The prepared stretching device then was left for one week at room temperature for equilibration. The swollen stick had reached the silicone rubber walls and was self-stretched in the silicone tubing to 2.9 cm. It revealed a small quadrupolar splitting $\Delta\nu_Q$ of D_2O in the deuterium (^2H) spectrum indicating partial alignment of the solvent. The deuterium spectra resulting from further stretching the silicone tubing and correlation of lengths and quadrupolar splittings are shown in Figure 6.17.

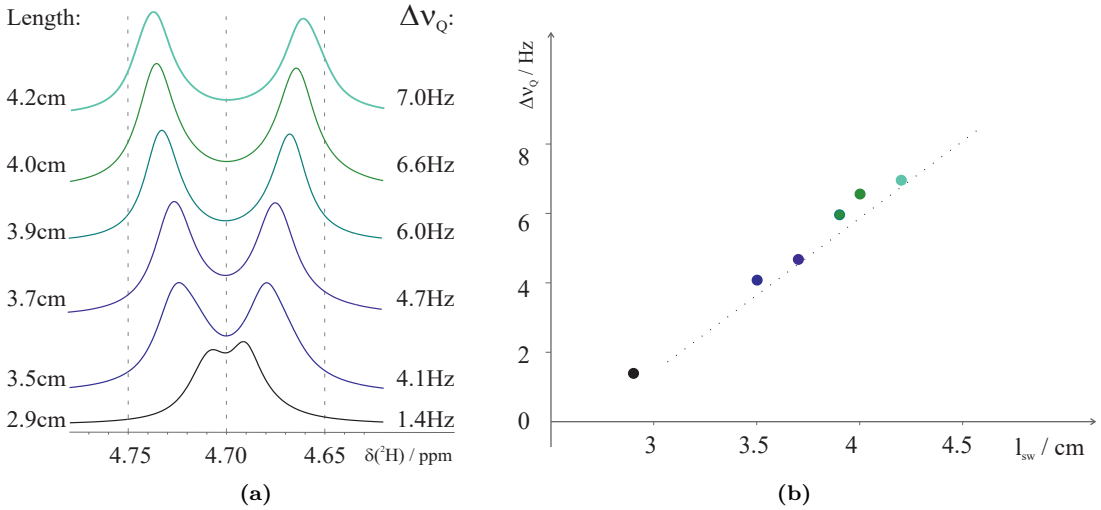

Figure 6.17: Quadrupolar splittings ($\Delta\nu_Q$) of D_2O in the respective deuterium (^2H) spectra scaled by the amount of stretching.

Since the initial state was already anisotropic, the theoretical length of the stick in an isotropic state is interpolated via linear regression (see Figure 6.17b), leading to a theoretical non-stretched length (l_0) of about 2.58 mm. With the extension factor Ξ from the work of Kuchel[162] defined as

$$\Xi = \frac{l_{stretched}}{l_0} - 1 \tag{6.1}$$

values of approximately 0.12, 0.35, 0.43, 0.51, 0.54, and 0.62 for the six different lengths shown in Figure 6.17a were yielded, respectively.

6.2.3 Influence of the mass content

Once the broad solvent compatibility and the applicability with stretching and compressing devices was proven, the influence of the mass content on the swelling was evaluated. Therefore, gel sticks of the 5 established formulations (Table 11.1) were prepared in teflon® tubes with an inner diameter of 2.7 mm and dried. Then they were left for free swelling for two days and the dimensions and weights of the dry and the swollen sticks were compared (Table 6.2).

To evaluate a theoretical stretching factor for the five swollen sticks (all with swollen diameters above 4 mm), they were transferred into a teflon® tube with an inner diameter of 3 mm and their length was measured. To achieve this, a conical pipette tip for 100µl micropipettes was cut such that the small end had an inner diameter of 3 mm and the other end was left, having an inner diameter of 5 mm. The short end was connected with a short piece of silicone tubing to the teflon®

tubes, serving as a funnel for the transfer via vacuum applied from a syringe at the other end (Figure 6.18).

Figure 6.18: Assembled pipette tip filler to transfer freely swollen gels.

Doing so, the PEO-DA stick with the highest mass ratio broke. Nevertheless, the other four sticks showed elongation factors above 1.74. The results are summarized in Table 6.2.

To be able to apply polymer gels as alignment media, the diameters in the swollen state play, as mentioned above, a crucial role. Therefore the influence on the relative increase of the diameter due to swelling with regard to the initial mass content is plotted in Figure 6.19a. Within the range of 16% to 50% the ratio of the swollen diameter to the dry diameter decreases linearly. The reason is assumed to be an increasing cross-link density and more entanglements within the polymeric network, that reduce the relative swelling capability. Interestingly, the absolute diameters in the swollen and dry state increase slightly with the mass content (Figure 6.19b), as there is more material left in the dry state, which is also resembled in the swollen state. Considering the mass and volume uptake, decreasing relative swelling is observed in accordance with the decreasing relative diameter(Figure 6.19c).

The relative elongation factor Ξ derived from the transferred sticks has a minimal value for the 20% stick. Therefore, the almost linear rising relative elongation factor Ξ above the polymerization mass fractions above 20% can be explained by the increasing absolute diameters caused by the increased amount of polymer within the gel. The higher amount of polymerschains, the more water can be taken up by the gel. The 16% sticks show higher swelling factors than expected. Since below 16 % only oligomers are found with PEO-DA-35000, this is related to a lower cross-link density and more defects within the network enabling a higher swelling behavior.

Mass content w_{poly}	$wt\%$	**16**	**20**	**25**	**30**	**50**
Preparation	#	45	46	47	48	UV
Dimensions of dry sticks						
l_{dry}	cm	1.14	1.44	1.40	1.28	1.62
$\varnothing_{dry}$	cm	0.12	0.13	0.15	0.16	0.21
m_{dry}	mg	14.3	19.4	23.9	27.0	55.9
Calculated volume and density						
V_{dry}	ul	14	18	23	26	53
ρ_{dry}	g/cm^3	1.06	1.06	1.04	1.05	1.05
Dimensions of swollen sticks						
l_{sw}	cm	3.80	4.31	3.80	3.56	3.59
$\varnothing_{sw}$	cm	0.43	0.43	0.46	0.47	0.48
m_{sw}	mg	575.4	635.0	665.0	681.0	697.9
Calculated volume and density						
V_{sw}	ul	552	611	632	618	650
ρ_{sw}	g/cm^3	1.04	1.04	1.05	1.10	1.07
Swelling ratios						
l_{sw}/l_{dry}		3.3	3.0	2.7	2.8	2.2
$\varnothing_{sw}/\varnothing_{dry}$		3.5	3.3	3.2	2.9	2.3
V_{sw}/V_{dry}		40.7	33.5	27.4	24.0	12.1
m_{sw}/m_{dry}		40.2	32.7	27.8	25.2	12.5
Dimensions of swollen sticks transferred into teflon® tubes with inner diameters of 3mm						
$l_{stretched}$	cm	6.9	7.5	7.7	8.7	broken
$V_{stretched}$	ul	488	530	544	615	-
$\Xi_{stretched}$		0.82	0.74	1.03	1.44	-

Table 6.2: Dimensions, weights and swelling behavior in D_2O of PEO-DA gel sticks of different mass content cast in a teflon tube with an inner diameter ($\varnothing_i$) of 2.7 mm.

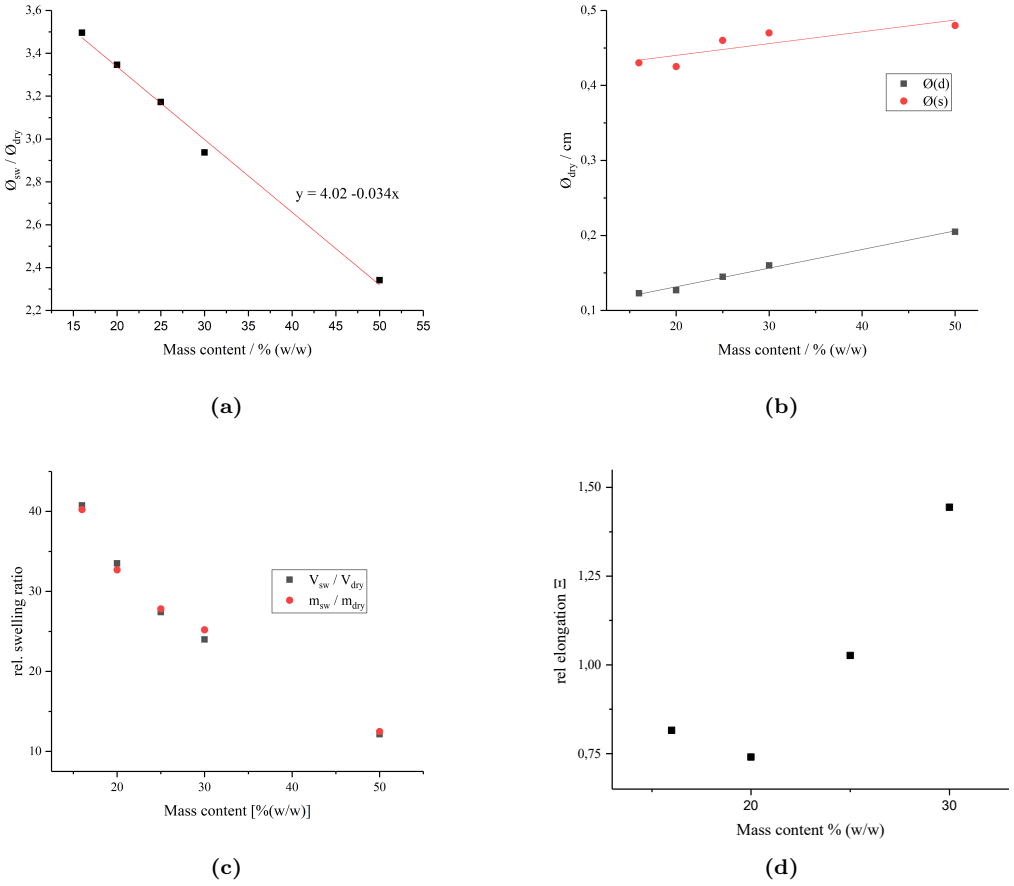

Figure 6.19: Behavior of PEO-DA35000 sticks depending on the mass content. (a) Influence of the initial mass content on the diameter swell ratio. (b) Influence of the initial mass content on the diameters of dry and swollen gel sticks, polymerized in a mold of the same diameter of 0.27 cm. Both graphs resemble a lower amount of PEO-DA. (c) Correlation of the relative swelling volumes and mass ratios. Higher *wt* fractions induce a smaller relative swelling. (d) Relative elongation Ξ when PEO-DA sticks cast in the same diameter of 0.27 cm are swollen to equilibrium freely in water and afterwards are transferred into a tube with an inner diameter of 0.3 cm.

6.2.4 Influence of the composition of the mixture

Since NMR measurements are also carried out in mixtures, the swelling behavior depending on the composition of a binary mixture was investigated. Trifuoroethanol (TFE) is a solvent, known for its helix-forming properties on peptides and proteins,[178] and used together with water for the structure elucidation of membrane associated biomacromolecules. To evaluate the influence of the water/trifluoroethanol (TFE)-ratio, PEO-DA35000 sticks with a mass content of 16%

were cast in teflon® tubes ($\varnothing_i$:3 mm) and cut and dried. Then the swelling behavior was measured in pure water and TFE and mixtures with 80%(v/v), 60%(v/v), 50%(v/v), 40%(v/v) and 20%(v/v). The resulting swollen diameters are shown in Figure 6.20.

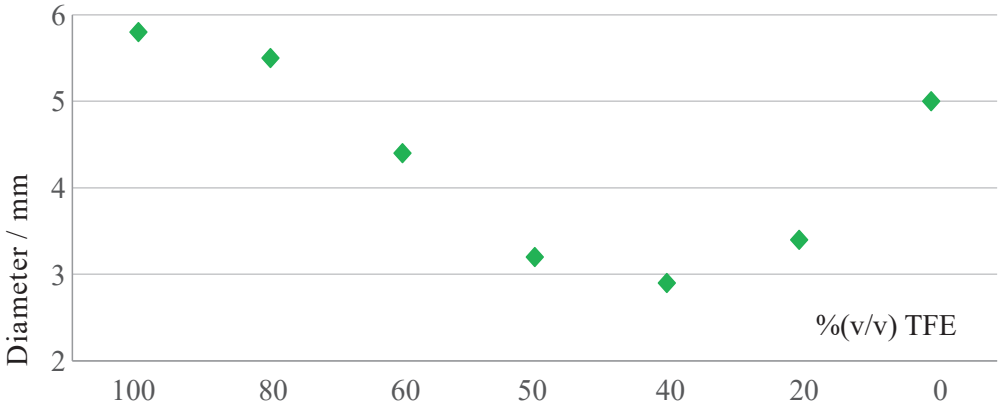

Figure 6.20: Influence of the TFE/water-ratio on the swollen diameter.

Both the pure liquids are good pure swelling agents, with TFE showing about 20% stronger swelling of the diameter. When mixing water and TFE, the transition of the swelling diameter is not linear, but possesses a minimum swelling that just resembles the diameter in which it was polymerized. Two possible mechanisms depending on the interaction taken up by the two components within the swollen network. One is that both the water and the TFE molecules compete with the PEO chains, leading to a hindrance of the interactions with the polymer chains. The other possibility is that TFE and water interact more with each other, than with the PEO chains, leading to a decreased swelling. Nevertheless, with the gained data it was possible to adapt the polymerization diameter for PEO-DA35000-16% gel sticks to measure biomacromolecules in this binary mixture. Moreover, it is shown that the swelling and therefore the resulting alignment can be scaled by the choice of the composition, when working with mixtures.

6.2.5 Adaptation of PEO-DA for the application in compressing apparati

As already stated in section 5.5, the compressing device offers fast preparation when a suitable diameter of the sticks is realized by the application of a pumping protocol to load or wash out analytes into or from the swollen gels, respectively.

Therefore the method was tested successfully with PEO-DA35000-20%, by comparing the NMR spectra before and after application of the repeated compressing and releasing protocol[174] in a 200 mmol solution of sucrose (Figure 6.21).

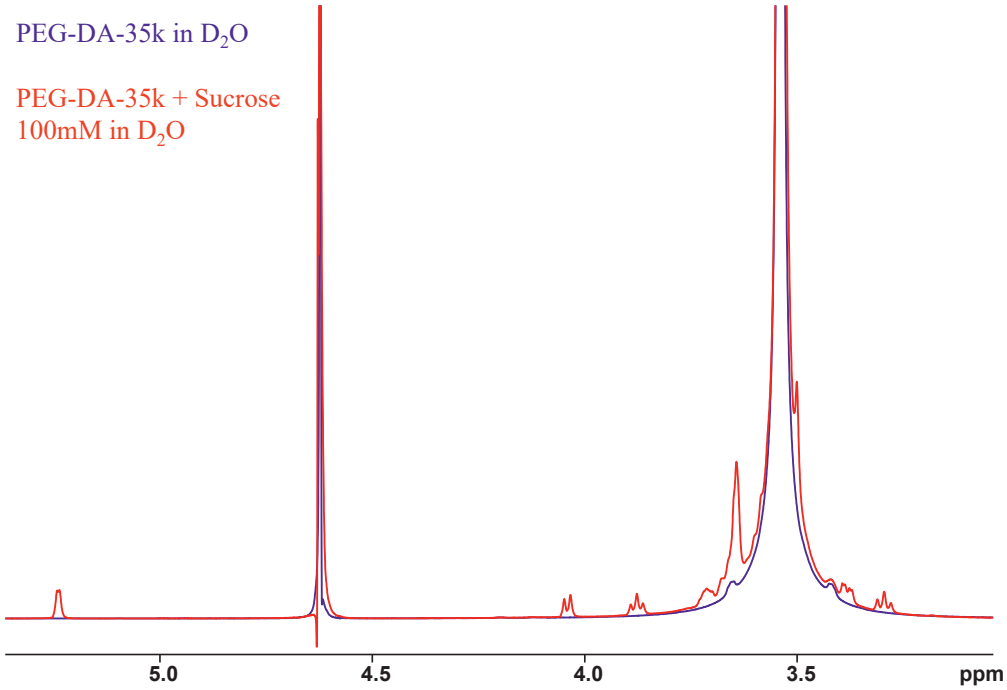

Figure 6.21: Fast preparation of an aligned sample within 20 min, starting from a pre-swollen PEO-DA35000-20% gel in D_2O before (purple) and after (red) four times of repeated compression and releasing the gel in the compressing apparatus (see Figure 5.4).

Since the initial swollen diameter was already 3.2 mm the change of the aspect ratio was to little, to determine a quadrupolar splitting in D_2O within the line width of the deuterium signal of 1.7 Hz. The quadrupolar splittings of D_2O (C_2 symmetry), are generally smaller than for deuterated chloroform. Therefore, numerous trials were carried out with deuterated chloroform, as it is more sensitively showing a quadrupolar splitting when partially aligned. Unfortunately, its strong swelling degrees (see Figure 6.15) regarded to cast PEO-DA35000 in very small diameters between 1.0 and 1.8 mm to accomplish swollen sticks with aimed diameters of 3.2 to 3.5 mm. Such cast sticks were to brittle and unstable and did shrink to diameters below 0.3 mm upon drying. Here, volume to surface effects render a reproducible cross-linking procedure impossible. Furthermore, small amounts of oxygen being absorbed or diffusing into the teflon® tube that also have smaller wall thickness at these small diameters perturbed the production of homogeneous sticks.

For the above stated reasons and regarding the possibility to decrease swelling

upon blending with agents showing less swelling, a method could be established, where a PEO-DA35000-50% (photo-polymerized) stick with a diameter of 1.8 mm put into a 1:1 (v/v) mixture of deuterated chloroform and deuterated DMSO in a compressing device, confining the stick directly afterwards. The stick was left for equilibration one week and then quadrupolar splittings in the initial state and upon releasing in several steps were determined including the fully released state with a non-stretched length of 8.2 cm.

Then the stick was transferred into a stretching device. During the transfer with a pipette tip, a fraction of 1.1 cm broke, leaving a non-stretched length of 7.1 cm. In the stretching apparatus, the remaining stick was elongated to 7.8 cm and the quadrupolar splitting was determined. The stick could be elongated further stepwise until a length of 13.5 cm was reached. The resulting elongation factors Ξ and the corresponding quadrupolar splittings are summarized in Table 11.4 and selected examples of the deuterium spectra are shown in Figure 6.22. In Figure 6.23 the resulting quadrupolar splittings $\Delta\nu_Q$ are plotted against the respective elongation factors.

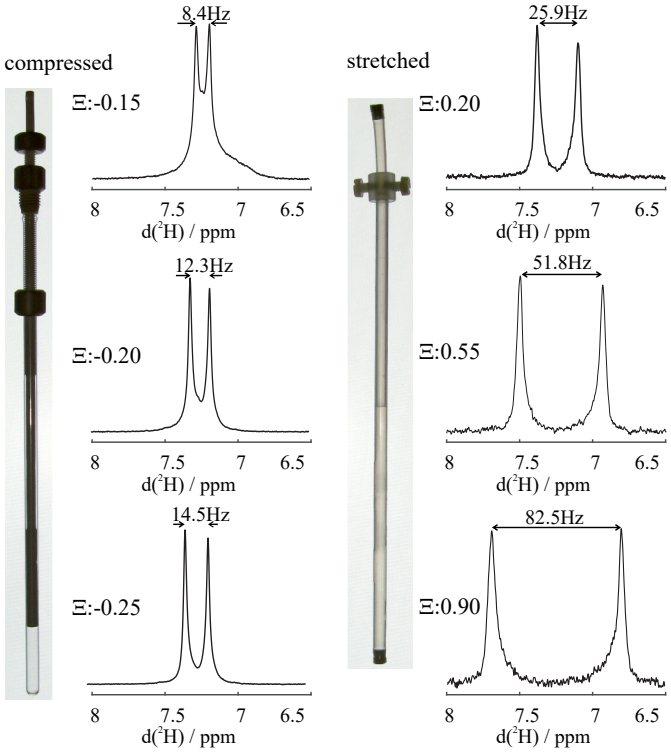

Figure 6.22: Compressing and stretching of the *same* PEO-DA35000-50% stick and corresponding quadrupolar split peaks of the deuterated chloroform revealing scaled alignment with negative to positive elongation factors Ξ.

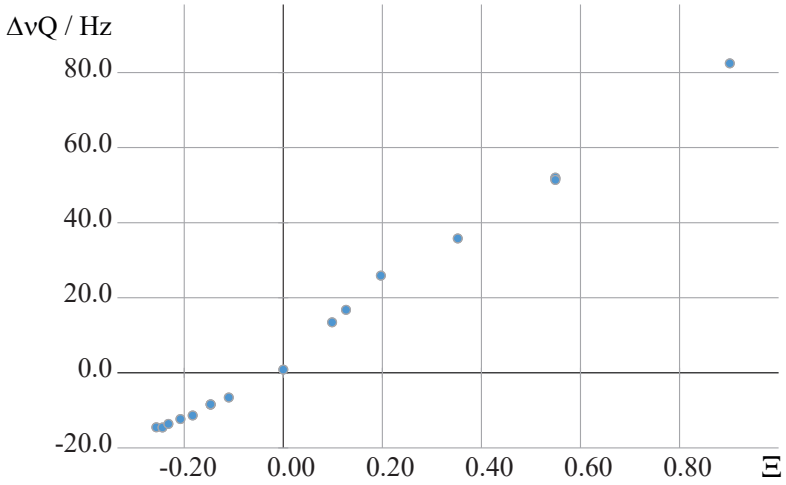

Figure 6.23: Quadrupolar couplings $\Delta\nu_Q$ derived from the same stick applied in a compressing and a stretching device. Note: the sign of the quadrupolar splittings are assumed to be positive for positive elongation regarding Equation 4.37 and Equation 4.38 with a positive value for eQ(^{2}H)=0.286fm^2 and an axially symmetric EFG.

6.3 Results

Commercially available PEO is a cheap educt that can be purchased in relatively narrow dispersities (for the tested educts PEO-6000 and PEO-35000 purchased from Sigma-Aldrich Đ was about 1.08). Also acryloyl chloride, APS and TEMED are commercially available standard chemicals. The two main reactions, the diacrylation and later cross-linking step can be applied using simple standard methods and can be carried out independently when storing produced PEO-DA in a fridge. Using syringes, teflon- and silicon tubes, it was possible to establish a method to reproducibly create cross-linked polymer sticks of arbitrary diameters for the use as alignment media. Here, argon was used for degassing and flushing the equipment, to avoid the exposition to atmospheric oxygen. The variability in the diameters is crucial to adapt the medium to the swelling behavior of the gels in the later measurements to have control over the strength of the induced partial alignment.

Based on the above investigations, extractions of RDCs are carried out on six different analyte/solvent systems. Finally, a self written program for the semi-automatic extraction of couplings is presented and evaluated.

7 | RDC extraction with PEO-DA

In the above sections, the swelling capabilities and the applicability with stretching and compressing devices has been evaluated. In the following sections, the suitability of PEO-DA as an alignment medium for the use in a variety of solvents and mixtures is demonstrated with six different molecules ranging from small organic molecules (sucrose, borneol, ethinylestradiol) over a peptide derivative (Gramicidin $S^{D\text{-}Pro\text{-}SW}$) to proteins (amyloid precursor protein (APP), malectin). To ease the extraction of couplings, in the following part of this chapter, a new semi-automatic method is invented and evaluated by comparison with manually extracted couplings.

7.1 Materials and methods

7.1.1 Spectrometers and data processing

All NMR experiments applied for assignment and the extraction of RDCs were carried out with the spectrometers listed in Table 7.1. Data processing was performed using the Bruker software TOPSPIN and the self-programmed PYTHON script for the semi-automatic extraction of couplings (subsection 11.2.1).

7.2 Semi-automatic extraction of couplings

As mentioned in subsection 4.5.1, manually extracting residual couplings with the overlaying method, can be laborious and subjective. To overcome the manual method, in this work a program that performs the semi-automatic extraction of RDCs from selected slices from 2D spectra with physically sound errors was invented. The method takes up the approach of the manual extraction, which essentially determines the frequency difference and its limits from the estimated maximum overlap of the peaks. Mathematically, this is the problem of finding the distance of the greatest (self-)similarity and can be solved by means of an auto- or cross correlation, respectively. To apply the method, slices of the corresponding

Table 7.1: NMR spectrometers for assignment and the extraction of couplings and their specifications.

Identifier	Location	^{1}H field strength	Console	Probe head	Frequency
A Pauli	IBG4	600 MHz	Avance II	5 mm BBI 5 mm TBI	^{1}H: 600.19 MHz ^{13}C: 151.91 MHz ^{2}H: 92.13 Mhz
B Ernst	IBG4	600 MHz	Avance III	5 mm cryo CPTCI	^{1}H: 599.70 MHz ^{13}C: 150.81 MHz ^{2}H: 92.06 Mhz
C IOC600	IOC	600 MHz	Avance I	5 mm TBI	^{1}H: 600.13 MHz ^{13}C: 150.90 MHz ^{2}H: 92.12 Mhz

peaks have to be extracted as in the manual approach. The region of interest within the slice is selected and exported to an ASCII file with the command *totext* in the Bruker Topspin software. This file then contains a finite sequence of discrete intensities, representing the real part of the selected Fourier transformed processed signal, each equally departed by the resolution in Hertz per point (Hz/pt) from each other.

7.2.1 Underlying principle and implementation

A very simple method to find the coupling at which the two peaks overlap most could be carried out by summing up all products of the signal function S(δ) with itself shifted point by point S($\delta + \Delta\delta$). The discrete auto-correlation G($\Delta\delta$) function is then given by

$$G(\Delta\delta) = \sum_{n=1}^{N} S(\delta)S(\delta + n\Delta\delta) \tag{7.1}$$

Unfortunately, the amount of points makes this procedure quite laborious, especially when processing many points, which is essentially the case when working at high resolution for example at 0.2 Hz/pt. A carbon proton coupled doublet is typically found within a range of 250 Hz, which means that it contains 1250 points. Applying the above formula means, n times n points must be multiplied, giving an effort of 1.562.500 multiplications. To circumvent the problem of incremental multiplication and summing up, the Wiener-Khinchin theorem[179] is applied, stating that the autocorrelation function is the inverse Fourier transform of the power

spectrum.

$$G(\tau) = \int_{-\infty}^{\infty} S(\delta)S(\delta+\tau)\ d\tau = \mathcal{F}^{-1}(|F(\omega)|^2) \tag{7.2}$$

It is well established in signal processing and where time-stationary continuous processes are analyzed to reveal periodicities. Even though it is unusual to apply the method to a signal function in the frequency domain, mathematically the only difference is the unit. Nevertheless, in literature the shifting parameter is called τ and denoted as a lag, furthermore, autocorrelations are often defined in terms of periodic time-series as can be also found in section 9.3 where the autocorrelation in time gives insights about molecular mobilities. Moreover, the *lag* τ can represent also other variables like a shift in space, or as is the case for the semi-automatic extraction of couplings, a frequency shift $\Delta\delta$. It is important to note that the so-called *power spectrum* term $|F(\omega)|^2$ contains the information how *frequencies* are periodically distributed in the frequency domain[a]. Its inverse Fourier transform, the autocorrelation function plots this distribution. The expression for the *power spectrum* can be evaluated with the use of *Parseval's equation*

$$|F(\omega)|^2 = |F(S(\delta))\overline{F(S(\delta))}| \quad . \tag{7.3}$$

Since the extracted rows are finite, the necessary periodicity must be introduced by adding the same amount of points containing zero value (*zero-filling*) and subsequently connecting the end points of the extracted data set. As the data is not continuous but discrete, a discrete fast Fourier transform technique is needed. The NumPy library (NumPy v1.18) for the Python programming language (Python 3.7.3) has the functionality for the above operations. Therefore a program was self written for the semi-automatic extraction of couplings. First, the extracted data set is zero-filled and Fourier transformed, then it is multiplied with its complex conjugate, and the product then inversely Fourier transformed. The resulting correlogram reveals the maximum overlap of peaks.

[a]This term is identical to the spectral density function used to explain the phenomenon of relaxation, see also subsection 9.3.2

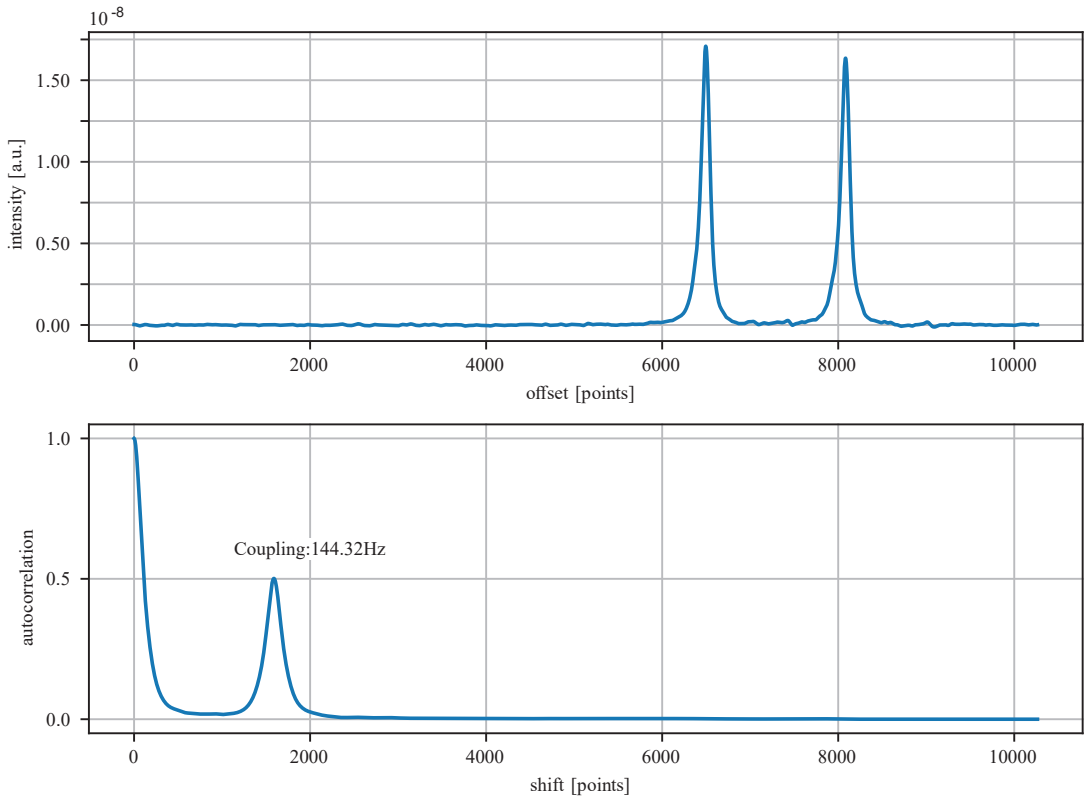

Figure 7.1: Simple autocorrelation example of the row of the H6 methylene protons exported with the command *totxt* (upper plot). The empty area on the the left serves later to evaluate the standard deviation of the noise. In the lower plot, half of the symmetric autocorrelation function $G(\tau)$ thereof (positive values) is shown for the extracted row. The second maximum points to the shift, where both peaks fit best onto each other and hence, represents the searched coupling in shifted points. Multiplication with the resolution of 0.9 Hz/pt yields in the coupling. The relative height of it approaches a value of 0.5 which can be translated into the correlation $R = 2 \times G(coupling) \cong 1$. This proofs that both peaks have a similar shape and the coupling is valid.

7.2.2 Error determination

For the evaluation of the errors, it is straightforward, to extract the standard deviation from the noise in an area with no signals. It allows to calculate an area of points centered around the maximum correlation, whose limits give the range of the error. So far, this area has to be chosen manually.

Another criterion for the quality of the overlapping peaks is given by the correlation coefficient R. In the ideal case of peaks with identical shape and no noise being present in the extracted slice, it must take up the value of 0.5, when the maximum intensity for τ=0 is normed to 1, since both peaks contain half of the

area when shifted onto each other. Therefore, both calculation of the error related to three times the standard deviation and the correlation coefficient are carried out and returned. The written python program for the semi-automatic extraction developed by the author can be found in subsection 11.2.1 and is tested in the next sections.

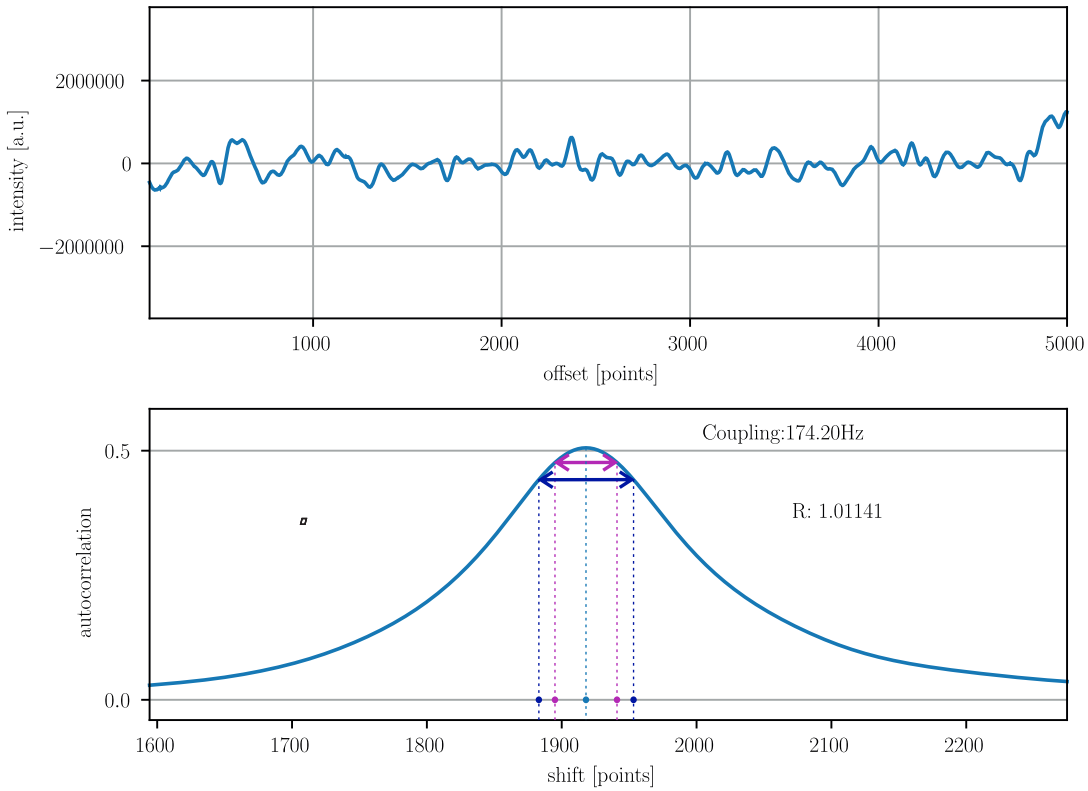

Figure 7.2: Error estimation scheme for the example shown in Figure 7.1 with the standard deviation (purple) of the selected noise region (upper plot) and with a fraction of about 0.997 (pink) of the correlation R (second maximum) gives two intervals (between the pink or the purple dots respectively) that can be interpreted as errors. When the autocorrelation function is not symmetric, the positive and the negative error are different.

7.3 Extraction of RDCs in water

7.3.1 Sucrose

A dry PEO-DA35000-25% stick (Table 11.1) with a length of 1.5 cm was placed into a stretching device with a silicone tubing and 500 µl of a 100 mM solution of sucrose in D_2O were added and left for two weeks to swell to equilibrium. Before inserting into the spectrometer, the silicone tubing was stretched to the maximum and the field was shimmed. In the insert in Figure 7.3 the resulting chemical shift profile of D_2O reveals the quadrupolar splitting along the tube of about 7 Hz, clearly proving that the solvent gets aligned in the stretched gel. A small inhomogeneity in the lower third of the active volume is visible. Nevertheless eleven RDCs were derived by subtracting the total couplings from scalar couplings measured in water (Table 7.2). A detailed table of the manually extracted data with errors is given in the appendix. The scalar (${}^1J_{\mathrm{CH}}$) and total (${}^1T_{\mathrm{CH}}$) splittings in Figure 7.3 were all extracted manually and then semi-automatically to validate the method with a real example. In the following, the extracted rows are processed with the self written python program described in section 7.2. In Table 7.2 the results from both approaches are summarized.

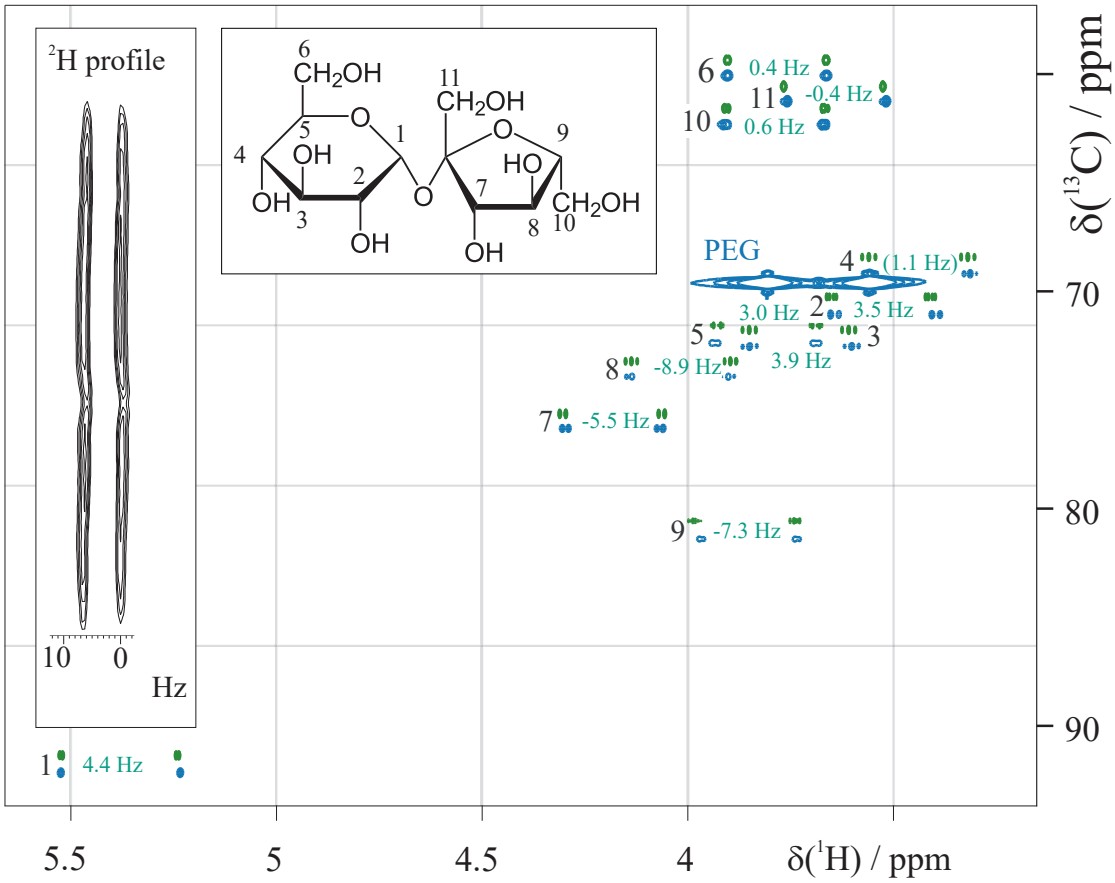

Figure 7.3: Assigned CLIP-HSQCs of sucrose (green) in D_2O and aligned (blue) in PEO-DA-35k. The ^{2}H chemical shift profile reveals an overall quadrupolar splitting $\Delta\nu_Q$ of 7 Hz along the active volume of the aligned sample with a small defect within the lower third. The isotropic peaks (green) were shifted slightly for better comparability. As expected the methylene protons 6, 11 and 10 show only small RDCs due to a higher mobility outside the rings. Besides H4, which is overlapped by the signal of the poly(ethylene oxide) and therefore can only be approximated, all RDCs (turquoise) could be extracted.

Semi-automatic extraction test

The following pictures illustrate the semi-automatic extraction with the extracted rows of both HSQCs from Figure 7.3(green). On the left side are the isotropic (e.g. 7.4a) and on the right side the respective anisotropic rows (e.g. 7.4b). The two plots below contain the two respective corelograms (blue) whose second maxima reveal the shift for a maximum overlap. Twice the value of its relative height corresponds to the cross-correlation of the shape of the two peaks and all other signals (noise, artifacts, overlapping neighbour signals) for the respective shift. This shift in points multiplied with the resolution (here: 0.090826 Hz/pt) is

assumed to be identical with the respective coupling and calculated as described in section 7.2. The plots are given in the order of the respective carbon chemical shift. The method is also applied with the row concerning the polymer signal from the ethylene oxide protons of the PEO-DA chains (Figure 7.6a).

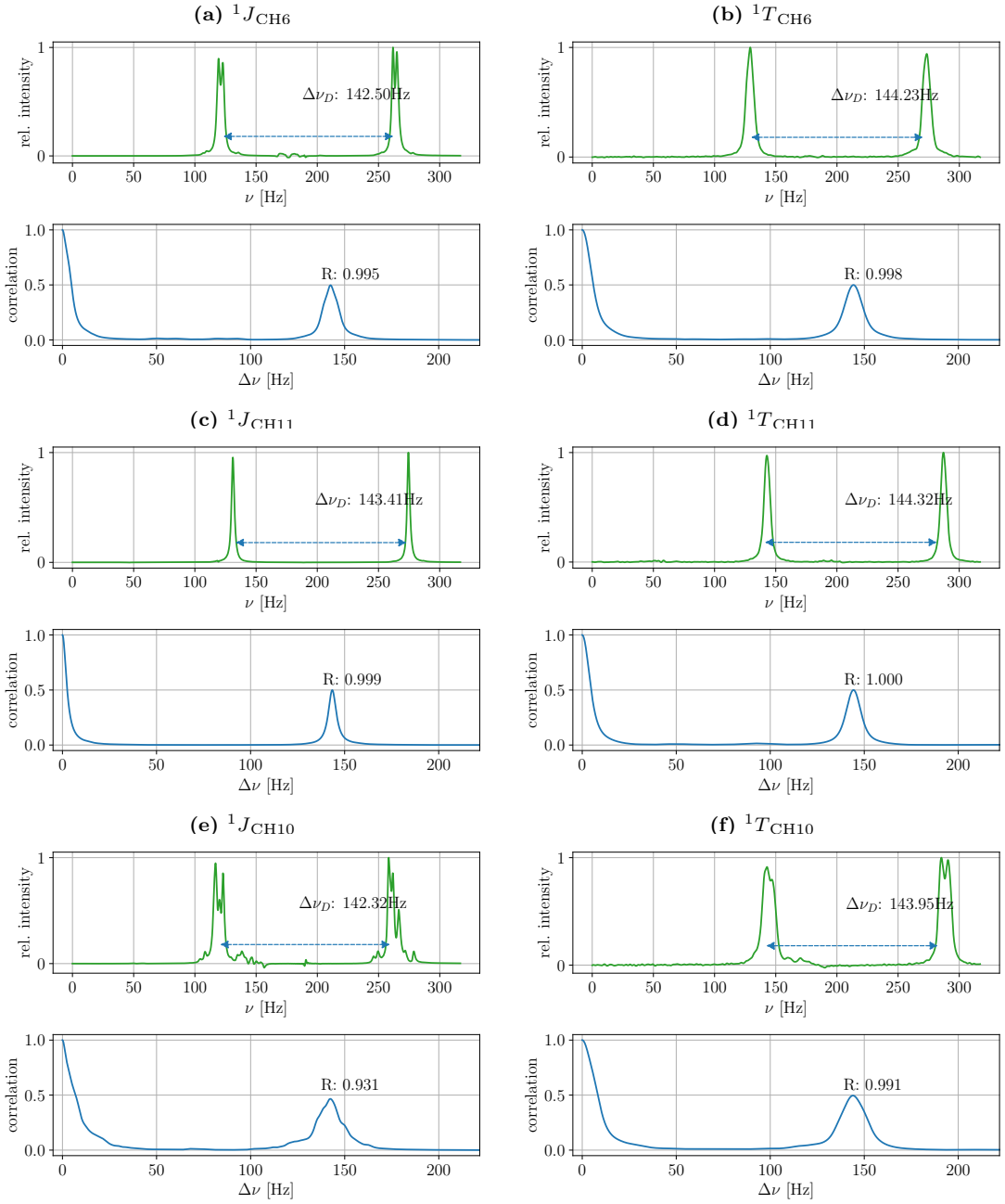

Figure 7.4: Semi-automatic extraction of the sucrose methenyl carbon proton couplings. On the left are the slices measured isotropically in deuterated water, on the right are the anisotropic slices containing the total couplings.

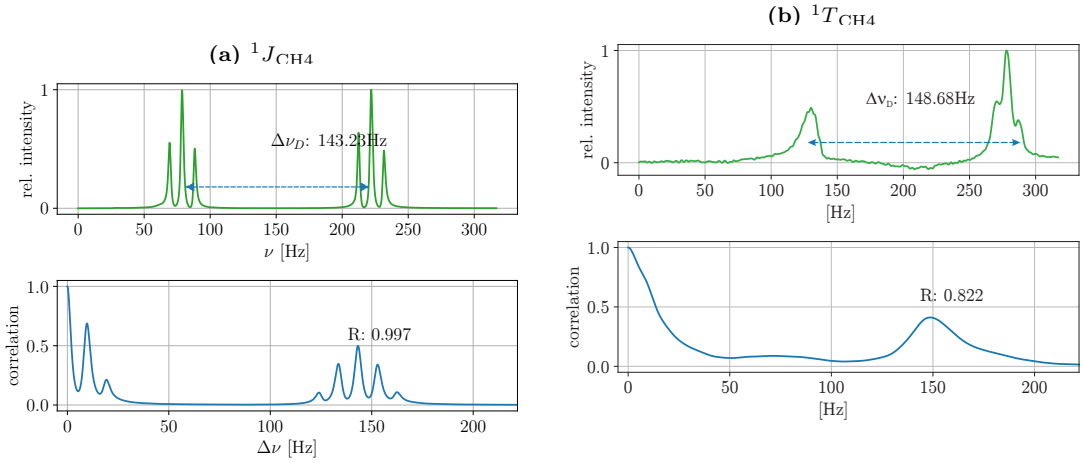

Figure 7.5: The sucrose H4 proton doublet overlaps with the PEO-DA35000 peaks and cannot be extracted precisly by hand nor with the algorithm and must be approximated. Nevertheless the J coupling can be extracted.

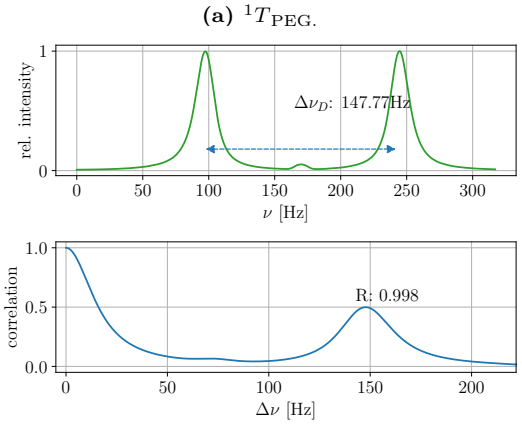

Figure 7.6: The methylene protons of the ethylene oxide units of the stretched PEO-DA35000 stick create a large doublet in the CLIP-HSQC that interferes not only with H4 and creates some small artifacts also visible in the following rows of the methinyl protons H2, H5 and H3.

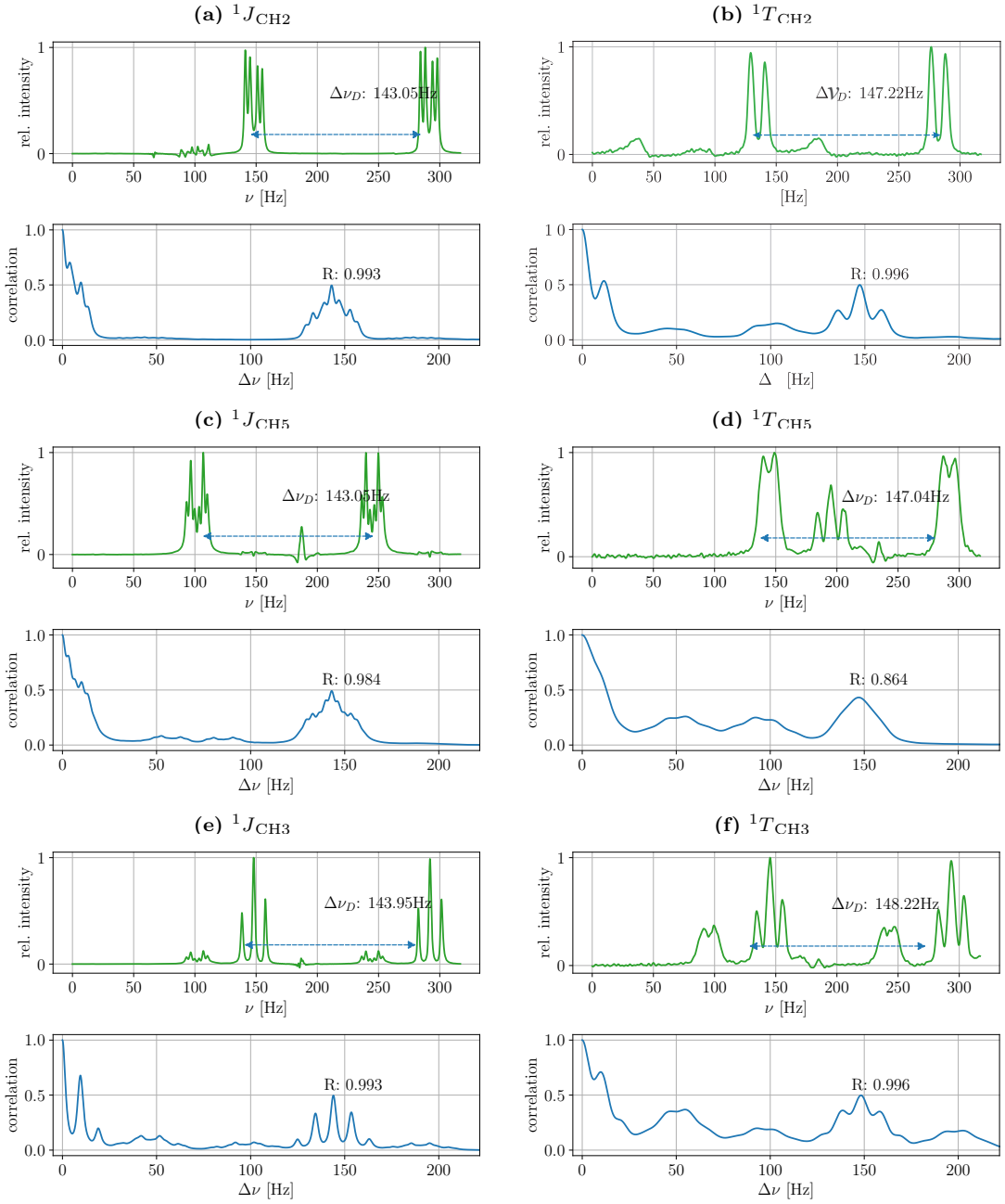

Figure 7.7: Rows of the split proton signals of H2, H5 and H3. All extracted rows have distortions caused by the polymer (Figure 7.6a) and second order artifacts. Since C5 and C3 have have similar carbon chemical shifts, their signals also interfere. The cross-correlation of the two peaks is declined significantly.

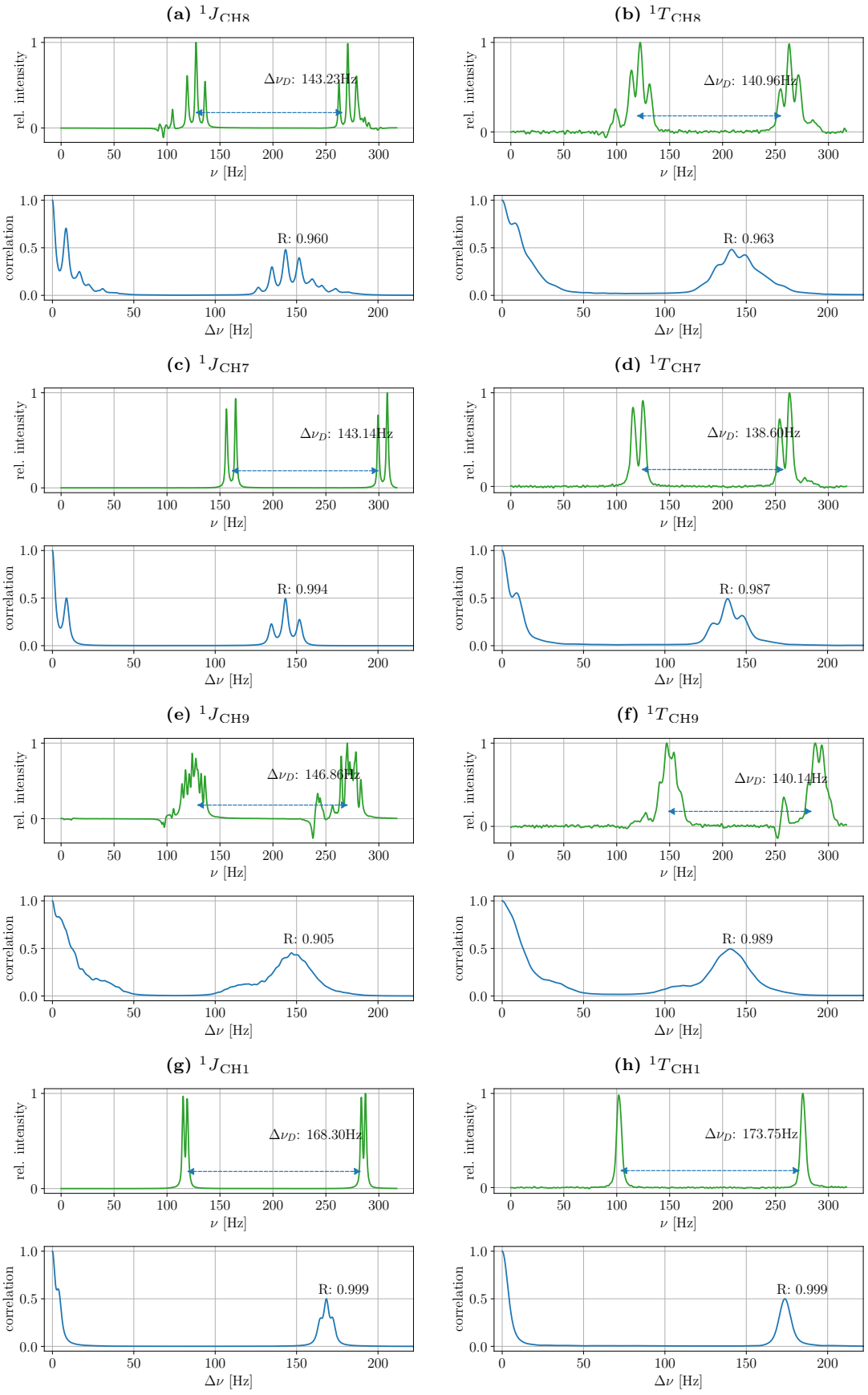

Figure 7.8: Rows for the split proton signals of H8, H7, H9 and H1.

Manually and semi-automatically extracted RDCs

CH	Manually		Semi-automatic		Difference	
	$^1J_{CH}$	Δ^1J_{CH}	$^1J_{CH}$	Δ^1J_{CH}	$^1J_{CH}$	Δ^1J_{CH}
CH6	143.68	0.09	143.70	-0.02	-0.02	0.11
CH11	144.62	0.09	144.60	0.02	0.02	0.07
CH10	143.38	0.09	143.51	-0.13	-0.13	0.22
CH4	144.41	0.09	144.43	-0.02	-0.02	0.11
CH2	144.35	0.09	144.25	0.10	0.10	-0.01
CH5	144.28	0.18	144.25	0.03	0.03	0.15
CH3	145.21	0	145.16	0.05	0.05	-0.05
CH8	144.45	0.09	144.43	0.02	0.02	0.07
CH7	144.48	0.09	144.34	0.14	0.14	-0.05
CH9	148.49	0.27	148.00	0.49	0.49	-0.22
CH1	169.67	0	169.71	-0.04	-0.04	0.04

Table 7.2: Comparison of the extraction methods and isotropic scalar couplings $^1J_{\mathrm{CH}}$ with errors Δ^1J_{CH} derived from a CLIP-HSQC of sucrose in D_2O. Because of the good quality, most or the errors are within the resolution of 0.9 Hz/pt.

7.3.2 Malectin

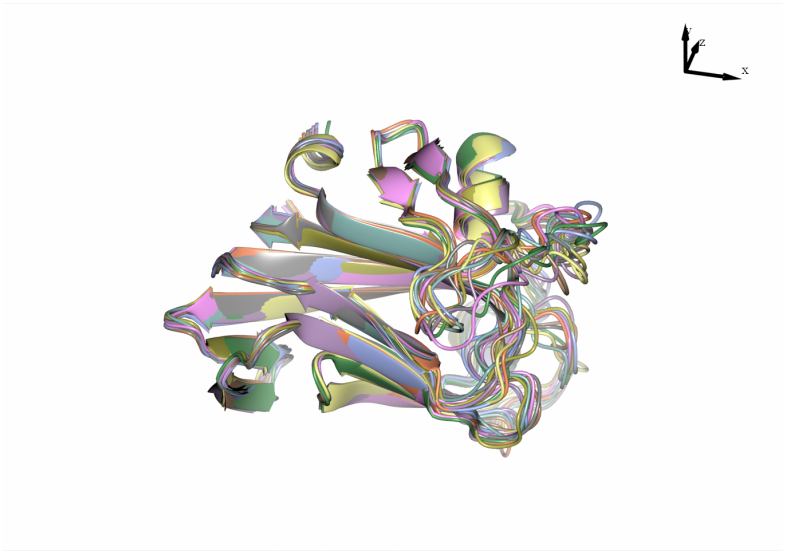

Figure 7.9: Overlay of 10 malectin structures[180] from *xenopus laevis* derived from NMR measurements. For the structure the entry *2JWP* was downloaded from the protein database.

Malectin is a carbohydrate-binding protein consisting of 174 amino acids.[180] A ^{15}N-enriched sample thereof was also partially aligned in PEO-DA and both isotropic $^{1}J_{\mathrm{NH}}$ and anisotropic $^{1}T_{\mathrm{NH}}$ couplings were extracted, using so-called ^{1}H^{15}N-IPAP-HSQC spectra.[181–183] For the isotropically measured spectra, ^{15}N marked malectin was dissolved 100 µM in 20 mM potassium diphosphate buffer, with a salt concentration of 150 mM sodium chloride and 2 mM Cleland's reagent (dithiothreitol (DTT)) in a mixture of 10%(v/v) D_2O in H_2O to sustain ^{1}H bound to ^{15}N. Then a first ^{1}H-1D spectrum was recorded, revealing a huge water peak and the need for water suppression. Instead of pre-saturating the water signal for peptides and proteins, it is common, to apply an improved so-called WATERGATE W5[184] pulse sequence, not to loose the NH-signals due to exchanging protons. The resulting 1D spectrum was recorded, using the *zggpw5* standard Bruker pulse program and is shown in **??**. The resulting spectra are shown below and in subsection 11.2.3. 150 extracted scalar couplings and 166 total couplings resulting in 139 evaluated RDCs can be found. There also a histogram is given.

1D-^{1}H spectrum with watersupression.

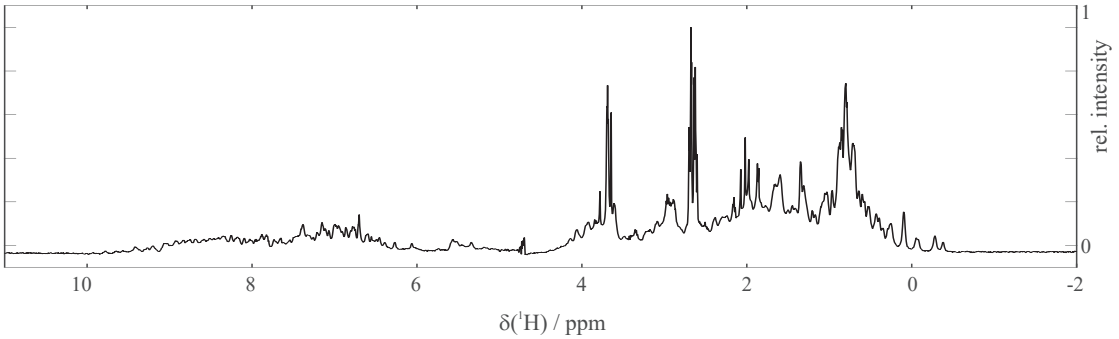

Figure 7.10: The protons of the ethylene oxide groups and the water are substantially decreased. The alignment is weak enough and the homogeneity of the field and the medium allows the distinction of lines.

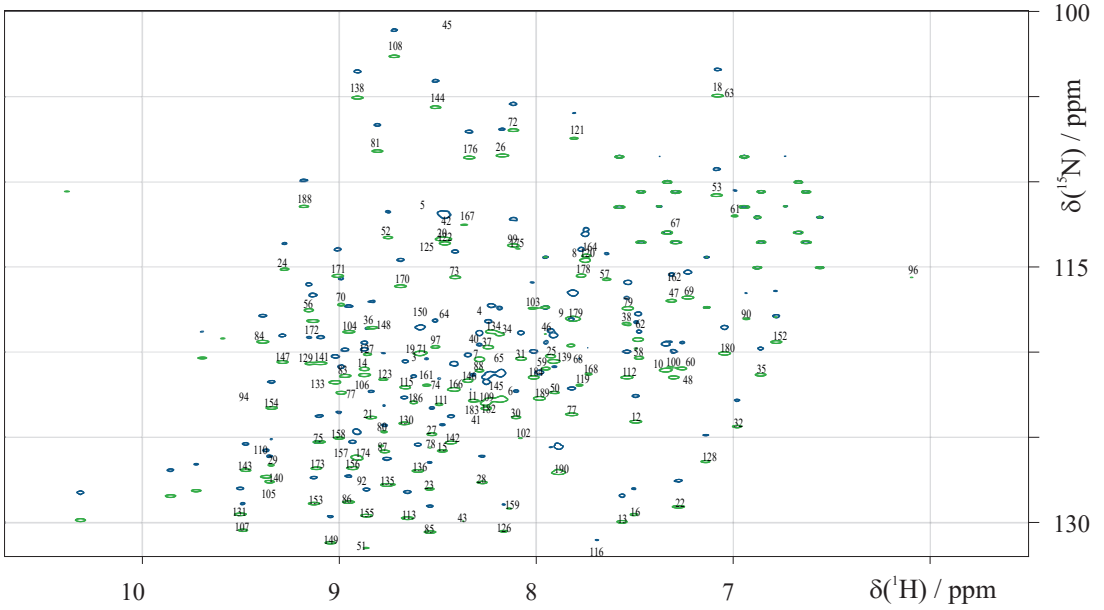

Figure 7.11: Shown are the peaks of the sum (blue, upper) and the difference (green, lower) of the split ^{1}H^{15}N-IPAP-HSQCs[67] within the NH-region. The peaks were assigned relative to the isotropic values, which were provided by Claudia Muhle-Goll and the scalar $^{1}J_{\mathrm{NH}}$ couplings were extracted. The numbers are according to residue numbers given in Table 11.5 together with the chemical shift assignment and the respective scalar and total couplings.

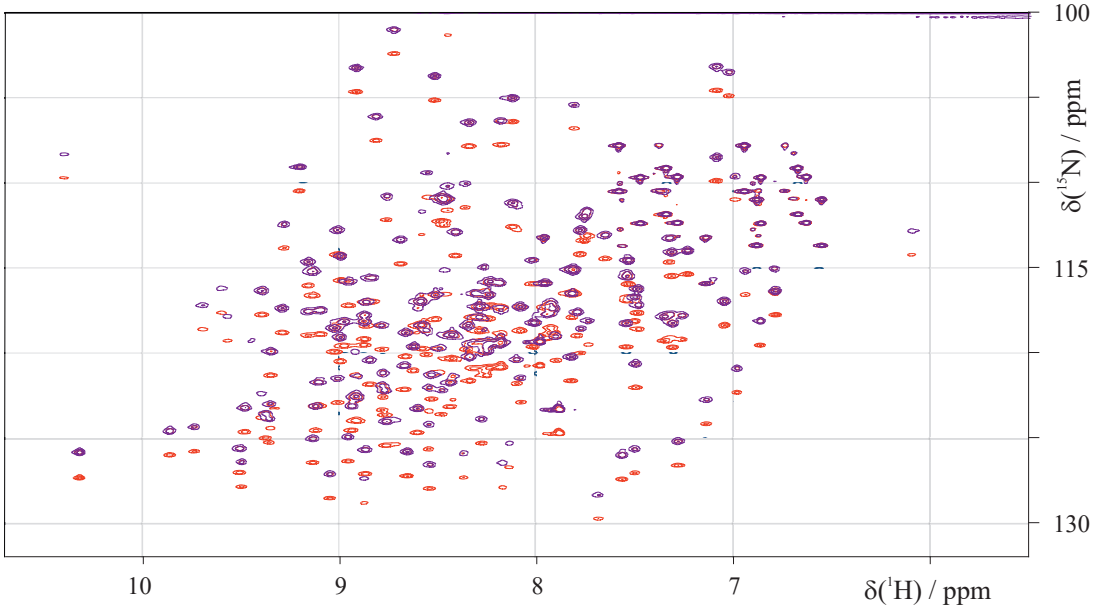

Figure 7.12: Anisotropic sum and difference spectra of malectin. The quality of the spectrum allowed the extraction of 166 couplings that are found in Table 11.5

7.4 Extraction of RDCs in chloroform

7.4.1 Sample preparation with d-(+)-borneol

The next solvent to test the applicability of PEO-DA as an alignment medium was chloroform, one of the standard solvents used for liquid NMR spectroscopy. As a test analyte, the small organic molecule d-(+)-borneol was prepared for testing in a stretching device. 600µl of a solution of 100 mM d-(+)-borneol in chloroform-d were transferred into an NMR tube sealed with a teflon cap. After recording CLIP-HSQC and P.E. HSQC spectra in isotropic solution, a dry PEO-DA35000-25% stick with a diameter of 2.5 mm and a length of 1.15 cm was placed in a Kalrez® tubing inside a cut NMR tube and closed with the special bottom screw to prevent slipping of the tubing when stretched as described previously in the work of Kummerlöwe.[172] A small amount of the borneol solution was added and the tube was left for one hour horizontally to prevent swimming of the PEO-DA stick with a lower density than chloroform. This step wise initial swelling with solvents of higher density than PEO-DA ($\approx 1\,g/cm^3$) ensures the sticks stay at the the very bottom without a gap. After this pre-swelling procedure, the residual borneol solution was added and sealed with Teflon® tape. The prepared stretching device was placed in a fridge and left for equilibration. After 2 days the PEO-DA35000 gel was self-stretched to 6 cm. Within the next 4 weeks no further elongation appeared.

Before inserting into to the spectrometer, the gel was stretched further to 10 cm. In the deuterium 1D experiment the chloroform signal was quadrupolarly split by 274 Hz, indicating a significant partial alignment. Nevertheless, after the sample was shimmed thoroughly, the proton 1D experiment showed sharp signals (Figure 7.13) and hence, CLIP-HSQC and P.E. HSQC spectra were recorded in the uniaxially stretched, aligned PEO-DA35000 sample. After the measurement, the sample was relaxed and stored at 8°C in a fridge. Four weeks later, the sample was again stretched to 8 cm and a quadrupolar splitting of 127 Hz was obtained.

Proton 1D experiment

In Figure 7.13 the corresponding 1D-^{1}H spectra are shown. The huge main peak in the anisotropic spectra arises from the ethylenoxide units. For the two anisotropic spectra, a second signal next to the polymer main peak is visible. It is broadened more pronounced than the analyte signals at higher alignment strength (blue).

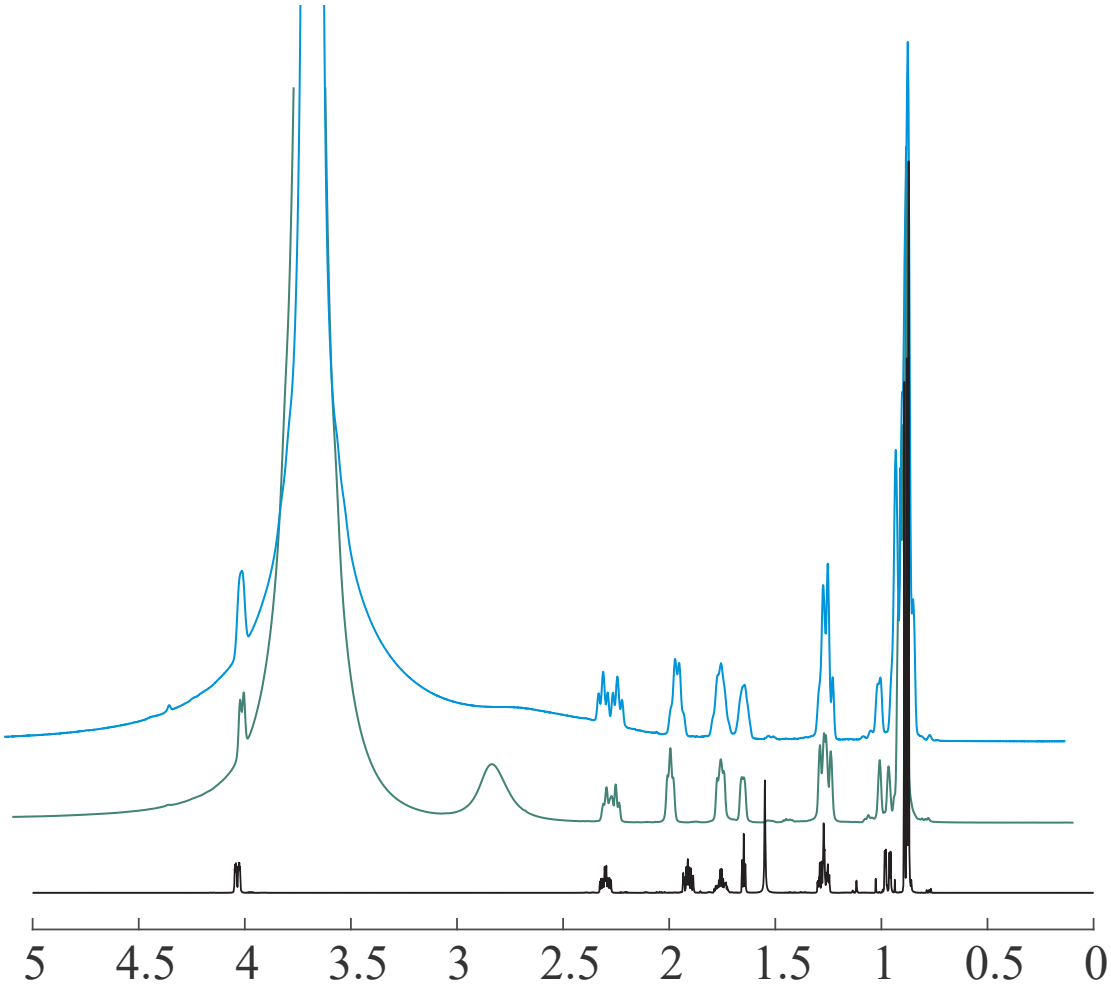

Figure 7.13: 1D-^{1}H-spectra of Borneol in $CDCl_3$/PEO-DA35000-25% isotropic (black) and with two different stretching degrees resulting in qadrupolar splittings of $\Delta\nu_Q$ 127 Hz (green) and 274 Hz (blue).

CLIP-HSQC

The CLIP-HSQC spectra of d-(+)-borneol are superposed in Figure 7.14 and Table 7.3 sums up the results for the extraction of one-bond RDCs with PEO-DA35000 in chloroform-d and a stretching device.

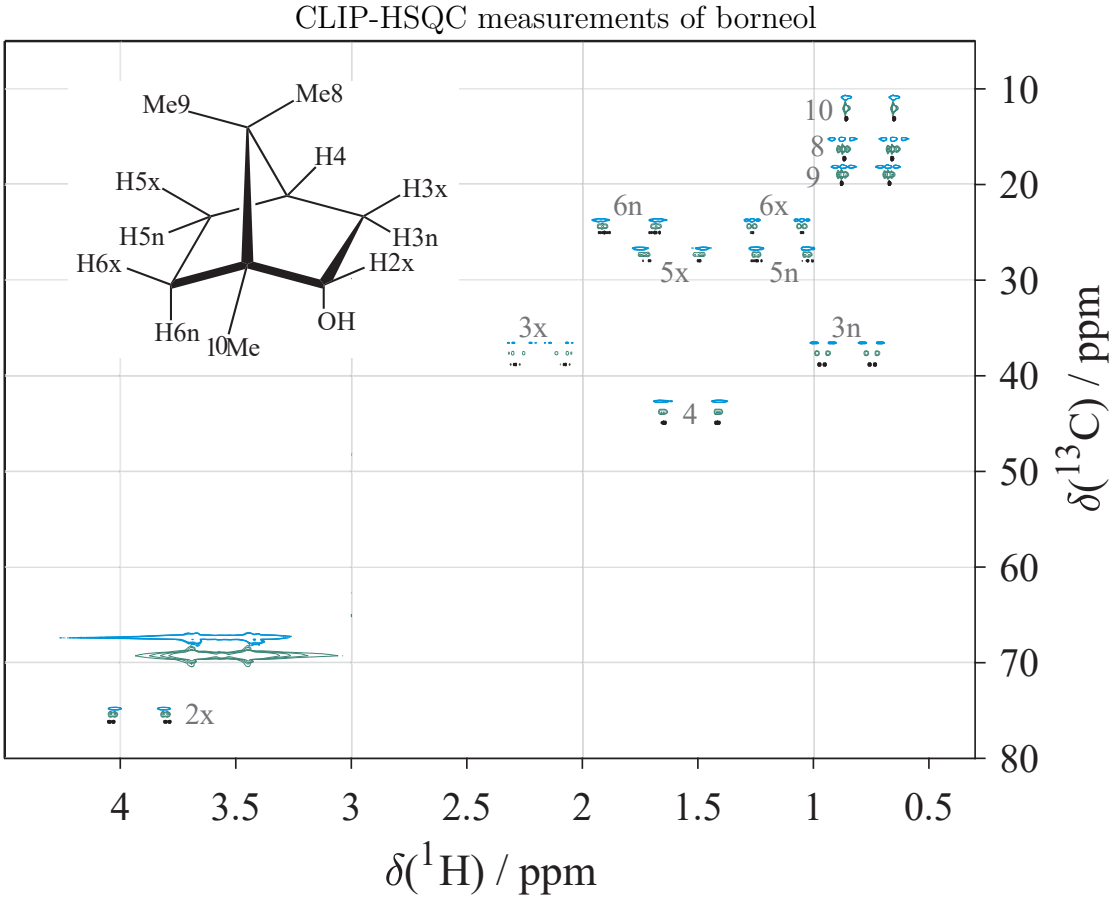

Figure 7.14: Overlay of the peaks from **CLIP-HSQC spectra of d-(+)-borneol** in chloroform- d/PEO-DA35000-25% from isotropic (black) and anisotropic at $\Delta\nu_Q$ 127 Hz (green) and 274 Hz (blue) CLIP-HSQCs. The chemical shifts δ refer to the green peaks recorded at $\Delta\nu_Q$ 127 Hz, the other two sets were centered around them, maintaining the splittings.

Group	^1J	$^1T^a$	$^1T^b$	$^1D^a$	ΔD^a	$^1D^b$	ΔD^b
Me10	124.1	124.2	124.5	0.1	0.3	0.4	1.0
Me8	124.3	128.8	133.8	4.5	0.3	9.5	0.8
Me9	124.4	120.8	116.7	-3.6	0.3	-7.7	0.2
H6x	130.1	129.8	129.4	-0.3	0.4	-0.7	0.3
H6n	131.2	139.1	147.8	8.0	0.6	16.6	1.0
H5n	131.8	131.9	131.9	0.0	0.5	0.1	0.6
H5x	130.1	143.4	160.2	13.3	0.8	30.1	0.9
H3n	130.5	128.1	125.3	-2.3	0.8	-5.1	1.0
H3x	129.5	115.0	103.0	-14.5	2.0	-26.5	3.0
H4	140.2	145.0	150.4	4.8	0.8	10.2	0.5
H2x	145.8	136.7	127.7	-9.1	0.3	-18.1	0.3

Table 7.3: Extracted RDCs from borneol at two different alignment strengths. The superscripts of the couplings T, D and their errors ΔD indicate the measured quadrupolar deuterium splitting of chloroform-d: (a) $\Delta\nu_Q$: 127 Hz and (b) $\Delta\nu_Q$: 274 Hz. All values in are given in Hz.

P.E.HSQC and semi-automatic extraction of geminal couplings

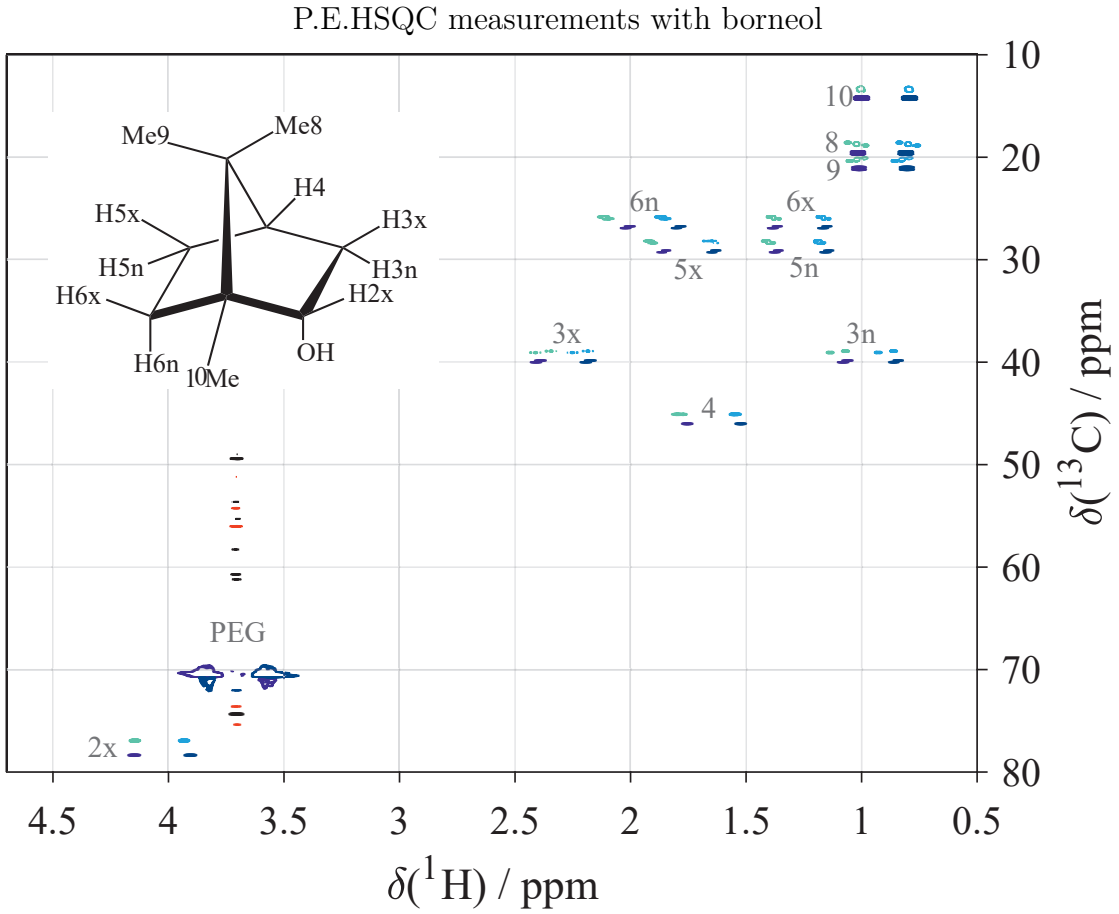

Figure 7.15: Overlay of the peaks from P.E.HSQC spectra of d-(+)-borneol in chloroform-d/PEO-DA35000-25% from isotropic (green and turquoise) and anisotropic (blue and purple), indicating the phase of the peaks. $\Delta\nu_Q$ was 274 Hz (blue). The chemical shifts δ refer to the anisotropic spectrum containing the signal of PEO-DA. Note that the tilts of the respective methylene protons H6n/x and H5n/x changes the direction when partially aligned indicating a positive total coupling $^2T_{\mathrm{HH}}$.

In the following plots, the semi-automatic extraction utilizing cross-correlation of the two extracted rows from the P.E.HSQC is illustrated. On the left are the rows, measured in chloroform-d containing the isotropic values (J), on the right are the anisotropic rows containing the total couplings T shown. The plot in the middle represents the superposed slices from above, shifted onto each other by the calculated coupling.

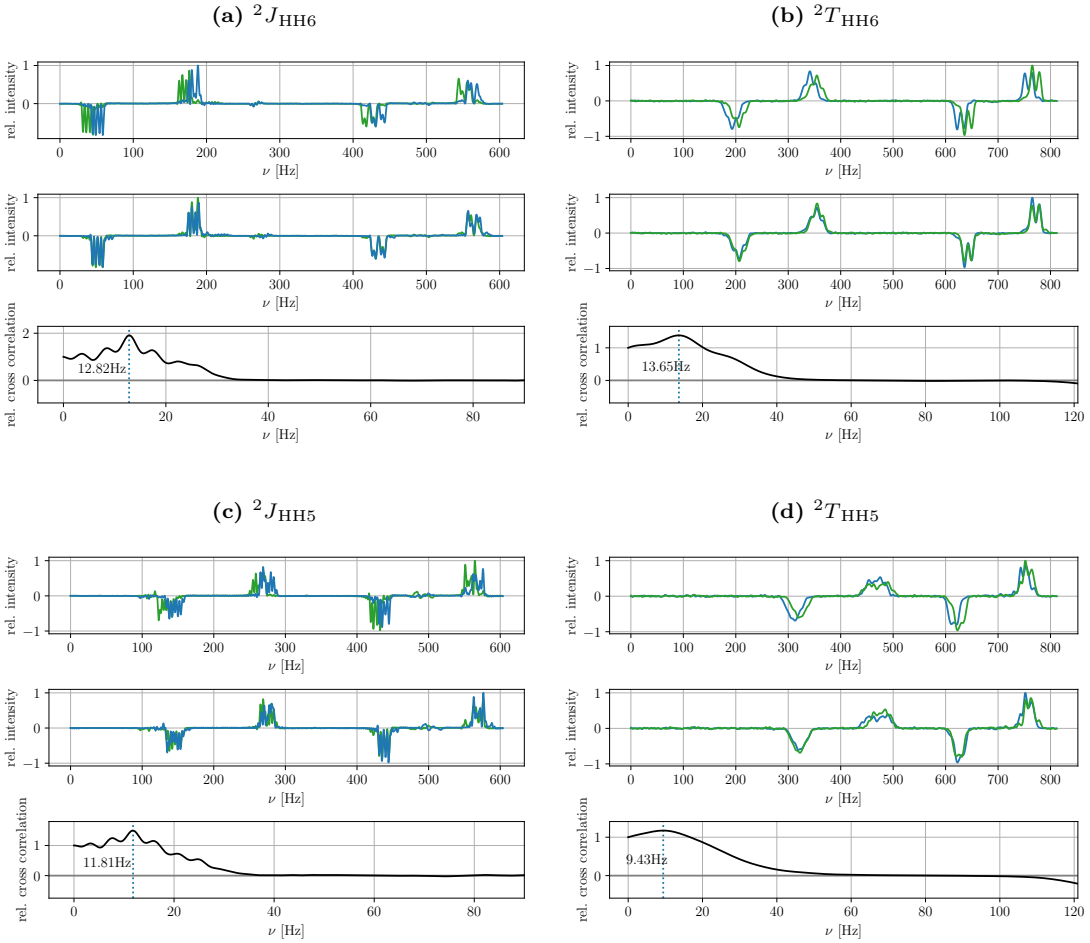

Figure 7.16: Semi-automatic extraction of the borneol methenyl homonuclear splittings from the respective slices in the P.E. HSQC in Figure 7.15. The isotropic values ($^2J_{\mathrm{HH}}$), measured in chloroform-d are on the left, on the right are the anisotropic rows containing the total couplings ($^2T_{\mathrm{HH}}$). In the middle of each figure, the superposed slices from above, shifted onto each other by the calculated coupling are shown. Note that the program cannot differentiate between positive and negative sign, which changes in the aligned case for both the *endo* and *exo* methylene protons of C6 and C5. Here, the upper rows (green) are to the right from the lower row (blue), indicating a positive sign.

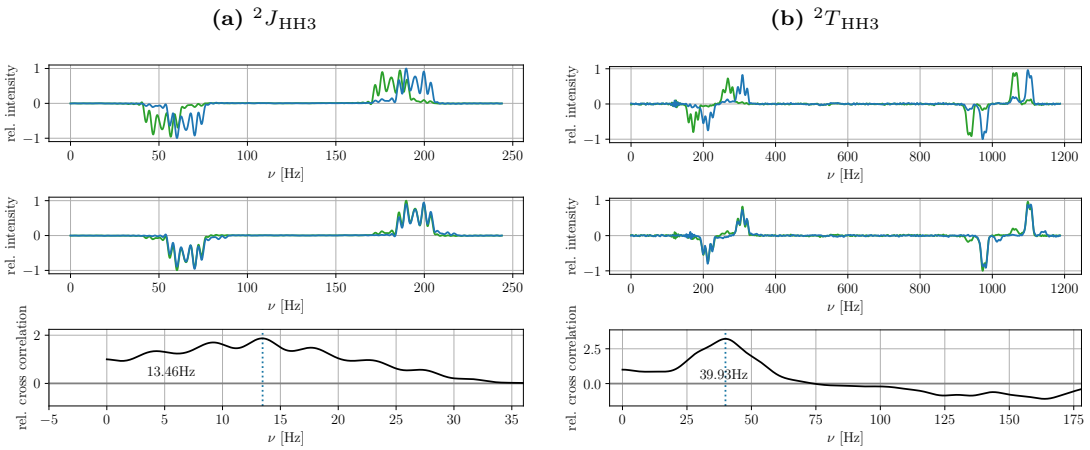

Figure 7.17: Semi-automatic extraction of the borneol methenyl homonuclear splittings from the respective slices in the P.E. HSQC in Figure 7.15. Here, the upper row (green) is to the right from the lower row (blue), indicating a positive sign. The partial orientation increases the geminal coupling significantly maintaining the order of rows, indicating a negative sign.

	Manual				Semi-automatic		
	$^2J_{HH}$[a]	$^2T_{HH}$[a]	$^2D_{HH}$[a]	ΔD^{ab}	$^1J_{HH}$[a]	$^2T_{HH}$[a]	$^2D_{HH}$[a]
H6	-12.9	13.6	26.4	1.1	-12.8	13.7	26.5
H5	-11.7	11.2	22.8	0.7	-11.8	9.4	21.2
H3	-13.4	-39.9	-26.5	0.2	-13.5	-39.9	-26.5

Table 7.4: Comparison of the results shown above with manually extracted geminal couplings.

Evaluation of the obtained RDC with SVD

Since borneol is a rigid molecule, a single tensor fit was aplied to a model that was optimized with the MMFF96 force field incorporated in the free software Avogadro. Then the 1-bond heteronuclear $^1D_{CH}$ and the homonuclear $^2D_{HH}$ RDCs were read into the program and a singular value decomposition (SVD) was carried out. The results are shown below.

[a] All values in Hz.
[b] Errors were estimated manually.

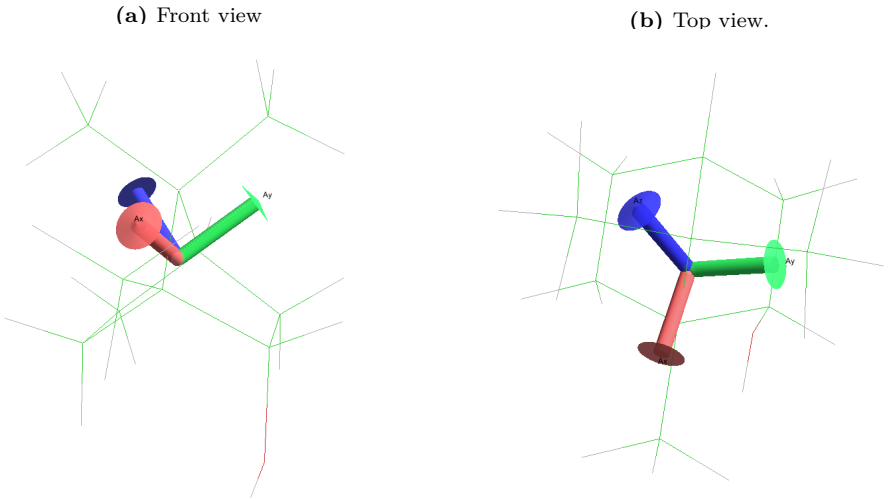

(a) Front view **(b)** Top view.

Figure 7.18: Illustration of the x, y and z components of the alignment tensor induced with the measurements at $\Delta\nu_Q$ of 274 Hz. Calculated experimental SVD derived values are shown in the table below.

Table 7.5: Singular value decomposition and back-calculation of the values with the program MSpin

	D_{exp}	D_{SVD}
C10-Me10	0.4	1.99
C8-Me8	9.5	8.56
C9-Me9	-7.7	-7.96
C6-H6x	-0.65	0.81
C6-H6n	16.6	15.79
C5-H5n	0.1	-2.83
C5-H5x	27.2	32.48
C3-H3n	-5.1	-7.98
C3-H3x	-26.5	-30.84
C4-H4	10.2	10.48
C2-H2x	-18.1	-16.15
H6n-H6x	26.4	26.89
H5n-H5x	22.8	25.95
H3n-H3x	-26.5	-23.53

The back-calculated values are in good accordance with the experimental values giving a Cornilescu's quality factor (Q) of 0.1.

7.5 Extraction of RDCs in DMSO

7.5.1 Ethinylestradiol

Another routinely used NMR solvent is DMSO-d_6. As a test analyte, the steroid 17α-ethinylestradiol, a derivative of the female hormon estrogen and part of some contraception pills, was prepared for testing in a compressing device. During a series of tests, no quadrupolar splittings were observed, when 17α-ethinylestradiol was dissolved in DMSO-d_6 and tested with the compressing apparatus. Nevertheless, comparing the isotropic with the anisotropic HSQCs revealed the presence of RDCs.

For the preparation, a 100mM solution of 17α-ethinylestradiol was dissolved in DMSO, and the isotropic data was extracted. Furthermore HSQC, HMBC, and NOESY spectra were recorded for assignment. Then a dry 30% PEO-DA35000 stick (cross-linked in a 3 mm diameter) was placed in a compressing device and the 500µl of the analyte solution were added. The stick had an equilibrated swollen length of 2.8 cm and was then compressed to 2.35 cm. As mentioned before, the quadrupolar splitting of DMSO was within the line width resulting in a broadened FWHM of the deuterium signal of 1 Hz.

In Figure 7.19 the corresponding 1D-^{1}H spectrum is shown for the aligned 17α-ethinylestradiol in DMSO-d_6. Sharp signals are obtained and even the satelites can be identified. Interestingly, the signal of the ethylene groups could be exposed for 3D shimming, resulting in narrow line-widths within 8 minutes. The corresponding CLIP-HSQC spectra are superposed in Figure 7.20 and Figure 7.21 sums up the assigned and extracted one-bond RDCs with PEO-DA35000 in DMSO-d and a compressing device.

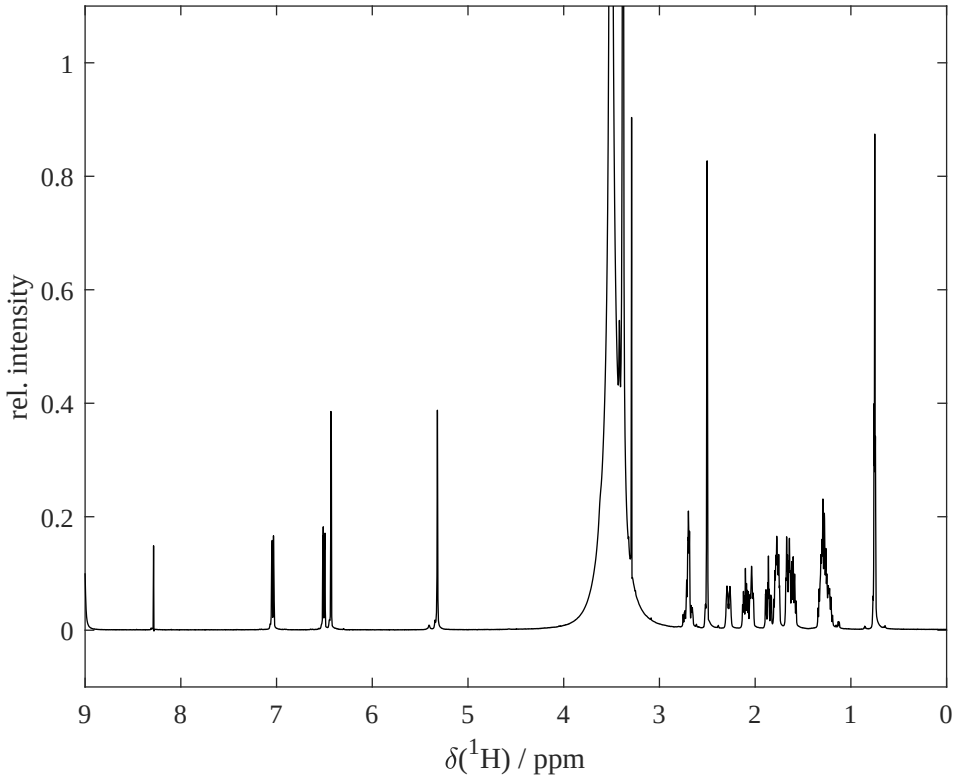

Figure 7.19: 1D-^{1}H-spectrum of ethinylestradiol in DMSO-d/PEO-DA35000-25%.

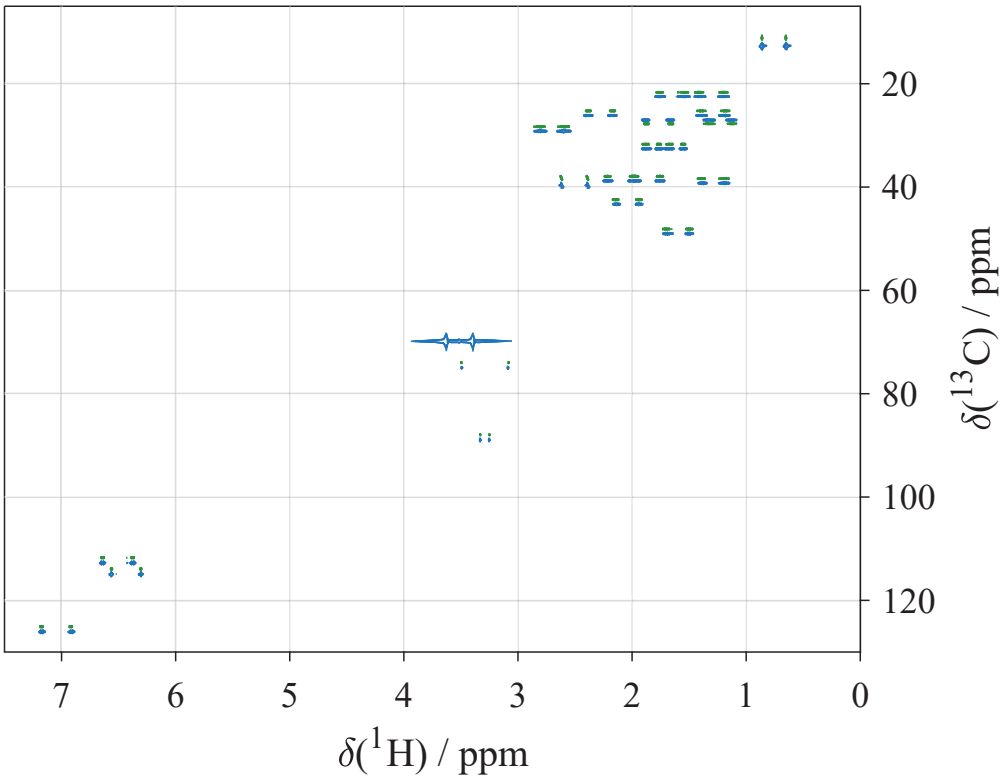

Figure 7.20: Overlay of anisotropic (blue) and isotropic (green) CLIP-HSQC spectra of ethinylestradiol in DMSO-d_6/PEO-DA35000-25%.

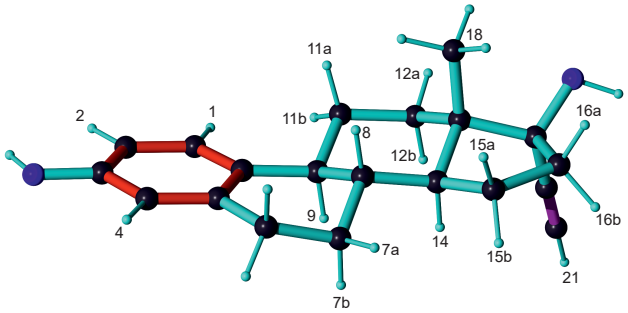

Coupling	$^1D_{CH}^{exp}$ [Hz]	$\Delta\,^1D_{CH}$ [Hz]
C1 H1	-1.6	0.1
C2 H2	-1.4	0.1
C4 H4	-1.7	0.1
C7 H7a	-0.9	0.3
C7 H7b	8.2	1.5
C8 H8	5.4	0.5
C9 H9	5.3	0.2
C11 H11a	5.4	0.3
C11 H11b	0.4	0.4
C12 H12a	0	0.2
C12 H12b	5.6	0.3
C14 H14	5.3	0.3
C15 H15a	3.8	0.3
C15 H15b	3.3	1.1
C16 H16a	4	0.4
C16 H16b	0.2	1.1
C18 H18	-1.8	0.1

Figure 7.21: Assignment and extracted couplings of ethinylestradiol.

7.6 Extraction of RDCs in methanol/water

7.6.1 Gramicidin-DPro-SW

Gramicidin D^{Pro}SW is a photo-switchable peptidomimetic[185] derived from the antibiotic Gramicidin S by inserting a thioarylethene group (Figure 7.22). 15.6 mg were dissolved in a 1:1 mixture of deuterated methanol and water and the isotropic measurements were carried out. Stretching the sticks resulted in a quadrupolar splitting for the deuterated hydroxy group of methanol-d_4 of 4.6 Hz and for the methyl group of 2.2 Hz in the 1D-^{2}H-spectra. The doublets of the alpha-C-region are shown in the overlay of the CLIP-HSQCs Figure 7.23. Note that for a better comparability, the doublets of the anisotropic spectra were shifted towards the underlying isotropic peaks.

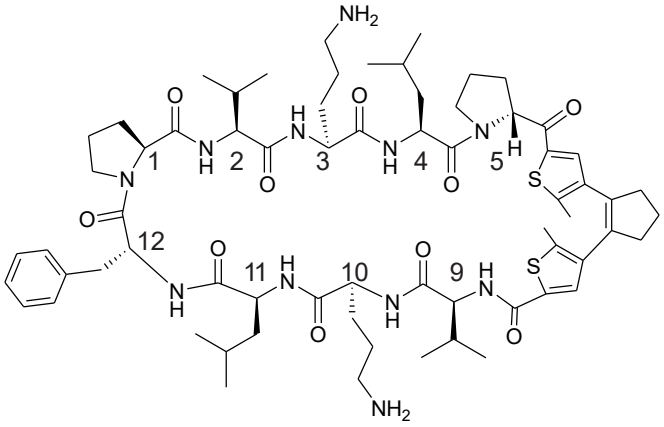

Figure 7.22: Configuration and numbering of Gramicidin D^{Pro}SW .

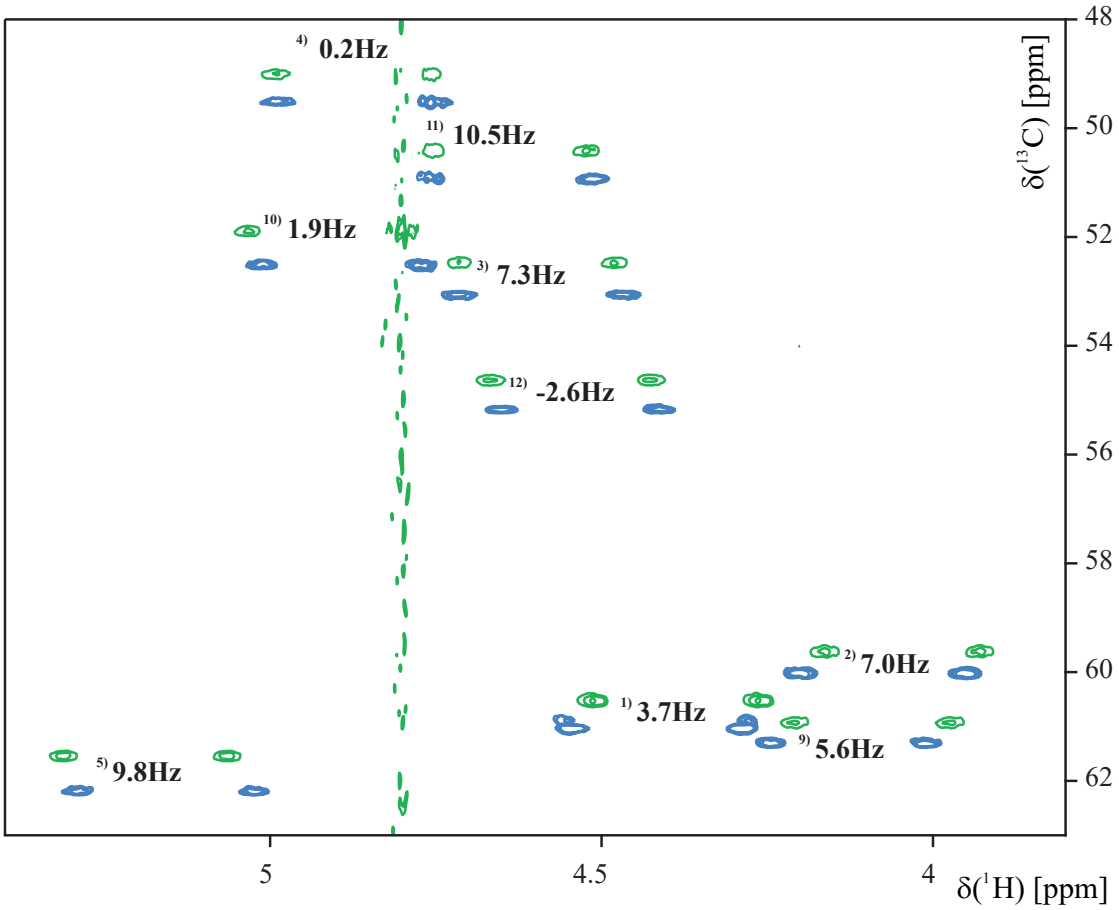

Figure 7.23: Overlay of the alpha-C-regions in the isotropic (green) and anisotropic (blue) CLIP-HSQC spectra of Gramicidin $D^{Pro}SW$. Numbering of the C-alphas according to Figure 7.22.

7.7 Extraction of RDCs in TFE/water

7.7.1 Amyloid precursor protein (APP)

The Amyloid precursor protein is known to form pathological β-amyloid plaques that are found in the brains of Alzheimers disease patients.[186] A selectively ^{15}N enriched sample thereof was prepared and couplings were extracted from isotropic and anisotropic $^{1}H^{15}N$-HSQC spectra with water suppression.

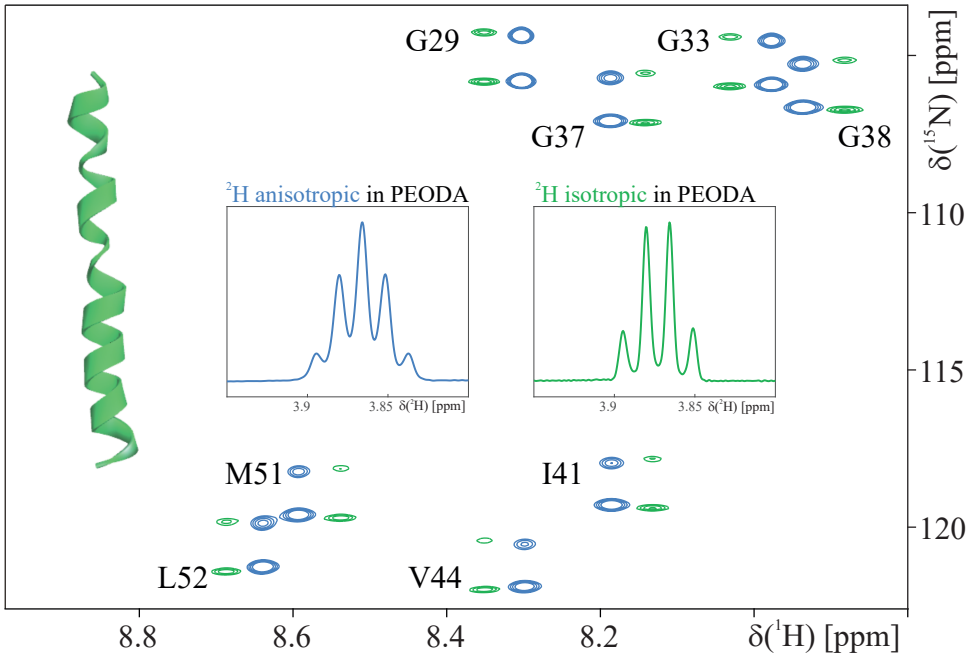

Residue	G29	G33	G37	G38	I41	V44	M51	L52
RDC [Hz]	14.1	10.1	14.1	13.1	11.1	7.1	12.1	12.1

Figure 7.24: Overlay of the isotropic (green) and anisotropic (blue) spectra of APP. Shown is the amide proton region with the eight ^{15}N labeled amino acids. The isotropic quartet of the deuterated TFE signal in the deuterium spectra appears as a quintet in the anisotropic case (blue) giving a quadrupolar splitting of about 1.7 Hz.

7.8 Results

In the above sections, the applicability of PEO-DA as an alignment medium was demonstrated and the suitability for the use in deuterated neutral and buffered water, chloroform-d, DMSO-d_6, a mixture of methanol-d_3 and water and a mixture of TFE and water was proven with sucrose, borneol, ethinylestradiol, Gramicidin $S^{D\text{-}Pro\text{-}SW}$, APP, and malectin. This is especially remarkable, since alignment media available are sensitive towards water and no alignment medium has been reported for TFE, which is often applied for membrane associated proteins. The extraordinary quality is reflected in the line width obtained in the deuterium spectra of the solvents. In the case of APP a quadrupolar splitting of 1.3 Hz could easily be resolved in the one-dimensional deuterium spectrum.

The spectra are affected of the medium only by the ethylene oxide units, but no further signals are visible. Their huge peak was exploited for automatic 3D shimming implemented on most modern spectrometers, allowing also less experi-

enced readers to achieve homogeneously shimmed field conditions. The big signal of PEO-DA was significantly reduced, when a WATERGATE sequence was applied. Suppressing the signal would hypothetically be possible for a perdeuterated PEO-DA material. Because of the price this approach was not followed, since it would also prevent the shimming possibilities. Yet, a source for ^{13}C depleted monomers was not found, which would also prevent signals of the polymer occurring in HSQC spectra while allowing to use of the proton signal for automatic shimming.

PEO-DA shows a remarkable swelling capability, the samples could be prepared within a week when swelling in a small diameter. The possibility to swell the gel outside and transfer it into a stretching device allowed the preparation within two days. The semi-automatic extraction program was tested and applied and were in good accordance with the established manual method. Furthermore, the program plots the slices, if desired, and documents the outcome. The auto- and cross-correlation can be used to approximate the validity of values. This is especially helpful, when strong coupling- or other artifacts are present. In contrast to the manual approach, the phase of the signal does not play a role, allowing a robust and reproducible data evaluation.

Together with the successfully developed preparation protocols presented in chapter 6 scientific personal is enabled, to prepare partially aligned samples and to measure anisotropic parameters without the need to know all kinds of materials that may be suitable and where to get these materials from. Therefore the above work resembles a cornerstone for the more routinely use of such parameters and opens their features to a wide scientific community. The five successfully developed formulations allow to set the desired alignment properties by the cross-linking concentration and the chosen mold diameter. This is especially true, since the approach was proven with molecules of very different sizes and polarities.

8 | Molecular dynamics with orientational constraints

In the next chapter molecular dynamics with orientational constraints are explained and applied with $^1D_{CH}$ RDCs as constraints. The results are compared with SVD based static method, implemented in MSpin. The software COSMOS (Computer Simulation of Molecular Structures) has implemented such molecular dynamics simulations (MD) with orienting boundary conditions. In this work, measured RDC data from anisotropic samples was used in the COSMOS software to obtain structural as well as dynamic information.

8.1 Molecular modelling

There are three different approaches to calculate molecular properties and to determine their structures: quantum mechanical methods, semi-empirical methods and empirical methods.

Quantum mechanical methods

In the quantum chemical description of molecules, the wave function of the molecule determines how the probability density of the electrons (orbitals) is arranged, within which the attractive atomic nuclei are centered. Depending on whether electrons are treated as individual particles or delocalized as a probability density, a distinction is made between *ab initio* methods (Hartree-Fock, post-Hartree Fock approaches) that only depend on fundamental physical constants and DFT methods, where the exchange-correlation energy as a functional of the electron density must be approximated.[187] None of them need to formulate explicit chemical bonds, as they are implicitly contained in the wave function and only fundamental physical constants and the initial connectivity need to be known. Furthermore, physical properties that are described quantum mechanically can be calculated and even chemical reactions and transition states can be described.

For structure determination, in the balance of attractive and repulsive energy components, a favorable arrangement of the electrons for resting nuclei (Born-Oppenheimer approximation) is determined. By optimizing the molecular structure, an equilibrium structure is sought in which the forces between the atoms are minimized. The difficulty is that the exact application of quantum mechanics leads to equations much too complicated to be solvable[188] and the computational effort in quantum chemical *ab initio*, and post-Hartree-Fock methods can become very large. These methods are therefore suitable only for simple molecules and DFT methods allow usually the calculation of systems with up to few hundred atoms.

Semi-empirical methods

Semi-empirical calculation methods are characterized by time-saving approximations, incorporating empirical parameters that would otherwise have to be calculated from the wave function of the system (for example, potentials and energy matrix elements). These parameters can be derived from experimental data as well as from other theoretical (*ab initio*) calculations. Such methods are much less computationally intensive than *ab initio* methods. The quality of a semi-empirical method depends therefore on the accuracy and validity of the empirical parameters and is in general limited to a certain class of molecules or bonding conditions. Depending on the method and the property to be calculated, it is possible to calculate systems of up to several thousand atoms.

Empirical methods

Empirical methods of molecular computation are not based on the quantum chemical wave function, but are based on purely classical mechanics. The structure of molecules is interpreted in simplified terms as mass points connected with springs. As a result, empirical methods are significantly less computationally intensive (the quantum mechanical calculation may require something like 10^4 times as much computation time as the equivalent molecular mechanics calculation for the same accuracy[189]), which means that ever larger systems such as protein complexes or cell membrane sections can be calculated. The energy is obtained as a sum of different system surface potentials that depend only on the atom position (distance, bond angle, dihedral angle, and non-bonding interaction potentials) and force field parameterization. The ground state again is where all the potentials are minimized representing the most probable conformation. Since the classic mechanical description neglects quantum effects, physical properties that are described quantum mechanically cannot be calculated and since the bonds are explicitly formulated between the mass points, no reactions can be simulated. Nevertheless,

force field calculations allow the prediction of geometries and relative energies and thus insights into the conformational space.

Limitations of molecular modeling

All of the above modeling methods have in common that the models are either simulated as single entities in vacuum without any borders, or assumptions are done, adding solvent molecules *e.g.* explicitly or as an averaged solvent field. In reality, many molecules are prone to collisions with each other, solvent molecules and walls all the time and at ambient temperatures higher energy conformations are adopted, differing from the ground state. When obtaining structures from the minimal energies, as described above, the found conformation *can* represent the global minimum (the ground state) but also a local minimum (representing a side conformation). For a better description of the conformational space, therefore, molecular dynamics simulations can be applied, where the trajectory of a molecule is determined and analyzed.

COSMOS software

The COSMOS program combines quantum mechanical methods for the calculation of molecular properties in combination with a parameterized, molecular-mechanical force field. This semi-empirical approach makes it possible to use NMR spectroscopic properties as boundary conditions in molecular dynamics calculations to obtain more realistic results. In addition, semi-empirical bond polarization theory (BPT)[190] can be used to calculate fluctuating single-atom charges that are more accurate than electronegativity scales for the calculation of chemical shift tensors[191] in each step of molecular dynamics simulations. Its main parameterization is for peptides and biomolecules with an extension for application with small organic molecules. In the works of Möllhoff[192] and Koch[193] the use of COSMOS force field is proven to be suitable. In this work, a method called molecular dynamics with orientational constraints (MDOC) has been applied utilizing one-bond carbon proton RDCs as constraints.[24]

8.2 Implementation of RDCs as constraints

In the following, the implementation of RDCs as orientational constraints for MD simulations is explained. At first the introduction of the pseudo energy and how it can be evaluated with the help of appropriate transformation matrices and an averaging procedure are outlined. Then it is explained, how this pseudo energy resembles a re-orienting potential, whose derivative pseudo forces alter the conventional force field.

Underlying principle

For the introduction of RDCs as constraints, a pseudo energy term E^{pseudo} is added to the potentials of bonding and non-bonding interactions (E^{bond}, $E^{non-bond}$) of the molecular-mechanical force field.

$$E^{total} = E^{bond} + E^{non-bond} + E^{pseudo} \tag{8.1}$$

The re-orientation energy potential $E_{i,j}^{pseudo}(t)$ at a single given time step arises from the deviation of a theoretical dipolar current coupling for a given pair of interacting nuclei I_i and I_j ($\mathrm{D}_{i,j}^{theo}$) from an experimental value ($\mathrm{D}_{i,j}^{exp}$) that was evaluated experimentally under anisotropic conditions (Equation 8.12). The experimentally derived dipolar couplings are always an average of the different vibrational states, conformations, and orientations being populated during the course of the measurement. For one bond dipolar couplings, a constant average of the bond length can be considered, since corresponding vibrational changes are very small and occur on the order of femtoseconds. The tensor of the dipolar coupling in the PAS is of the form

$$\boldsymbol{D^{PAS}(i,j)} = \begin{pmatrix} -b_{ij}/2 & 0 & 0 \\ 0 & -b_{ij}/2 & 0 \\ 0 & 0 & b \end{pmatrix} \tag{8.2}$$

with the constant of proportionality b_{ij} from Equation 4.30.

Transfomation from the PAS to the laboratory frame

The tensorial components in its principal axis system (PAS) representation are then transformed into the laboratory frame by a rotation matrix $\boldsymbol{T}(i,j)$. This transformation is expressed by a double sum over the components of the transformation matrix $T_{\alpha\beta}$.

$$D_{\alpha\beta}^{L}(i,j) = \sum_{\alpha'} \sum_{\beta'} T_{\alpha\alpha'} T_{\beta\beta'} D_{\alpha'\beta'}^{PAS}(i,j) \tag{8.3}$$

with the Cartesian components $\alpha, \beta \in \{x, y, z\}$ in the laboratory frame (indicated by the index L) and $\alpha', \beta' \in \{x', y', z'\}$ in the principle axis system, respectively. The calculated dipolar coupling $D_{\alpha\beta}^{L}$ after a given time within the simulation, containing more than one step, must therefore represent a vibrational, conformational and rotational tumbling average over the course of the MD.

The scaling factor s_{AM}

Furthermore, a scaling factor s_{AM} is introduced, since the experimentally derived RDCs ($\equiv D_{\alpha\beta}^{exp}(i,j)$) are commonly on the order of 10^{-3} compared to dipolar

couplings. Subsequently, an averaged calculated dipolar coupling in the laboratory frame is obtained by the following expression.

$$\left\langle D^{L}_{\alpha\beta}(i,j)\right\rangle = s_{AM}\left\langle \sum_{\alpha'}\sum_{\beta'} T_{\alpha\alpha'}T_{\beta\beta'}D^{PAS}_{\alpha'\beta'}(i,j)\right\rangle_{t\to\infty} \tag{8.4}$$

The scaling factor s_{AM} is related (but not identical) to the order parameter of the applied alignment conditions and needs to be estimated empirically via scaling MD runs. As a good starting point, the biggest RDC is assumed be aligned with the magnetic field $\vec{B_0}$. Then s_{AM} can be estimated via

$$s_{AM} \geqq \frac{max(D^{exp}_{\alpha\beta}(i,j))}{max(D^{ss}(i,j))} \tag{8.5}$$

by dividing the the biggest measured RDC through the dipolar coupling value when aligned with the field in solid-state $D^{ss}(i,j)$. For example, if the largest measured one-bond sp^3 CH RDC has a value of 43 Hz, setting s_{AM} to 10^{-3} would scale down the dipolar coupling of 43 kHz to a maximum achievable value of 43 Hz. When the molecule in the course of the MD takes up also different orientations, it is possible that in average this value cannot be reached anymore because of s_{AM} limiting the range of occurring values. If s_{AM} is chosen too big, the re-orienting pseudo forces (*vide infra*) cannot act efficiently as constraints, since the energy criterion in Equation 8.12 is weakened, leading to incomplete sampling of the conformational space.

Exponential decaying memory time function

The application of a pure arithmetic running average would overreach the initial state and conserve initial values over time, preventing any conformational changes that might occur. This is especially problematic when a chosen starting conformation is not the correct one or more than one conformations need to be adopted during the MD to obtain a conformational ensemble that reflects the experimental data. Therefore, a so-called memory time function, invented by Torda and van Gunsteren,[194,195] is introduced to *forget* former events after a so-called memory time has passed (Equation 8.6). This running memory time function weights values the less, the more time has passed since they occurred by introducing an exponential decay term to the pure arithmetic average. Values that occurred more than five times of τ ago contribute then with less than 1% to the actual running mean value.

$$\left\langle \boldsymbol{D^L}(i,j)\right\rangle_t = \frac{1}{N(t)} \int_{t'=t_0}^{t} \exp^{\frac{t'-t}{\tau}} \boldsymbol{D^L}(i,j;t')dt' \tag{8.6}$$

$$N(t) = \int_{t'=t_0}^{t} \exp^{\frac{t'-t}{\tau}} dt' \tag{8.7}$$

Here, N(t) is a time-dependent norming term. The running mean values with an exponentially decaying memory introduce effectively a new time-scale for rotational re-orientations and fluctuations with τ representing the lifetime of an orientation of the molecule or of a mobile segment.

The equations of motion in MD simulations are solved for finite time steps. Therefore, the integral in Equation 8.6 can be implemented as a discrete sum. Instead of summing up all values that occurred during the MD, memory and computing time are efficiently saved by evaluating the running mean value in a recursive manner only once after every time step (Equation 8.8).

$$\left\langle \boldsymbol{D^L}(i,j)\right\rangle_t = \frac{1}{N_{m+1}} \left\{ N_m \left\langle \boldsymbol{D^L}(i,j)\right\rangle_{m\Delta t} e^{\frac{-\Delta t}{\tau}} + \boldsymbol{D^L}(i,j;t) \right\} \tag{8.8}$$

$$\text{with } t = (m+1)\Delta t \tag{8.9}$$

Here, m denotes the number of passed steps. For the starting conditions, the norming term N_0 is initially set to one and for the successional steps evaluated by

$$N_{m+1} = N_m e^{\frac{-\Delta t}{\tau}} + 1 \ . \tag{8.10}$$

Since there are no former values to average, the initial running mean of the dipolar tensor $\left\langle \boldsymbol{D^L}(i,j)\right\rangle$ is substituted by the first current dipolar tensor evaluated from the respective pair of coupling nuclei I_i and I_j.

$$\left\langle \boldsymbol{D^L}(i,j)\right\rangle_0 = \boldsymbol{D^L}(i,j;t=t_0=0) \tag{8.11}$$

Calculation of the pseudo energy

The difference of this calculated dipolar coupling from the experimentally derived RDC can be translated into a re-orienting potential energy of a given spin pair.

$$E_{i,j}^{pseudo}(t) = \frac{k}{2} \sum_{\alpha} \sum_{\beta} \left(\left\langle D_{\alpha\beta}^{L}(i,j)\right\rangle_t - D_{\alpha\beta}^{exp}(i,j) \right)^2 \tag{8.12}$$

The force constant k is also chosen via preliminary scaling MD runs to adjust size and units of this pseudo-energy term. The experimental RDC constraints $\boldsymbol{D^{exp}}$ are introduced into the COSMOS via

$$\boldsymbol{D^{exp}(i,j)} = \begin{pmatrix} -D^{exp}(i,j)/2 & 0 & 0 \\ 0 & -D^{exp}(i,j)/2 & 0 \\ 0 & 0 & D^{exp}(i,j) \end{pmatrix} \tag{8.13}$$

which conforms the vanishing trace of the dipolar interaction, leaving the xx- and yy-components minus half the size of the zz-component (see also Equation 4.31 in subsection 4.2.4).

Deriving the pseudo force

From classical mechanics it is known that the force F on an object is the negative of the derivative of the potential function E.

$$F_\gamma = -\frac{dE_{pot}}{d\gamma} \tag{8.14}$$

whereby γ is a coordinate in space ($\gamma \in x, y, z$). Therefore, the re-orienting pseudo forces F_γ are obtained as derivatives from the respective pseudo energy contributions with respect to the Cartesian coordinates of the atoms. For the orientational pseudo force the transformation matrices $\boldsymbol{T}(i,j)$ with respect to the atom coordinates (see also Sternberg *et al.*[63]) need to be derived from the unit vectors that define the directions of the dipolar coupling spins. Here, the unit vector $\boldsymbol{e}_{z'} = \boldsymbol{e}_{(i,j)}$ and hence, is the internuclear vector, while $\boldsymbol{e}_{x'}$ and $\boldsymbol{e}_{y'}$ are perpendicular to it. At any given time t the transformation matrix $\boldsymbol{T}(i,j;t)$ is then constructed with the unit vectors as columns

$$\boldsymbol{T} = \begin{pmatrix} \boldsymbol{e}_{x'} \\ \boldsymbol{e}_{y'} \\ \boldsymbol{e}_{z'} \end{pmatrix} \tag{8.15}$$

The pseudo forces in the Cartesian directions $\gamma \in x, y, z$ are then given by

$$F_\gamma = k \sum_{\alpha\beta} f_{\alpha\beta}\Big(\Delta D_{\alpha\beta}\,(i,j)\,\Big)\frac{\partial}{\partial\gamma} D^L_{\alpha\beta}(i,j;t) \tag{8.16}$$

$$\frac{\partial}{\partial\gamma} D^L_{\alpha\beta}(i,j;t) = \sum_{\alpha'}\sum_{\beta'}\left(T_{\beta\beta'}\frac{\partial}{\partial\gamma}T_{\alpha\alpha'}(i,j;t) + T_{\alpha\alpha'}\frac{\partial}{\partial\gamma}T_{\beta\beta'}(i,j;t)\right) D^{PAS}_{\alpha'\beta'}(i,j;t) \tag{8.17}$$

This way the calculation of the pseudo force is simplified to determining the elements of the transformation matrices $\boldsymbol{T}(i,j;t)$ with respect to the Cartesian coordinates of the atoms at the time t. Its direction is set by the current orientation of the internuclear vector of the coupling spins I_i and I_j, while the magnitude depends on the deviation of the exponentially decaying time weighted running mean $\left\langle D^L_{\alpha\beta}(i,j)\right\rangle_t$ and the corresponding experimental dipolar coupling tensor components $D^{exp}_{\alpha\beta}(i,j)$ expressed here as the function $f_{\alpha\beta}\Big(\Delta D_{\alpha\beta}(i,j)\Big)$.

Adapted pseudo force potential

The standard harmonic potential in Equation 8.12 is useful, particularly near the pseudo energy minimum, but leads to extensively rising and fluctuating forces, when the exponentially decaying time weighted running mean $\left\langle D^L_{\alpha\beta}(i,j)\right\rangle_t$ and the corresponding experimental dipolar coupling tensor components $D^{exp}_{\alpha\beta}(i,j)$ vary largely, for example in the beginning of an MD. To avoid these strong pseudo forces that would render unrealistic motions and conformers or even break bonds or alter the chiral configuration, the expression of the harmonic potential is multiplied with a hyperbolic tangent weighting function, leading to

$$f^w_{\alpha\beta}\Big(\Delta D_{\alpha\beta}(i,j;t)\Big) = \tanh\left(\frac{\left\langle D^L_{\alpha\beta}(i,j)\right\rangle_t - D^{exp}_{\alpha\beta}(i,j)}{\Delta D(i,j)}\right) \quad . \tag{8.18}$$

The width of this potential $\Delta D(i,j)$ is ideally chosen to be proportional to the experimental error ($\Delta D(i,j) \approx \Delta D^{exp}(i,j)$). As long as the condition $\left\langle D^L_{\alpha\beta}(i,j)\right\rangle_t - D^{exp}_{\alpha\beta}(i,j) < \Delta D(i,j)$ is fulfilled, the function behaves similarly to the derivative of the harmonic potential Equation 8.12 divided by the experimental error according to Equation 8.18. For the case that $\left\langle D^L_{\alpha\beta}(i,j)\right\rangle_t - D^{exp}_{\alpha\beta}(i,j)$ exceeds the experimental error $\Delta D^{exp}(i,j)$, it now gives rise to nearly constant forces.

In comparison to the other bonding and non-bonding forces within the force field, the orientational pseudo-forces need to be tuned in continuously to prevent strong and unrealistic oscillating motions in the beginning that could overcome configurational barriers and inadvertently alter the molecular model. This is achieved by an additional inverse damping function term with another time constant ρ.

$$f_{\alpha\beta}\Big(\Delta D_{\alpha\beta}(i,j;t)\Big) = (1 - e^{-t/\rho}) f^w_{\alpha\beta}\Big(\Delta D_{\alpha\beta}(i,j;t)\Big) \tag{8.19}$$

The time constant ρ is like the memory time constant τ on the order of 200 ps resulting in the pseudo forces reaching 99% of their maximum strength after the first nanosecond.

8.3 Processing and interpretation of data

The COSMOS program offers different outputs for the evaluation of an MD run. As there are normally more than ten million steps with a stepsize of 0.5 to 2 fs simulated to have an overall MD time of at least 5 to 20 nanoseconds, it is convenient to take a data snapshot after equidistant intervals, *e. g.* every 10000 steps. In the options (cos) file, type, interval and the respective group of atoms can be selected. This way data snapshots of the occurred structures (coo files) and a text file (txt) containing the constraining experimental residual dipolar couplings ($D^{exp}(i,j)$) followed by the time course of the calculated residual dipolar coupling tensors ($\left(\left\langle D^{L}_{\alpha\beta}(i,j;t)\right\rangle_{t}\right)$) arising from the trajectory, are created. The coordinate snapshots can then be overlayed and analyzed further, for example with multivariate statistical techniques such as principal component analysis (PCA) to identify conformers.[196,197] The dipolar tensorial snapshot file is in a format that can be evaluated by Mathematica, Matlab or a python script developed in this work.

Evaluation of the back-calculated dipolar coupling

The back-calculated dipolar coupling of the created (conformational and rotational) ensemble of snapshots is obtained by arithmetically averaging n values after the first nanosecond.

$$D^{cal}(i,j) = \frac{\sum(\left\langle D^{L}_{\alpha\beta}(i,j;t>1ns)\right\rangle_{t})}{n} \tag{8.20}$$

The reason is that the MD is then considered to be *equilibrated*, meaning that the influence of wrong starting conformations is *forgotten* and non-physical modes of motion induced by an initial distribution of random momenta are canceled out via dissipation within the force field. An example for the trajectories of the time course of the back-calculated values of a constrained spin couple during an MDOC is given on page 121. The first nanosecond clearly contains strong fluctuating values. Nevertheless, their cumulative average (bright blue) converges, as the time points after the first ns adopt a smaller range.

Quality factors for the evaluation of the fits

To assess the quality and validity of the MD runs, the agreement of the experimental and the back-calculated RDCs for one given coupled spin pair is expressed through the inverse of the so-called $\mathcal{X}^2$ value.

$$\frac{1}{\mathcal{X}^2(i,j)} = \frac{\left(\Delta D^{exp}(i,j)\right)^2}{(D^{exp}(i,j) - D^{cal}(i,j))^2} \tag{8.21}$$

To sum up the overall quality of all back-calculated constraints a normed sum of the inverse $\mathcal{X}_i^2$ values, the so called total $^n/\chi^2$ is evaluated with the following equation.

$$\frac{n}{\mathcal{X}^2} = \frac{n}{\sum\limits_{(i,j)} \mathcal{X}^2(i,j)} \tag{8.22}$$

In this work, the lowest accomplished $^1/\chi^2$ value (Equation 8.21) from all constrains implemented on the molecular models was regarded to just reach a value above one for the validity of a simulation. Therefore, in a set-up for discrimination, all but one competing models ideally have at least one outlier, not fulfilling the experimental data. In the examples shown in Figure 8.1, the overall quality criterion Equation 8.22 exceeds one for the correct (SRRR) and a competing model (SRSR). Nevertheless, the constrained spin couple achieving the poorest $^1/\chi^2$ (*H3p/C3p*) allows not only to assign the right configuration, but also the correct starting conformation (chair).

The difficulty is, to arrange a combination of scaling parameter s_{AM} and pseudo force constant k to achieve the former mentioned conditions. Since the number of constraints, their magnitudes and of course the topology of molecules all influence those two parameters, they have to be found empirically. The described workflow in the next section describes, how this is performed.

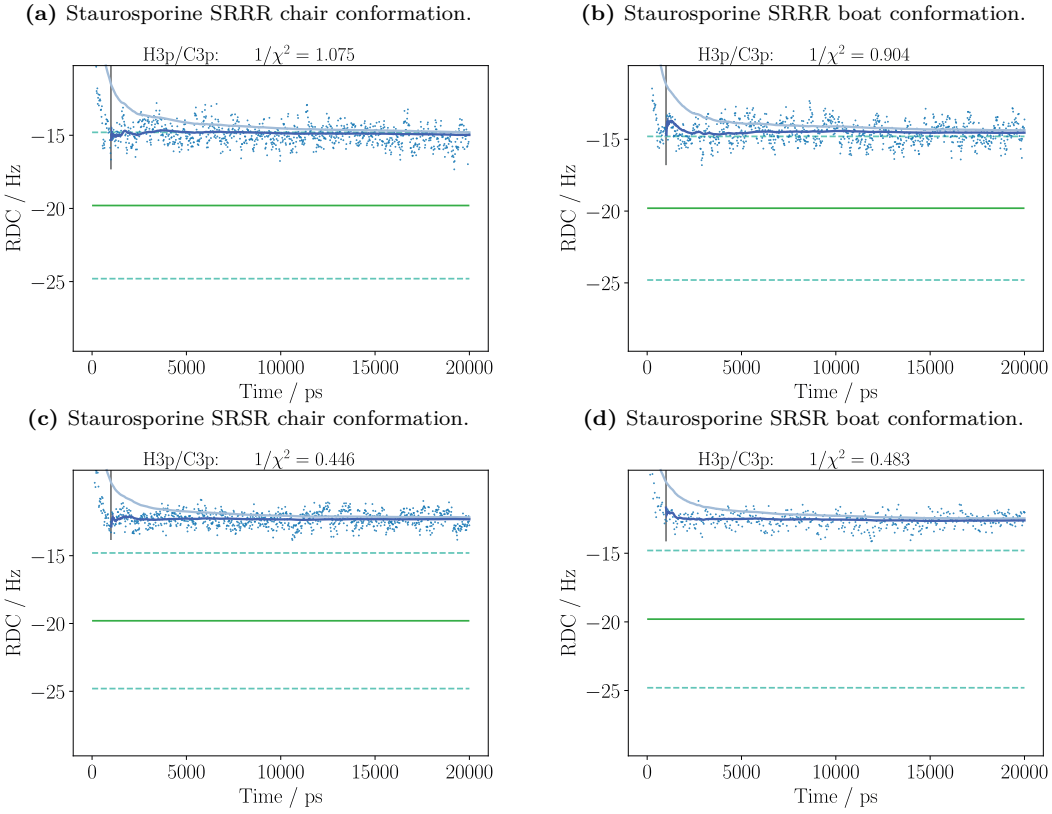

Figure 8.1: Resulting time course of the back-calculated dipolar couplings of H3p/C3p for 4 different structural starting models. The green line indicates the experimental value centered between the error limits (turquoise). The blue dots represent the value of the RDC at a respective time point. The cumulated averages are shown for the whole (bright blue) and the time excluding the first nanosecond (marineblue). The possible configurations of staurosporine are illustrated in Figure 8.10, the starting conformations (boat and chair) for the correct assigned staurosporine SRRR are presented in Figure 8.12.

8.4 Workflow for MDOC simulations

The implemented MDOC approach marks a fundamentally new way to use tensorial NMR parameters for the elucidation of structures. Therefore, extended tests had to be carried out to identify and remove bugs with known structures. Starting with COSMOS version 3, more than 350 molecular dynamics simulations were repeatedly carried out only with the molecules staurosporine, spiroindene and ethinylestradiol. This way defective code could be identified, leading to an evolved stable and reliable COSMOS version 6. The need to scale the MD runs with every new version required an effective workflow, which is presented in the following section. After a short introduction into the needed files, an invented iterating script is described, allowing the effective execution of the COSMOS back-end on an hpc cluster. For the processing of the tremendous amounts of data generated by MDOC runs, a python script for the back-calculation and evaluation by means of individual $^1/_{x^2}$ values was written for this work.

8.4.1 Classification of file types

The relevant files for MDOC runs with the COSMOS software can be differentiated into two classes: The executable binary files for the graphical user interface (GUI) based frontend (cosmos.exe) and the command line based backend (cosback) with their parameter files in the configuration directory, containing the code, force field parameters and also the so called .pol files that contain information about dipolar couplings of certain differently hybridized spin couples. The second class are input files, including the COSMOS coordinate file (.coo), a COSMOS data file (.cod) and a COSMOS options file (.cos) that contain the starting structure, experimental values and the settings of the simulation.

To set-up an MDOC simulation, the windows executable GUI of COSMOS offers a multitude of tools, to edit, sketch and build molecular structures or just to view and rotate them. Since its initial purpose aimed on the treatment of peptides and proteins, it has implemented a sophisticated masking functionality, to mark and group atoms for example by their names. Furthermore up to 24 groups can be defined arbitrarily, allowing to switch different constraints on or off, or to define overlaying sites for the created ensemble of conformers. The frontend is very helpful for the search of errors and the illustration of results and even provides a POV-Ray output, to create rendered pictures. Furthermore, the frontend allows analyzing and overlaying whole trajectories. Even though the whole MD can be performed locally on a desktop computer, the simulations carried out for this work were applied with the back-end on the high performance computing (bwHPC) BwUniCluster.

To start an MDOC on the bwHPC, a so-called *job* is submitted via the *msub* command, followed by information regarding the number of nodes, the needed memory and the so-called *wall time* that sets a maximum duration for the processed job. This information is needed by the job scheduling manager (MOAB) that controls how individual programs will run and best fit into the available resources of the cluster.[198] Subsequently, the backend of the COSMOS program is entered together with the information regarding

- the COSMOS options file (.cos) containing several hundred options that specify the overall settings for the MD, (*e. g.* temperature, cut-off radii, ...), but more importantly, the scaling parameter s_{AM} and the force constant k (the weight) for the re-orienting energy potential and information on the desired output (after the parameter *-c*).
- the COSMOS data file (.cod) containing the experimental data, grouping and fixed sites as well as remarks about the data (after the parameter *-a*)
- the location of the COSMOS configuration directory (after the parameter *-f*),
- the location of the COSMOS output directory for the data snapshots (after the parameter *-y*),
- the starting structure (the .coo file) that will be processed.

A typical command line for the start on the cluster then reads as

```
msub -l nodes=1:ppn=1,walltime=3:00:00,pmem=2000mb /home/kit/ibg/yi5156/COSMOS/bin
/cosback.x86_64-STATIC -dw -c /home/kit/ibg/yi5156/COSMOS/Staurosporine/exp_op002_
DD0007_err_10MSteps_2fs_ver3_16th_noFx.cos -a /home/kit/ibg/yi5156/COSMOS/Staurosp
orine/Staurosporine_.cod -f /home/kit/ibg/yi5156/COSMOS/config -y /work/kit/ibg/yi
5156/Staurosporine/Staurosporine_ver3_16th_exp_1_SRRR_boat /home/kit/ibg/yi5156/CO
SMOS/Staurosporine/Staurosporine_1_SRRR_boat.coo
```

which is a pretty inconvenient and error-prone way to run even a single MD. Fortunately, this command line can also be saved as a short executable bash script. This way, former runs are also documented, which helps for failure analysis or repeating and modifying the following MDs.

8.4.2 Executing MDOC

When carrying out MDOC for relative pro-chiral assignment, all possible relative stereo-configurations are modelled and processed with the same constraints. A molecule with n_s stereocenters can form 2^{n_s-1} pairs of enantiomers. For example for the reserpine derivatives in the work of Sager,[173] 6 unknown stereogenic centers lead to 32 possible relative configurations. Instead of creating 32 times a bash

script, to start the MDOC, a looping script was adapted[a] that iterates over a set of given models and creates individual job subscripts that are submitted to the cluster. Furthermore, the output folders are named and created automatically and the simulations are processed in parallel. In Figure 8.2 the operational steps for parallel MDOC of several stuctures, and/or setups are summed up.

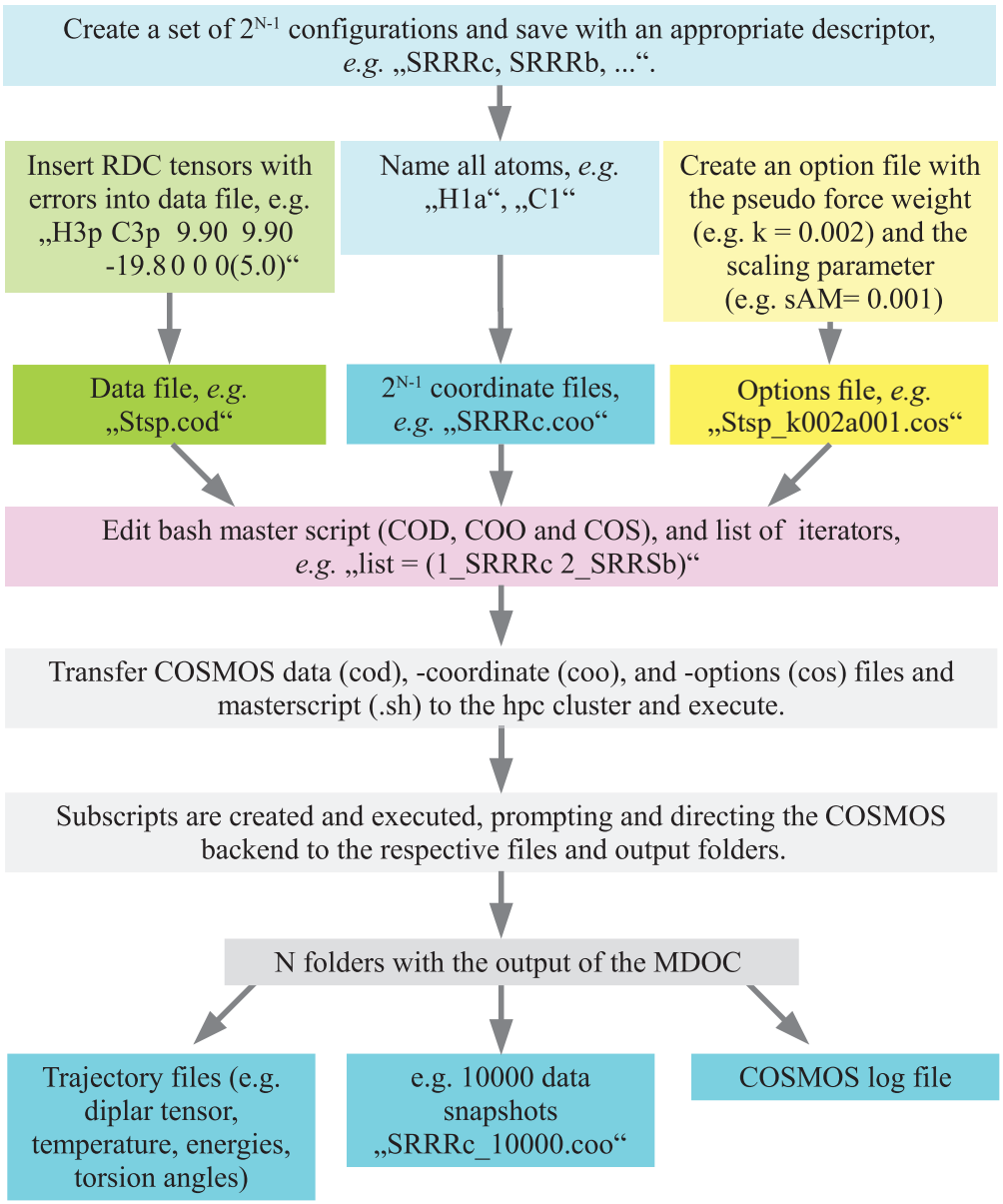

Figure 8.2: Operational steps for parallel MDOC and related input and output files.

[a]In cooperation with Robert Barthel from the Steinbuch Centre for Computing (SCC) at KIT

8.4.3 Evaluation of scaling factor and pseudo force weight

The iterating script also allows to start MDOCs with different *options* to find an optimal setting for the pseudo force constant k and the scaling factor s_{AM}. In this work, an optimal setup for an s_{AM} and k is accomplished, when the smallest individual $^1/\chi^2$ value of a constrain just exceeds one and the temperature converges. This way it is provided that the pseudo-forces act on, and by that, *heat* the molecular model as little as necessary. The quality criterion furthermore ensures that the back-calculated average of the constrain is approached (sufficient high s_{AM}), but not too easily (too high s_{AM}). An example on the influence of the scaling of the pseudo force k and the total $^n/\chi^2$ value is shown in Figure 8.3 for two possible configurations of a synthetic spiroindene derivative. Here, the MDOCs were applied with five different pseudo force constants (k) while keeping the order scaling factor constant ($s_{AM} = 2 \times 10^{-3}$)

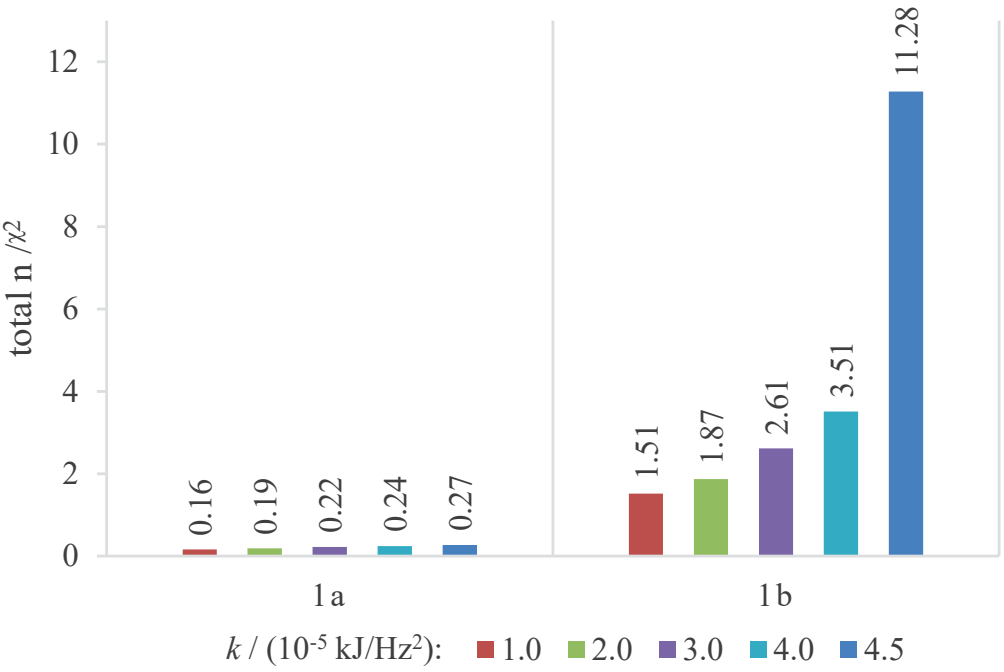

Figure 8.3: Different scaling of the pseudo force constant k and resulting total quality factors $^n/\chi^2$ of the RDC data for two possible spiroindene configurations.

Even though the first setup with $k = 1.0$ gives a clear discrimination by the total $^n/\chi^2$ criterion differing between one order of magnitude for the two structural proposals (red bars in Figure 8.3), the configuration that fulfills the experimental data the best (*1b*) still contains back-calculated constraints that were not fulfilled. How the value of the minimum individual quality factor $^1/\chi^2$ is influenced by increased pseudo force scaling is shown in Figure 8.4 for both configurations.

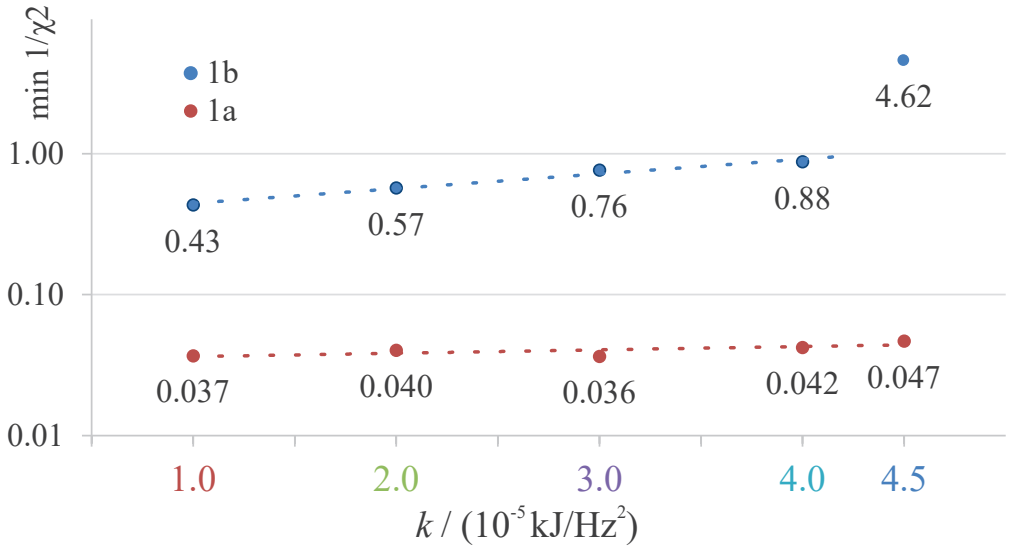

Figure 8.4: Different scaling of the pseudo force constant k and resulting lowest individual quality factors ${}^{1}/\chi^{2}{}_{min}(k)$ for two spiroindene configurations.

The first four attempts with increased pseudo force constant k ($1.0, 2.0, 3.0, 4.0 \times 10^{-5}\,\mathrm{kJ/Hz^2}$) resulted in increasing minimum ${}^{1}/\chi^{2}(k)$ values for both configurations, yet the correct one (1b) has a higher slope (note the exponential scale) and depart about one order of magnitude from the competing configuration. Since the value of ${}^{n}/\chi^{2}(k)$ was close to one, k was finally increased only to $4.0 \times 10^{-5}\,\mathrm{kJ/Hz^2}$, resulting in a MDOC where all experimental constrains could be reproduced.

8.5 Evaluation of MDOC with borneol

In section 7.4 the obtained RDCs could be correlated with the model using the *static* single tensor approach. The experimental values were in good accordance with the calculated ones. The established data will be exploited to test the MDOC and describe its features. Therefore different settings were tested and a scaling procedure was worked out. The size of d-(+)-borneol furthermore allowed to simulate 20 million steps within three to four hours on the bwHPC cluster. Finally a set up was found (s_{AM}= 0.002 and k= 0.003) that fulfills all orientational constraints (see Figure 8.5).

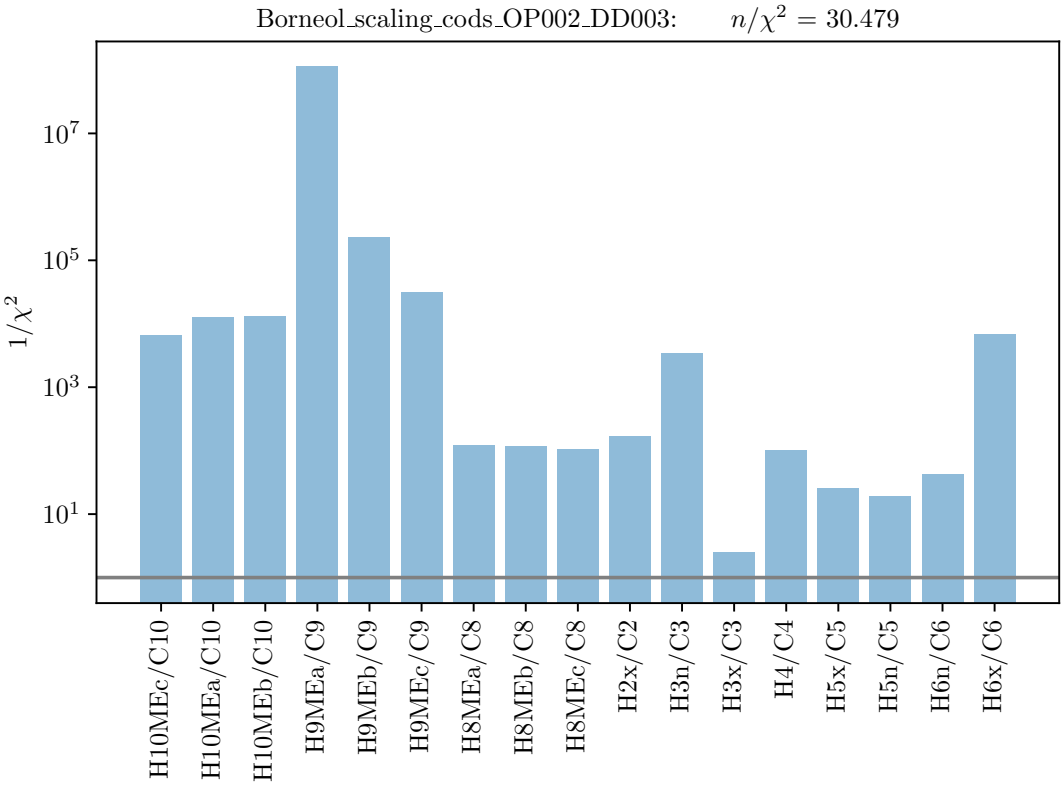

Figure 8.5: Setup for an MDOC run to fulfill all orientational constraints.

As a test, the exo protons H3x and H5x were switched for falsification and the simulations was repeated.

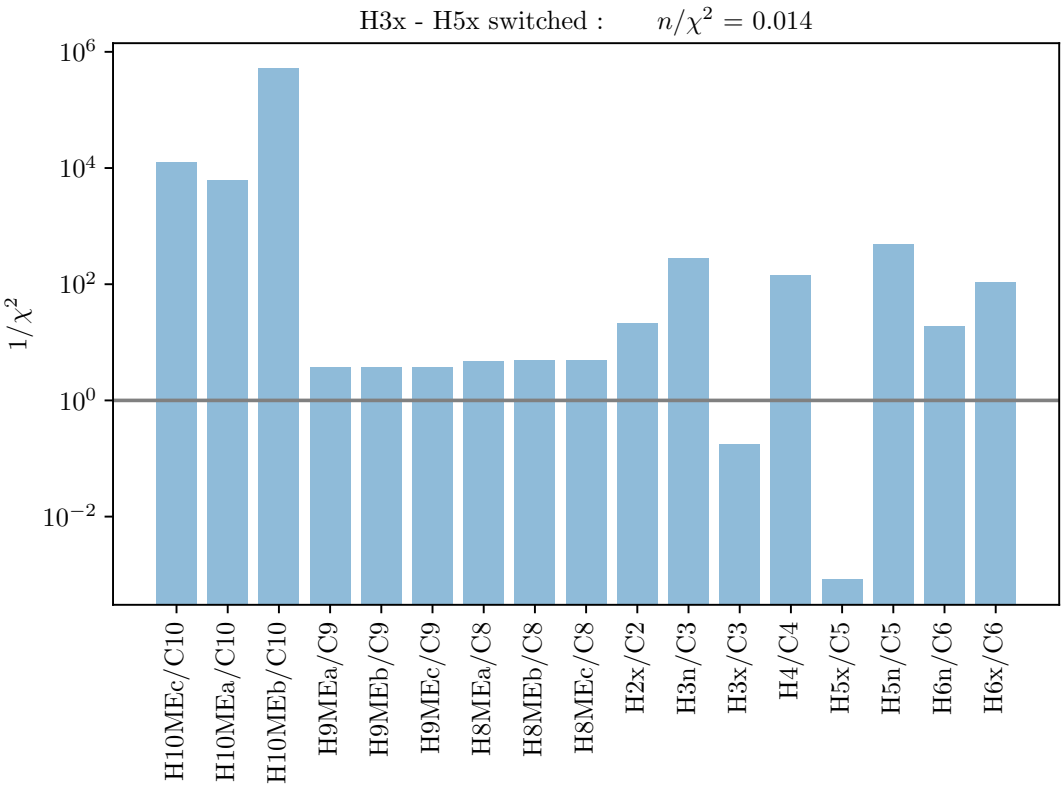

Figure 8.6: Exchanging the assignment of the constraints of the *exo* protons H3x and H5x. The wrong assignment worsens directly the total n/χ^2 value and the two individual wrong assigned protons can unequivocally be identified by their low $1/\chi^2$ values.

8.6 Assignment of the configuration and conformation of spiroindene

A second test was carried out to discriminate between diastereoisomeric structures of the two synthetic spiroindene derivatives shown in Figure 8.7. The configuration of the molecule, according to X-ray analysis[199] has been determined to be 1S1aS6aR, which corresponds to configuration 1b (Figure 8.7b). Previous RDC analysis obtained in a stretched cross linked poly(dimethylsiloxane)/chloroform gel resulted in one bond CH RDCs that could be fitted well using the SVD-fitting procedure as well as the steric prediction method implemented in the program PALES.[200] A good discrimination between 2a (1R1aS6aR) and its diastereoisomer 2b was observed. In the following we use this well-studied test case to evaluate the ability of the MDOC simulations to discriminate the diastereoisomers 1a and 1b. More than 150 MDs were carried out, since at that time, the calculation for the coupling and the force field contained a bug. As the force field of COSMOS does not preserve the configuration at the spiro carbon atom, distances between the neighboring atoms were fixed. The resulting total and individual quality factors are shown for both configurations in Figure 8.8 and in Figure 8.8.

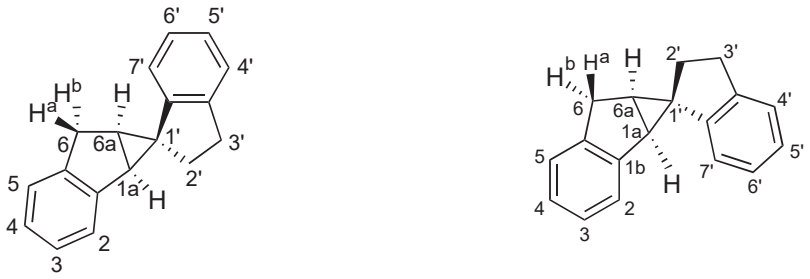

(a) Spiroindene 1a

(b) Spiroindene 1b

Figure 8.7

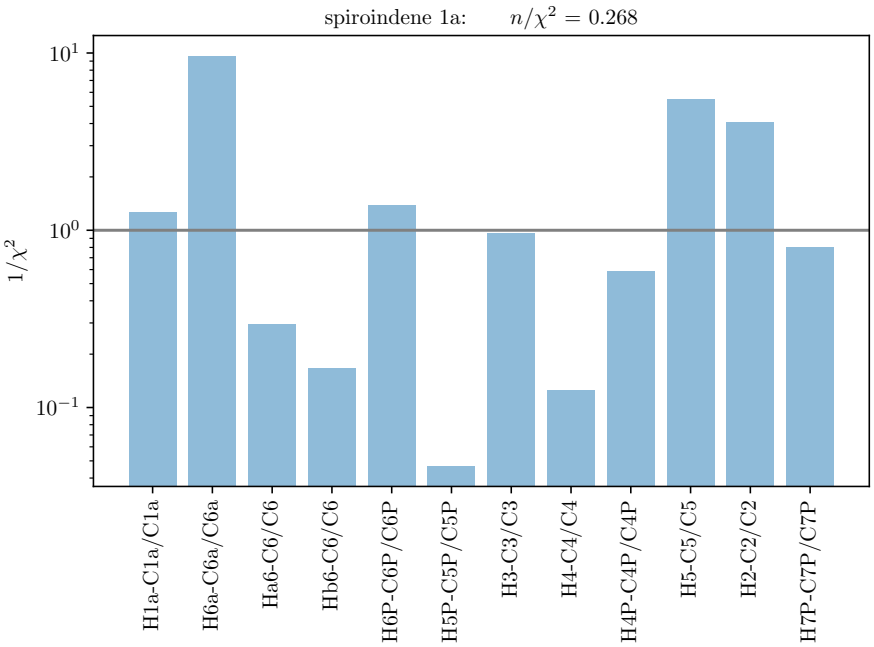

Figure 8.8: Achieved individual and total quality factors for spiroindene 1a

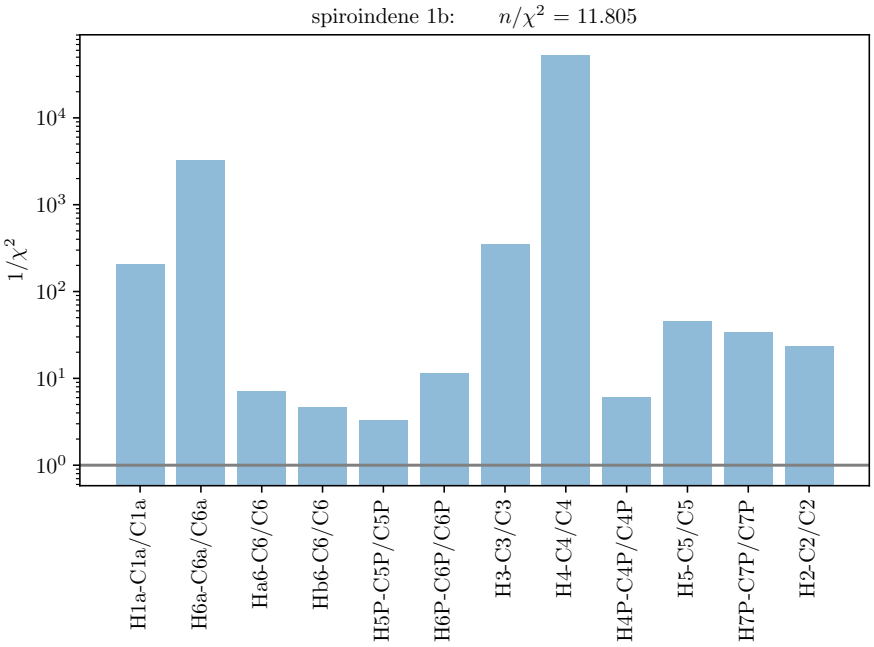

Figure 8.9: Achieved individual and total quality factors for spiroindene 1b

The data in combination with MDOC clearly reveals the correct configuration of the spiroindene derivative. Altering the force field only conserved the chirality at the carbons next to the spiro atom. The scaling behavior of increased pseudo force scaling k is shown in Figure 8.3.

8.7 Assignment of the configuration and conformation of staurosporine

Staurosporine is a molecule of a higher flexibility than borneol and has 4 stereogenic centers that were discriminated by simulations of the four different configurations shown in Figure 8.10. Furthermore, the six-membered aliphatic ring can take up boat and chair conformation. Its absolute configuration has been determined by single crystal X-ray analysis of its N-methyl iodide derivative to be 2′S3′R4′R6′R. $^1D_{\mathrm{CH}}$ RDCs were available from measurements taken in stretched perdeuterated polystyrene/chloroform gels.[158] In Table 8.1 the results are summarized with values achieved from a SVD carried out with the program MSpin.[201]

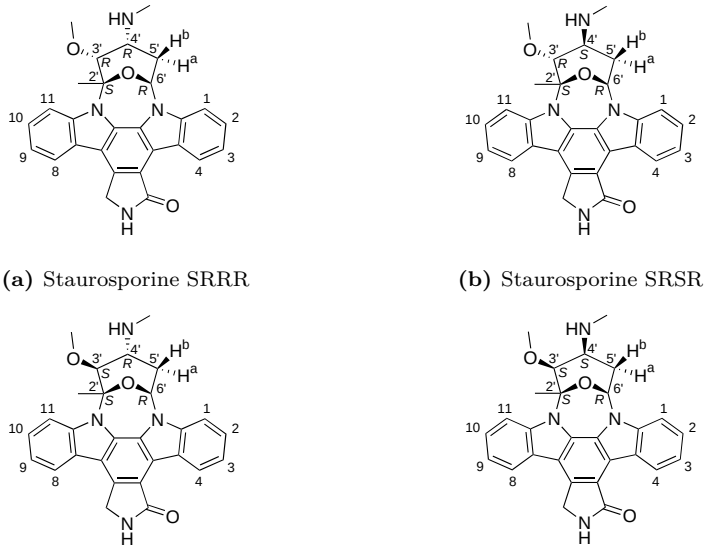

(a) Staurosporine SRRR

(b) Staurosporine SRSR

(c) Staurosporine SSRR

(d) Staurosporine SSSR

Figure 8.10

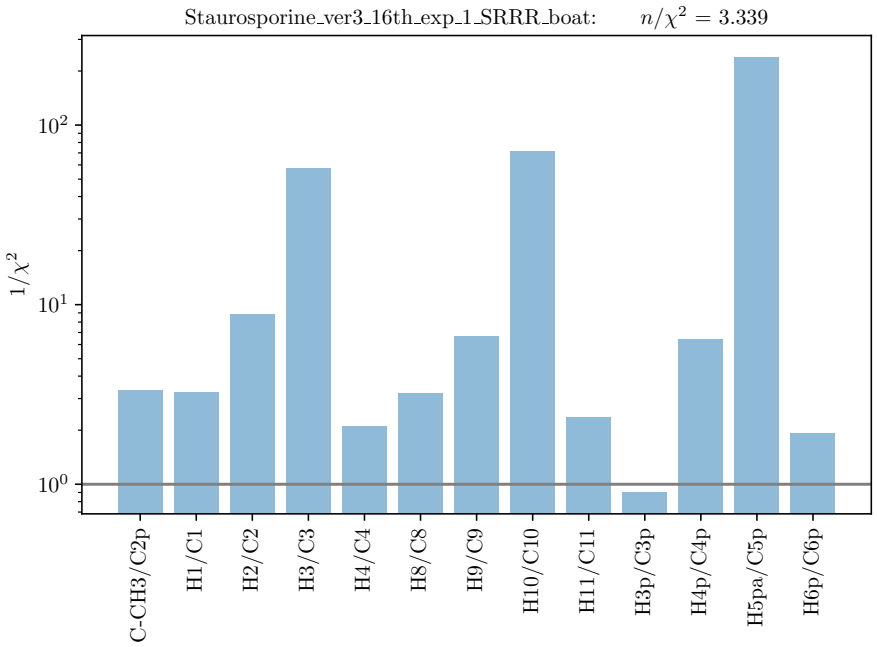

Figure 8.11: Discrimination of the correct conformation: Even though the total n/χ^2 value is above one, one outlier differentiates the wrong starting conformation (boat) from the correct staurosporine configuration (chair).

Table 8.1: Achieved (minimal) individual and total quality factors compared with the static SVD approach. The number in the brackets indicates the amount of constraints with individual quality factors below one.

	MDOC		**SVD**	
	$n/\mathcal{X}^2$	$1/\mathcal{X}^2$	$n/\mathcal{X}^2$	$1/\mathcal{X}^2$
SRRRb	3.344	0.905 (1)	0.108	0.014 (8)
SRRRc	4.139	1.074 (0)	5.392	0.617 (1)
SRSRb	2.657	0.481 (1)	0.049	0.004 (5)
SRSRc	2.469	0.446 (1)	1.377	0.160 (3)
SSRRb	2.454	0.374 (1)	0.032	0.005 (10)
SSRRc	1.573	0.184 (2)	0.118	0.014 (7)
SSSRb	1.601	0.220 (2)	0.116	0.017 (8)
SSSRc	1.575	0.219 (2)	1.575	0.219 (2)

The molecular trajectories of the correct assigned configurations starting with boat (SRRRb) and chair (SRRRc) conformation are analyzed according to the torsion angle along the atoms of CH_3-C2'-C3'-C6' and H6'-C6'-C5'-C4' in Figure 8.12 (left side). Shown on the right are the respective histograms. The plots reveal that

the correct assigned model remains in the chair conformation (E-H). The Trajectories were plotting using the COSMOS utility implemented in the Software MSpin. Note that the scale in E is much smaller. The trajectories in A and C (boat) show deviating initial dihedral angles of 80 or -100°. The peaks visible at around the 220th snapshot in A and C, and at the 20th, 100th and 470th snapshot in G are artifacts arising from the plotting method, when the absolute values exceed ±180° and are not contained in the COSMOS output. Clearly, the model starting with the boat conformation forms an intermediate twisted ring that further flips into the chair conformation, where it remains.

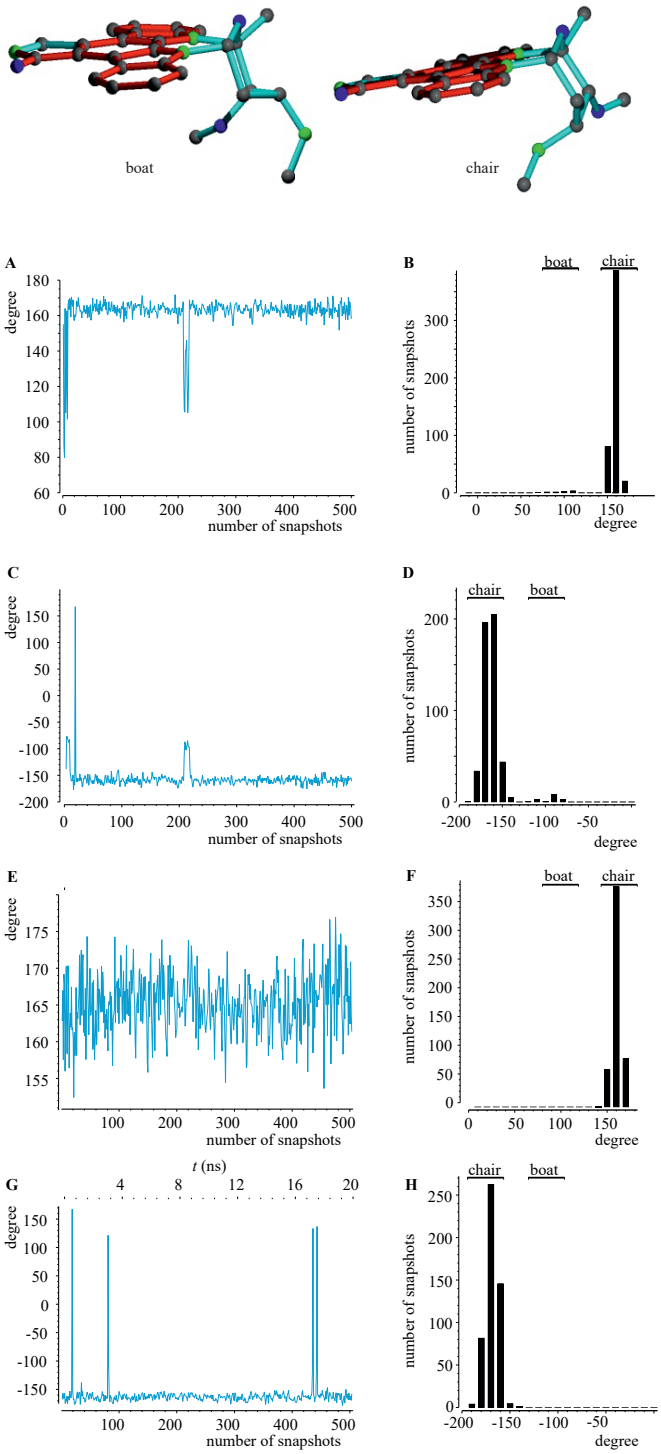

Figure 8.12: Trajectory (left) and histograms (right) of dihedrals along CH_3-C2'-C3'-C6' (A/B, E/F) and H6'-C6'-C5'-C4' (C/D, G/H) of correct staurosporine configuration starting with boat (SRRRb, upper left) and chair (SRRRc, upper right) conformation.

8.8 Assignment of prochiral protons in ethinylestradiol

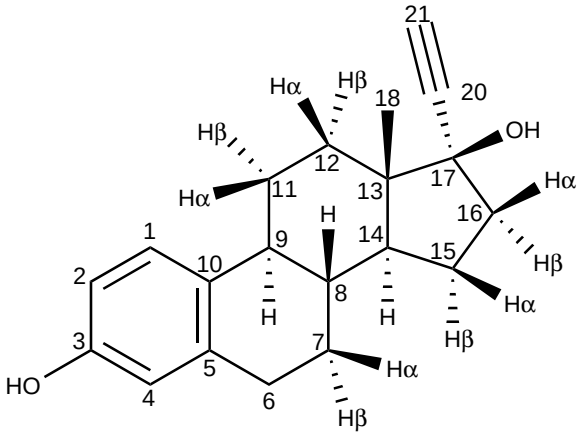

Figure 8.13: 17α-ethinylestradiol

RDCs of ethinylestradiol were measured in DMSO-d_6 and PEO-DA (section 7.5) a model was created with COSMOS. After the adaption of the order and the force scaling parameters, enantiodiscrimination was carried out by exchanging the prochiral methylene protons H7, H11, H12, H15 and H16 leading to the competing models (X7, X11, X12,X 15, X16) and evaluating the results after the MDOC by the quality criterions. The outcome is summarized in Figure 8.14

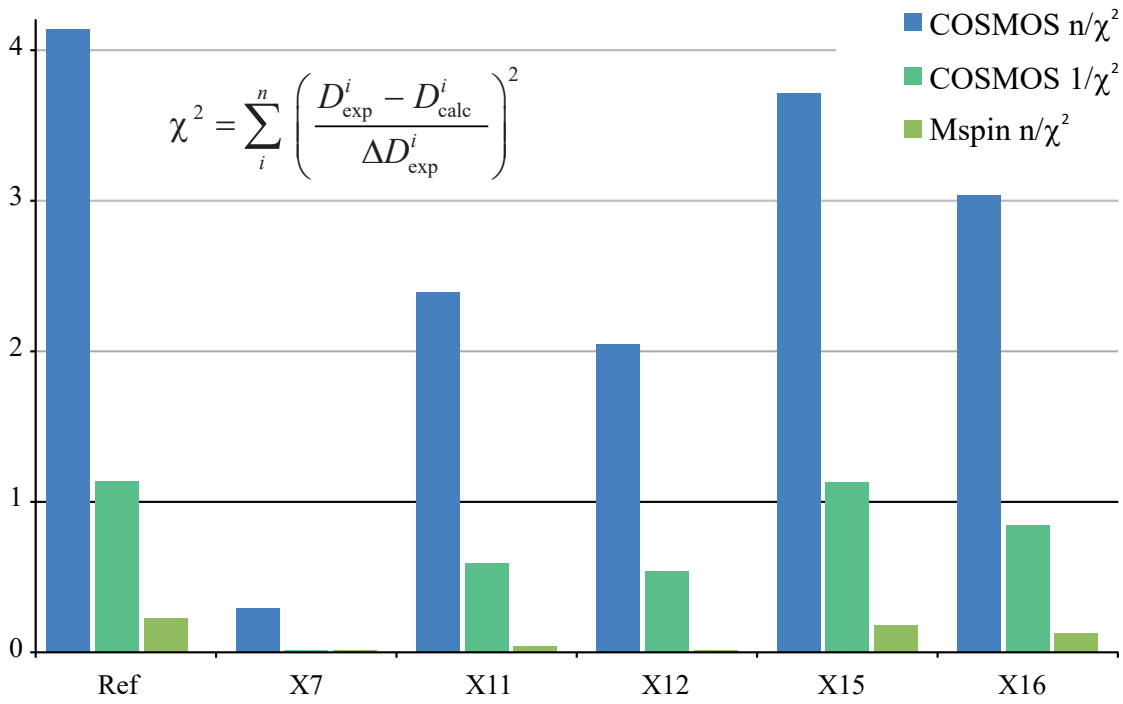

Figure 8.14: Resulting quality criterions for the prochiral assignment of protons with ethinylestradiol. The correct assigned structure competes with the assignment, where the protons 15a and b are exchanged. A closer look reveals that both these protons suffer from secondary order effects. The two constraints for H15a and b are 3.8±0.3 Hz and 3.3±1.1 Hz, which does not allow a clear differentiation. Moreover they are part of a five membered ring that bears a higher mobility, averaging out anisotropic values.

8.9 Results

In the previous chapter the MDOC approach was tested with three different molecules for prochiral discrimination and configurational and conformational elucidation. The main problem of finding a set up to run an MD with orientational constraints was crucially eased by the development of two scripts for the execution and the evaluation of the data. With these tools, reliable optimization of the runs could be carried out and by using the $\mathcal{X}^2$ criterion, the method could be falsified. All the models posses a high mobility within the runs and fill out the conformational space much faster than feasible with conventional MD approaches, while no effort has to be taken to add solvent molecules or to find a correct starting conformation.

9 | Properties

When investigating polymers the repeating monomer units lead to overlapping spectral lines for containing chemically and magnetically almost equivalent spins. With standard NMR methods clear assignments and revealing the inner relations of cross-links, dangling ends and network defects is therefore hardly amenable. For swollen polymer sticks used as alignment media, the property not to show to many signals is actually desired, to avoid covering signals from the analyte guest molecule. In the case of cross-linked PEO-DA networks, most of the chains consist of ethoxy groups whose chemical shift δ is almost invariant towards its position within about 800 units. Nevertheless, another type of so-called time-domain relaxometry NMR methods, withdrawing chemical shift resolution, is able to identify and separate network fractions within the samples. In the previous chapters it has been described, how nuclear spins are manipulated intentionally (*external spin interactions*[31]) and how the Fourier transformed FID contains a large variety of structural information based on chemical shifts (δ), scalar couplings (J) or NOE distances according to the applied pulse sequence. Due to *relaxation* the perturbed state (bulk magnetization) returns back to its equilibrium. The way, NMR active nuclei relax, is related to their dynamics and environment. In the next chapters it will be explained, how apparent dynamic information can be deduced from time domain relaxometric measurements and how topological insights to polymeric networks can be achieved. According to the components of magnetization – transversal and longitudinal – two types of relaxation can be differentiated and evaluated separately.

9.1 T_1 relaxation

In the absence of magnetic fields, the energy states of spins are degenerated and the nuclear magnetic spins take up all possible orientations (Fig. 9.1A). If spins are exposed to a homogeneous magnetic field $\vec{B_0}$, however, the energy levels split (Zeeman interaction) and their axes of precession is oriented with (α) or against (β) its direction (z). Since the α-state is energetically preferred, z-components of

a fraction of spins don't cancel each other out anymore (Fig. 9.1 B) raising a so called net magnetization along z- $\mathbf{M_z}$.

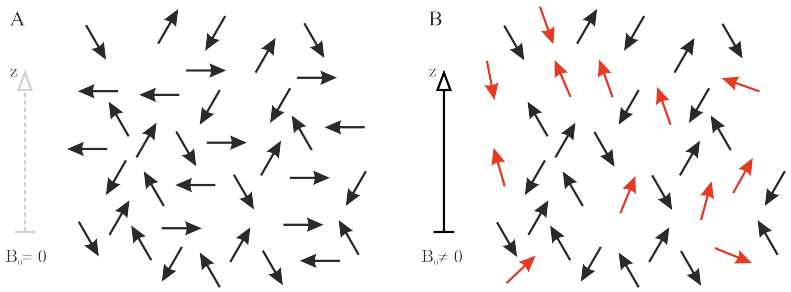

Figure 9.1: Schematic description on the properties of an ensemble of spins without (A) and within (B) an outer homogeneous magnetic field ($\vec{B_0}$). In A, the direction of the nuclear magnetic moments are evenly distributed, compensating each other to zero. Arrows indicated in red (B) represent the fraction of spins causing a remaining z-component.

The saturated initial state builds up net z-magnetization M_z being proportional to the occupation difference (Equation 9.1) until the thermal equilibrium M_0 described by the Boltzmann distribution Equation 9.2 is achieved:

$$M_0 \propto (N_\alpha - N_\beta) \tag{9.1}$$

$$\frac{N_\alpha}{N_\beta} = \exp\frac{-\Delta E}{k_b T} = \exp\frac{-\gamma\hbar\vec{B_0}}{k_b T} \approx 1 - \frac{-\gamma\hbar\vec{B_0}}{k_b T} \tag{9.2}$$

The ratio of the number of spins occupying α- (N_α) and β-state (N_β) depends on the magnetic field strength $\vec{B_0}$ and the magnetogyric ratio (γ) describing the energy difference ΔE between the respective energy levels at the absolute temperature (T)[a]. The built-up to this equilibrium doesn't occur instantaneous but is characterized by the time T_1. The perturbed state dissipates energy to the surroundings (the lattice) as heat that is why the so-called spin-lattice or longitudinal relaxation is an enthalpic process. The temporal return of the z-magnetization to equilibrium is expressed by the Bloch equation Equation 9.3:[202]

$$\frac{dM_z}{dt} = \frac{M_z - M_0}{T_1} \tag{9.3}$$

The initial net magnetization NMR experiments operate on is gained within 5 times T_1. This is the reason, why the longitudinal T_1 relaxation determines how fast NMR experiments can be repeated and has therefore a great impact on the

[a] At room temperature, this difference is on the order of 1 ppm, since thermal motion is permanently inducing transitions

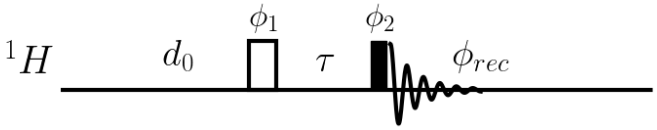

Figure 9.2: Pulse sequence of the *inversion recovery* experiment. Bold rectangles indicate 90° pulses, open rectangle 180° inversion pulses. τ is increased stepwise and the respective 1D spectra are recorded. To ensure equilibrium magnetization is restored, the recovery delay d_0 is typically set between 5 to 10 times of an approximated T_1 time. Phases ϕ_i can be set to x for a simple version or phase cycling can be applied to compensate imperfections especially of the inversion pulse ($\phi_1 = x, -x; \phi_2 = \phi_{rec} = x, x, -x, -x, y, y, -y, -y$)

.

total acquisition time especially when recording numerous scans for a better S/N or for incrementing *e.g.* on 2D experiments. The value of T_1 can be determined with the so-called *inversion recovery* experiment (Figure 9.2).

During its course the equilibrium magnetization is inverted to $-M_0$ which is allowed to return for an incremented delay τ. A final 90° pulse turns the z-magnetization into the transversal plane, where the intensity of the FID for different delays τ depends on T_1 by an exponential built-up function:

$$M_z(\tau) = -M_0 + 2M_0 \exp \frac{-\tau}{T_1} \tag{9.4}$$

For the zero-crossing of the intensity built-up (see M_z in Figure 9.6) the following relation can be applied to evaluate T_1:

$$T_1 = \frac{\tau(M_z = 0)}{\ln 2} \tag{9.5}$$

An additional and more quantitative method to measure T_1 is the *saturation-recovery* experiment, where the initial inversion pulse is replaced by a series of *saturation* pulses. T_1 is here evaluated by fitting the recovery of the magnetization according to the following expression:

$$M_z = M_0(1 - e^{-\frac{\tau}{T_1}}) \tag{9.6}$$

9.2 T_2 relaxation

In a static magnetic field $\vec{B_0}$, the spins can be pictured to precess on a cone pointing along the field in z-direction. M_z arises from the unequally occupied α- and β-states (*vide infra*), but the x- and y-components of the spins are randomly

distributed and cancel each other, so no x- or y-magnetization is observable. The situation changes, when rf pulses are applied, turning the z-magnetization into the transversal plane. Here, the precession leads to a coherently oscillating so-called x,y- or transversal magnetization, rotating all with the same phase (Figure 9.3).

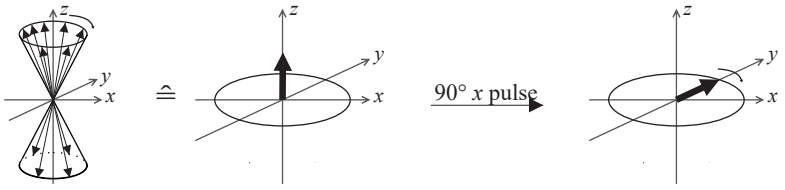

Figure 9.3: Schematic illustration of precessing spins in a static magnetic field for spin 1/2 nuclei with a positive magnetogyric ratio γ before and after a 90° pulse. The overall equilibrium z-magnetization (M_z) is represented by the excess of positive z-components of the spins (thin arrows) precessing in the x/y-plane. x- and y-components are randomly distributed causing zero magnetization in the transversal plane but creating net z-magnetization. A 90° pulse transforms (M_z) into oscillating x/y-magnetization ($M_{x/y}$) inducing the FID.

The oscillations induce a current in the receiver coil of the spectrometer that is recorded as the FID. The so-called T_2 relaxation time describes this decay of the transversal magnetization – its lifetime – and therefore determines the line widths ($\omega_{1/2}$, $\nu_{1/2}$) of signals Equation 9.7 in the frequency domain. This lifetime dependent line broadening is also classified as *homogeneous* line broadening in contrast to line broadening due to superposition of many sharp lines (*heterogeneous* line broadening). To differentiate between intrinsic T_2 relaxation originating from interacting spins and T_2 relaxation arising from field inhomogeneities an *effective* T_2^* is defined.

$$\omega_{1/2} = \frac{1}{T_2^*} \qquad \nu_{1/2} = \frac{1}{2\pi T_2^*} \tag{9.7}$$

Note, that with the observed line widths the T_2^* time is calculated, which is shorter than one would expect from the underlying atomic and molecular mechanisms between spins (*vide infra*). The acceleration is induced from inhomogeneities in the magnetic field, which may originate from intrinsic defects in the magnet or susceptibility-induced distortions produced by inhomogeneities in the sample itself or the tube. The contribution of the "true" T_2 relaxation and the component induced by sample and field inhomogeneities to T_2^* sums up inversely.

$$\frac{1}{T_2^*} = \frac{1}{T_2} + \frac{1}{T_2^{inh}} \tag{9.8}$$

The knowledge of T_2 is important for dynamic NMR experiments and investigations of spin-diffusion. The decay occurs, because fluctuating fields mostly originating from other spins induce a dephasing on the initially coherent spins

(*vide infra*). This is the reason why this entropically driven, energy conserving process is also called spin-spin relaxation. The T_2 time can be evaluated with the *Carr-Purcell-Meiboom-Gill* (CPMG) sequence.[203]

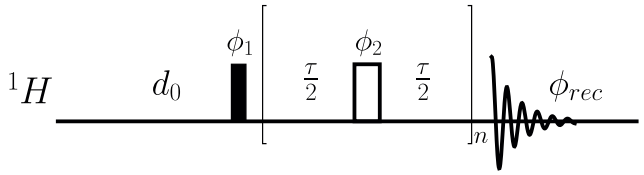

Figure 9.4: Pulse sequence of the CPMG experiment.

The sequence starts with a 90° excitation pulse to create transversal magnetization, where the spins precess coherently. Then, after an incrementable time $\tau/2$ allowing the spins to relax is followed by an inversion pulse. Within the subsequent second delay, the spins refocus and a so-called spin-echo or Hahn-echo is derived (Figure 9.4).

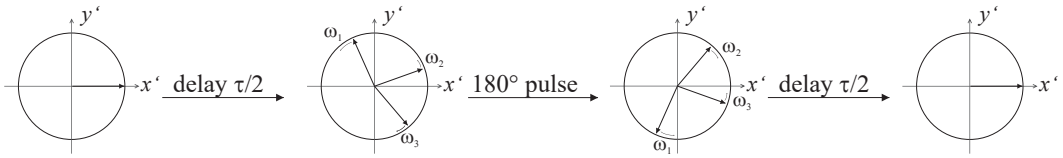

Figure 9.5: Evolution of the transversal magnetization in the rotating frame. once an excitation pulse has been applied, the spins precess in phase. During a delay $\tau/2$ the spins having different chemical shifts begin to dephase. Shown here are three exemplary spins with chemical shifts ($\omega_1 > \omega_2 > \omega_3$) different from each other and the irradiation frequency (off-resonant). When a 180°-x-pulse is applied, their positions get mirrored at the x-axis, changing the sign of their y-component and preserving their x-component. Because the direction of their gyration remains, they refocus after another delay $\tau/2$.

The decay of transversal magnetization can be described with the following linear differential Bloch equations:[202]

$$\frac{dM_x}{dt} = -\frac{M_x}{T_2} \qquad \frac{dM_y}{dt} = -\frac{M_y}{T_2} \tag{9.9}$$

which are resolved as:

$$M_{x,y}(\tau) = M_{x,y}(0) \exp \frac{-\tau}{T_2} \tag{9.10}$$

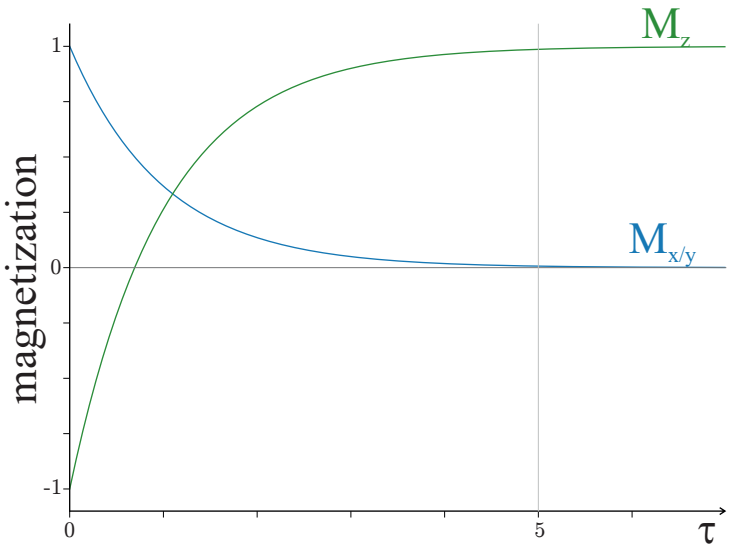

Figure 9.6: Comparison of the course of T_1 and T_2 time relaxation of a single component. The longitudinal magnetization M_z built-up after an inversion (green) and the relaxation of the transversal $M_{x/y}$ magnetization after a 90° excitation pulse (blue). Time τ is in units of T_1 and T_2 respectively. Note, that after 5 times T_1, more than 98.6% of the initial magnetization are recovered. (T_1 and T_2 are here of the same value; in general $T_2 \leq T_1$).

9.3 Relaxation mechanisms

In the above chapters the behavior of an ensemble of free precessing spins has been described. There it was also explained, how manipulation of spins requires transverse magnetic fields oscillating near the Larmor frequency. The key for relaxation is that such oscillating fields occur *naturally* (*internal spin interactions*).[31] A premise for their appearance is a combination of present local inhomogeneous fields or field gradients in the sample and motion of particles or segments within these fields or moving fields, respectively. All *relaxation pathways* therefore can be categorized by the type of interaction that enables it, and a type of motion that drives it.[204] For a general description of such stochastic motions the so-called correlation time τ_c is introduced.

9.3.1 The correlation function

The correlation function describes and quantifies magnitude and distribution of thermal motion. A rough approximation for the so-called rotational correlation time τ_c of a spherical neutral particle in a homogeneous fluid gives the Stokes-Einstein-Debye relation from hydrodynamic theory, the relationship between τ_c, viscosity η, the hydrodynamic radius r_h and the temperature T.

$$\tau_c = \frac{4\pi\eta r_h^3}{3k_BT} = \frac{V\eta}{k_BT} \tag{9.11}$$

It states that the rotational correlation time τ_c increases linearly with the hydrodynamic volume V and viscosity η of the fluid and decreases with the temperature T. In liquids, even small molecules do not rotate freely but are subject to collisions at all times and in between they rotate by small amounts about arbitrary directions. This motion is called *rotational diffusion*. The rotational correlation time τ_c^{rot} is equivalent to the average time it takes, until a tumbling molecule has turned by one radian. Another correlation time denoted with τ_c^{conf} is the mean life time of conformations or exchanging species. In general, τ_c is the crucial part of the *correlation function* $G(\tau)$. It assumes that moving spins experience time-dependent local fields $B_{loc}(t)$ that change after an interval τ to $B_{loc}(t+\tau)$. The correlation function $G(\tau)$ then is given by the average over all spins of the product:

$$G(\tau) = \overline{B_{loc}(t)B_{loc}(t+\tau)} \tag{9.12}$$

The random variations of local fields $B_{loc}(t)$ do not depend on a point in time and therefore G(τ) is a stationary function. The correlation function G(τ) hence only depends on the interval τ.[74] Its maximum for $\tau = 0$ corresponds to the average of the square of the local field B_{loc}^2, so it only depends on the average size of the interaction. The behavior of $G(\tau)$ depends on the type of interaction but can be expressed for simple cases like rotational diffusion as an exponential whose decay rate is set by τ_c and an amplitude B_{loc}^2.

$$G(\tau) = \overline{B_{loc}^2}\exp\{\frac{-|\tau|}{\tau_c}\} \tag{9.13}$$

Because the exponential part of this function does not depend on the local field it is therefore common to define it as the *reduced correlation function* $g(\tau_c)$, which is independent of the size of local fields.

$$g(\tau) = \exp\{\frac{-|\tau|}{\tau_c}\} \tag{9.14}$$

9.3.2 The spectral density

To find out the fraction of oscillations that is present at the Larmor frequency and therefore effectively contributing to relaxation, the correlation function $G(\tau)$ is Fourier-transformed to obtain the so-called (power) spectral density function $J(\omega)$.[179,205] For the exponential decay (Equation 9.13), the spectral density $J(\omega)$ has Lorentzian shape.

$$G(\tau) = \overline{B_{loc}^2} \exp\{\frac{-|\tau|}{\tau_c}\} \xrightarrow{FT} \overline{B_{loc}^2} \frac{2\tau_c}{1+\omega^2\tau_c^2} = J(\omega) \tag{9.15}$$

Whereas the correlation function $G(\tau)$ depends on the *time* of an interval τ, the spectral density function $J(\omega)$ provides information on the distribution of *frequencies* ω for given correlation times τ_c (see Fig. 9.7). The spectral density shows a maximum $2\overline{B_{loc}^2}\tau_c$ at $\omega = 0$ and then decreases steadily for higher frequencies. Note that for shorter correlation times, the function covers a broader range to higher frequencies ω. To find the most effective correlation time for relaxation in a given field, one has to evaluate $J(\omega)$ in Equation 9.15 with $\omega = \omega_0$.

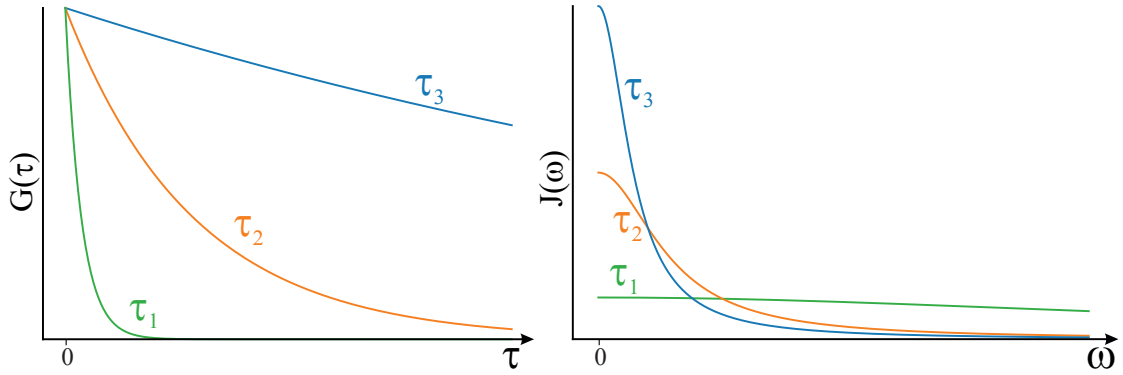

Figure 9.7: Comparison of the correlation function $G(\tau)$ and its Fourier transform, the spectral density function $J(\omega)$ for different correlation times τ_c. ($\tau_1 < \tau_2 < \tau_3$)

When plotting $J(\tau_c; \omega = \omega_0)$ a maximum appears where $\tau_c\omega_0 = 1$. This point indicates the correlation time τ_c with the maximum spectral density for a given Larmor frequency ω_0 (see Figure 9.8 on page 145). The *reduced spectral density* is given by

$$j(\omega_0) = \frac{2\tau_c}{1+\omega_0^2\tau_c^2} \tag{9.16}$$

9.3.3 Motional regimes

Depending on the magnitude of τ_c and ω_0 the spectral density converges against two limits that correspond to two *motional regimes*. The so-called *fast motion* or *extreme narrowing* limit is mathematically defined for $\omega_0\tau_c \ll 1$, which is the case for small molecules at sufficiently high field strength. At the Larmor frequency, the reduced spectral density $j(\omega_0)$ then converges to

$$\text{fast motion:} \qquad j(\omega_0) = 2\tau_c \tag{9.17}$$

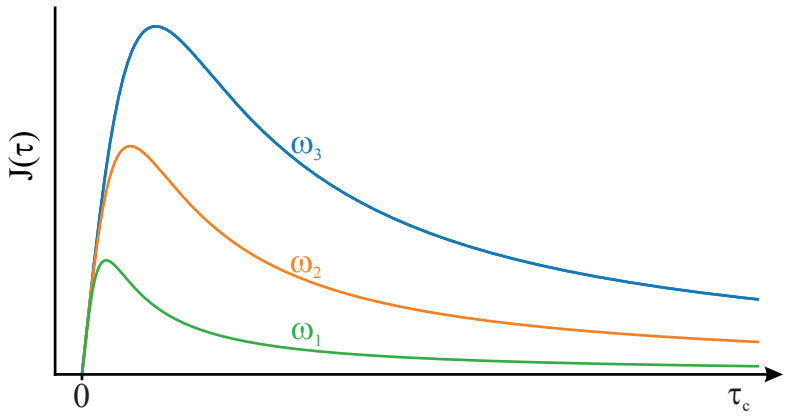

Figure 9.8: Illustration of spectral density functions $J(\tau_c)$ at different Larmor frequencies $(\omega_{0,1}, \omega_{0,2}, \omega_{0,3})$. The maximum effective relaxation rate takes place for spins with $\tau_c = {}^1/_{\omega_0}$.

which means that here the relaxation behavior is linearly dependent on the squared average of oscillating fields raised by some interactions (*vide infra*) and the correlation time τ_c, but independent with respect to the Larmor frequency ω_0. Since $j(0) = \tau_c$ it follows that $j(\omega_0) = j(0)$. In Figure 9.7 such a behavior is shown by τ_1, where the spectral density is almost constant over a wide range. The other extreme case – the *slow motion* or *spin diffusion* limit – occurs when $\omega_0\tau_c \ll 1$, which reflects the situation in macromolecules like proteins or backbones of polymers.

$$\text{slow motion:} \qquad j(\omega_0) = \frac{2}{\omega_0^2\tau_c} \tag{9.18}$$

With the relation $j(0) = 2\tau_c$ Equation 9.18 can be rewritten as

$$j(\omega_0) = \frac{j(0)}{\omega_0^2\tau_c^2} \tag{9.19}$$

Here, the spectral density $J(\omega_0)$ declines quickly from the maximum at $J(0)$. This behavior is illustrated in Fig. 9.7, where τ_3 decreases fast with rising frequency ω. When operating at a Larmor frequency of 600 MHz ($\omega_0 = 3.77 \times 10^9\ rad\ s^{-1}$) for small molecules with correlation times of 10 ps the product $\omega_0\tau_c = 0.038$, which allocates them to the fast motion limit. For a small protein with a correlation time of 10 ns, $\omega_0\tau_c = 37.7$ assigning it to the slow motion limit.

9.3.4 Interactions enabling relaxation

The origin of motion for spins and thus the experience of fluctuating fields is mostly *molecular tumbling* and *conformational exchange*. The fluctuating fields will cause

the spins to precess differently causing faster loss of coherence (a T_2 effect). The varying components of this local fields support transitions towards the thermal equilibrium with higher probability, re-establishing the equilibrium populations. In the following, the origins for these local field fluctuations are explained

Dipoles

The most important source contributing to relaxation arises from magnetic dipoles. In the classical picture, the spins behave much like tiny bar magnets with north and south poles (the *dipole*). Any charged particle with a magnetic spin (*e.g.* nucleus, unpaired electron) possesses its own field, leading to a deviation in the strong outer magnetic field $\vec{B}_0$. For the case of a methinyl group, the magnetic field ($\vec{B}_0$) both nuclei experience is amplified or attenuated depending on the orientation of the bond (see Figure 9.9).

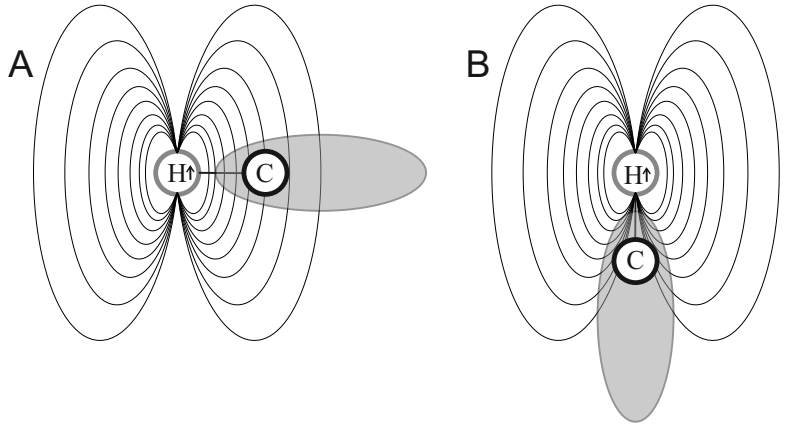

Figure 9.9: Dipolar interaction of a ^{1}H nucleus inducing an additional field on an attached carbon.

Thus, the direct *dipole-dipole* (DD) interaction operates through space and depends principally on the internuclear distance and the magnetogyric ratios of the involved nuclei. For the contribution of a heteronuclear DD interaction between carbon and an attached proton the relaxation rate R_1 (*extreme narrowing limit*, see Equation 9.17) follows the equation

$$\frac{1}{T_{1,DD}} = R_{1,DD} = \frac{\gamma_I^2 \gamma_S^2 \hbar^2 \tau_c}{r_{IS}^6} \tag{9.20}$$

with the internuclear distance r_{IS} between the nuclei I and S and the molecular correlation time τ_c. This explains, why ^{13}C displays faster relaxation, the more protons are directly attached and nearby. The distance of protons to quaternary carbons is at least two bonds further and therefore comparatively longer

slowing down their relaxation rates significantly. The interaction takes also place *intermolecularly* but can be neglected in liquids with low viscosity.

As the Brownian motion prompts the molecules to tumble and rotate, the associated dipolar magnetic field also fluctuates at a given point in space. Depending on the molecular correlation time τ_c (and the outer magnetic field $\vec{B_0}$ outside the extreme narrowing limit), a larger or smaller fraction of spins is exerted to fluctuations matching the Larmor frequency and consequentially relaxation is more or less effective, respectively. Since the magnetic moment of electrons ($9.274{\times}10^{-24} J/T$) is almost 3 orders of magnitude higher than the magnetic moment of protons ($1.411{\times}10^{-26} J/T$), unpaired electrons provide highly efficient *paramagnetic relaxation* pathways via the dipolar interaction. That is why paramagnetic impurities like metal cations but also dissolved oxygen with its unpaired electrons enhance relaxation in an often unwanted manner, leading to line broadened spectra. On the other hand this is exploited by the PRE technique, where paramagnetic (*e.g.* nitroxide) spin-labels are tagged to macromolecules. Within a radius up to 35 Å, the paramagnetic center broadens signals such that they disappear due to paramagnetic relaxation uncovering information about structural aspects within the macromolecule.

Chemical shift anisotropy

In liquids, molecules tumble and rotate very fast compared to the time scale of the measurement, resulting in an averaged isotropic chemical shift Equation 4.22, with line widths below 1 Hz. The anisotropic nature of the chemical shift causes the local field $\vec{B_{loc}}$ to oscillate due to stochastic motion of the molecule. The resulting T_1 relaxation caused by the chemical shift anisotropy (CSA) is described by the term

$$\frac{1}{T_1} = R_{1,CSA} = \frac{1}{15}\gamma^2 B_0^2 (\Delta\sigma)^2 \frac{2\tau_c}{1+\omega_0^2\tau_c^2} \tag{9.21}$$

Nuclear relaxation governed by CSA therefore is particularly effective for such nuclei as ^{13}C, ^{15}C, ^{19}F and ^{31}P, having large CSA values. Nonetheless, when operating at high field strengths, the CSA relaxation pathway becomes more dominant, even for protons with relatively low $\Delta\sigma$ values ($\sim$20 ppm).

The CSA spin-spin relaxation time is expressed by

$$\frac{1}{T_2} = R_{2,CSA} = \frac{1}{90}\gamma_I^2 B_0^2 (\Delta\sigma)^2 \left(8\tau_c + \frac{6\tau_c}{1+\omega_I^2\tau_c^2}\right) \tag{9.22}$$

It is also field dependent and as Equation 9.21 proportional to B_0^2, when operating under fast motion conditions. In the extreme narrowing limit the ratio from Equation 9.21 and Equation 9.22 becomes

$$T_{1,CSA}/T_{2,CSA} \quad = \quad 7/6 \tag{9.23}$$

which can reveal CSA relaxation when comparing longitudinal and transversal relaxation times.[206]

Scalar coupling

If a nucleus is coupled via scalar (J) coupling to another one, whose spin state is changing quickly, additional local oscillating fields $\vec{B_{loc}}$ arise that effectively open a relaxation pathway also for the first nucleus. This mechanism becomes important, the closer resonance frequencies of the interacting nuclei are. For heteronuclear couplings, the difference is big and scalar coupling practically does not contribute to relaxation, especially at high fields. When operating at lower field strength, *e.g.* 2.3 Tesla, in case of ^{13}C bound to ^{79}Br, $\omega_0(^{13}\mathrm{C})$ is 25.144 MHz and $\omega_0(^{79}\mathrm{Br})$ is 25.050 MHz, the given carbon signal will be broadened due to scalar coupling.

In the case of homonuclear J couplings between protons in organic molecules, resonance frequencies are close to each other or even the same (for example in the case of chemically and magnetically equivalent geminal nuclei) and although the coupling may be unobservable the contribution to relaxation still remains. For $^3J_{\mathrm{HH}}$ coupling of vicinal protons the efficiency of the J coupling interaction crucially depends on the dihedral angle ϕ spanned by the three bonds. Fast interconverting rotamers show a coupling constant ^3J as the temperature dependent average over all $^3J(\mathrm{t})$ components with approximate lifetimes given by the individual rotamers affecting relaxation. Following the Karplus equation, the mean amplitude of $^3J(\mathrm{t})$ is in the range of 10 Hz.

When considering that relaxation rates correlate with the square of the variable component of the enabling interaction, it seems that scalar relaxation would always be negligible compared to dipolar relaxation being stronger by a factor of 10^6. On the other hand, one also must take into account the different character of correlation times τ of the random motions driving the respective relaxation pathway. For dipolar relaxation it is the rotational diffusion time τ_c^{rot} concerning the *orientation* whereas for the scalar interaction it is the conformational lifetime τ_c^{conf} of a *conformation*. The respective spectral density functions become proportional towards the correlation time when operating in the extreme narrowing limit (Equation 9.17), which allows an arrangement, where τ_c^{conf} can compensate τ_c^{rot} for the difference in the mean amplitudes of the interactions. This becomes more clear when comparing the bandwidths of the correlation times. Rotational diffusion times τ_c^{rot} vary between tens of picoseconds for small molecules to tens of microseconds for large proteins. The conformational lifetimes τ_c^{conf}, however, can be just as low as τ_c^{rot} values but can be elongated as long as relaxation times

on the order of seconds, depending on internal conformational barriers and the temperature. For sufficiently slow inter-converting conformers, separate lines are observed, faster conformational *exchange* causes the rotamer spectral lines coalescing into one. At this coalescence point, scalar relaxation may dominate over dipolar relaxation.[204]

Quadrupolar coupling

The majority of NMR active nuclei have a spin $I > 1/2$ and possess a quadrupolar moment Q. It is the result of a non spherical distribution of charge in these nuclei. This non spherical distribution of charge interacts with an electric field gradient (EFG) posed by an asymmetric distribution of electron density around the nucleus. This is reflected in peaks being broadened the more, the less symmetric the nucleus is surrounded by electrons. Like for the dipolar interaction, the Brownian motion induces rapid changes in this distribution causing the EFG to fluctuate, contributing to relaxation. Depending on the magnitude of the electric quadrupole moment Q of the nucleus, the relaxation behavior will be similar to a spin $1/2$ nucleus for small values of Q (^{2}H, ^{6}Li), or for large values, nuclei will have short T_1 times, making their observation difficult. The rapid quadrupolar relaxation also prohibits any indication of coupling between these nuclei and adjacent carbons or protons, they decouple themselves via quadrupolar relaxation. Both T_{1q} and T_{2q} times are related to the rotational correlation time τ_c and the quadrupole moment through

$$\frac{1}{T_1} = \frac{1}{T_2} = \frac{3\pi^2}{10}\frac{2I+3}{I^2(2I-1)}\mathcal{X}_q\left(1+\frac{1}{3}\eta^2\right)\tau_c \tag{9.24}$$

with the *nuclear quadrupole coupling* constant $\mathcal{X}_q$ that can be calculated by

$$\mathcal{X}_q = e^2 q_{zz} Q/h \tag{9.25}$$

where the electronic charge is e, the largest component in the electric field gradient represented by q_{zz} (its zz-component) and Planck's constant h. The asymmetry parameter η is a positive number between 0 and 1 (see also Equation 4.25 in page 16) and given by

$$\eta = (q_{yy} - q_{xx})/q_{zz} \tag{9.26}$$

The quadrupole coupling constant does not require any static outer magnetic field, which is exploited in nuclear quadrupole resonance (NQR) *Nuclear Quadrupole Resonance* (NQR) experiments. Besides avoiding nuclei that possess quadrupolar moments, *e.g.* by isotope enriching or depleting protocols, a simpler way to increase relaxation times for sharper lines are all measures that shorten

the correlation time τ_c, for example by increasing temperatures or low solvent viscosities.

9.4 Double quantum proton NMR

Understanding the morphology and dynamic behavior of polymer networks on the molecular-scale is basis for efficient design of new materials. Furthermore the function of polymer networks and gels depend not only on their molecular composition but also their supramolecular arrangement and resulting mobility on very large distance and time scales. Swelling, *e.g.* is strongly affected by the degree of cross-linking, chain length distribution, occurring entanglements, the amount of network defects and other elastically inactive fractions like dangling ends or loops and the presence of functional groups. Unfortunately, X-ray and neutron scattering methods normally applied on condensed matter need the materials under investigation to be single crystals and fail to indicate the positions of hydrogen atoms due to their low scattering cross-section. To reveal the composition of amorphous networks far above T_g, like elastomers, swollen gels and gelling systems, Multiple-Quantum Proton NMR relaxometry (MQ-^{1}H-NMR) has been carried out comprehensively as one of the most promising non-invasive methods.[207–211] In the following chapters the basic principles of the method are explained and a fitting procedure is developed, tackling intrinsic issues of low concentrated polymer gels with swollen PEO-DA-35k gels as an example.

9.4.1 Basic principle

The different interactions enabling numerous relaxation pathways are as stated above dependent on the molecular dynamics and contain information on motional regimes within 11 orders of time magnitudes. Whereas in the solid state due to high order dipolar couplings enable the fast return into equilibrium magnetization, in liquids, especially small to medium sized molecules tumble and rotate too fast to effectively contribute to relaxation, giving rise for competing relaxation pathways. When assuming that inner topological relations are reflected by the dynamics of networks, they can be analyzed by the relaxation behavior, provided all components contributing to relaxation are known. Dipolar (and also quadrupolar) couplings inherently contain structural information because of their axially symmetric dependence concerning the distance r and angle θ between the internuclear vector of coupled spins and the main magnetic field $\vec{B}_0$. In polymeric materials like hydrogels, these interactions fluctuate rapidly and mirror the segmental motions of chains between cross-links. Since the relaxation due to dipolar coupling declines with the inverse of the sixth power of distance, intramolecular homonuclear

dipolar relaxation dominates over intermolecular interactions. Accordingly, very fast and local motions of the single monomer units give rise to a pre-averaged *segmental* dipolar tensor. The pre-averaging rescales the static-limit dipolar coupling D_{static} by a factor k and θ becomes the angle of the symmetry axis of the interaction, namely the backbone of the chain. Its fluctuations are then mirrored by the time dependent angle $\theta(t)$. The associated segmental autocorrelation function can simply be written as

$$G(\tau) = G(|t_a - t_b|) = \frac{1}{2}\left(3\cos^2\theta(t_a)\right)\frac{1}{2}\left(3\cos^2\theta(t_b)\right) \tag{9.27}$$

The segmental autocorrelation function $G(\tau)$ depicts the time it takes for a segment to change its orientation. The dipole-dipole (DD) induced longitudinal relaxation rate R_1 (T_1^{-1}) is given in the Bloembergen-Purcell-Pound (BPP) theory[212,213] by

$$\frac{1}{T_{1,DD}} = R_{1,DD} = \frac{3}{10}\left(\frac{\mu_0}{4\pi}\right)^2 \frac{\hbar^2\gamma^4}{r^6}\Big(J(\tau_c,\omega_0) + 4J(\tau_c,2\omega_0)\Big) \tag{9.28}$$

with the magnetogyric ratio of protons γ, the correlation time τ_c, the Larmor circular frequency ω_0 and the internuclear distance r. Analyzing relaxation allows differentiating network fractions by their different rates, when different correlation times are apparent. To do this, as stated above, the relaxation pathway needs to be known, for a proper characterization. In principle, one could measure the transversal relaxation decay and deduce relaxation times by fitting FID curves, but the contribution of relaxation pathways other than the dipolar relaxation would have to be approximated, hampering quantitative results. To quantitatively differentiate the dipolar coupling contribution from other interactions, ^{1}H-MQ-NMR relaxometry is used.

9.4.2 The coupled two-spin system

In the case of an isolated uncoupled spin ½ nucleus, there are only two possible energy states, and only single quantum (SQ) transitions that change the magnetic quantum number ±1 are allowed inevitably. In a coupled two-spin ½ system, nevertheless, there are 4 energy states with 6 possible transitions. Four of them are again SQ transitions (W_1) changing the state of only one of the two spins. One transition (W_0) is a zero quantum (ZQ) transition, where the two spins just flip conserving their mutual energy and the other one (W_2) is a double quantum (DQ) transition, where both spins change their spin state (Fig. 9.10). The latter two are also called multi-quantum (MQ) transitions, since more than one spin changes its state. The populations of the respective states in thermal equilibrium can be evaluated with the Boltzmann distribution. MQ transitions cannot be

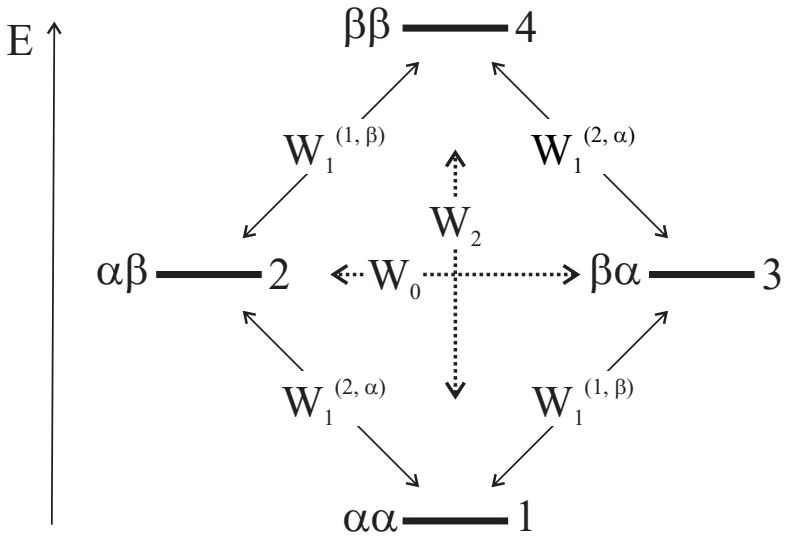

Figure 9.10: Possible transitions W causing relaxation in a coupled two-spin system. Four of them are single quantum transitions and change the total magnetic quantum number M by ±1, indicated with a subscript "1". The superscripts in brackets indicate, which spin flips and the state of the passive spin.

observed directly in contrast to SQ transitions that are directly observable. SQ transitions $\alpha\alpha$ or $\beta\beta \leftrightarrow \alpha\beta$ or $\beta\alpha$ have the highest transition probability to occur for excitation and relaxation. For swollen hydrogels or elastomers, the DQ and ZQ coherences are accessible exclusively via couplings, and can be excited with suitable experiments. The most simple experiment to excite DQ coherences is a two pulse sequence of the form $\frac{\pi_x}{2} - \tau_{DQ} - \frac{\pi_x}{2}$. During the delay τ_{DQ} homonuclear dipolar coupling creates two- and higher spin antiphase coherences. For a better efficiency of double quantum transitions another π_y pulse is applied in the middle of τ_{DQ} to refocus the chemical shift evolution. The second π pulse transforms the antiphase coherences into various MQ coherences, which can be observed only by converting them back into observable transversal magnetization by an appropriate detection pulse (commonly a $\pi/2$ pulse).

For the measurement of DQ coherence built-ups an improved[214] pulse sequence based on the Baum-Pines-Sequence[214] is applied (Figure 9.11). This so-called back-to-back (BaBa) DQ experiment is the homonuclear analogue of the very similar popular rotational-echo double-resonance (REDOR)[215] heteronuclear pulse sequence, used in solid state NMR for recoupling heteronuclear dipole-dipole coupling under magic angle spinning (MAS).[b]

[b] when applying MAS, the sample is rotated rapidly with a frequency $\nu_R = 1/\tau_c$ around an axis tilted by $\theta_M = 54.7°$ against the outer magnetic field direction averaging all tensorial NMR properties like DD couplings and CSA to zero.

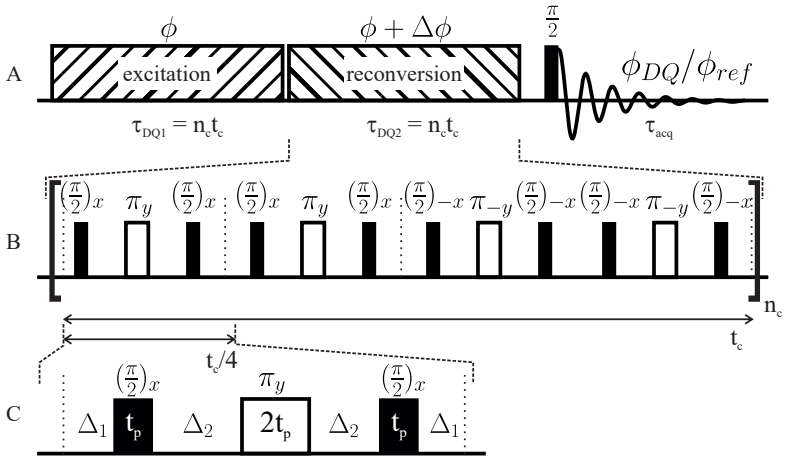

Figure 9.11: Pulse scheme of the improved Baum-Pines sequence:[214] A) DQ excitation and time reversed SQ reconversion block pulses are shifted by a phase Φ. B) Detailed view of the pulsetrain of the upper block comprising 4 sets of $\pi/2 - \pi - \pi/2$-elements. C) Delay and pulse durations therof.

During τ_{DQ1}, multiple quantum coherence is excited via dipolar coupled spins. At the end of τ_{DQ1} z-magnetization and DQ coherences are built-up. Subsequently the reconversion is achieved by applying the former multipulse train time reversed with a shifted phase $\Delta\Phi$. The last π-pulse reads out the respective single and double quantum coherences excited by the first block with the respective delay τ_{DQ}. As typical for relaxometry, intensity is measured only by the first point, when working at low field. The effective dipolar or pure double-quantum Hamilton operator $\hat{H}_{dip}^{ij}$ of the pulse sequence in terms of angular momentum operators $\hat{I}_q$ for two spins i, j is

$$\begin{aligned} \hat{H}_{dip}^{ij} &= \omega_D^{ij}\left(3\hat{I}_z^i\hat{I}_z^j - \hat{I}^i\hat{I}^j\right) \\ &= \omega_D^{ij}\left(3\hat{I}_x^i\hat{I}_x^j - \hat{I}_y^i\hat{I}_y^j\right) \\ &= \omega_D^{ij}\left(3\hat{I}_+^i\hat{I}_+^j - \hat{I}_-^i\hat{I}_-^j\right) \end{aligned} \tag{9.29}$$

Starting with initial z-magnetization, the $\frac{\pi_x}{2} - \tau_{DQ} - \frac{\pi_x}{2}$-element, being part of the BaBa-sequence (Figure 9.11, C) evolves according to product operator formalism as follows.

$$
\begin{aligned}
\hat{I}_z^i + \hat{I}_z^j \xrightarrow{\frac{\pi}{2}\hat{I}_y} \quad & \hat{I}_x^i + \hat{I}_x^j \\
\xrightarrow{\tau_{DQ}\hat{H}_{dip}^{ij}} \quad & \left(\hat{I}_x^i \hat{I}_x^j\right) \cos\phi_{DQ} \qquad + \left(2\hat{I}_y^i \hat{I}_z^j + 2\hat{I}_z^i \hat{I}_y^j\right) \sin\phi_{DQ} \\
\xrightarrow{\frac{\pi}{2}\hat{I}_y} \quad & -\left(\hat{I}_z^i \hat{I}_z^j\right) \cos\phi_{DQ} \qquad + \left(2\hat{I}_x^i \hat{I}_y^j + 2\hat{I}_y^i \hat{I}_x^j\right) \sin\phi_{DQ} \qquad (9.30) \\
= & -\left(\hat{I}_z^i + \hat{I}_z^j\right) \cos\phi_{DQ} \; - i\left(2\hat{I}_+^i \hat{I}_+^j + 2\hat{I}_-^i \hat{I}_-^j\right) \sin\phi_{DQ} \qquad (9.31)
\end{aligned}
$$

with the respective angular momentum components $\hat{I}_q$ and the phase $\phi_{DQ} = {}^3/_2\, \omega_{eff}\, \tau_{DQ}$. The last row Equation 9.31 can be deduced from the relation $\hat{I}_\pm = (\hat{I}_x^i \pm i\hat{I}_y^j)$ revealing the DQ coherence terms denoted by $\hat{I}_\pm$. At the end, the $\sin\phi_{DQ}$ and $\cos\phi_{DQ}$ terms contain DQ coherence and modulated longitudinal z-magnetization, respectively. By altering the phase in a 4 step manner by 90° ($\Delta\Phi = 0, {}^\pi/_2, \pi, {}^{3\pi}/_2$, *phase cycling*), the DQ coherences S_{DQ} and the SQ reference signals S_{ref} are accessible. The above treatment is valid for a pure Hamiltonian $\hat{H}_{dip}^{ij}$ acting on a single spin pair and neglects the situation in multispin systems. Here, the general non-commutativity of different pair operators $\hat{H}_{dip}^{ij}$ permits an analytical description and leads to unwanted dephasing effects for longer τ_{DQ}. However, the fourfold repeated pulse element in Figure 9.11 on page 153 is robust meaning it excites multiple quantum (MQ) coherences of even order (2n) at longer τ_{DQ} and thereby ensures an effective pure dipolar Hamiltonian $\hat{H}_{dip,eff}^{ij}$ allowing quantitative fitting strategies. For a deeper explanation of the phase cycle and coherence selection paths the author refers on the literature.[216]

9.4.3 Double quantum build-up

As stated above, the implemented modified Baum-Pines sequence yields two datasets, S_{DQ} and S_{ref}. S_{DQ} is much lower in intensity than S_{ref} because the probability for DQ transitions is lower than for SQ transitions. The DQ transition probability rises with time since more suitable *Eigenstates* are getting populated (see also Figure 9.10). However, S_{DQ} decreases again due to relaxation. Relaxation takes place already with the first transversal magnetization arising. This attenuation in networks caused by relaxation contributes nearly equally to S_{DQ} and the sum intensity.

$$S_{\Sigma MQ} = S_{DQ} + S_{ref} \qquad (9.32)$$

Consequently relaxation effects arising from other origins than segmental anisotropic motion (*e.g.* from molecular isotropic motion, see also section 9.3) on S_{DQ}

can be removed through point-by-point division to give S_{nDQ}, the *normalized* DQ intensity.

$$S_{\mathrm{nDQ}}(\tau_{DQ}) = S_{\mathrm{DQ}}(\tau_{DQ})/S_{\Sigma\mathrm{MQ}}(\tau_{DQ}) \tag{9.33}$$

The sum intensity $S_{\Sigma MQ}$ contains all excited quantum coherences and represents the total magnetization as a function of τ_{DQ}. Since the population of the spin states equalizes the longer the excitation takes place, for long times, magnetization is distributed equally and for $\tau_{DQ} \to \infty$

$$S_{\mathrm{DQ}} = S_{\mathrm{ref}} \quad . \tag{9.34}$$

From Equation 9.33 and Equation 9.34 follows that S_{nDQ} converges against $1/2$ for rising τ_{DQ}

$$S_{\mathrm{nDQ}} \xrightarrow{\tau_{DQ1} \uparrow} \frac{1}{2} \tag{9.35}$$

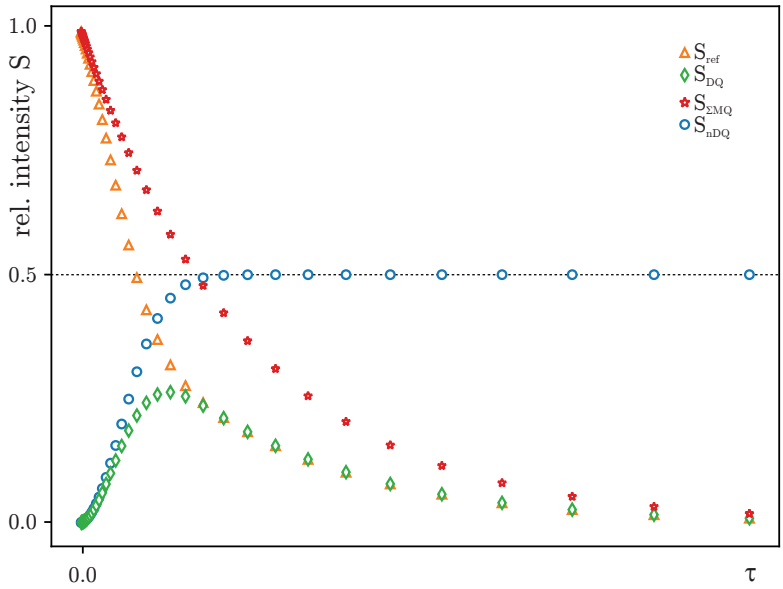

Figure 9.12: Schematic behavior of the normalized signal functions S_{ref}, S_{DQ}, the total magnetization $S_{\Sigma MQ}$ and the point-by-point-normalized DQ intensity S_{nDQ}.

9.5 Double Quantum Proton NMR with PEO-DA-35k

Only little is known about the factors that improve or worsen the properties of alignment media. It is for example not clear, if the alignment of guest molecules takes place at the network chains, or if network defects like loops and dangling ends induce the partial orientation of analytes. Since cross-linked PEO-DA is swelling in a broad range of solvents and mixtures, it represents a model system, where different polymerization and swelling conditions can be compared and characterized. Therefore, the above methodology was applied to covalently cross-linked PEO-DA-35k gels. Three common deuterated solvents, DMSO-d6, chloroform-d and deuterated water, were chosen to examine the network fractions when swollen to equilibrium. Furthermore the influence of the initial *monomer* concentration on the cross-linking degree was investigated with the four different mass concentrations (16, 20, 25 and 30%) established as alignment media.

To assess the sol fraction more quantitatively, a sample was polymerized with 20% α,ω-bisacrylated PEO (PEO-DA-35000) and 5% PEO as a known part of the network, unable to form any covalent cross-links. This approach is called *spiking* and is used to identify or quantify components *e. g* in metabolomics studies. For the initiator and the co-catalyst, the protocol for 25% (see Table 11.1) was applied.

9.5.1 Sample preparation

PEO-DA-35k was cross-linked in deionized water via free radical polymerization with APS and TEMED at the four established concentrations following the standard protocol from subsection 6.0.4 in a water bath at 40°C including the steps of degassing centrifuging and overlaying with argon.

For the measurements in D_2O, the educts were mixed in a precellis homogenizer (see Fig. 9.13) without beads (as a lockable container), whose inner diameter were adapted with a short teflon® tube of approximately 35 mm length to an inner diameter of 5.5 mm. The samples for swelling in DMSO-d_6 were also mixed in a precellis homogenizer adapted the same way with a cut teflon tube to an inner diameter of 6.0 mm. The polymerization mixtures for measurement in chloroform-d were prepared in 50 ml Falcon tubes (see also subsection 6.0.4) and drawn into teflon tubes of increasing diameters with a syringe. Vacuum degasification was applied to all mixtures 3 times in the precellis and the Falcon tubes and afterwards they were covered with Argon. Mixing was performed on a vortexer and defoaming was achieved for the precellis samples by centrifuging 1 minute at 12000 rounds per minute and for the falcon tubes by centrifuging 1 minute at 6000 rounds per minute. The polymerization then was carried out in a water bath at 40°C.

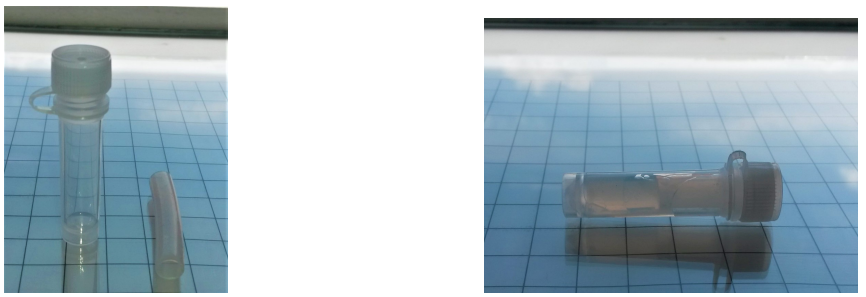

(a) **(b)**

Figure 9.13: Empty Precellis homogenizer and cut teflon® tube (a). With cross-linked PEO-DA-35k gel (b).

After 16 hours the polymerized gel sticks were removed from their molds and weight, length and diameter were measured (Figure 9.14a). The covalently cross-linked PEO-DA-35k gel sticks for D_2O and DMSO-d_6 were placed upright in open top-screw 10 ml vials and dried at 40° for another 3 days in an exsiccator at 40°C over calciumchloride ($CaCl_2$) (Figure 9.14b) and the sticks for chloroform-d were dried upright in open 2 ml glass vials (Figure 9.14d). After weighing them and measuring length and diameter of the dry state, the sticks were put into the sample tubes with an initial amount of solvent, covering more than half of the sticks. Then swelling solvent was added gradually until supernatant liquid remained while monitoring the progressing swelling degree with a marking line. After swelling to equilibrium, weight, length and diameter were measured and afterwards the non-cylindrical, conic tips stemming from the Precellis homogenizers were cut off, to yield cylindrically shaped gel sticks (Figure 9.14c). The samples in D_2O and DMSO-d_6 were closed with a rubber plug to prevent evaporation, while the samples with chloroform-d as swelling agent were sealed with PVC lids and teflon®

tape until equilibration and finally fused. The measurement of PEO-DA-35k-gels swollen in chloroform was carried out by cutting each to the same length within three fused standard NMR tubes at once with an inner diameter of 4.2 mm and PEO-DA-35k sticks of the same length.

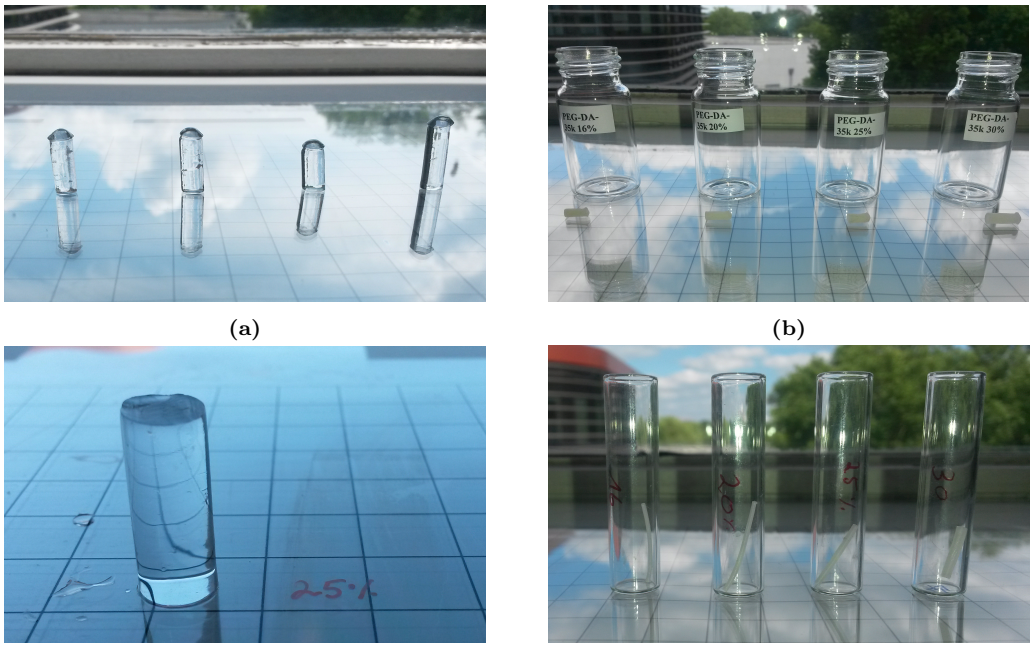

Figure 9.14: PEO-DA-35k gel: after polymerization (a), after drying (b), equilibrated and cut in D_2O (c). Dried Sticks for swelling in chloroform (d).

Since the DQ built-up is mediated via segmental averaged dipolar couplings and reflects all anisotropic motion, care was taken that the swollen samples under investigation were in an unstressed isotropic state to avoid additional contributions from aligned chains tampering the real proportions between cross-linked chains and defects. For this reason the swelling degree was taken into account, to arrange the covalently cross-linked PEO-DA-35k sticks with swollen diameters just below the inner diameter of 8 mm within the tube. This way four sets of cross-linked PEO-DA-35000 (polymerized with mass contents of 16, 20, 25 and 30%(w/w) of PEO-DA-35000) were swollen to equilibrium in $CDCl_3$, D_2O and deuterated DMSO with diameters below 8 mm (see also Figure 9.14c). To *spike* the polymer sol fraction (C) a sample was cross-linked with a composition of 20% PEO-DA and 5% of PEO as a known component, not able to form any cross-links. Because the PEO-DA cross-linking takes place in water, and is washed and dried for application with other solvents, only for water a spiking sample was realized, omitting the washing step. This way 13 samples were created (see also Figure 9.19).

9.5.2 Low field NMR experiments

The ^{1}H-DQ-NMR, saturation recovery and CPMG experiments of the swollen gels were carried out on the low-field device *Bruker the minispec mq20* from Bruker. The field strength of $\vec{B}_0$ is approximately 0.47 T and the proton resonance frequency ν_0 accordingly at 20 MHz. The measurement parameters of the DQ pulse sequence and the DQ build-up curve are decisive for the duration of the entire measurement. Based on the selected parameters, the resulting measuring time was approximately 42 hours for the DQ experiment. The long time to measure the DQ build-up curves S_{DQ} and S_{Ref} arose from the high number of scans (512) needed to gain reasonable S/N for the low polymer concentrations in the swollen gels.

The high solvent proportion furthermore led to long relaxation times compared to polymer melts and solids and the number of points had to be adapted accordingly. In Table 11.6 the parameter set applied for all samples presented are summed up.

9.5.3 Adaptation of the fitting procedure

In the following, the adaption of the fitting procedure is described. Two main approaches to fit the curves and to extract S_{nDQ} have been applied: The figures are normed to the maximum, which should be represented by the first point of S_{ref} and than either exponential fits are carried out, or mono-exponential decays are approximated step wise and subtracted.[210,217] In the case of all the gels, signal to noise was low and long incremental times up to 500 ms had to be measured, recording 512 points per time step (resulting in an experimental duration of about 42 h). Despite the high amount of points per increment noisy curves were obtained. For this reason the simple exponential fitting method failed. Step wise manual fitting led to too many dis-ambiguities about where to choose the start and which points are valid. Many tryouts did not lead S_{nDQ} to converge against $1/2$.

As an example, the normed data for the 16% PEO-DA gel is shown in see Figure 9.12. Even though, S_{ref} can be fit with a tri-exponential decay resulting in a correlation of R bigger than 0.998, the factors for A (≈ 0.56), B (≈ 0.25), and C (≈ 0.15), cannot explain the whole composition leaving a uncertainty of the network fractions of about 0.1. Because of this and the problem to identify fitting intervals within very noisy and distorted regions, step wise fitting of S_{ref} to create S_{red} led to very variable results within a single measurement and prevented physically sound values that could be compared among the samples.

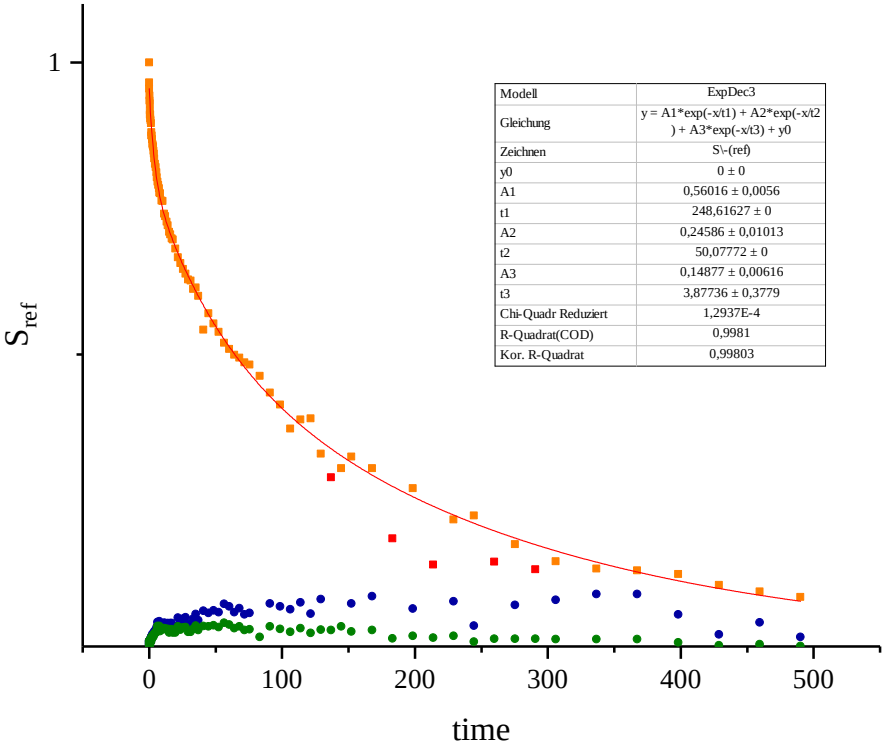

Figure 9.15: Recorded relaxation of S_{ref} (orange) and DQ-build up curve (green) with no corrections and tri-exponential fit for the PEO-DA35000-16% gel in water. The points marked in red were excluded from the fitting. Since the fluctuations appeared in all experiments and their origin is most probably arising from electronic circuits and the electricity net static.

9.5.4 Development of a robust fitting procedure

As a new fitting strategy to process the available data as good as possible, the region of S_{DQ} short after the maximum was taken into account. Since it has to converge against $1/2$, a difference term that helps to find a reduced reference S_{red} could be fit bi-exponentially. The assumption is that S_{red} contains all the sol (C) and defect fractions (B) (the so-called *tail*), and can then be differentiated from the signal build-up induced by the network fractions with the lowest mobility. This represents the fraction (A) of the cross-linked chains. Then the curves of S_{DQ} were fit mono-exponentially after the maximum resulting in the respective curves S_{DQ-fit} (see Figure 9.16).

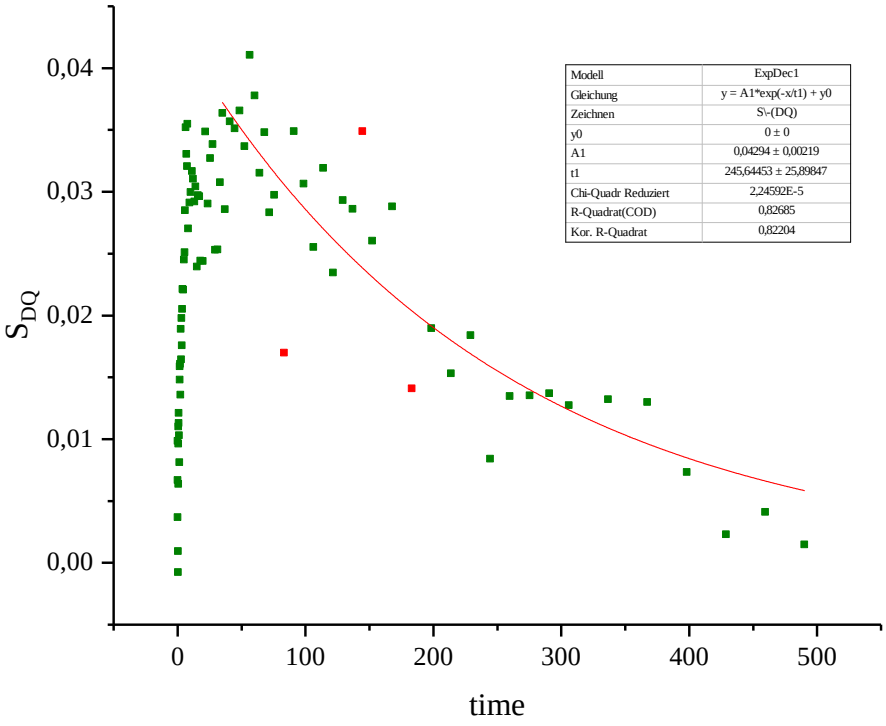

Figure 9.16: Monoexponential fitting after the maximum of S_{DQ}.

This exponentially decaying curve (in Figure 9.16) is subtracted from S_{ref}, resulting in the reduced decay S_{red} that can now be bi-exponentially fit to obtain the (*sum* of) network fractions B and C. Since this part of the curve has a low signal to noise ratio, a much lower correlation factor is obtained. In Figure 9.17 the resulting curve for the example of a PEO-DA35000-16% gel is plotted and the mono-exponential fit has a correlation R of only 0.8. Because of this, care needs to be taken, when interpreting the later created curve S_{red} concerning the fractions B and C (the sol and defect fractions within the gel network).

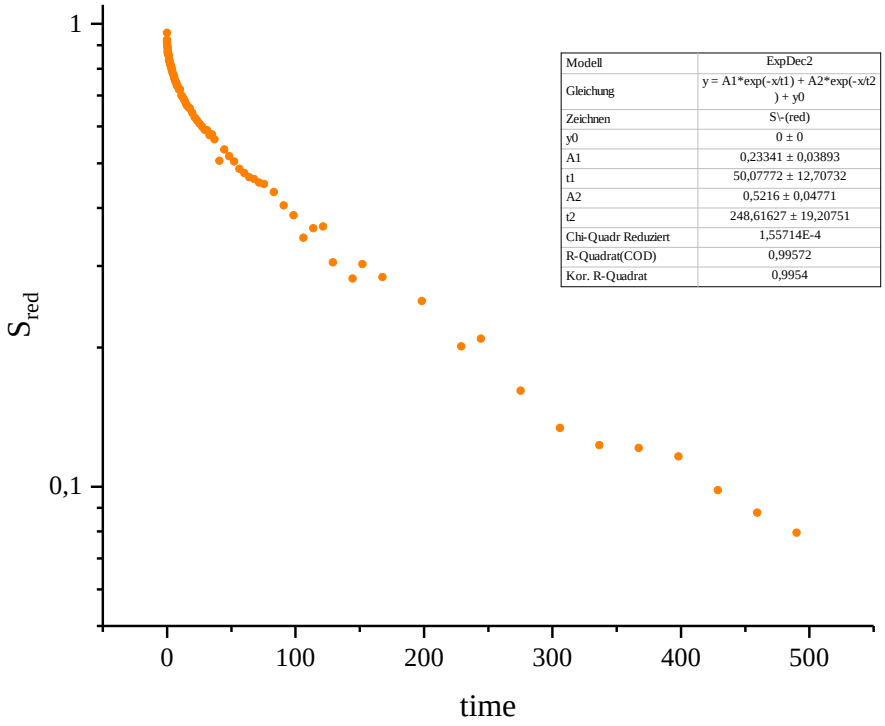

Figure 9.17: Resulting reduced decay curve for the fitting of PEO-DA35000-16%. The red points were excluded from the fitting.

Evaluation of Equation 9.33 is then adapted to

$$S_{\mathrm{nDQ}}(\tau_{DQ}) = \frac{S_{\mathrm{DQ}}(\tau_{DQ})}{S_{red}(\tau_{DQ}) + S_{DQ}(\tau_{DQ})} \tag{9.36}$$

The resulting curve of $S_{nDQ,fit}$ is compared in Figure 9.18 with the curve of S_{nDQ} (black) shown in Figure 9.15, showing the corrected curve (blue) converging against $1/2$. The results for all testes samples are presented in subsection 9.5.5.

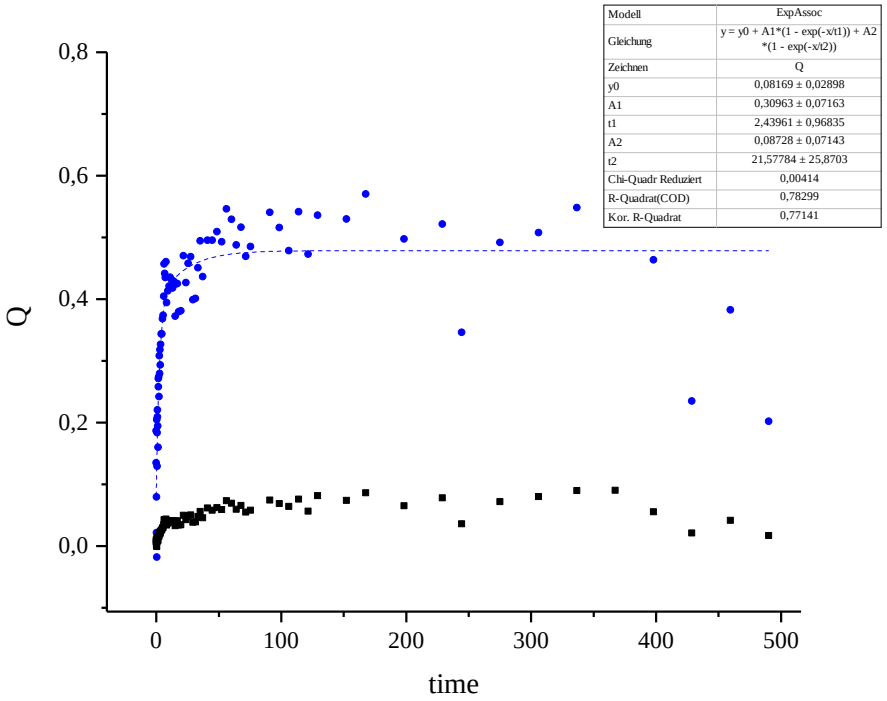

Figure 9.18: After the fitting procedure described above, $S_{nDQ,fit}$ (blue) converges against 1/2 despite a poor signal to noise ratio.

9.5.5 Results

In the following the network fractions evaluated with the adapted method for the fitting procedure in PEO-DA from the measurements described in subsection 9.5.2 are summarized in the bar plots of Figure 9.19.

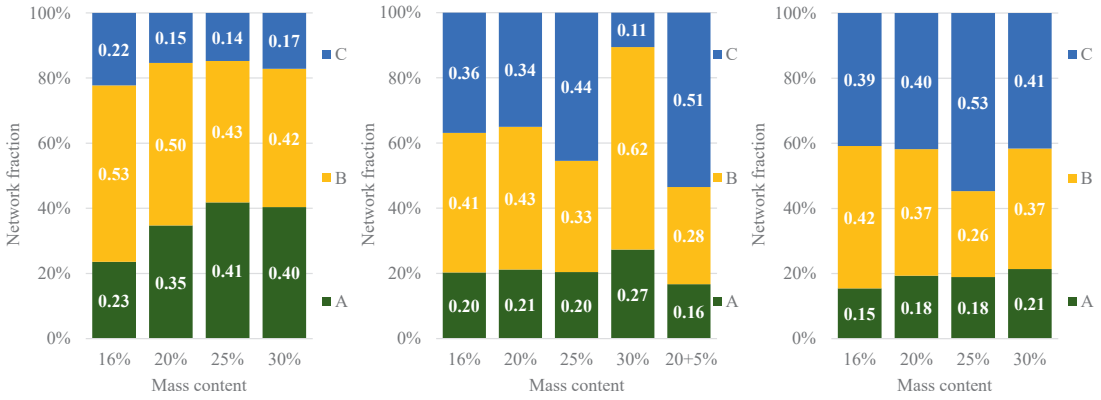

(a) DMSO-d_6 **(b)** D_2O **(c)** Chloroform-d

Figure 9.19: Evaluated network fractions of the swollen PEO-DA gels in DMSO-d_6, D_2O and chloroform-d. The bars are normed to 100%, the numbers inside present the absolute fitted values.

Only in DMSO-d_6, a significant increase of the derived network fraction A (green) is observed, rising from 23% to 40% depending on the initial mass content during the cross-linking. For deuterated water and chloroform-d, the trend (Figure 9.19a) is less pronounced or cannot be validated. Here, the fraction of cross-linked chains remains around 20%. The stronger slope for DMSO-d_6 can be explained with the lower swelling degree. Lower swelling degree means that the chains are not as elongated and much more entangled also due to the lower amount of *solvent* leading to a bigger value for network fraction A. To maintain a larger diameter, a higher absolute amount of PEO-DA was used and the diameters of the gel sticks were adapted accordingly. This effect also leads to better signal to noise ratios for the measurements taken in DMSO-d_6. An interesting outcome is the evaluated network fraction A for the 20% sample, spiked with 5% PEO (20+5%) as a known component within the network.

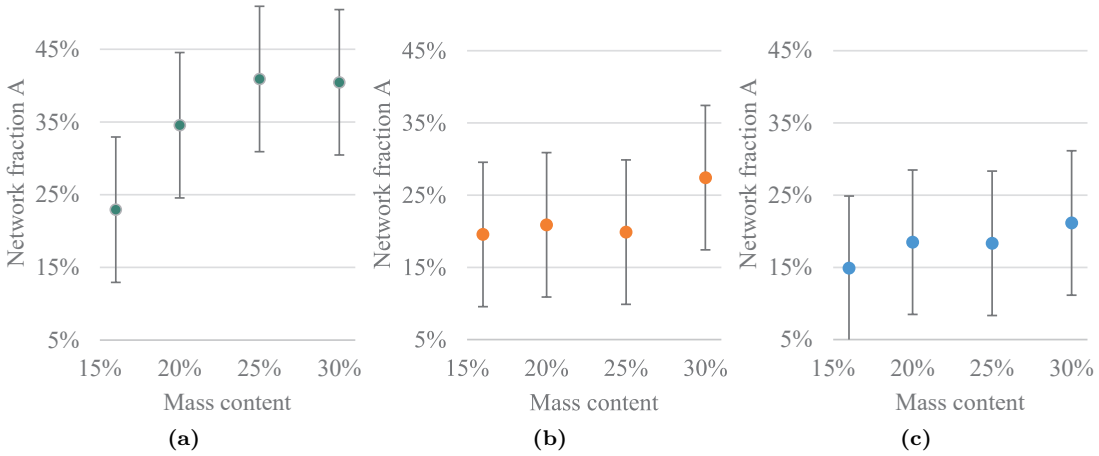

Figure 9.20: Comparison of the network fraction A.The highest network cross-linked network fractions are observed with DMSO-d_6 and an apparent rise of the cross-linked fraction is visible. Nevertheless, the data was very noisy and between 100 and 400 ms strong distortions occured. The error therefore is assumed to be 10%.

The *thinned* composition of 20% PEO-DA35000 blended with 5% of PEO, bearing no cross-linkable groups shows the lowest value for the network fraction A. This is related to a less efficient polymerization induced through non-reacting chains, hindering the propagation of the formed radicals and decreasing the amount of the cross-linked network fraction. The higher swelling degree in water and chloroform enables the polymer chains to unfold while dangling ends are less hindered through entanglements.

10 | Summary

The importance of the results achieved within this work could be briefly put together in the following: major point was the development of a universal alignment medium for the extraction of RDCs and structure elucidation with tensorial constraints. After a short introduction of the standard NMR parameters, the benefits of anisotropic NMR parameters were introduced and explained (chapter 4). An important point was the introduction of the experiments carried out to monitor and measure aligned samples. The best achievements with the use of anisotropic parameters are reached, when all possible methods and media to induce the necessary partial alignment are followed and the benefits of the respective methods and media are taken into account. Therefore in chapter 5 an extensive review of the existing approaches with the their different advantages and obstacles were presented before the reader could be introduced to the development of PEO-DA. As PEO-DA works in combinations with a number of different solvents, this alignment medium could be used as a universal alignment medium and its preparation was evaluated in chapter 6 together with all considerations and measures taken, to produce homogeneous polymer sticks. The resulting alignment media sticks were tested in chapter 7 and their universal application was proven with the extraction of RDCs from 5 different test molecules of various sizes using pure solvents and mixtures covering different polarities. In chapter 8, a fundamentally new type of orientationally constrained molecular dynamic simulations (MDOC) as implemented in the program COSMOS was thoroughly tested and evaluated. This approach was used within this thesis with the falsification of three examples (borneol, staurosporine and spiroindene) and the accuracy of the simulations was controlled. The workflow is significantly improved by generating scripts for the parallel execution on a high computational power cluster and for the evaluation of the obtained data. The understanding of the network composition of the derived alignment media gels plays a crucial role for the further improvements of the alignment media as the knowledge of the best network composition would allow targeted synthesis of desired polymer networks. This knowledge is gained by applying low field DQ-NMR experiments to a selected set of PEO-DA swollen sticks in three common solvents as described in chapter 9.

The literature sources presently available demonstrate that the common alignment media are rather restricted for application with small organic molecules or big macromolecules, and could be used with a narrow range of particular solvents. Earlier developed cross-linked PEO gels were reported to show remarkable swelling in solvents ranging from polar ones, like water, to very apolar ones, like toluene, however, had an extremely low practical application due to the inconvenient methods for synthesis by irradiation with β-, γ- or UV-rays. To overcome these problems and allow the use of the swelling benefits of PEO based alignment media, such a synthesis route was chosen that the end groups of PEO are diacrylated with acryloyl chloride and cross-linking was performed via thermally and photochemically induced free radical polymerization. Two molecular weights (6000 and 35000 g/mol) of PEO with low dispersities were used as educts, giving the opportunity, to create a network with known inter-cross-link distances. No additional cross-linking agents were used to have as little as possible background signals in the later spectra induced by the proton and carbon-13 nuclei of the medium.

To establish reproducible casting of cylindrical cross-linked PEO-DA gels in varying diameters five different formulations were developed regarding working life and handling under low oxygen conditions. Since the reactions were carried out in quantities between 50 mg and 2 g, it turned out to be most effective, to use a setup of connected syringes and teflon® tubes to lose as little as possible material and to have the desired variability in the diameters. This enabled the adaption for the different strategies to scale the alignment (Figure 5.2) and thus to get the predefine swelling of the initial dry stick for the various solvents. In order to reach this stage the swelling properties of these different formulations were investigated in a big set of solvents and mixtures. Additionally the applicability in the common devices: so-called stretching and compression devices was succesfully tested, while defining the most suitable conditions. A desired property of this alignment media is the naturally limited dispersity within the polymer yielding quite homogeneous gels with narrow line-widths. Different mass containing swollen PEO-DA gels are therefore investigated with DQ-NMR experiments to reveal the amounts of cross-linked network fractions and the sol fraction.

Within this thesis it was proven that PEO-DA allows inducing scalable anisotropy both in compressing as well as in stretching devices. A major contribution is the successful application to pure solvents and mixtures. Furthermore a method is introduced which allows fast equilibration and transfer into the sample tubes, speeding significantly up the sample preparation time and thus giving the opportunity to apply the method in a more industrialized environments. In accordance with parameter fine-tuning, cross-linked PEO-DA is shown to be suitable for the alignment of solutes reaching from small natural products up to proteins, mak-

ing it a universal alignment medium and making it one of the most advantageous alignment media currently available.

The standard workflow as an existing method of extraction of RDCs relies on manual procedure, which is time-consuming and quite subjective as it relies on the experience of the person performing the manual extraction steps. In order to remove the subjectivity and speed up the extraction procedure a method for the semi-automated extraction of couplings is introduced, utilizing an fitting method based on autocorrelation.

Typically the RDCs data is used for structure evaluation where the most commonly used approached relies on a predefined model and having certain approximations for its validity. Mostly these approaches are not applicable or are prone to huge errors when the molecule under investigation is flexible or shows some degree of flexibility. Within this work the RDC data evaluation on small organic molecules used the so-called MDOC approach, which does not require a predefined model conformation. It enables the elucidation of the conformational space based on experimentally derived anisotropic experimental data that is incorporated as tensorial constraints into the force field. When solute molecules show flexibility and occur in different conformations, data interpretation with so far existing approaches mostly fail because of the averaged nature of extracted data. The MDOC approach is preferred as the RDC evaluation is not hampered based on the modeling of choice and the implementation of the simulation allows the system to forget previous states (i.e. conformations) and freely samples potential other states which on average fulfill the experimental data. Thus, the presence of different conformations within the according NMR timescales are revealed. Within this thesis the optimization of the performance of these relatively exotic molecular dynamics simulations was performed and the applicability of the approach was proven.

In the last chapter, DQ measurements were carried out with PEO-DA gels. They contain a lot of solvent and therefore non-deuterated impurities need to be filtered out for reliable results. A further obstacle was the appearance of strong fluctuations above 100 ms in combination with a low signal to noise ratio. Based on the known fitting procedures reported in the literature, a variant was developed that lacks the ability to differentiate network fraction B and C, but reproducibly retains the fraction of main interest, the part of chains being cross-linked forming the network. Besides, a spiking approach was suggested and applied, offering to add a known component. This way, the limits of low field NMR have been extended for the application of low concentrated polymer gels.

Although the parts of this work belong to quite different areas of chemistry, the knowledge from polymerchemistry, structural elucidation, NMR spectroscopy and computational chemistry was bundled. The synergies led to an improvement of the whole methodology of applying anisotropic NMR parameters in terms of a

simple production route, the fast preparation of samples and their measurement, and a workflow established for the quick evaluation of the results, creating the basis for a broader application in an academic and industrial context.

11 | Appendix

11.1 Supplemental material for chapter 6

11.1.1 Dispersity evaluation

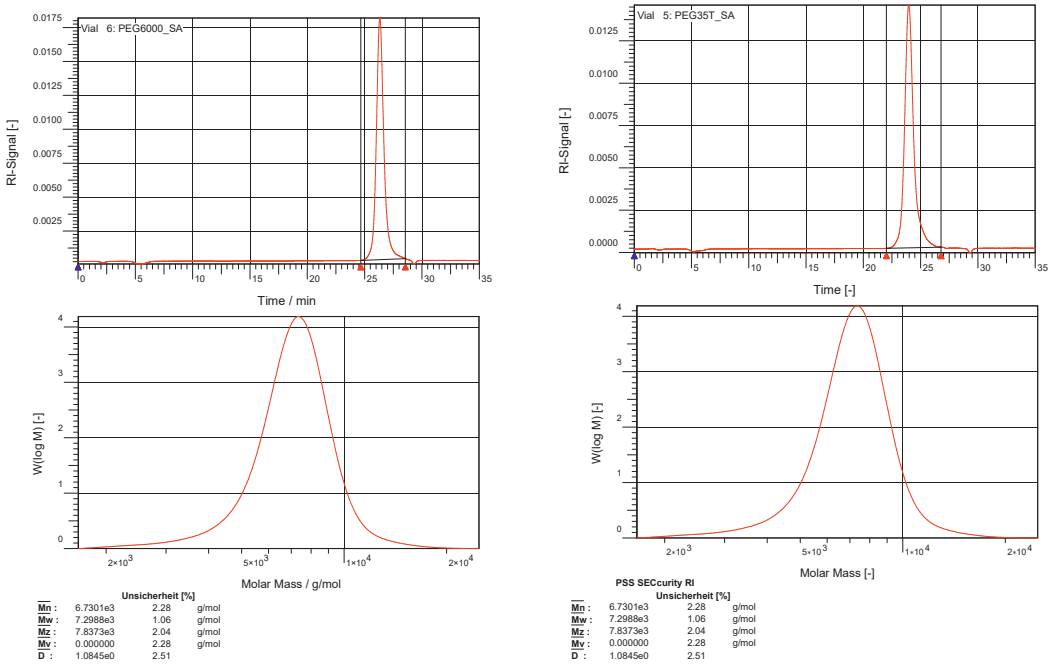

(a) **(b)**

Figure 11.1: Measurement of the distribution of mass weights in commercially available PEO-6000 and PEO-35000 with size exclusion chromatography (SEC). Both educts resemble the dispersity given from the supplier.

11.1.2 Cross-linking

Table 11.1: Cross-linking studies for the development of a reproducible polymerization protocol to derive homogeneous cross-linked PEO-DA 35000 polymer sticks. The final trials (no. 45 to 48 in green) are the ones established for cross-linking and casting cylindrical polymer gels for the use as alignment media.

#	%(w/w)	m(PEO-DA 35k) /g	V(H_2O) /ml	V(TEMED, 10%)/µl	V(APS, 10%)/µl	T	mold	remarks
1	0.385	0.237	0.378	1.0	5.0	RT	glass tube	too viscous
2	0.375	0.152	0.253	1.3	6.7	RT	glass tube	too viscous
3	0.379	0.231	0.378	1.0	5.0	RT	glass tube	too viscous
4	0.233	0.152	0.500	1.5	7.5	RT	glass tube	hardened after max 2h
5	0.230	0.105	0.351	0.5	2.5	RT	glass tube	not hardened in teflon®
6a	0.222	0.100	0.350	0.8	3.8	RT	glass tube	non-hardened layer on top
6b	0.379	0.231	0.378	1.0	5.0	RT	glass tube	very viscous, foam
6c	0.233	0.152	0.500	1.5	7.5	RT	glass tube	hardened
NMR-glasstube, 4mm								
7	0.266	0.204	0.564	1.5	6.0	70°C	NMR tube	hardened after heating, formation of bubbles, yellowish, dried @ 4°C
8	0.279	0.194	0.500	1.5	6.0	RT	NMR tube	hardened the next day, yellowish, broke into 2 parts, dried @ 4°C
9	0.171	0.206	1.000	1.5	6.0	RT	NMR tube	increased water ratio to prevail yellowing, degassing of reaction mixture, dried @ 4°C
teflon® tube (for varying diameters)								
9a	0.191	0.137	0.583	0.5	1.0	40°C	teflon®	not hardened
10	0.176	0.106	0.498	2.0	8.0	40°C	teflon®	hardened after heating to 70°C, yellowish
11	0.176	0.107	0.500	10.0	10.0	RT	teflon®	hardened
12	0.300	0.109	0.255	10.0	10.0	RT	teflon®	too fast polymerization
13	0.238	0.094	0.301	8.0	8.0	40°C	teflon®	hardened
14	0.256	0.102	0.298	8.0	8.0	40°C	teflon®	hardened after at least 2 h
14a	0.250	0.250	0.750	20.0	15.0		NMR-Tube	too fast polymerization, impossible to transfer into NMR-tube
14b	0.250	0.152	0.456	4.0	4.0	40°C	NMR-Tube	hardened after at least 2 h
15	0.251	0.252	0.750	4.0	4.0	40°C	NMR-Tube	hardened after 1 h
16	0.251	0.251	0.750	3.0	3.0	40°C	NMR-Tube	hardened after 10 min
TEMED 5% /µl								
17	0.254	0.255	0.750	6.0	4	40°C	NMR-Tube	hardened after 1h
18	0.250	0.250	0.750	3.0	3	40°C	NMR-Tube	hardened after 1h
19	0.250	0.250	0.750	2.0	2	40°C	NMR-Tube	hardened after 1h
TEMED 1% /µl								

Table 11.1: Cross-linking studies for the development of a reproducible polymerization protocol to derive homogeneous cross-linked PEO-DA 35000 polymer sticks. The final trials (no. 45 to 48 in green) are the ones established for cross-linking and casting cylindrical polymer gels for the use as alignment media.

#	%(w/w)	m(PEO-DA 35k) /g	V(H_2O) /ml	V(TEMED, 10%)/µl	V(APS, 10%)/µl	T	mold	remarks
25	0.250	0.250	0.750	2.0	2.0	40°C	NMR-Tube	not hardened after 1h @ 40°C and additional 1h @ 70°C, overnight @40°C: hardened, upper layer liquid.
26	0.253	0.254	0.750	6.0	6.0	40°C	NMR-Tube	next day hardened, upper layer liquid
27	0.251	0.251	0.751	8.0	8.0	40°C	NMR-Tube	hardened after 40 min
27b	0.251	0.177	0.528	5.6	5.6	40°C	teflon®	not hardened! Double amount of APS/TEMED for next trial
28	0.254	0.179	0.525	11.2	11.2	40°C	teflon®	hardened, but very slow. "Worm" within half of the tube I, 90% in tube II liquid.
37	0.200	0.200	0.800	10.0	10.0	40°C	NMR-Tube	1d
38	0.251	0.251	0.750	10.0	10.0	40°C	NMR-Tube	1d
39	0.302	0.303	0.700	10.0	10.0	40°C	NMR-Tube	1d
43	0.376	0.244	0.400	200.0	50.0	40°C	teflon®	1h
45	0.160	0.060	0.264	18.0	18.0	40°C	teflon®	15 min
46	0.200	0.075	0.263	18.8	18.8	40°C	teflon®	15 min
47	0.250	0.100	0.260	20.0	20.0	40°C	teflon®	15 min
48	0.300	0.129	0.257	21.4	21.4	40°C	teflon®	15 min

11.1.3 Solvent compatibility

Swelling tests with selected mixtures

Table 11.2: Resulting swelling behavior of PEO-DA gels cross-linked with a mass content of 16% and swollen to equilibrium in selected mixtures. The factors Q_V and Q_m correspond to the volume increase (V) and the mass increase (m). In the first column the number of the stick and its state (d=dry, s=swollen) are given.

#	solvent mixture	l/cm	d/cm	m [g]	V/ml	Q_V	Q_m	Δ V/ml	V/ml	Q_V (m/ρ)	Q_m/ρ	ρ g/ml
1d	-	0.79	0.145	0.0147	0.013	1.0	1.00		0.013	1		
1s	Acetone H2O 1:1	2.42	0.450	0.3889	0.385	**29.7**	26.46	0.372	0.429	**33.1**	29.15	0.91
2d	-	0.72	0.145	0.0140	0.012	1.0	0.95		0.012	1.0		
2s	MeCN H2O 1:1	2.30	0.440	0.3480	0.350	**29.4**	23.67	0.338	0.382	**32.2**	26.01	0.91
3d	-	0.72	0.150	0.0140	0.013	1.0	0.95		0.013	1.0		
3s	C_6H_6 $CHCl_3$ 1:9	2.54	0.500	0.7100	0.499	**39.5**	48.30	0.486	0.526	**41.6**	35.79	1.35
4d	-	0.72	0.150	0.0140	0.013	1.0	0.95		0.013	1.0		
4s	$CHCl_3$ MeOH 7:3	2.55	0.505	0.6800	0.511	**40.4**	46.26	0.498	0.500	**39.6**	34.01	1.36
5d	-	0.76	0.150	0.0150	0.013	1.0	1.02		0.013	1.0		
5s	DMF H2O 1:1	2.34	0.455	0.3933	0.380	**28.3**	26.76	0.367	0.357	**26.6**	24.28	1.10
6d	-	0.76	0.145	0.0148	0.013	1.0	1.01		0.013	1.0		
6s	DMSO H_2O 1:1	2.20	0.420	0.3370	0.305	**24.3**	22.93	0.292	0.319	**25.4**	21.68	1.06
7d	-	0.77	0.150	0.0148	0.014	1.0	1.01		0.014	1.0		
7s	EtOH Cyclohex-ane	1.45	0.280	0.0662	0.089	**6.6**	4.50	0.076	0.089	**6.6**	6.04	0.75
7d	-	0.77	0.150	0.0148	0.014	1.0	1.01		0.014	1.0		
7s	EtOH Cyclo-hexane @40°C	2.05	0.380	0.1640	0.232	**17.2**	11.16	0.219	0.230	**17.0**	15.67	0.71
8d	-	0.75	0.145	0.0148	0.012	1.0	1.01		0.012	1.0		
8s	MeOH H_2O	2.38	0.455	0.4100	0.387	**31.5**	27.89	0.375	0.448	**36.4**	30.45	0.92
9d	-	0.75	0.145	0.0154	0.012	1.0	1.05		0.012	1.0		
9s	TFE H2O	2.00	0.400	0.2860	0.251	**20.4**	19.46	0.239	0.241	**19.6**	16.40	1.19
7d	-	0.77	0.150	0.0148	0.014	1.0	1.01		0.014	1.0		
7s	EtOH Cyclo-hexane @40°C	2.05	0.380	0.1640	0.232	**17.2**	11.16	0.219	0.230	**17.0**	15.67	0.71

Second virial coefficients and relative mass increase factors

Solvent	$\mathbf{Q_m}$	$\mathbf{B_2}$ [a]	**T°**	**Ref**
1,4-Dioxane	18.96	-1190	25.0	[218,219]
TFE	76.03	-1155	25.0	[219,220]
Acetone	8.21	-2016	25.0	[221]
Acetonitrile	11.59	-3902	25.0	[221]
Chloroform	35.67	-1093	25.0	[221]
DCM	29.24	-872	25.0	[221]
DMSO	16.21	-6900	25.0	[219,222]
Ethanol	11.92	-3166	25.0	[221]
Methanol	10.99	-1698	25.0	[221]
DMF	14.37	-2165	25.0	[219]
THF	18.53	-1310	28.7	[223]
Toluol	10.59	-2567	30.0	[224]
Water	18.39	-1062	25.0	[225]

Table 11.3: [2nd] Virial coefficients B_2 in cm^3/mol at given temperatures °C with references and relative mass swelling factors Q_m of the respective solvents.

11.1.4 Quadrupolar splittings of step-wise compressed and stretched gel

l_0 / cm	l / mm	Ξ	$\Delta\nu_Q$
compressing device			
8.2	6.1	-0.26	-14.5
8.2	6.2	-0.24	-14.5
8.2	6.3	-0.23	-13.6
8.2	6.5	-0.21	-12.3
8.2	6.7	-0.18	-11.3
8.2	7	-0.15	-8.4
8.2	7	-0.15	-8.4
8.2	7.3	-0.11	-6.5
8.2	8.2	0.00	0.9
stretching device			
7.1	7.8	0.10	13.5
7.1	8.5	0.20	25.9
7.1	9.6	0.35	35.8
7.1	11	0.55	51.8
7.1	11	0.55	52.0
7.1	11	0.55	51.4
7.1	13.5	0.90	82.5
7.1	8	0.13	16.8

Table 11.4

11.2 Supplemental material for chapter 7

11.2.1 Python script for the semi-automatic extraction of couplings

```
# -*- coding: utf-8 -*-
"""
Autocorrelate 1D ASCII files that were created from rows or coloumns from 2D
coupled spectra to measure couplings.(use topspin command: "totxt")

written by Thomas Gloge at the AK Luy @ KIT
mailto: thomas.gloge@gmail.com
07/2017

"""
import numpy as np
import matplotlib.pyplot as plt
```

```
from matplotlib import rcParams

plt.close()
""" set up color scheme, fonts """
colormap = ['#1f77b4', '#ff7f0e', '#2ca02c', '#d62728', '#9467bd',
'#8c564b', '#e377c2', '#7f7f7f', '#bcbd22', '#17becf']

plt.rc('text', usetex=True )
plt.rc('font', family='dejavuserif', weight='normal', size=9)
plt.rcParams['mathtext.fontset'] = 'dejavuserif'

""" read data file (ASCCII-file export of row/coloumn from Topspin via the command
     "totext" -> row 3038) """

filename = "C:/Users/3038"


f = open(filename)
data = np.loadtxt(filename)
f.close()

# noise generator for evaluation
#noise = np.random.normal(0, 0.25, data.shape)

#data = data * (1+noise)
#data[1000:] = signal [1000:]

# remove noise and data below a threshold
#data[np.absolute(data) < 1000000] = 0
#data = np.clip(data, avdata, maxdata)

# more data manipulation
#data[data<200000]=0
#data = np.sqrt(data)
#data[np.absolute(data) <0.2*1e7] = 0
#data[1000:1315] = 0
#data[:500] = 0
#data[1750:]=0
#data[np.absolute(data) < 2000000] = 0
#data = np.square(data)

""" set up resolution in Hz/Point to convert point to Hz
needs to be set manually!!!"""
#res=2.017691
res=0.183179

""" get length N of data """
N = len(data)

""" get absolute values of data """
adata = np.absolute(data)
""" primitive searching of min and max peaks and their indices """

sortval = np.sort(data)
rawminval = sortval[0]  #Minimum value
rawmaxval = sortval[-1] #MAximum value


""" find max value for normalisation """
if np.abs(rawminval) < np.abs(rawmaxval):
normmax = np.abs(rawmaxval)
else:
```

```
normmax = np.abs(rawminval)


rawminindex = np.where(data==rawminval) #index therof as tuple
rawmaxindex = np.where(data==normmax)   #index therof


rawmaxindex=rawmaxindex[0][0]           #index therof as number
rawminindex=rawminindex[0][0]

#primitive distance from peakdifference
rawcoup = (rawmaxindex - rawminindex)*res
#convert to text
rawcoup= r"$\Delta\nu_{D}^{extr}$:␣"+"{:.{}f}".format( rawcoup, 2 )+"Hz"

""" prepare normed data """
ndata=0.5*data/data[rawmaxindex]  #normed data

""" prepare frequency scale from 0 to N"""
scale=np.arange(N)
scale=scale*res

""" set up first plot of raw data with point scale to search noise"""
plt.subplot(311)

plt.ylabel(r'rel.␣intensity')
plt.xlabel(r'$\nu$␣[Hz]')
plt.plot(ndata, color = '0.3')
plt.grid(True)

""" calculate 3*std from selected region in normed data
needs to be set manually !!! """
SD = 3*(np.std(ndata[0:40]))

""" start processing of data: convert to absolute values """
data = np.absolute(data)                #/data[rawmaxindex]
""" absolute normed data """
adata = data /data[rawmaxindex]

"""---autocorrelation-----------------"""
"""   ft data and process data = pdata """
pdata = np.fft.ifft(data, n=2*N)
"""  multiply with complex conjugate -> ft(data)* ck(data)"""
pdata = pdata * np.conjugate( pdata )
"""  inverse ft -> ift(ft(data) * ck(data)) """
pdata = np.fft.ifft( pdata )
"" "␣␣cut␣data␣to␣N␣points␣␣"""
pdata = pdata[:N]
"""  remove imaginary """
pdata = np.real( pdata )

""" set starting point from where Maximum/Minimum is searched (to exclude main
maximum @ tau=0), needs to be set manually !!! """
x=80

""" norm maximum by first point for relative intensity"""
pdata = pdata / pdata[0]
""" get max or min """
min = np.min(pdata)
max = np.max(pdata[x:])

#find index of biggest autocorelation value , call it indexmax
```

```
indexmax=np.argmax(pdata[x:])
#add threshold x to recreate original index
indexmax=indexmax+x

""" evaluate correlation from max value at second maximum = F(0)/2 if R=1 """
ratio = pdata[indexmax]*2

#assign coupling value from index
coupling=indexmax*res
""" set up second plot to show processed data with frequency scale"""
plt.subplot(312)
plt.ylabel(r'rel.␣intensity')
plt.xlabel(r'$\nu$␣[Hz]')
plt.plot(scale, adata, color= colormap[2])
plt.grid(True)

""" add difference from extrema """
plt.annotate( rawcoup , xy=(indexmax*res, max),  xycoords='data', xytext=(0.55,
0.66), textcoords='axes␣fraction',
horizontalalignment='center', verticalalignment='top')
plt.annotate(s='', xy=(rawmaxindex*res,0.5 ), xytext=(rawminindex*res,0.5),
arrowprops=dict(arrowstyle='<|-|>',linestyle ='--', lw=1,
color='r'))


middle =((rawmaxindex*res)+(rawminindex*res))/2
""" add couplings from autocorrelation """
plt.annotate(s='', xy=((indexmax/2*res+middle),0.18 ),
xytext=((middle-indexmax/2*res),0.18),  arrowprops=dict(arrowstyle
='<|-|>',linestyle ='--',lw=1, color=colormap[0]))

""" evaluate coupling and maximum correlation R,  """
coupling = r"$\Delta\nu_{D}^{cor}$:␣"+"{:.{}f}".format( coupling, 2 )+"Hz"
plt.annotate( coupling, xy=(indexmax*res, max),  xycoords='data',
xytext=(0.55, 0.33), textcoords='axes␣fraction',
horizontalalignment='center', verticalalignment='top')

ratio = "R:␣"+str(ratio)[:5]

""" create correlogram """
plt.subplot(313)
plt.xlim(-5, scale[-1]*0.68)
plt.ylabel(r'correlation')
plt.xlabel(r'$\Delta\nu$␣[Hz]')
plt.plot(scale, pdata,color= colormap[0])
plt.axhline( y=0.5, xmin=0, xmax=1, color='grey',linestyle =':')
plt.grid(True)

""" errorestimation: yError = 2*F(tau)*std """

""" find values in autocorrelation function that deviate by -2std from the
max around 0.5 """
error_list=np.argwhere(pdata[x:]>=max*(1-2*SD))

""" find left /right intervall """
error_left=error_list[0]-indexmax
error_right=error_list[-1]-indexmax

""" put infos together """
infotext = (r"$\Delta_{-}$:␣" + str((error_left+x)*res)[1:6]
+ "Hz,␣" + r"$\Delta_{+}$:␣" + str((error_right+x)*res)[1:5]
+ "Hz,␣res:␣" + str(res)[0:4] +"␣Hz/pt,␣" + r"$\sigma_{I}$:␣"
```

```
+ str(100*(np.abs(SD)))[:4] + "\%,␣" + ratio +"\n")

plt.annotate( infotext, xy=(indexmax*res, max),  xycoords='data',
xytext=(0.05, -0.4), textcoords='axes␣fraction',
horizontalalignment='left', verticalalignment='top')
plt.show()
"""find values in the range of 3 fold standart deviation (3sd: 99.7300204% of
maximum), put them into the list error_list """

print ("Splitting␣:",indexmax,"Points,␣or:",coupling,"Hz\n␣")
print ("left␣error",(error_left+x)*res,"Hz\nright␣error",(error_right+x)*res,
"Hz,\n@", res,"␣Hz/Pt", "\nSD:",np.abs(SD) )
```

11.2.2 Sucrose assignment and extracted RDCs

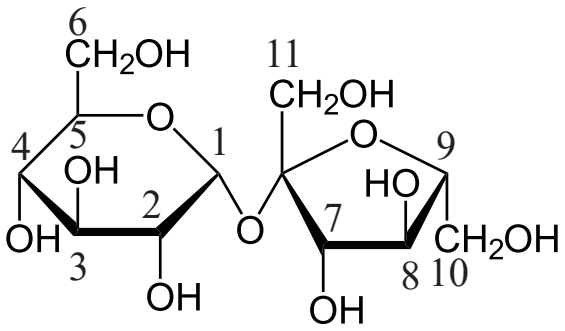

Figure 11.2

Assignment	13C CS	$^{1}J_{CH}$ [Hz]	± Error	1H CS	row	$^{1}T_{CH}$ [Hz]	$^{L\,1}T_{CH}$ [Hz]	$^{R\,1}T_{CH}$ [Hz]	L- Error	R- Error	$^{1}D_{CH}$=T-J	± Error
6	60.02	143.83	0.49	3.75	586.00	144.28	144.53	143.98	-0.25	0.30	0.4	0.50
11	61.25	144.71	0.42	3.60	577.00	144.30	144.37	144.27	-0.07	0.03	-0.4	0.42
10	62.29	143.54	0.67	3.75	569.00	144.11	145.23	143.65	-1.12	0.46	0.6	1.12
4	69.13	144.32	0.36	3.35 - 3.50	519	145.66	163.74	120.54	-18.08	25.12	1.3	18.08
2	70.99	143.82	0.37	3.48	505.00	147.28	147.45	147.13	-0.17	0.15	3.5	0.37
5	72.32	144.26	0.62	3.78	496.00	147.23	147.71	146.51	-0.48	0.72	3.0	0.72
3	72.48	144.54	0.49	3.69	494.00	148.40	148.90	148.19	-0.50	0.21	3.9	0.50
8	73.90	149.88	0.44	3.98	484.00	141.01	141.50	140.95	-0.49	0.06	-8.9	0.49
7	76.30	143.74	1.11	4.15	467.00	138.26	138.95	138.19	-0.69	0.07	-5.5	1.11
9	81.30	147.59	0.71	3.82	430.00	140.33	140.66	139.33	-0.33	1.00	-7.3	1.00
1	92.11	169.56	0.36	5.34	651.00	173.79	174.04	173.68	-0.25	0.11	4.2	0.36

Figure 11.3: Extraction of RDCs from Sucrose in D_2O.

11.2.3 Malectin RDCs

Table 11.5: Assignment and determination of scalar (J), total (T) and residual dipolar (D) couplings from ^{15}N-enriched malectin. The scalar (J) and total (T) couplings were determined from the isotropic ^{1}H^{15}N-IPAP-HSQC and the anisotropic ^{1}H^{15}N-IPAP-HSQC spectra shown in Figure 7.11 and Figure 7.12, respectively.

#[a]	$\delta\,^{1}H$[b]	$\delta\,^{15}N$[c]	$^{1}J_{NH}$[d]	$^{1}T_{NH}$[e]	$^{1}D_{NH}$[f]
3M	8.61	119.84	94.83	n/a	n/a
4D	8.27	117.18	94.83	88.77	-6.06
5K	8.55	111.09	92.81	93.69	0.88
6V	8.18	122.03	94.83	84.75	-10.09
7I	8.29	119.66	92.82	86.76	-6.05
10V	7.35	120.30	94.83	n/a	n/a
11N	8.32	122.10	90.80	110.97	20.18
12A	7.50	123.34	92.82	96.85	4.03
13G	7.57	129.19	92.82	106.94	14.12
14G	8.87	120.24	94.83	102.90	8.07
15E	8.48	125.03	92.86	100.88	8.02
16S	7.51	128.79	92.82	92.82	0.00
17H	10.39	109.84	92.09	76.59	-15.50
18V	7.08	104.21	93.88	82.73	-11.15
20V	8.48	112.65	92.82	95.71	2.89
21H	8.84	123.08	92.78	80.71	-12.07
22G	7.28	128.32	92.82	84.75	-8.07
23I	8.54	127.26	96.84	81.44	-15.40
24H	9.28	114.39	90.80	104.92	14.12
25Y	7.93	119.49	92.82	88.90	-3.91
26R	8.17	107.72	94.83	92.81	-2.02
27K	8.53	124.04	92.82	92.81	0.00
28D	8.28	126.89	92.81	88.78	-4.03
29P	9.35	125.88	94.83	75.15	-19.68
30L	8.10	123.08	92.82	86.76	-6.05
31E	8.08	119.64	90.80	108.96	18.16
32G	6.98	123.61	92.81	82.72	-10.09
34V	8.19	118.21	94.83	86.76	-8.07
35G	6.86	120.57	94.83	102.90	8.07
37A	8.24	118.96	92.82	89.64	-3.17
40Y	8.32	118.79	92.82	95.15	2.33
41A	8.32	123.17	n/a	94.83	n/a
42M	8.46	111.92	92.81	95.83	3.02

Table 11.5: Assignment and determination of scalar (J), total (T) and residual dipolar (D) couplings from ^{15}N-enriched malectin. The scalar (J) and total (T) couplings were determined from the isotropic ^{1}H^{15}N-IPAP-HSQC and the anisotropic ^{1}H^{15}N-IPAP-HSQC spectra shown in Figure 7.11 and Figure 7.12, respectively.

#[a]	$\delta\,^{1}H$[b]	$\delta\,^{15}N$[c]	$^{1}J_{NH}$[d]	$^{1}T_{NH}$[e]	$^{1}D_{NH}$[f]
43K	8.37	129.15	92.81	100.88	8.07
46I	7.96	118.18	94.83	94.83	0.00
47L	7.31	116.22	94.83	84.74	-10.09
48R	7.30	120.72	92.82	78.69	-14.13
50N	7.91	121.62	92.82	102.90	10.09
51P	8.87	130.71	92.81	108.96	16.15
52E	8.75	112.55	92.81	76.67	-16.15
53D	7.08	110.05	94.33	86.76	-7.57
54N	8.91	124.00	n/a	79.23	n/a
56L	9.16	116.78	90.80	92.82	2.02
57Y	7.64	114.98	91.70	93.28	1.58
58Q	7.48	119.57	94.83	80.71	-14.12
59T	7.96	120.22	92.82	86.76	-6.05
60E	7.26	120.20	90.80	88.78	-2.02
61R	6.99	111.27	90.80	82.73	-8.07
63N	7.02	104.53	90.80	96.85	6.05
64E	8.47	117.33	92.81	90.21	-2.60
65D	8.19	119.84	90.80	92.39	1.59
67D	7.30	111.27	106.38	n/a	n/a
68G	7.79	120.04	90.79	96.84	6.05
69Y	7.23	116.05	90.80	98.87	8.07
70D	8.99	116.47	92.81	94.83	2.02
72P	8.12	106.23	94.83	94.83	0.00
73I	8.41	114.86	90.80	97.82	7.02
74K	8.56	121.18	92.82	n/a	n/a
75E	9.10	124.52	90.79	98.86	8.07
77G	7.82	122.91	92.82	88.78	-4.03
78E	8.54	124.85	90.80	85.80	-4.99
79Y	7.54	116.67	92.80	82.73	-10.08
80V	8.77	123.91	92.82	96.85	4.03
81V	8.81	107.47	92.88	98.86	5.98
82E	7.48	118.46	n/a	101.47	n/a
83L	8.97	120.64	94.83	100.89	6.05
84K	9.39	118.64	94.83	104.92	10.09
85F	8.54	129.82	92.81	104.92	12.11
86A	8.95	128.06	92.81	106.94	14.13

Table 11.5: Assignment and determination of scalar (J), total (T) and residual dipolar (D) couplings from ^{15}N-enriched malectin. The scalar (J) and total (T) couplings were determined from the isotropic ^{1}H^{15}N-IPAP-HSQC and the anisotropic ^{1}H^{15}N-IPAP-HSQC spectra shown in Figure 7.11 and Figure 7.12, respectively.

#[a]	$\delta\,^{1}H$[b]	$\delta\,^{15}N$[c]	$^{1}J_{NH}$[d]	$^{1}T_{NH}$[e]	$^{1}D_{NH}$[f]
87E	8.77	125.07	92.81	102.90	10.09
88V	8.29	120.32	92.82	96.85	4.03
89F	9.68	119.60	n/a	90.44	n/a
90F	6.94	117.32	90.79	88.77	-2.02
94Q	9.47	122.15	92.82	n/a	n/a
96K	6.10	114.88	92.81	n/a	n/a
97V	8.51	118.94	94.83	n/a	n/a
99D	8.10	113.10	94.83	n/a	n/a
100V	7.33	120.14	90.58	n/a	n/a
102V	8.08	124.26	94.83	90.80	-4.03
103N	8.02	116.68	90.80	90.80	0.00
104G	8.95	118.06	92.82	96.85	4.03
105H	9.36	126.86	88.78	94.83	6.05
106T	8.87	120.60	90.80	100.89	10.09
107V	9.49	129.68	96.85	96.85	0.00
108V	8.72	101.91	94.39	84.74	-9.65
109K	8.26	122.25	92.82	92.82	0.00
110D	9.39	125.25	94.83	90.80	-4.03
111L	8.49	122.31	92.82	98.87	6.05
112D	7.54	120.74	90.80	88.78	-2.02
113I	8.65	128.99	92.81	94.83	2.02
114HN	9.73	127.37	95.36	86.98	-8.38
115D	8.67	121.32	92.82	88.78	-4.03
116R	7.69	131.79	90.79	90.73	-0.07
119H	7.78	121.17	94.83	n/a	n/a
120S	7.75	113.83	90.79	86.76	-4.03
121T	7.81	106.72	90.80	90.19	-0.61
122A	8.46	112.83	94.83	92.81	-2.02
123H	8.78	120.85	92.81	88.77	-4.04
125E	8.57	113.50	90.80	86.76	-4.04
126I	8.17	129.73	94.83	88.77	-6.06
127I	8.86	119.39	92.81	98.87	6.05
128P	7.14	125.67	92.82	94.83	2.02
129I	9.15	119.92	92.81	100.89	8.07
130S	8.67	123.44	92.82	102.90	10.09
131I	9.50	128.75	92.82	98.87	6.05

Table 11.5: Assignment and determination of scalar (J), total (T) and residual dipolar (D) couplings from ^{15}N-enriched malectin. The scalar (J) and total (T) couplings were determined from the isotropic ^{1}H^{15}N-IPAP-HSQC and the anisotropic ^{1}H^{15}N-IPAP-HSQC spectra shown in Figure 7.11 and Figure 7.12, respectively.

#[a]	$\delta\,^{1}H$[b]	$\delta\,^{15}N$[c]	$^{1}J_{NH}$[d]	$^{1}T_{NH}$[e]	$^{1}D_{NH}$[f]
133K	9.02	121.02	92.81	100.88	8.08
134G	8.23	118.03	92.82	104.92	12.10
135K	8.76	127.03	92.82	96.85	4.03
136L	8.60	126.21	94.83	104.92	10.09
137HN	9.86	127.69	93.08	104.20	11.13
138V	8.91	104.33	94.83	92.81	-2.02
139Q	7.91	119.79	92.82	98.19	5.37
140G	9.38	126.56	96.85	98.87	2.02
141E	9.09	119.89	92.81	102.90	10.09
142V	8.43	124.55	94.83	90.79	-4.03
143S	9.48	126.16	92.82	92.82	0.00
144T	8.51	104.88	92.82	104.92	12.11
145F	8.23	122.05	92.82	107.96	15.14
146T	8.35	120.93	90.79	98.87	8.08
147G	9.29	119.82	96.85	98.87	2.02
149L	9.05	130.41	92.82	92.82	0.00
150S	8.61	117.32	94.83	n/a	n/a
152E	6.78	118.66	92.82	90.80	-2.02
153F	9.13	128.12	92.81	100.88	8.07
154V	9.34	122.51	92.82	92.82	0.00
155K	8.86	128.82	92.82	104.92	12.10
156G	8.93	126.05	94.83	97.96	3.12
158Y	9.01	124.30	92.82	95.55	2.73
159D	8.14	128.42	92.82	88.78	-4.04
160G	9.58	120.44	n/a	77.75	n/a
161P	8.56	120.95	92.81	n/a	n/a
162K	7.32	115.17	92.82	94.83	2.02
164C	7.75	113.61	92.81	n/a	n/a
166Q	8.42	121.42	92.47	94.83	2.36
167F	8.37	111.79	92.81	92.81	0.00
168I	7.74	120.52	92.81	95.96	3.14
169A	7.81	118.75	n/a	77.75	n/a
170K	8.69	115.37	92.82	104.92	12.10
171G	9.01	114.76	94.83	106.94	12.11
172T	9.13	117.43	92.81	104.92	12.11
173A	9.12	126.21	93.69	110.97	17.28

Table 11.5: Assignment and determination of scalar (J), total (T) and residual dipolar (D) couplings from ^{15}N-enriched malectin. The scalar (J) and total (T) couplings were determined from the isotropic ^{1}H^{15}N-IPAP-HSQC and the anisotropic ^{1}H^{15}N-IPAP-HSQC spectra shown in Figure 7.11 and Figure 7.12, respectively.

#[a]	$\delta\,^{1}H$[b]	$\delta\,^{15}N$[c]	$^{1}J_{NH}$[d]	$^{1}T_{NH}$[e]	$^{1}D_{NH}$[f]
175D	8.11	114.99	94.58	n/a	n/a
176L	8.34	107.85	91.12	86.76	-4.36
177M	8.99	121.65	92.82	86.76	-6.06
178L	7.78	114.78	92.82	78.69	-14.13
179D	7.81	117.30	n/a	80.70	n/a
180Q	7.05	119.32	92.81	98.87	6.05
182H	8.25	122.53	94.83	96.85	2.02
184G	8.01	120.72	92.82	96.85	4.03
186E	8.62	122.20	94.83	94.58	-0.26
188K	9.18	110.71	94.83	92.82	-2.02
189E	7.99	121.98	92.82	96.85	4.03
190E	7.89	126.33	92.81	94.83	2.02
12HE	10.32	129.07	98.01	98.44	0.43
The following peaks were excluded due to noise and overlapping.					
45P	8.45	117.68	93.20	n/a	n/a
9A/179L	7.82	117.32	94.83	n/a	n/a
19D/71I	8.59	119.33	92.82	n/a	n/a
36R/148K	8.83	117.80	92.82	n/a	n/a
41G/183P	8.34	123.03	98.87	n/a	n/a
62Y/38S	7.54	117.58	91.13	n/a	n/a
174D/157	8.92	125.43	-92.81	n/a	n/a
87L	8.76	124.89	n/a	105.65	n/a
3G noisy	8.61	119.84	n/a	98.87	n/a
19E/71F	8.59	123.03	n/a	89.60	n/a
36G/148T	8.83	117.91	n/a	99.38	n/a
38V/62Q	7.51	117.67	n/a	107.72	n/a
45G noisy	8.431	100.522	n/a	80-85	n/a
62Q/38V	7.51	117.66	n/a	90.80	n/a
67N/sidechain	7.28	112.16	n/a	183.61	n/a
71F/19E	8.59	119.40	n/a	84.75	n/a
74D/161Y	8.43	1121.47	n/a	96.85	n/a
92V noisy	8.79	127.13	n/a	93.39	n/a
96Q noisy	6.09	114.80	n/a	82.73	n/a
10V/100K	7.32	120.29	n/a	92.82	n/a
116D noisy	7.70	131.76	n/a	102.90	n/a

Table 11.5: Assignment and determination of scalar (J), total (T) and residual dipolar (D) couplings from ^{15}N-enriched malectin. The scalar (J) and total (T) couplings were determined from the isotropic ^{1}H^{15}N-IPAP-HSQC and the anisotropic ^{1}H^{15}N-IPAP-HSQC spectra shown in Figure 7.11 and Figure 7.12, respectively.

#[a]	$\delta\,^{1}H$[b]	$\delta\,^{15}N$[c]	$^{1}J_{NH}$[d]	$^{1}T_{NH}$[e]	$^{1}D_{NH}$[f]
117I noisy	9.74	125.46	n/a	92.89	n/a
119D noisy	7.76	121.19	n/a	84.75	n/a
148T/36G	8.82	117.85	n/a	98.93	n/a
150T noisy	8.61	117.23	n/a	76.67	n/a
157F/174K	8.91	125.37	n/a	98.86	n/a
161Y/74D	8.56	121.06	n/a	87.65	n/a
164N/120R	7.56	113.15	n/a	94.83	n/a
174K/157F	8.91	125.41	n/a	98.86	n/a
99Q/175G	8.10	113.05	n/a	82.73	n/a
183L noisy	8.28	122.48	n/a	118.70	n/a

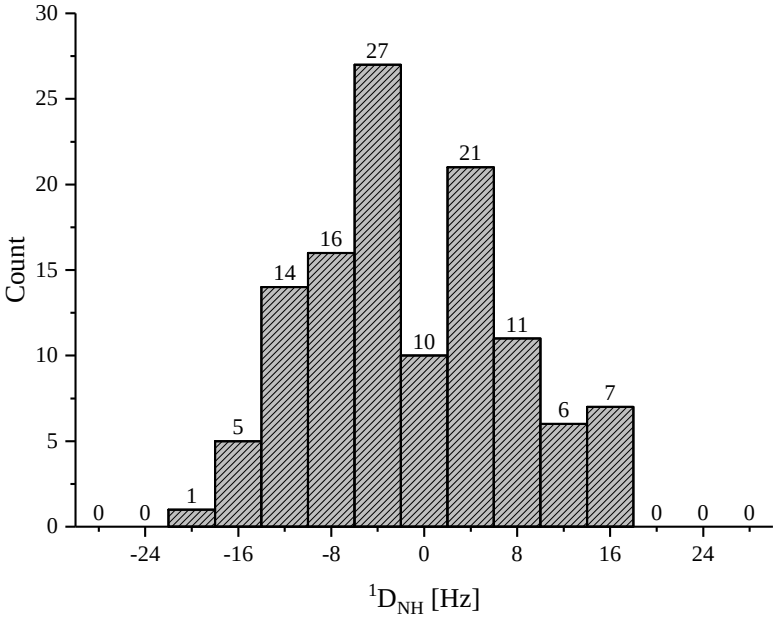

Figure 11.4: Histogram of the extracted $^{1}D_{\mathrm{NH}}$ RDCs.

[a]Number of amino acid residue.
[b]Proton (^{1}N) chemical shift δ in ppm.
[c]Nitrogen (^{15}N) chemical shift δ in ppm.
[d]Scalar coupling $^{1}J_{NH}$ in Hz.
[e]Total coupling $^{1}T_{NH}$ in Hz.
[f]Residual dipolar coupling $^{1}D_{NH}$ in Hz.

11.3 Supplemental material for chapter 8

11.3.1 Iterating script for MDOC on the bwHPC cluster

```
#!/bin/bash
#####################################################
## Purpose: Master script to submit single jobs    ##
## based on the Job run template for bwUniCluster ##
## (ver.  : 2014-09-15, Robert Barthel, KIT, SCC) ##
## to run M independent sub jobs on N cores       ##
#####################################################

##-> Do NOT submit this script to MOAB !!

## Use variables !!! to shorten script code
## -> Don't run your code in $HOME!!

## Location of the COSMOS backend and config directory
EXE=$HOME/COSMOS/bin/cosback.x86_64-STATIC
CONF=$HOME/COSMOS/config
## Location of the COSMOS options file (cos)
COS=$HOME/COSMOS/Staurosporine/exp_op002_DD0007_err_10MSteps_2fs_ver3_16th_noFx.
    cos
## Location of the COSMOS data file (cod)
COD=$HOME/COSMOS/Staurosporine/Staurosporine_.cod

## Use loops !!! to shorten script code
## -> put your numbers in a bash array
## the entries within in the bracket specify the descriptor of the respective
    COSMOS options-, coordinate-, or data-file
list=(1_SRRR_boat 2_SRRR_chair 3_SRSR_boat 4_SRSR_chair 5_SSRR_boat 6_SSRR_chair 7
    _SSSR_boat 8_SSSR_chair)

## Count the number of jobs from the number of elements in $list array
NoJ=${#list[@]}
echo "Number␣of␣Jobs␣in␣is:␣$NoJ"

## Before starting loop, set loop counter
i=1

## Run loop as long as loop counter is smaller then maximum no. of jobs
while [ $i -le $NoJ ] ; do
##
echo "Generate␣Sub␣job␣no:␣$i"
##
## generate 2 digit version of bash array elements
y=$(printf ${list[i-1]})
##
## set output path
OUT=${WORK}/Staurosporine/Staurosporine_ver3_16th_exp_${y}
##
## build MOAB script per job:
sub_script=${0%.sh}_${i}.sh
echo "#!/bin/bash"                    > ${sub_script}
echo "#MSUB␣-l␣nodes=1:ppn=1"        >> ${sub_script}
echo "#MSUB␣-l␣walltime=03:00:00"    >> ${sub_script}
echo "#MSUB␣-l␣pmem=2000mb"          >> ${sub_script}
## set jobname
echo "#MSUB␣-N␣Staurosporine_exp_16th_${list[i-1]}"   >> ${sub_script}
```

```
##
echo "#MSUB␣-m␣abe"                    >> ${sub_script}
echo "#MSUB␣-M␣thomas.gloge@kit.edu" >> ${sub_script}
## set jobinfo name
echo "#MSUB␣-o␣jobinfo_Staurosporine_exp_16th_${list[i-1]}"  >> ${sub_script}
##
echo "${EXE}␣-dw␣-c␣${COS}␣-a␣${COD}␣-f␣${CONF}␣-y␣${OUT}␣␣$HOME/COSMOS/
    Staurosporine/Staurosporine_${list[i-1]}.coo" >> ${sub_script}
##
## generate output directories
mkdir ${OUT}
## before executing
echo "|--␣Executing␣via␣␣:␣msub␣${sub_script}"
##
## execute command
msub ${sub_script}
##
## increase counter
let i+=1
done
```

11.4 Supplemental material for chapter 9

Relaxometry

Table 11.6: Experimental parameters of the DQ experiment for the *Bruker - the minispec - mq20*

DQ experiment	
Initial cycle time /ms	0.04
cycle time increment	0.06
Number of cycles	2
Number of DQ build-up points	87
double increment after ... points	10
FID Evaluation Interval /ms	0.05
Scans	512
Recycle Delay / s	1.5
Gain / dB [a]	86
Dummy shots	4
Pulse attenuation	12
Detection mode	complex
Bandwidth	narrow

[a] This parameter varies according to the homogeneity of the field and the sample due to the initial tuning and matching.

List of Figures

List of Tables

12 | Acknowledgments

Although writing a dissertation is a solitary activity, this work would not have been possible without the participation of many remarkable people and institutional financial and infrastructural involvement. Therefore, I want to thank everyone that contributed to the outcome of my work.

As such, I particularly would like to thank **Prof. Dr. Burkhard Luy**, who welcomed me in his group at KIT and gave me the opportunity to do research on an exciting topic, which connects interdisciplinary the fields of high and low resolution NMR, polymer chemistry and molecular mechanics. Furthermore I want to thank him for his confidence and fruitful discussions that helped sharpening my scientific perspective and the opportunities to take part in several conferences, where I could present my results to a broad scientific community.

Moreover, I want to express my special appreciation and respect to my supervisor **Dr. Pavleta Tzvetkova**, whose untiring support and scientific experience enabled the successful outcome of this work. I also want to thank for her time taken to guide, teach and carefully counter checking this thesis. Her advice and time spend have been invaluable.

Another important person that has an inestimably influence on this work is **Dr. Ulrich Sternberg**, who created the COSMOS software and always was open for critics and proposals towards his program. I especially appreciate his contagious scientific enthusiasm and I am grateful having been able to become acquainted with him and having spent the time in Zagreb at the Ruđer Bošković Institute, also thanks to the **DAAD**.

I also want to thank ALL current and former members of the working group of Prof. Dr. Burkhard Luy (the AK *Bulu*) for the open and good atmosphere. Special

thanks to:

- **Prof. Dr. Raiker Witter** and **Dr. Igor Jakovkin** for the interesting discussions and the introduction to COSMOS.
- **Dr. Sebastian Ehni** for providing the Matlab and Mathematica scripts and his critical eye on the COSMOS program.
- **Dr. Emine Sager** from Novartis, for sharing her deep knowledge about practical aspects of NMR assignments and the fruitful cooperation with COSMOS.
- **Dr. Christian Merle** and **Dr. Grit Kummerlöwe** whose preliminary works on alignment media have build one of the bases of my work.
- **Dr. Tony Reinsperger** for the fruitful and hilarious conversations regarding not only scientific but also societal and cultural (music!) questions.
- **Dr. Malin "Randale" Reller** for taking the time to counter read my work and patiently tolerating antonymic nicknames.
- **PD Dr. Claudia Muhle-Goll** for providing me a sample of malectin and together with **Mara Silber** a sample of selectively ^{15}N and ^{13}C enriched APP.

As my work was funded by the DFG via the SFB1176, I want to thank the executive board, namely **Prof. Dr. Michael A. R. Meier, Prof. Dr. Peter Roesky, Prof. Dr. Manfred Willhelm, Prof. Dr. Stefan Bräse, Prof Dr. Burkhard Luy** and **Prof. Dr. Christopher Barner-Kowollik** who took a great effort, to establish it, and for its confidence, giving me the chance to work under excellent conditions and financing the participation at four conferences abroad. Also to be mentioned are **Dr. Dominik Voll, Cornelia Weber** and **Dr. Marc von Czapiewski** who did great work organizing the workshops, providing research materials for us and having always an open ear to solve bureaucratic or organizational issues as simple as possible.

From our cooperation partners within the SFB1176 I want to thank:

- **Prof. Dr. Leonie Barner** and **Prof. Dr. Patrick Theato**, the former and current leaders of the soft matter lab at the Institute for Chemical Technology and Polymer Chemistry and especially here **Birgit Huber** for providing me PEO-DA with excellent quality and the dispersity measurements of the educt PEO.

- **Prof. Dr. Manfred Willhelm** from the Institute for Chemical Technology and Polymer Chemistry for his passionate commitment for polymer science. Moreover from the workgroup of Prof. Dr. Manfred Willhelm, I want to thank **Dr. Lukas Arens** and **Christian Fengler** for their shear modulus measurements and **Dr. Christoph Pfeiffer** for the discussions regarding the relaxometric low field measurements and data interpretation.

- from the Institute of Mechanical Process Engineering and Mechanics (MVM) and the Engler-Bunte-Institute I want to thank explicitly **Prof. Dr. Gisela Guthausen** for the excessive measurement time at the 20 MHz minispec and valuable tips concerning the interpretation of the data. Furthermore I want to thank **Dr. Xiaoai Guo** and **Solveigh Theissen** for their relaxometric measurements on the gels that I provided.

From the working group of **Prof. Dr. Anne Ulrich** I want to thank **Prof. Anne Ulrich, Dr. Tim Schober, Dr. Sergiy Afonin** and **Dr. Oleg Babii** for providing me several samples of the photo-switchable gramicidin S derivatives. Furthermore I want to thank **Markus Schmitt** for providing substitute probe heads, when one of ours needed to be repaired.

I also want to thank **Prof. Dr. Stefan Bräse** and his former PhD student **Dr. Eduard Spuling** for providing me a sample of hydroxymethylparacyclophane.

From the Institute of Organic Chemistry I like to say thanks to the service people, as they provide the infrastructure that is the base for all scientific work. Here I want to thank especially **Richard von Boenninghausen-Budberg, Jakob Mayer** and **Carlos Miguelez-Böbel**. A unique feature for my thesis was that I was allowed to use the 600 Mhz spectrometer in the basement of IOC in an almost spontaneous manner. Thanks to the confidence of **Pia Lang** and **Dr. Andreas Rapp** I felt privileged.

From outside the academic work I thank you **Golaleh Gloge**. Thanks for your patience and support since we met but especially in the last year! Man bemiram baraye to! I want to further thank my mother **Maria Röll** and **Erwin Röll** for all their care and support. I also want to thank my sister in law **Atefeh Pourahmadi** and my brother **Stefan Braun** and for their positive energy and their support.

Acknowledgements also for the support by the state of Baden-Württemberg through bwHPC and **Robert Bartel** from the Steinbuch Centre for Computing (SCC) at KIT for providing a basic script that allows to loop COSMOS MD runs on the bwHPC cluster over an arbitrary number of options, coordinates and data-sets.

Thanks to **Dr. Christian Ihmels** from the Dortmund Database, for providing me 2nd virial coefficients of DMSO, 1,4-dioxane, DMF and TFE for free.

Finally I want to thank all the people that are missing in this list, as there were so many, who contributed directly and indirectly, here at KIT, but also from my friends.

Bibliography

[1] J. D. Graybeal, *Molecular Spectroscopy*, McGraw-Hill, 1988.

[2] H.-R. Loosli, H. Kessler, H. Oschkinat, H.-P. Weber, T. J. Petcher, A. Widmer, Peptide conformations. Part 31. The conformation of Cyclosporin A in the crystal and in solution, *Helv. Chim. Acta*, 68(3):682–704, 1985.

[3] K. Wüthrich, *NMR of Proteins and Nucleic Acids*, John Wiley & Sons, 1986.

[4] G. Wagner, NMR investigations of protein structure, *Prog Nucl Magn Reson Spectrosc*, 22(2):101–139, 1990.

[5] A. Bax, Weak alignment offers new NMR opportunities to study protein structure and dynamics, *Protein Sci.*, 12(1):1–16, 2003.

[6] J. H. Prestegard, C. M. Bougault, A. I. Kishore, Residual dipolar couplings in structure determination of biomolecules, *Chem. Rev.*, 104(8):3519–3540, 2004.

[7] G. Kummerlöwe, B. Luy, Residual dipolar couplings for the configurational and conformational analysis of organic molecules, in *Annu Rep NMR Spectrosc*, 193–232, Elsevier, 2009.

[8] G. Kummerlöwe, B. Luy, Residual dipolar couplings as a tool in determining the structure of organic molecules, *Trends Anal. Chem.*, 28(4):483–493, 2009.

[9] R. R. Gil, Constitutional, configurational, and conformational analysis of small organic molecules on the basis of NMR residual dipolar couplings, *Angew. Chem. Int. Ed.*, 50(32):7222–7224, 2011.

[10] G. Kummerlöwe, B. Crone, M. Kretschmer, S. F. Kirsch, B. Luy, Residual dipolar couplings as a powerful tool for constitutional analysis: The unexpected formation of tricyclic compounds, *Angew. Chem. Int. Ed.*, 50(11):2643–2645, 2011.

[11] P. Lesot, J. Courtieu, Natural abundance deuterium NMR spectroscopy: Developments and analytical applications in liquids, liquid crystals and solid phases, *Prog Nucl Magn Reson Spectrosc*, 55(2):128–159, 2009.

[12] M. Sarfati, P. Lesot, D. Merlet, J. Courtieu, Theoretical and experimental aspects of enantiomeric differentiation using natural abundance multinuclear NMR spectroscopy in chiral polypeptide liquid crystals, *Chem. Commun.*, 2069–2081, 2000.

[13] B. Luy, A. Frank, H. Kessler, *Conformational Analysis of Drugs by Nuclear Magnetic Resonance Spectroscopy*, chap. 9, 207 – 254, Wiley-VCH, 2007.

[14] Y. Liu, J. Saurí, E. Mevers, M. W. Peczuh, H. Hiemstra, J. Clardy, G. E. Martin, R. T. Williamson, Unequivocal determination of complex molecular structures using anisotropic NMR measurements, *Science*, 356(6333), 2017.

[15] J. A. Losonczi, M. Andrec, M. W. Fischer, J. H. Prestegard, Order matrix analysis of residual dipolar couplings using singular value decomposition, *J. Magn. Reson.*, 138(2):334 – 342, 1999.

[16] A. O. Frank, C. J. Freudenberger, A. K. Shaytan, H. Kessler, B. Luy, Direct prediction of residual dipolar couplings of small molecules in a stretched gel by stochastic molecular dynamics simulations, *Magn. Reson. Chem.*, 53(3):213–217, 2015.

[17] A. Ferrarini, Modeling of macromolecular alignment in nematic virus suspensions. Application to the prediction of NMR residual dipolar couplings, *J. Phys. Chem. B*, 107(31):7923–7931, 2003.

[18] E. E. Burnell, C. A. de Lange, Prediction from molecular shape of solute orientational order in liquid crystals, *Chem. Rev.*, 98(6):2359–2388, 1998.

[19] H. F. Azurmendi, C. A. Bush, Tracking alignment from the moment of inertia tensor (TRAMITE) of biomolecules in neutral dilute liquid crystal solutions, *J. Am. Chem. Soc.*, 124(11):2426–2427, 2002.

[20] P. Trigo-Mouriño, M. C. de la Fuente, R. R. Gil, V. M. Sánchez-Pedregal, A. Navarro-Vázquez, Conformational analysis of the anti-obesity drug lorcaserin in water: How to take advantage of long-range residual dipolar couplings, *Chem.: Eur. J.*, 19(44):14989–14997, 2013.

[21] L. N. Wirz, J. R. Allison, Fitting alignment tensor components to experimental RDCs, CSAs and RQCs, *J. Biomol. NMR*, 62(1):25–29, 2015.

[22] A. Navarro-Vázquez, R. R. Gil, K. Blinov, Computer-assisted 3D structure elucidation (CASE-3D) of natural products combining isotropic and anisotropic NMR parameters, *J. Nat. Prod.*, 81(1):203–210, 2018.

[23] G.-W. Li, H. Liu, F. Qiu, X.-J. Wang, X.-X. Lei, Residual dipolar couplings in structure determination of natural products, *Nat. Prod. Bioprospect.*, 8(4):279–295, 2018.

[24] P. Tzvetkova, U. Sternberg, T. Gloge, A. Navarro-Vázquez, B. Luy, Configuration determination by residual dipolar couplings: Accessing the full conformational space by molecular dynamics with tensorial constraints, *Chem. Sci.*, 10(38):8774–8791, 2019.

[25] C. Merle, G. Kummerlöwe, J. C. Freudenberger, F. Halbach, W. Stöwer, C. L. v. Gostomski, J. Höpfner, T. Beskers, M. Wilhelm, B. Luy, Crosslinked poly(ethylene oxide) as a versatile alignment medium for the measurement of residual anisotropic NMR parameters, *Angew. Chem. Int. Ed.*, 52(39):10309–10312, 2013.

[26] W. Demtröder, *Experimentalphysik 4*, Springer Berlin Heidelberg, 2017.

[27] H. Günther, *NMR spectroscopy: Basic principles, concepts and applications in chemistry*, Wiley-VCH, Weinheim, 3. edn., 2013.

[28] R. R. Ernst, W. A. Anderson, Application of fourier transform spectroscopy to magnetic resonance, *Rev. Sci. Instrum.*, 37(1):93–102, 1966.

[29] R. R. Ernst, Sensitivity enhancement in magnetic resonance, in *Advances in Magnetic and Optical Resonance*, 1–135, Elsevier, 1966.

[30] J. Mason, Conventions for the reporting of nuclear magnetic shielding (or shift) tensors suggested by participants in the NATO ARW on NMR shielding constants at the University of Maryland, College Park, July 1992, *Solid State Nucl. Magn. Reson.*, 2(5):285 – 288, 1993.

[31] M. Levitt, *Spin Dynamics: Basics of Nuclear Magnetic Resonance*, Wiley, 2001.

[32] M. Karplus, Contact electron-spin coupling of nuclear magnetic moments, *J. Chem. Phys.*, 30(1):11–15, 1959.

[33] C. A. G. Haasnoot, F. M. de Leeuw, C. Altona, The relationship between proton-proton NMR coupling constants and substituent electronegativities - I: An empirical generalization of the Karplus equation, *Tetrahedron*, 36(19):2783–2792, 1980.

[34] W. J. Colucci, S. J. Jungk, R. D. Gandour, An equation utilizing empirically derived substituent constants for the prediction of vicinal coupling constants in substituted ethanes, *Magn. Reson. Chem.*, 23(5):335–343, 2019.

[35] E. Díez, J. San-Fabián, J. Guilleme, C. Altona, L. A. Donders, Vicinal proton-proton coupling constants, *Mol. Phys.*, 68(1):49–63, 1989.

[36] M. Quack, Quantum vibrational motion in polyatomic molecules from femtoseconds to days, in *Springer Proceedings in Physics*, 3–7, Springer Berlin Heidelberg, 1994.

[37] G. E. Pake, Nuclear resonance absorption in hydrated crystals: Fine structure of the proton line, *J. Chem. Phys.*, 16(4):327–336, 1948.

[38] F. H. Allen, O. Kennard, D. G. Watson, L. Brammer, A. G. Orpen, R. Taylor, Tables of bond lengths determined by X-ray and neutron diffraction. Part 1. Bond lengths in organic compounds, *J. Chem. Soc.*, 1–19, 1987.

[39] A. Saupe, Kernresonanzen in kristallinen Flüssigkeiten und in kristallinflüssigen Lösungen. Teil I, *Z. Naturforsch. A*, 19a(2):191 – 171, 1964.

[40] A. Saupe, G. Englert, High-resolution nuclear magnetic resonance spectra of orientated molecules, *Phys. Rev. Lett.*, 11(10):462–464, 1963.

[41] C. M. Thiele, A. Marx, R. Berger, J. Fischer, M. Biel, A. Giannis, Determination of the relative configuration of a five-membered lactone from residual dipolar couplings, *Angew. Chem. Int. Ed.*, 45(27):4455–4460, 2006.

[42] A. Schuetz, J. Junker, A. Leonov, O. F. Lange, T. F. Molinski, C. Griesinger, Stereochemistry of Sagittamide A from residual dipolar coupling enhanced NMR, *J. Am. Chem. Soc.*, 129(49):15114–15115, 2007.

[43] A. Schuetz, T. Murakami, N. Takada, J. Junker, M. Hashimoto, C. Griesinger, RDC-enhanced NMR spectroscopy in structure elucidation of Sucro-Neolambertellin, *Angew. Chem. Int. Ed.*, 47(11):2032–2034, 2008.

[44] C. Farès, J. Hassfeld, D. Menche, T. Carlomagno, Simultaneous determination of the conformation and relative configuration of Archazolide A by using nuclear overhauser effects, *J* couplings, and residual dipolar couplings, *Angew. Chem. Int. Ed.*, 47(20):3722–3726, 2008.

[45] J. W. Emsley, Liquid-crystalline materials, in *Solid-State NMR Spectroscopy Principles and Applications*, 512–562, Blackwell Science Ltd, 2007.

[46] G. Kummerlöwe, *Measurement and application of Anisotropic NMR parameters in stretched polymer gels: Stucture determination of small molecule*, Ph.D. thesis, Technische Universität München, 2010.

[47] S. Marčelja, Chain ordering in liquid crystals. I. Even-odd effect, *J. Chem. Phys.*, 60(9):3599–3604, 1974.

[48] S. Sinton, D. Zax, J. Murdoch, A. Pines, Multiple-quantum NMR study of molecular structure and ordering in a liquid crystal, *Mol. Phys.*, 53(2):333–362, 1984.

[49] J. W. Emsley, G. R. Luckhurst, C. P. Stockley, A theory of orientational ordering in uniaxial liquid crystals composed of molecules with alkyl chains, *Pro. Roy. Soc.*, 381(1780):117–138, 1982.

[50] B. Stevensson, D. Sandström, A. Maliniak, Conformational distribution functions extracted from residual dipolar couplings: A hybrid model based on maximum entropy and molecular field theory, *J. Chem. Phys.*, 119(5):2738–2746, 2003.

[51] E. Troche-Pesqueira, C. Anklin, R. R. Gil, A. Navarro-Vázquez, Computer-assisted 3D structure elucidation of natural products using residual dipolar couplings, *Angew. Chem. Int. Ed.*, 56(13):3660–3664, 2017.

[52] M. W. F. Fischer, J. A. Losonczi, J. L. Weaver, J. H. Prestegard, Domain orientation and dynamics in multidomain proteins from residual dipolar couplings, *Biochemistry (Mosc.)*, 38(28):9013–9022, 1999.

[53] H. Al-Hashimi, H. Valafar, M. Terrell, E. Zartler, M. Eidsness, J. Prestegard, Variation of molecular alignment as a means of resolving orientational ambiguities in protein structures from dipolar couplings, *J. Magn. Reson.*, 143(2):402–406, 2000.

[54] A. O. Frank, *About the Interplay of NMR Spectroscopy and Molecular Modeling within Bioorganic and Medicinal Chemistry*, Ph. d. thesis, Technische Universität München, 2009.

[55] B. Hess, R. Scheek, Orientation restraints in molecular dynamics simulations using time and ensemble averaging, *J. Magn. Reson.*, 164(1):19–27, 2003.

[56] J. Meiler, W. Peti, C. Griesinger, Dipocoup: A versatile program for 3D-structure homology comparison based on residual dipolar couplings and pseudocontact shifts, *J. Biomol. NMR*, 17(4):283–294, 2000.

[57] G. Clore, A. M. Gronenborn, A. Bax, A robust method for determining the magnitude of the fully asymmetric alignment tensor of oriented macromolecules in the absence of structural information, *J. Magn. Reson.*, 133(1):216–221, 1998.

[58] H.-J. Sass, G. Musco, S. J. Stahl, P. T. Wingfield, S. Grzesiek, An easy way to include weak alignment constraints into NMR structure calculations, *J. Biomol. NMR*, 21(3):275–280, 2001.

[59] N. Tjandra, J. Marquardt, G. M. Clore, Direct refinement against proton–proton dipolar couplings in NMR structure determination of macromolecules, *J. Magn. Reson.*, 142(2):393–396, 2000.

[60] J. Klages, C. Neubauer, M. Coles, H. Kessler, B. Luy, Structure refinement of Cyclosporin A in chloroform by using RDCs measured in a stretched PDMS-gel, *ChemBioChem*, 6(9):1672–1678, 2005.

[61] M. U. Kiran, A. Sudhakar, J. Klages, G. Kummerlöwe, B. Luy, B. Jagadeesh, RDC enhanced NMR spectroscopy in organic solvent media: The importance for the experimental determination of periodic hydrogen bonded secondary structures, *J. Am. Chem. Soc.*, 131(43):15590–15591, 2009.

[62] R. Witter, W. Prie, U. Sternberg, Chemical shift driven geometry optimization, *J. Comput. Chem.*, 23(2):298–305, 2001.

[63] U. Sternberg, R. Witter, A. S. Ulrich, All-atom molecular dynamics simulations using orientational constraints from anisotropic NMR samples, *J. Biomol. NMR*, 38(1):23–39, 2007.

[64] U. Sternberg, R. Witter, Molecular dynamics simulations on PGLa using NMR orientational constraints, *J. Biomol. NMR*, 63(3):265–274, 2015.

[65] U. Sternberg, M. Klipfel, S. L. Grage, R. Witter, A. S. Ulrich, Calculation of fluorine chemical shift tensors for the interpretation of oriented 19F-NMR spectra of Gramicidin A in membranes, *Phys. Chem. Chem. Phys.*, 11(32):7048, 2009.

[66] D. Grasnick, U. Sternberg, E. Strandberg, P. Wadhwani, A. S. Ulrich, Irregular structure of the HIV fusion peptide in membranes demonstrated by solid-state NMR and MD simulations, *Eur. Biophys. J.*, 40(4):529–543, 2011.

[67] M. Ottiger, F. Delaglio, A. Bax, Measurement of J and dipolar couplings from simplified two-dimensional NMR spectra, *J. Magn. Reson.*, 131(2):373–378, 1998.

[68] J. C. Rowell, W. D. Phillips, L. R. Melby, M. Panar, NMR studies of some liquid crystal systems, *J. Chem. Phys.*, 43(10):3442–3454, 1965.

[69] P. Lesot, M. Sarfati, D. Merlet, B. Ancian, C. Brevard, Determining enantiomeric purity by NMR: Deuterium 2D NMR at natural abundance in weakly oriented chiral liquid crystals enantiomer discrimination using NAD-NMR in PBLG background, Tech. rep., Laboratoire de Chimie Structurale Organique, Université de Paris-Sud, 2001.

[70] D. Merlet, W. Smadja, J. Courtieu, P. Lesot, B. Ancian, Analysis of natural abundance deuterium NMR spectra of enantiomers in chiral liquid crystals via 2D auto-correlation experiments, *Chem. Commun.*, 2301–2302, 1998.

[71] P. Trigo-Mouriño, C. Merle, M. R. M. Koos, B. Luy, R. R. Gil, Probing spatial distribution of alignment by deuterium NMR imaging, *Chem.: Eur. J.*, 19(22):7013–7019, 2013.

[72] J. Yan, A. D. Kline, H. Mo, M. J. Shapiro, E. R. Zartler, A novel method for the determination of stereochemistry in six-membered chairlike rings using residual dipolar couplings, *J. Org. Chem*, 68(5):1786–1795, 2003.

[73] L. Castañar, M. Garcia, E. Hellemann, P. Nolis, R. R. Gil, T. Parella, One-shot determination of residual dipolar couplings: Application to the structural discrimination of small molecules containing multiple stereocenters, *J. Org. Chem*, 81(22):11126–11131, 2016.

[74] J. Keeler, *Understanding NMR Spectroscopy*, Wiley, Chichester, West Sussex, 2. ed., repr. edn., 2011.

[75] A. Enthart, J. C. Freudenberger, J. Furrer, H. Kessler, B. Luy, The CLIP/CLAP-HSQC: Pure absorptive spectra for the measurement of one-bond couplings, *J. Magn. Reson.*, 192(2):314–322, 2008.

[76] P. Tzvetkova, S. Simova, B. Luy, P.E.HSQC: A simple experiment for simultaneous and sign-sensitive measurement of $(^1J_{\mathrm{CH}} + D_{\mathrm{CH}})$ and $(^2J_{\mathrm{HH}} + D_{\mathrm{HH}})$ couplings, *J. Magn. Reson.*, 186(2):193 – 200, 2007.

[77] L. Mueller, P.E.COSY, a simple alternative to E.COSY, *J. Magn. Reson.*, 72(1):191–196, 1987.

[78] C. Griesinger, O. W. Sørensen, R. R. Ernst, Correlation of connected transitions by two-dimensional NMR spectroscopy, *J. Chem. Phys.*, 85(12):6837–6852, 1986.

[79] C. Griesinger, O. W. Sørensen, R. R. Ernst, Two-dimensional correlation of connected NMR transitions, *J. Am. Chem. Soc.*, 107(22):6394–6396, 1985.

[80] M. Huenges, H. Kessler, Structural chemistry using NMR spectroscopy, peptides, in *Encyclopedia of Spectroscopy and Spectrometry*, 2246–2260, Elsevier, 1999.

[81] G. Kummerlöwe, S. Schmitt, B. Luy, Cross-fitting of residual dipolar couplings, *Open Spectrosc. J.*, 4(1):16–27, 2010.

[82] J. Lohman, C. MacLean, Magnetic susceptibility anisotropies from quadrupolar magnetic field effects in high field ^{2}H NMR, *Mol. Phys.*, 38(4):1255–1261, 1979.

[83] J. R. Tolman, J. M. Flanagan, M. A. Kennedy, J. H. Prestegard, Nuclear magnetic dipole interactions in field-oriented proteins: Information for structure determination in solution, *PNAS*, 92(20):9279–9283, 1995.

[84] H. C. Kung, K. Y. Wang, I. Goljer, P. H. Bolton, Magnetic alignment of duplex and quadruplex DNAs, *J. Magn. Reson. B*, 109(3):323–325, 1995.

[85] M. Schmiedeskamp, R. E. Klevit, Paramagnetic cobalt as a probe of the orientation of an accessory DNA-binding region of the yeast ADR1 zinc-finger protein, *Biochemistry (Mosc.)*, 36(46):14003–14011, 1997.

[86] V. Gaponenko, A. Dvoretsky, C. Walsby, B. M. Hoffman, P. R. Rosevear, Calculation of z-coordinates and orientational restraints using a metal binding tag, *Biochemistry (Mosc.)*, 39(49):15217–15224, 2000.

[87] R. D. Spence, H. A. Moses, P. L. Jain, The proton magnetic resonance line in liquid crystals, *J. Chem. Phys.*, 21(2):380–380, 1953.

[88] E. Sackmann, S. Meiboom, L. C. Snyder, Nuclear magnetic resonance spectra of enantiomers in optically active liquid crystals, *J. Am. Chem. Soc.*, 90(8):2183–2184, 1968.

[89] N. Tjandra, Direct measurement of distances and angles in biomolecules by NMR in a dilute liquid crystalline medium, *Science*, 278(5340):1111–1114, 1997.

[90] M. Ottiger, A. Bax, Bicelle-based liquid crystals for NMR-measurement of dipolar couplings at acidic and basic pH values, *J. Biomol. NMR*, 13(2):187–191, 1999.

[91] J. A. Losonczi, J. H. Prestegard, Improved dilute bicelle solutions for high-resolution NMR of biological macromolecules, *J. Biomol. NMR*, 12(3):447–451, 1998.

[92] K. Fleming, D. Gray, S. Prasannan, S. Matthews, Cellulose crystallites: A new and robust liquid crystalline medium for the measurement of residual dipolar couplings, *J. Am. Chem. Soc.*, 122(21):5224–5225, 2000.

[93] S. M. Douglas, J. J. Chou, W. M. Shih, DNA-nanotube-induced alignment of membrane proteins for NMR structure determination, *PNAS*, 104(16):6644–6648, 2007.

[94] J. Lorieau, L. Yao, A. Bax, Liquid crystalline phase of G-tetrad DNA for NMR study of detergent-solubilized proteins, *J. Am. Chem. Soc.*, 130(24):7536–7537, 2008.

[95] J. Sass, F. Cordier, A. Hoffmann, M. Rogowski, A. Cousin, J. G. Omichinski, H. Löwen, S. Grzesiek, Purple membrane induced alignment of biological macromolecules in the magnetic field, *J. Am. Chem. Soc.*, 121(10):2047–2055, 1999.

[96] G. M. Clore, M. R. Starich, A. M. Gronenborn, Measurement of residual dipolar couplings of macromolecules aligned in the nematic phase of a colloidal suspension of rod-shaped viruses, *J. Am. Chem. Soc.*, 120(40):10571–10572, 1998.

[97] M. R. Hansen, L. Mueller, A. Pardi, Tunable alignment of macromolecules by filamentous phage yields dipolar coupling interactions, *Nat. Struct. Biol.*, 5(12):1065–1074, 1998.

[98] H. Desvaux, J.-C. P. Gabriel, P. Berthault, F. Camerel, First use of a mineral liquid crystal for measurement of residual dipolar couplings of a nonlabeled biomolecule, *Angew. Chem. Int. Ed.*, 40(2):373–376, 2001.

[99] J.-C. P. Gabriel, F. Camerel, B. J. Lemaire, H. Desvaux, P. Davidson, P. Batail, Swollen liquid-crystalline lamellar phase based on extended solid-like sheets, *Nature*, 413(6855):504–508, 2001.

[100] S. Cavagnero, H. J. Dyson, P. E. Wright, Improved low pH bicelle system for orienting macromolecules over a wide temperature range, *J. Biomol. NMR*, 13(4):387–391, 1999.

[101] R. S. Prosser, J. A. Losonczi, I. V. Shiyanovskaya, Use of a novel aqueous liquid crystalline medium for high-resolution NMR of macromolecules in solution, *J. Am. Chem. Soc.*, 120(42):11010–11011, 1998.

[102] L. G. Barrientos, C. Dolan, A. M. Gronenborn, Characterization of surfactant liquid crystal phases suitable for molecular alignment and measurement of dipolar couplings, *J. Biomol. NMR*, 16(4):329–337, 2000.

[103] M. Rückert, G. Otting, Alignment of biological macromolecules in novel nonionic liquid crystalline media for NMR experiments, *J. Am. Chem. Soc.*, 122(32):7793–7797, 2000.

[104] K.-V. Schubert, E. W. Kaler, Nonionic microemulsions, *Ber. Bunsen. Phys. Chem.*, 100(3):190–205, 1996.

[105] B. Bendiak, Sensitive through-space dipolar correlations between nuclei of small organic molecules by partial alignment in a deuterated liquid solvent, *J. Am. Chem. Soc.*, 124(50):14862–14863, 2002.

[106] A. Meddour, I. Canet, A. Loewenstein, J. M. Pechine, J. Courtieu, Observation of enantiomers, chiral by virtue of isotopic substitution, through deuterium NMR in a polypeptide liquid crystal, *J. Am. Chem. Soc.*, 116(21):9652–9656, 1994.

[107] J. P. Bayle, J. Courtieu, E. Gabetty, A. Loewenstein, J. M. Pechine, Enantiomeric analysis in a polypeptide lyotropic liquid-crystal through proton decoupled deuterium NMR, *New J. Chem.*, 837 – 838, 1992.

[108] C. M. Thiele, S. Berger, Probing the diastereotopicity of methylene protons in strychnine using residual dipolar couplings, *Org. Lett.*, 5(5):705–708, 2003.

[109] C. M. Thiele, Simultaneous assignment of all diastereotopic protons in strychnine using RDCs: PELG as alignment medium for organic molecules, *J. Org. Chem*, 69(22):7403–7413, 2004.

[110] C. Aroulanda, M. Sarfati, J. Coutieu, P. Lesot, Investigation of the enantioselectivity of three polypeptide liquid-crystalline solvents using NMR spectroscopy, *Enantiomer*, 6(5):281–28, 2001.

[111] L. Arnold, A. Marx, C. M. Thiele, M. Reggelin, Polyguanidines as chiral orienting media for organic compounds, *Chem.: Eur. J.*, 16(34):10342–10346, 2010.

[112] A. Marx, C. Thiele, Orientational properties of poly-γ-benzyl-L-glutamate: Influence of molecular weight and solvent on order parameters of the solute, *Chem.: Eur. J.*, 15(1):254–260, 2009.

[113] W. C. Pomerantz, V. M. Yuwono, R. Drake, J. D. Hartgerink, N. L. Abbott, S. H. Gellman, Lyotropic liquid crystals formed from ACHC-rich β-peptides, *J. Am. Chem. Soc.*, 133(34):13604–13613, 2011.

[114] X. Lei, Z. Xu, H. Sun, S. Wang, C. Griesinger, L. Peng, C. Gao, R. X. Tan, Graphene oxide liquid crystals as a versatile and tunable alignment medium

for the measurement of residual dipolar couplings in organic solvents, *J. Am. Chem. Soc.*, 136(32):11280–11283, 2014.

[115] M. Leyendecker, N.-C. Meyer, C. M. Thiele, Development of new supramolecular lyotropic liquid crystals and their application as alignment media for organic compounds, *Angew. Chem. Int. Ed.*, 56(38):11471–11474, 2017.

[116] M. Leyendecker, *Supramolekulare lyotrop flüssigkristalline Alignment-Medien auf Basis von Benzol-1,3,5-tricarboxamiden*, Ph.D. thesis, Technische Universität Darmstadt, Darmstadt, 2019.

[117] M. Zweckstetter, A. Bax, Characterization of molecular alignment in aqueous suspensions of Pf1 bacteriophage, *J. Biomol. NMR*, 20(4):365–377, 2001.

[118] S. Fraden, G. Maret, D. L. D. Caspar, R. B. Meyer, Isotropic-nematic phase transition and angular correlations in isotropic suspensions of tobacco mosaic virus, *Phys. Rev. Lett.*, 63(19):2068–2071, 1989.

[119] H. Wang, M. Eberstadt, E. T. Olejniczak, R. P. Meadows, S. W. Fesik, A liquid crystalline medium for measuring residual dipolar couplings over a wide range of temperatures, *J. Biomol. NMR*, 12(3):443–446, 1998.

[120] P. Ram, J. Prestegard, Magnetic field induced ordering of bile salt/phospholipid micelles: New media for NMR structural investigations, *Biochim Biophys Acta Biomembr*, 940(2):289–294, 1988.

[121] B. W. Koenig, J.-S. Hu, M. Ottiger, S. Bose, R. W. Hendler, A. Bax, NMR measurement of dipolar couplings in proteins aligned by transient binding to purple membrane fragments, *J. Am. Chem. Soc.*, 121(6):1385–1386, 1999.

[122] H. Singh, M. Shukla, B. J. Rao, K. V. R. Chary, Flagella as a novel alignment medium for the measurement of residual dipolar couplings in proteins, *Chem. Commun.*, 49(97):11403, 2013.

[123] U. V. Reddy, N. Suryaprakash, Scalable weak aligning medium for enantiodiscrimination of water soluble chiral molecules, *Chem. Commun.*, 47(29):8364, 2011.

[124] V. Klochkov, A. Klochkov, C. Thiele, S. Berger, A novel liquid crystalline system for partial alignment of polar organic molecules, *J. Magn. Reson.*, 179(1):58–63, 2006.

[125] L. G. Barrientos, K. Gawrisch, N. Cheng, A. C. Steven, A. M. Gronenborn, Structural characterization of the dilute aqueous surfactant solution

of cetylpyridinium bromide/hexanol/sodium bromide, *Langmuir*, 18(10):3773–3779, 2002.

[126] M. Dama, S. Berger, Ionic liquid crystals as alignment medium to measure residual dipolar couplings for carbohydrates, *Carbohydr. Res.*, 377:44–47, 2013.

[127] H.-J. Sass, G. Musco, S. J. Stahl, P. T. Wingfield, S. Grzesiek, Solution NMR of proteins within polyacrylamide gels: Diffusional properties and residual alignment by mechanical stress or embedding of oriented purple membranes, *J. Biomol. NMR*, 18(4):303–309, 2000.

[128] S. A. Riley, J. R. Giuliani, M. P. Augustine, Capture and manipulation of magnetically aligned Pf1 with an aqueous polymer gel, *J. Magn. Reson.*, 159(1):82–86, 2002.

[129] K. Ruan, J. R. Tolman, Composite alignment media for the measurement of independent sets of NMR residual dipolar couplings, *J. Am. Chem. Soc.*, 127(43):15032–15033, 2005.

[130] Lokesh, N. Suryaprakash, Weakly ordered chiral alignment medium derived from 5'-GMP: Guanosine, *Chem. Commun.*, 49(20):2049, 2013.

[131] Lokesh, N. Suryaprakash, Self-assembly of folic acid: A chiral-aligning medium for enantiodiscrimination of organic molecules in an aqueous environment, *Chem.: Eur. J.*, 18(37):11560–11563, 2012.

[132] E. Troche-Pesqueira, M.-M. Cid, A. Navarro-Vázquez, Disodium cromoglycate: exploiting its properties as a NMR weak-aligning medium for small organic molecules, *Org. Biomol. Chem.*, 12(12):1957–1965, 2014.

[133] S. Hansmann, V. Schmidts, C. M. Thiele, Synthesis of poly-γ-S-2-methylbutyl-L-glutamate and poly-γ-S-2-methylbutyl-D-glutamate and their use as enantiodiscriminating alignment media in NMR spectroscopy, *Chem.: Eur. J.*, 23(38):9114–9121, 2017.

[134] M. Schwab, D. Herold, C. M. Thiele, Polyaspartates as thermoresponsive enantiodifferentiating helically chiral alignment media for anisotropic NMR spectroscopy, *Chem.: Eur. J.*, 23(58):14576–14584, 2017.

[135] S. Jeziorowski, C. M. Thiele, Poly-γ-p-biphenylmethyl-glutamate as enantiodifferentiating alignment medium for NMR spectroscopy with temperature-tunable properties, *Chem.: Eur. J.*, 24(58):15631–15637, 2018.

[136] M. Hirschmann, M. Schwab, C. M. Thiele, Molecular weights: The key for lyotropic liquid crystalline phases of poly-β-benzyl-L-aspartate, *Macromolecules*, 52(15):6025–6034, 2019.

[137] N.-C. Meyer, A. Krupp, V. Schmidts, C. M. Thiele, M. Reggelin, Polyacetylenes as enantiodifferentiating alignment media, *Angew. Chem. Int. Ed.*, 51(33):8334–8338, 2012.

[138] M. Dama, S. Berger, Polyacetylenes as a new alignment medium to measure residual dipolar couplings for chiral organic molecules, *Tetrahedron Lett.*, 53(47):6439–6442, 2012.

[139] M. Dama, S. Berger, Polyisocyanides as a new alignment medium to measure residual dipolar couplings for small organic molecules, *Org. Lett.*, 14(1):241–243, 2011.

[140] X. Lei, F. Qiu, H. Sun, L. Bai, W.-X. Wang, W. Xiang, H. Xiao, A self-assembled oligopeptide as a versatile NMR alignment medium for the measurement of residual dipolar couplings in methanol, *Angew. Chem. Int. Ed.*, 56(42):12857–12861, 2017.

[141] W. Zong, G.-W. Li, J.-M. Cao, X. Lei, M.-L. Hu, H. Sun, C. Griesinger, R. X. Tan, An alignment medium for measuring residual dipolar couplings in pure DMSO: Liquid crystals from graphene oxide grafted with polymer brushes, *Angew. Chem. Int. Ed.*, 55(11):3690–3693, 2016.

[142] B. Deloche, E. T. Samulski, Short-range nematic-like orientational order in strained elastomers: A deuterium magnetic resonance study, *Macromolecules*, 14(3):575–581, 1981.

[143] R. Tycko, F. J. Blanco, Y. Ishii, Alignment of biopolymers in strained gels: A new way to create detectable dipole-dipole couplings in high-resolution biomolecular NMR, *J. Am. Chem. Soc.*, 122(38):9340–9341, 2000.

[144] S. Meier, D. Häussinger, S. Grzesiek, Charged acrylamide copolymer gels as media for weak alignment, *J. Biomol. NMR*, 24(4):351–356, 2002.

[145] T. Cierpicki, J. H. Bushweller, Charged gels as orienting media for measurement of residual dipolar couplings in soluble and integral membrane proteins, *J. Am. Chem. Soc.*, 126(49):16259–16266, 2004.

[146] P. Haberz, J. Farjon, C. Griesinger, A DMSO-compatible orienting medium: Towards the investigation of the stereochemistry of natural products, *Angew. Chem. Int. Ed.*, 44(3):427–429, 2005.

[147] M. Schmidt, H. Sun, A. Leonov, C. Griesinger, U. M. Reinscheid, Chiral discrimination of amines by anisotropic NMR parameters using chiral polyacrylamide-based gels, *Magn. Reson. Chem.*, 50:38–44, 2012.

[148] K. Kobzar, H. Kessler, B. Luy, Stretched gelatin gels as chiral alignment media for the discrimination of enantiomers by NMR spectroscopy, *Angew. Chem. Int. Ed.*, 44(20):3145–3147, 2005.

[149] J. Ma, G. I. Goldberg, N. Tjandra, Weak alignment of biomacromolecules in collagen gels: An alternative way to yield residual dipolar couplings for NMR measurements, *J. Am. Chem. Soc.*, 130(48):16148–16149, 2008.

[150] U. Eliav, G. Navon, Collagen fibers as a chiral agent: A demonstration of stereochemistry effects, *J. Am. Chem. Soc.*, 128(50):15956–15957, 2006.

[151] G. Kummerlöwe, M. U. Kiran, B. Luy, Covalently cross-linked gelatin allows chiral distinction at elevated temperatures and in DMSO, *Chem.: Eur. J.*, 15(45):12192–12195, 2009.

[152] T. Montag, C. M. Thiele, Cross-linked helically chiral poly-(γ-benzyl-L-glutamate) as enantiodiscriminating alignment medium, *Chem.: Eur. J.*, 19(7):2271–2274, 2013.

[153] P. Tzvetkova, D. E. Mendez, M. Dobrowolska, L. Barner, B. Luy, Enantiodiscrimination by NMR with chiral polystyrene based alignment media, unpublished.

[154] J. C. Freudenberger, S. Knör, K. Kobzar, D. Heckmann, T. Paululat, H. Kessler, B. Luy, Stretched poly(vinyl acetate) gels as NMR alignment media for the measurement of residual dipolar couplings in polar organic solvents, *Angew. Chem. Int. Ed.*, 44(3):423–426, 2004.

[155] J. C. Freudenberger, P. Spiteller, R. Bauer, H. Kessler, B. Luy, Stretched poly(dimethylsiloxane) gels as NMR alignment media for apolar and weakly polar organic solvents: An ideal tool for measuring RDCs at low molecular concentrations, *J. Am. Chem. Soc.*, 126(45):14690–14691, 2004.

[156] R. R. Gil, C. Gayathri, N. V. Tsarevsky, K. Matyjaszewski, Stretched poly(methyl methacrylate) gel aligns small organic molecules in chloroform. Stereochemical analysis and diastereotopic proton NMR assignment in ludartin using residual dipolar couplings and $3J$ coupling constant analysis, *J. Org. Chem*, 73(3):840–848, 2008.

[157] B. Luy, K. Kobzar, H. Kessler, An easy and scalable method for the partial alignment of organic molecules for measuring residual dipolar couplings, *Angew. Chem. Int. Ed.*, 43(9):1092–1094, 2004.

[158] G. Kummerlöwe, S. Knör, A. O. Frank, T. Paululat, H. Kessler, B. Luy, Deuterated polymer gels for measuring anisotropic NMR parameters with strongly reduced artefacts, *Chem. Commun.*, 5722–5724, 2008.

[159] G. Kummerlöwe, J. Auernheimer, A. Lendlein, B. Luy, Stretched poly(acrylonitrile) as a scalable alignment medium for DMSO, *J. Am. Chem. Soc.*, 129(19):6080–6081, 2007.

[160] G. Kummerlöwe, M. Behl, A. Lendlein, B. Luy, Artifact-free measurement of residual dipolar couplings in DMSO by the use of cross-linked perdeuterated poly(acrylonitrile) as alignment medium, *Chem. Commun.*, 46(43):8273, 2010.

[161] B. Luy, K. Kobzar, S. Knör, J. Furrer, D. Heckmann, H. Kessler, Orientational properties of stretched polystyrene gels in organic solvents and the suppression of their residual ^{1}H NMR signals, *J. Am. Chem. Soc.*, 127(17):6459–6465, 2005.

[162] P. W. Kuchel, B. E. Chapman, N. Müller, W. A. Bubb, D. J. Philp, A. M. Torres, Apparatus for rapid adjustment of the degree of alignment of NMR samples in aqueous media: Verification with residual quadrupolar splittings in ^{23}Na and ^{133}Cs spectra, *J. Magn. Reson.*, 180(2):256–265, 2006.

[163] B. E. Ramirez, A. Bax, Modulation of the alignment tensor of macromolecules dissolved in a dilute liquid crystalline medium, *J. Am. Chem. Soc.*, 120(35):9106–9107, 1998.

[164] L. F. Gil-Silva, R. Santamaría-Fernández, A. Navarro-Vázquez, R. R. Gil, Collection of NMR scalar and residual dipolar couplings using a single experiment, *Chem.: Eur. J.*, 22(2):472–476, 2015.

[165] M. E. García, S. R. Woodruff, E. Hellemann, N. V. Tsarevsky, R. R. Gil, Di(ethylene glycol) methyl ether methacrylate (DEGMEMA)-derived gels align small organic molecules in methanol, *Magn. Reson. Chem.*, 55(3):206–209, 2016.

[166] P. Kaden, J. C. Freudenberger, B. Luy, Noncovalently and covalently cross-linked polyurethane gels as alignment media and the suppression of residual polymer signals using diffusion-filtered spectroscopy, *Magn. Reson. Chem.*, 50:22–28, 2012.

[167] J. Courtieu, D. W. Alderman, D. M. Grant, J. P. Bayles, Director dynamics and NMR applications of nematic liquid crystals spinning at various angles from the magnetic field, *J. Chem. Phys.*, 77(2):723–730, 1982.

[168] J. Courtieu, Variable angle sample spinning NMR in liquid crystals, *Prog Nucl Magn Reson Spectrosc*, 26:141–169, 1994.

[169] C. M. Thiele, Scaling the alignment of small organic molecules in substituted polyglutamates by variable-angle sample spinning, *Angew. Chem. Int. Ed.*, 44(18):2787–2790, 2005.

[170] Y. Liu, J. H. Prestegard, A device for the measurement of residual chemical shift anisotropy and residual dipolar coupling in soluble and membrane-associated proteins, *J. Biomol. NMR*, 47(4):249–258, 2010.

[171] G. Kummerlöwe, F. Halbach, B. Laufer, B. Luy, Precise measurement of RDCs in water and DMSO based gels using a silicone rubber tube for tunable stretching, *Open Spectrosc. J.*, 2(1):29–33, 2008.

[172] G. Kummerlöwe, E. F. McCord, S. F. Cheatham, S. Niss, R. W. Schnell, B. Luy, Tunable alignment for all polymer gel/solvent combinations for the measurement of anisotropic NMR parameters, *Chem.: Eur. J.*, 16(24):7087–7089, 2010.

[173] E. Sager, *Residual dipolar couplings: A complementary tool for stereochemistry determination of drug compounds*, Ph.D. thesis, Karlsruhe Institute of Technology (KIT), 2019.

[174] C. Gayathri, N. Tsarevsky, R. Gil, Residual dipolar couplings (RDCs) analysis of small molecules made easy: Fast and tuneable alignment by reversible compression/relaxation of reusable PMMA gels, *Chem.: Eur. J.*, 16(12):3622–3626, 2010.

[175] A. Raic, L. Rödling, H. Kalbacher, C. Lee-Thedieck, Biomimetic macroporous PEG hydrogels as 3D scaffolds for the multiplication of human hematopoietic stem and progenitor cells, *Biomaterials*, 35(3):929–940, 2014.

[176] M. S. Hahn, J. S. Miller, J. L. West, Laser scanning lithography for surface micropatterning on hydrogels, *Adv. Mater.*, 17(24):2939–2942, 2005.

[177] O. Bayer, H. Meerwein, E. Müller, K. Ziegler, *Methoden der organischen Chemie, Band XIV/1: Makromolekulare Stoffe*, Thieme, 4th edn., 1962.

[178] P. Luo, R. L. Baldwin, Mechanism of helix induction by trifluoroethanol: A framework for extrapolating the helix-forming properties of peptides from trifluoroethanol/water mixtures back to water, *Biochemistry (Mosc.)*, 36(27):8413–8421, 1997.

[179] A. J. Khintchine, Korrelationstheorie der stationären stochastischen Prozesse, *Math. Ann.*, 109(1):604–615, 1934.

[180] T. Schallus, C. Jaeckh, K. Fehér, A. S. Palma, Y. Liu, J. C. Simpson, M. Mackeen, G. Stier, T. J. Gibson, T. Feizi, T. Pieler, C. Muhle-Goll, Malectin: A novel carbohydrate-binding protein of the endoplasmic reticulum and a candidate player in the early steps of protein N-glycosylation, *Mol. Biol. Cell*, 19(8):3404–3414, 2008.

[181] A. G. Palmer, J. Cavanagh, P. E. Wright, M. Rance, Sensitivity improvement in proton-detected two-dimensional heteronuclear correlation NMR spectroscopy, *Journal of Magnetic Resonance (1969)*, 93(1):151–170, 1991.

[182] L. Kay, P. Keifer, T. Saarinen, Pure absorption gradient enhanced heteronuclear single quantum correlation spectroscopy with improved sensitivity, *J. Am. Chem. Soc.*, 114(26):10663–10665, 1992.

[183] J. Schleucher, M. Schwendinger, M. Sattler, P. Schmidt, O. Schedletzky, S. Glaser, O. Sørensen, C. Griesinger, A general enhancement scheme in heteronuclear multidimensional NMR employing pulsed field gradients, *J. Biomol. NMR*, 4(2), 1994.

[184] M. Liu, X. an Mao, C. Ye, H. Huang, J. K. Nicholson, J. C. Lindon, Improved WATERGATE pulse sequences for solvent suppression in NMR spectroscopy, *J. Magn. Reson.*, 132(1):125–129, 1998.

[185] O. Babii, S. Afonin, L. V. Garmanchuk, V. V. Nikulina, T. V. Nikolaienko, O. V. Storozhuk, D. V. Shelest, O. I. Dasyukevich, L. I. Ostapchenko, V. Iurchenko, S. Zozulya, A. S. Ulrich, I. V. Komarov, Direct photocontrol of peptidomimetics: An alternative to oxygen-dependent photodynamic cancer therapy, *Angew. Chem. Int. Ed.*, 55(18):5493–5496, 2016.

[186] A. Götz, N. Mylonas, P. Högel, M. Silber, H. Heinel, S. Menig, A. Vogel, H. Feyrer, D. Huster, B. Luy, D. Langosch, C. Scharnagl, C. Muhle-Goll, F. Kamp, H. Steiner, Modulating hinge flexibility in the APP transmembrane domain alters γ-secretase cleavage, *Biophys. J.*, 116(11):2103–2120, 2019.

[187] J. P. Perdew, Jacob's ladder of density functional approximations for the exchange-correlation energy, in *AIP Conference Proceedings*, AIP, 2001.

[188] P. A. M. Dirac, Quantum mechanics of many-electron systems, *Pro. Roy. Soc.*, 123(792):714–733, 1929.

[189] N. L. Allinger, *Molecular Structure*, John Wiley & Sons, Inc., 2010.

[190] U. Sternberg, Theory of the influence of the second co-ordination sphere on the chemical shift, *Mol. Phys.*, 63(2):249–267, 1988.

[191] E. Hallas, U. Sternberg, New aspects of the semiempirical theory of 27Al-chemical shift and its application to glasses, *Mol. Phys.*, 68(2):315–326, 1989.

[192] M. Möllhoff, U. Sternberg, Molecular mechanics with fluctuating atomic charges - a new force field with a semi-empirical charge calculation, *J. Mol. Model.*, 7(4):90–102, 2001.

[193] F.-T. Koch, *Entwicklung eines quantenchemischen Verfahrens basierend auf der Bindungspolarisationstheorie zur Ladungsberechnung in großen molekularen Systemen und dessen Anwendung in Kraftfeldrechnungen und ^{13}C-NMR-Spektrenberechnungen*, Ph.D. thesis, TU München, 2004.

[194] A. E. Torda, R. M. Scheek, W. F. van Gunsteren, Time-dependent distance restraints in molecular dynamics simulations, *Chem. Phys. Lett.*, 157(4):289–294, 1989.

[195] A. E. Torda, W. F. van Gunsteren, The refinement of NMR structures by molecular dynamics simulation, *Comput. Phys. Commun.*, 62(2-3):289–296, 1991.

[196] F. Sittel, A. Jain, G. Stock, Principal component analysis of molecular dynamics: On the use of cartesian vs. internal coordinates, *J. Chem. Phys.*, 141(1):014111, 2014.

[197] C. Farès, J. B. Lingnau, C. Wirtz, U. Sternberg, Conformational investigations in flexible molecules using orientational NMR constraints in combination with 3J-couplings and NOE distances, *Molecules*, 24(23):4417, 2019.

[198] B. Barney, MOAB workload manager description, 2020, `https://computing.llnl.gov/tutorials/moab/`.

[199] J. Jovanovic, W. Elling, M. Schürmann, H. Preut, M. Spiteller, Spiro[1,1a,6,6a-tetrahydrocyclopropa[a]indene-1,1'-2',3'-dihydro-1'H-indene], *Acta Crystallogr., Sect. E: Struct. Rep. Online*, 58(1):67–68, 2001.

[200] M. Zweckstetter, NMR: Prediction of molecular alignment from structure using the PALES software, *Nat. Protoc.*, 3(4):679–690, 2008.

[201] A. Navarro-Vázquez, MSpin-RDC. A program for the use of residual dipolar couplings for structure elucidation of small molecules, *Magn. Reson. Chem.*, 50:73–79, 2012.

[202] F. Bloch, Nuclear induction, *Phys. Rev.*, 70:460–474, 1946.

[203] H. Y. Carr, E. M. Purcell, Effects of diffusion on free precession in nuclear magnetic resonance experiments, *Phys. Rev.*, 94:630–638, 1954.

[204] S. Sykora, A primer on scalar relaxation in NMR, 2009, http://www.ebyte.it/library/educards/nmr/Nmr_ScalarRelaxation.html.

[205] N. Wiener, Generalized harmonic analysis, *Acta Math.*, 55(0):117–258, 1930.

[206] V. I. Bakhmutov, *Practical NMR Relaxation for Chemists*, John Wiley & Sons, Ltd, 2004.

[207] K. Saalwächter, W. Chassé, J.-U. Sommer, Structure and swelling of polymer networks: Insights from NMR, *Soft Matter*, 9(29):6587, 2013.

[208] K. Saalwächter, Proton multiple-quantum NMR for the study of chain dynamics and structural constraints in polymeric soft materials, *Progr Nucl Magn Reson Spectrosc*, 51(1):1–35, 2007.

[209] W. Chassé, J. López Valentín, G. D. Genesky, C. Cohen, K. Saalwächter, Precise dipolar coupling constant distribution analysis in proton multiple-quantum NMR of elastomers, *J. Chem. Phys.*, 134(4):044907, 2011.

[210] J. Höpfner, G. Guthausen, K. Saalwächter, M. Wilhelm, Network structure and inhomogeneities of model and commercial polyelectrolyte hydrogels as investigated by low-field proton NMR techniques, *Macromolecules*, 47(13):4251–4265, 2014.

[211] K. Saalwächter, Multiple-quantum NMR studies of anisotropic polymer chain dynamics, in *Modern Magnetic Resonance*, 1–28, Springer, 2017.

[212] G. Guthausen, V. Räntzsch, C. Biquet, S. Schlabach, M. Wilhelm, Investigation of polymer-filler interactions in TiO_2-filled poly(n-alkyl methacrylates) by low-field NMR relaxometry, *Macromol. Chem. Phys.*, 215(9):851–858, 2014.

[213] N. Bloembergen, E. M. Purcell, R. V. Pound, Relaxation effects in nuclear magnetic resonance absorption, *Phys. Rev.*, 73(7):679–712, 1948.

[214] K. Saalwächter, P. Ziegler, O. Spyckerelle, B. Haidar, A. Vidal, J.-U. Sommer, ^{1}H multiple-quantum nuclear magnetic resonance investigations of molecular order distributions in poly(dimethylsiloxane) networks: Evidence for a linear mixing law in bimodal systems, *J. Chem. Phys.*, 119(6):3468–3482, 2003.

[215] T. Gullion, J. Schaefer, Rotational-echo double-resonance NMR, *J. Magn. Reson.*, 81(1):196–200, 1989.

[216] K. Saalwächter, Robust NMR approaches for the determination of homonuclear dipole-dipole coupling constants in studies of solid materials and biomolecules, *ChemPhysChem*, 14(13):3000–3014, 2013.

[217] X. Guo, S. Theissen, J. Claussen, V. Hildebrand, J. Kamphus, M. Wilhelm, B. Luy, G. Guthausen, Topological insight into superabsorbent hydrogel network structures: A ^{1}H double-quantum NMR study, *Macromol. Chem. Phys.*, 219(13):1800100, 2018.

[218] B. Giner, I. Gascón, H. Artigas, C. Lafuente, A. Galindo, Phase equilibrium of binary mixtures of cyclic ethers + chlorobutane isomers: Experimental measurements and SAFT-VR modeling, *J. Phys. Chem. B*, 111(32):9588–9597, 2007.

[219] C. Ihmels, e-mail correspondence, DDBST - Dortmund Data Bank Software & Separation Technology GmbH, 1989, unpublished data from Technische Hochschule Carl Schorlemmer Leuna-Merseburg.

[220] S. Cabani, G. Conti, L. Lepori, Thermodynamic study on aqueous dilute solutions of organic compounds. Part 2 - Cyclic ethers, *Trans. Faraday Soc.*, 67(0):1943–1950, 1971.

[221] J. H. Dymond, K. N. Marsh, R. C. Wilhoit, K. C. Wong, Inorganic Compounds, Second Virial Coefficients, in *Virial Coefficients of Pure Gases*, 23–81, Springer, 2002.

[222] R. Philippe, C. Jambon, P. Cléchet, Thermodynamic properties of dimethylsulfoxide + halomethane mixtures II. Vapour pressures and excess thermodynamic functions, *J. Chem. Thermodyn.*, 5(3):431–444, 1973.

[223] I. Hossenlopp, D. Scott, Vapor heat capacities and enthalpies of vaporization of six organic compounds, *J. Chem. Thermodyn.*, 13(5):405–414, 1981.

[224] J. A. Hopkins, V. R. Bhethanabotla, S. W. Campbell, Total pressure measurements for chloroform + acetone + toluene at 303.15K, *J. Chem. Eng. Data*, 39(3):488–492, 1994.

[225] M. L. McGlashan, A. G. Williamson, Isothermal liquid-vapor equilibriums for system methanol-water, *J. Chem. Eng. Data*, 21(2):196–199, 1976.